CRANFIELD INSTITUTE OF TECHNOLOGY

SCHOOL OF MECHANICAL ENGINEERING

Ph.D. THESIS

W. S. MOHAMMAD

SPACE AIR-CONDITIONING OF MECHANICALLY-VENTILATED ROOMS : COMPUTATION OF FLOW AND HEAT TRANSFER

SUPERVISORS

G.P. HAMMOND
F. ALAMDARI

JUNE 1986

DEDICATED TO MY SON AND DAUGHTER

WAEEL & RASHA

A B S T R A C T

Computational studies of two- and three-dimensional, turbulent recirculating flows within mechanically-ventilated enclosures are reported. Two principal cases are examined: (i) two-dimensional offset jets: and (ii) three-dimensional flow induced in rooms by supply jets emanating from low or high side-wall registers. The calculations were undertaken using iterative finite-domain proceedures which solve the conservation equations for mass, momentum and enthalpy, together with additional transport equations for the turbulent kinetic energy and its dissipation rate . The effect of buoyancy was explicitly accounted for when modelling these equations, in order that they could be employed to simulate buoyant flow in ventilated rooms. Computations of the mean velocity, temperature and convective heat transfer distribution are reported, and compared with experimental data where available.

A modified version of the two-dimensional elliptic code of Pun and Spalding (1977) was employed to simulate the offset jet case. These involve the discharge of a turbulent jet parallel to a flat surface and eventually attaching to it. The investigations covered a wide range of offset ratio (3.5-32.4), and the computed flow properties are compared with measurements from several sources. These comparisons show good agreement downstream of the reattachment point, while some discrepancies are evident upstream from this location. The differences therefore occur mainly in the recirculating flow region, and are believed to arise from shortcoming in the starting profiles, the turbulance model and the treatment of the near-wall flow.

A three-dimensional elliptic finite-domain code was developed to simulate the complex, jet-induced flow within rectangular enclosures. The code was verified using both laminar and turbulent flow test cases on simpler geometries. Comparisons with the measurements and predictions reported by previous researchers were employed for this purpose. Subsequently, the ventilated room simulations were undertaken using three different ventilation arrangements with thermal

conditions corresponding to isothermal, non-buoyant (constant property) and buoyancy-affected flows. The computations were again compared with experimental and numerical predictions of previous researchers. This comparison displayed generally good agreement with these sources.

A study of the flow and convective heat exchange within a warm-air heated room, for which buoyancy effects are significant, is also reported in a bound paper (Alamdari, Hammond and Mohammad, 1986) for three different heat loads. Its aim to assess the balance between accuracy and economy provided by the present higher-level method compared with the intermediate-level convection model of Alamdari and Hammond (1982) when used to supply building thermal simulation programs with accurate convection heat transfer data. The computed results of both models were compared, and indicate that the intermediate-level is a valuable alternative source that can satisfy the needs of building thermal modellers. It provides resonable accuracy at a very modest cost in computing terms.

ACKNOWLEDGEMENTS

I would sincerely like to thank Mr. G.P. Hammond, who beyond the task of supervising the work reported here, has been a constant friendly source of inspiration, encouragement and guidance throughout the course of the study. His critical assessment at all stages of the work was very valuable in bringing the research to a fruitful conclusion.

I also wish to express my gratitude to my co-supervisor Dr. F. Alamdari for his assistance and the way in which he shared with me his numerical computation experience at various stages of this study.

For continuous and warm support, my thanks are directed to my father and sister in Iraq, and to my wife who, with patience and determination, managed to cope as a mother and wife in the difficult circumstances that we had to face during the course of the study.

I am grateful to Mrs. A. Berezuik, Miss L. Sibley and Mrs. A. Walshe for their care and patience in producing the typescript of this thesis.

* * * * * * * * *

CONTENTS OF THESIS — PAGE No.

CONTENTS OF THESIS CONT. PAGE No.

CONTENTS OF THESIS CONT.

CONTENTS OF THESIS CONT. PAGE No.

CONTENTS OF THESIS CONT. PAGE No.

LIST OF FIGURES

LIST OF FIGURES CONT.

LIST OF FIGURES CONT. PAGE No.

LIST OF TABLES

NOTATION

a_1, a_2, a_3, a_4	Coefficients in quadric wake function equation
$a_E, a_W, a_N, a_S, a_U, a_D$	Coefficients in general finite-domain equation
A_g	Grille area (m^2)
A_e, A_w, A_s ... etc.	Area of finite-domain cell boundaries
A_i, B_i, C_i	Coefficients in finite-domain equations (TDMA)
b	The source term in general finite-domain equation
b_x, b_y	Velocity half width for three-dimensional wall-jet (m)
C_1, C_2, C_D	Coefficients in turbulence models
C_f	Skin friction coefficient
C_{ps}	Pressure coefficient
d_e, d_w, d_s ... etc.	Coefficient in pressure correction terms
D_e, D_w, D_s ... etc.	Diffusion terms
D_h	Hydraulic diameter
D_k	Coefficient in block correction equation (TDMA)
F_e, F_w, F_s ... etc.	Convection coefficients ($Kg\ s^{-1}$)
F_x, F_y	Grid expansion factors in x and y direction respectively

g	Gravitational acceleration (ms^{-2})
G_B	Buoyancy production
G_K	Generation rate of turbulence energy
h_c	Convective heat transfer coefficient ($Wm^{-2}K^{-1}$)
H	Time-averaged enthalpy ($J\ Kg^{-1}$)
H_g	Grille height (m)
H_r	Offset ratio
J	Total (convection + diffusion) flux
$J_{\phi j}$	Diffusion flux in direction j
K	Turbulent kinetic energy ($m^2\ s^{-2}$)
l	Length scale
L	Room length (m)
L_ε	Dissipation length scale (m)
M	Mass flow rate ($kg\ s^{-2}$)
n	Normal distance from a wall (m)
N_x, N_y	Number of grid nodes in x and y direction respectively
P	pressure ($N\ m^{-2}$)
P_e	Finite-domain cell Peclet number

P_J	Jaytillaks's p-parameter
P_{tot}	Total pressure ($N\ m^{-2}$)
Pr	Prandtl number
q''	Heat flux (Wm^{-2})
R	Residual source
Re	Reynolds number
Re_m	Maximum Reynolds number
Sc	Schmidt number
S_p, S'_p	Coefficient in linearised finite-domain source expression
S_Φ	General source term
t	Time (s)
T	Temperature (K)
T_R, T_W	Room and wall temperature respectively
u,v,w	Velocity components in x,y and z direction respectively (ms^{-1})
U,V,W	Mean velocity components (ms^{-1})
U_J	Jet inlet velocity (ms^{-1})
U_τ	Friction velocity (ms^{-1})

W_g	Grille width
x,y,z	Coordinate directions
X_r	Reattachment distance (m)
X_{sp}, Y_{sp}, Z_{sp}	Width, height and location of the starting profile
y^+	Dimensionless distance from the wall

Greek Symbols

α	Relaxation factor
β	Coefficient of thermal expansion
Γ	Diffusion coefficient
δ	Wall-jet velocity or temperature width, and also distance between near boundary and boundary node (m)
$\delta_x, \delta_y, \delta_z$	Inter-nodal distances
$\Delta_x, \Delta_y, \Delta_z$	Dimensions of the computational cell
ε	Rate of dissipation of K ($m^2\ s^{-3}$)
κ	Von Karman's constant
θ	Excess temperature (K)
λ	Convergence criteria
μ	Dynamic viscosity ($m^2\ s^{-1}$)

ν	Kinematic viscosity ($m^2\ s^{-1}$)
ζ	Large positive number
ρ	Fluid density ($Kg\ m^{-3}$)
σ	Prandtl/Schmidt number
τ	Stress tensor
τ_w	Wall shear stress ($N\ m^{-2}$)
ϕ	General scalar property
Φ	Time-averaged value of ϕ
Ω	Vorticity

<u>Subscripts</u>

c	Centerline value
eff	Effective value
e,w,n,s,u,d	Control volume faces
i,j,l	Component in cartesian tensor notation
i,j,k	Location of point in a cartesian grid
P,E,W,S,N,U,D	Central node and its neighbours
l	Laminar flow condition
m	Maximum value
O,in	Centreline value in inlet
R	Room value

ref	Reference value
t	Turbulent flow condition
w	Condition at wall

Superscripts

+	Dimensionless value
-	Time-averaged values of products of fluctuating quantitles
~	Approximate solution
*	Previous iteration value
'	Correction to starred values, and also fluctuations relative to the time-averaged values

CHAPTER 1

INTRODUCTION

1.0 INTRODUCTION

1.1 THERMAL COMFORT AND THE BUILT ENVIRONMENT

1.1.1 The Need for Space Air-conditioning

The control of indoor climate, either for human comfort or for the proper performance of some industrial or scientific process, is of great importance throughout the world. People cannot live comfortably and work effectively all the year round without winter heating and/or summer cooling, except in a few favoured areas of the earth's temperate zones. The practice of creating a controlled climate in indoor spaces (for example in homes, schools, hospitals, hotels, commercial offices, and even factories) is no longer a luxury, but an essential part of the modern living and working. Air conditioning implies that the velocity, temperature, relative humidity and sometimes contamination of the air must be controlled within limits imposed by some prior specification. However, air-conditioning distribution systems have traditionally been designed to offset heat gains or losses from the occupied spaces without sufficient attention being devoted to the local pattern of air movement required for human comfort. These patterns usually depend on a number of factors including the entry velocity, the supply-return temperature differential, the dimension of the space, the ventilation air change rate, and the location of the supply terminal devices (1-6). Recent studies of the air flow patterns within building spaces, and particularly the interaction of jets within such enclosures, have been directed toward ensuring compliance with these comfort criteria (4-9).

1.1.2 Air Movement in Rooms

Air movement within mechanically-ventilated enclosures is characterized by the existence of turbulent convective and diffusive transport in all three directions. The flow properties at a given location are consequently dependent on both the upstream and the downstream conditions; the governing partial differential equations are therefore 'elliptic' in nature. Such flows are often called recirculating or elliptic flows, the latter term referring to the type of the governing differential equations. Whatever the terminology, the

important point is that the complexity of these flows has, until recently, been such as to hinder all but approximate forms of analysis. The latter relied on calculation routines based on estimates of the velocity field produced by various inlet opening geometries, such as those giving rise to free or wall-jets. These tools are of limited applicability and cannot provide a detailed description of the air motion. They are only intended to ensure that the velocity is reduced to a low value before the air enters the occupied area of the ventilated spaces (see, for example, the ASHRAE Handbook of Fundamentals, 1977).

The flow patterns and velocity and temperature distributions within mechanically-ventilated enclosures may be obtained by flow visualization and measurements respectively, using either scale-model or full-size rooms. However, these kind of investigations are usually elaborate, expensive to undertake, and sometimes inaccurate. It can be difficult to alter the models geometry. Research dating from the early 1970's has therefore turned toward an alternative approach based on the numerical solution of the governing flow equations for mass, momentum, and scalar properties. This is because recent advances in numerical calculation procedures for fluid flow and heat transfer have brought computer useage within reasonable cost limits for practical design problems.

In the presence of a turbulent motion these numerical procedures usually contain two elements; a turbulence model which attempts to simulate the basic mechanism of turbulent flow, and a computer program which facilitate the solution of the relevant equations by means of numerical integration techniques using a modern computer. The attractive feature of such procedures is that they solve general flow equations which allow modelling of different industrial and environmental flow problems. They also provide the flexibility of altering the flow geometry to fit a particular flow case, and produce field distributions for the flow and associated variables. Thus, valuable design data may be obtained for many engineering projects.

The development, assessment and validation of numerical calculation procedures for complex turbulent flows have shown considerable progress in the recent years. However, few

studies have been undertaken for practical ventilation and heat transfer problems in building spaces (10-17). The research described in this thesis represents a further step in the validation and assessment of these methods for predicting two- and three-dimensional elliptic flows such as those encountered in spaces subjected to artificial heating and ventilation.

1.2 BUILDING THERMAL PERFORMANCE

1.2.1 Thermal Comfort and Energy Conservation

The provision of spatial comfort in building, as is well known, requires a great deal of energy (18). This has led many industrial countries, in the aftermath of the energy crisis of the mid 1970's, to introduce new conservation measures to reduce energy consumption in this area (19). In most of these countries, domestic and commercial buildings consume more than 40-50 percent of the total delivered energy (20), and a high proportion of this (60 percent in the case of the United Kingdom) is used for space heating, cooling and ventilation requirements. The introduction of conservation measures has therefore been accompanied by a vigorous research effort, particularly in regard to the simulation of building thermal performance. This has been undertaken in order to permit a rapid appraisal of alternative design strategies. In such simulation studies, a building is treated as a complex network of thermal resistances and capacitances linked by conductive, convective and radiative processes. The ways in which this complex circuit is treated, forms the so-called building thermal model. However, a weakness of all modern building thermal models is that emphasis has been placed on simulating the transient performance of the building fabric, while the air flow and heat exchange in and around the structure are modelled using only rough approximations (21). Indeed, a comprehensive study of the new generation of building dynamics thermal models by the International Energy Agency (22) concluded that their accuracy is presently limited by uncertainties in the input data, particularly for air infiltration and convective heat transfer rates.

1.2.2 Alternative Approaches for Evaluating Convection Coefficients

Building thermal modellers have typically utilized the empirical data recommended by the ASHRAE (23) and CIBSE (24) design guides when specifying convection coefficients within dwelling and offices. In these data, both guides seem to ignore the possibility of 'forced' convective heating, and employ only buoyancy-driven (traditionally called 'free' or 'natural') convective internal surface coefficients to obtain fabric 'U-values'. The CIBSE guide, however, has provided an approximate correction factor to the buoyancy-driven data when the air velocity over individual surfaces has non-zero values. Unfortunately, this practice is not very helpful; as Alamdari and Hammond (25) have noted that the designer generally has no means of determining this velocity a priori. They also observed that such a procedure neglects variations in surface coefficients due to different heating system/room configurations. Recent field and laboratory 'environmental chamber' measurements (26-27) have, not surprisingly, shown that forced convective heating and/or mechanical ventilation of enclosures give rise to internal convective transfer rates that are much higher than the guides values. Water (28) has also demonstrated that the accuracy of his building thermal models is strongly dependent on the correct choice of internal exchange coefficient when simulating mechanically-ventilated structures.

In an effort to obtain improved convective heat transfer data appropriate to the need of building thermal models, a 'hierarchy' of interacting and interdependent approaches to calculate surface coefficients have been developed at Cranfield (21,25). These models were initially developed for mechanically-ventilated enclosures, such as warm-air heated rooms or air-conditioned offices in which the forced convective motion induced by the air supply jets predominates. The calculation methods themselves range from 'lower-level' approaches, such as wall-jet profile analysis (29-30) and improved data correlations for buoyancy-driven convection (31), to the deployment of a 'high-level' flow model that solve a discretized form of the governing elliptic equations for complex, jet induced room air flow (21,32). Both the higher- and lower-level models have been used to develop and verify an 'intermediate-level' computer code (25), which formed the basis for generating input convection heat transfer

data for dynamic building thermal models. It has been argued (21,25) that this code appears to offer the best prospect of meeting the needs for building thermal simulation in terms of accuracy, economy and user friendliness. This is in part due to the fact that dynamic building thermal models employ multiple (space and time) averaged heat transfer coefficients of individual structure elements: ceilings, floors, roofs, walls and windows. The success of this approach led to the development of an anologous intermediate-level computer code for wind-induced, external convective from building (21).

1.2.3 The Development and Verification of Intermediate-level Convective Models

The way in which the various calculation methods interact is illustrated in figure (1.1). The classification scheme adopted for these methods 'levels' was intended (21) to reflect the potential generality of their range of application, rather than their scientific sophistication (see (21) for a fuller explanation of the term). The iterative process of developing and verifying the intermediate level methods is represented in figure (1.1) by the blocks within the dashed line. Both experimental data obtained from full- and model-scale tests, and the computed results of a higher-level computer code have been used for verification purposes. This was conceived by Alamdari etal (21) as a feedback process from which ad hoc corrections would be made to the intermediate level computer codes.

1.2.4 Limitation of the Intermediate-level Approaches

An apparent limitation of the intermediate-level model is that, having been developed as a 'generalization' of the lower-level methods (21) which are only valid for simple shear flows, they cannot deal with the consequences of flow interactions. The model for mechanically-ventilated enclosures, for example, uses the known characteristics of turbulent wall-jets (29-30) to simulate air distribution systems in which the supply air jet is emitted near, and runs parallel to, one of the room surfaces. However, such wall-jets will inevitably be influenced by jet-impingement against backward-facing walls, and by 'secondary flows' or longitudinal vortices along stream-wise corners. Alamdari, Hammond and Montazerin

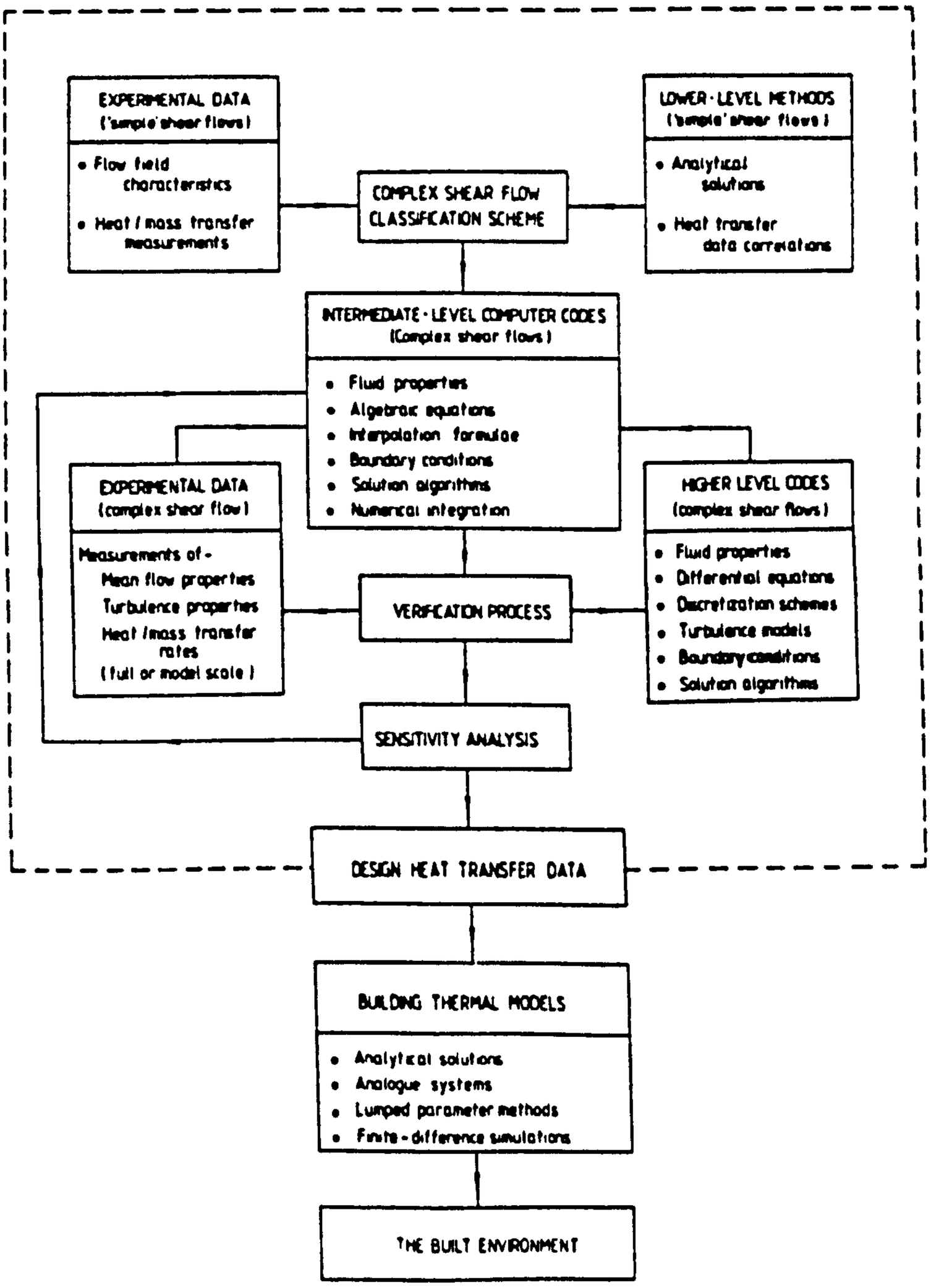

Fig 1.1 : Development sequence of intermediate-level computer programs for building convective heat transfer
[after Alamdari etal [21]]

(33) observed that the former phenomenon is likely to have only a relatively small effect, on surface-averaged convective coefficients. Nevertheless, they cause a significant deviation in the local heat transfer distribution between the computations from both the intermediate- and high-level models and experimental measurements (33).

The high-level flow model previously used at Cranfield (21,32,33) was limited to cases involving two-dimensional non-buoyant flows. Most practical flow problems in buildings are three-dimensional in nature, and are often accompanied by significant buoyancy effects. In order to assess the effects of the latter phenomenan, which are more important with three dimensional flows, and to verify the intermediate-level calculation methods it is necessary to have reliable validation data. There are two potential sources of such data, either experimental measurements or the computations of a three-dimensional, high-level flow model. The full-scale experimental measurements (as have been mentioned in section 1.1.2) are expensive in terms of man-power and other resources. The development of higher-level models, on the other hand, in addition to satisfying this particular need, also enable the simulation of other elliptic flow problems of industrial and environmental importance. The development of a three-dimensional, high-level flow model was therefore the main purpose of the present study.

1.3 THE AIM OF THE PRESENT WORK

The present work was aimed at developing a three-dimensional finite-domain computer program that could handle a steady (statistically stationary) elliptic flows. It was intended to test and validate the 'predictions' of this program by comparison with available measurements, and the numerical computation of previous researchers for a range of complex laminar and turbulent flows applicable to the built environment. The program would then be used to predict the air flow and convective heat transfer within mechanically-ventilated rooms for both isothermal and buoyancy-effected flows. However, in the first instance, the two-dimensional elliptic code of Pun and Spalding (34), (The CHAMPION 2/E/FIX program) was used to predict the behaviour of turbulent off-set jet flows, in order to gain familiarity with the numerical computation techniques. These

jet-flows are, in any case, of considerable importance in their own right.

1.4 LAYOUT OF THE THESIS

The present work concentrate on two main areas; the first was concerned with the use of the CHAMPION 2/E/FIX code to predict two-dimensional turbulent offset jet flows, while the second dealt with the development, validation, verification and implementation of the three-dimensional elliptic code. The mathematical foundation of the present work is first presented in a general (three-dimensional) form in chapter 2, while the corresponding finite-domain formulation and the numerical calculation procedures are discussed in chapter 3. This is followed in chapter 4 by a description of the two-dimensional off-set jet studies, including comparisons with the available data. The solution procedure used in the three-dimensional elliptic code is presented in chapter 5, where its use for two laminar flow test cases (flow through a sudden expansion and flow in a three-dimensional cavity with moving wall) is discussed. A comparison with experimental and numerical data from other sources are also presented for these test cases in order to verify the performance of the present code. The use of the code to simulate developing turbulent flow in square ducts is discussed in chapter 6. Computations were again compared with experimental and computational results of previous researchers in order to assess the predictability of the code for turbulent flow situations. In the following chapter 7, computations for isothermal and buoyancy-affected flows in mechanically-ventilated rooms of different geometries are presented. The computed flow field variables and surface heat transfer coefficients were again compared with various data sets. General conclusions are drawn concerning the validity of the various calculations in chapter 8, where recommendations are made also for further research. Finally, a bounded paper entitled "computation of air flow and convective heat transfer within space-conditioned, rectangular enclosures" (Alamdari, Hammond and Mohammad, 1986) reports the results of a comparative study of the performance of both the higher- and intermediate-level models for calculating heat transfer in warm-air heated rooms.

CHAPTER 2

MATHEMATICAL FRAMEWORK

2.0 MATHEMATICAL FRAMEWORK

2.1 INTRODUCTION

Practical situations involving fluid flow and heat transfer, including mechanical ventilation, are governed by the principles of conservation of mass, momentum and any general scalar properity of the flow. These principles can be expressed in terms of partial differential equations (PDE's) for both laminar and turbulent flow regimes. The present chapter summarises these PDE's and explains how they are formulated to permit the solution of practical problems.

2.2. GENERAL CONSERVATION EQUATIONS

2.2.1 Time Dependent Continuity and Momentum Equations

The conservation equations may be expressed in a cartesian tensor notation as follows (35):

(i) Mass Conservation (continuity)

$$\frac{\partial \rho}{\partial t} + \frac{\partial}{\partial x_i} (\rho u_i) = 0.0 \qquad 2.1$$

(ii) Momentum conservation (Navier-Stokes-equations)

$$\frac{\partial}{\partial t} (\rho u_i) + \frac{\partial}{\partial x_j}(\rho u_j u_i) = - \frac{\partial P}{\partial x_i} + \frac{\partial \tau_{ij}}{\partial x_j} + S_{b,i} \qquad 2.2$$

where u_i are the instantaneous velocity components in the i-direction, i = 1,2,3 ;

P is the instantaneous pressure ;

ρ is the density of the flow ;

τ is the stress tensor (see section 2.2.3) ;

t is time ;

x_i, x_j are the space co-ordinates system, when subscript is repeated in a term a summation of N terms is implied, (N = 2 or 3 depending on whether two- or three-dimensional flow is considered).

$S_{b,i}$ are buoyancy source or sink terms.

Equation 2.2 represents a set of N second order elliptic differential equations, corresponding to the N components of velocity in the cartesian co-ordinates. This set must be solved simultaneously with the first order diferential equation for continuity (equation 2.1) in order to obtain the volocity and pressure field.

2.2.2 Conservation Equation for Scalar Property.

The conservation equations governing the dispersion of certain scalar properties of the flow, such as enthalpy/temperature, turbulence kinetic energy K or turbulence dissipation rate ε, have similarity of form. They can therefore be represented by a single differential equation for some general scalar property (ϕ) as follows:

$$\frac{\partial(\rho\phi)}{\partial t} + \frac{\partial}{\partial x_j}(\rho u_j \phi) = \frac{\partial J_{\phi,j}}{\partial x_j} + S_\phi \qquad 2.3$$

Where S_ϕ represents a source or sink for ϕ, and $J_{\phi,j}$ is the diffusion flux in j-direction. The form of the latter flux will be discussed below.

2.2.3 Auxiliary Relations

The molecular diffusion of mementum, τ_{ij}, and scalar property flux, $J_{\phi j}$, in equation (2.2-2.3) can be related to gradient of velocity components and scalar properties respectively. In constant-property flows these constitutive relation are as follows (36):

$$\tau_{ij} = \mu \left(\frac{\partial u_i}{\partial x_j} + \frac{\partial u_j}{\partial x_i}\right) \qquad 2.4$$

$$J_{\phi j} = \frac{\mu}{\sigma_\phi} \left(\frac{\partial \phi}{\partial x_j}\right) \qquad 2.5$$

Where μ and σ_ϕ are the dynamic viscosity and Prandtl/Schmidt number of fluid respectively.

2.3 TIME-AVERAGED EQUATIONS FOR STATISTICALLY STATIONARY TURBULENT FLOW

Some scientists have recently tackled the turbulent flow problem by attempting to solve the time-dependent Navier-Stokes equations directly using numerical methods. These calculations, which are very expensive, are made to explore the physics of the turbulence itself rather than to solve an engineering problem. In many practical situations the details of the small-scale motion of the flow are unimportant. Therefore, the problem may be approached by utilising the time-averaged version of the Navier-Stokes and associated equations, in which the instantaneous properties of the flow are replaced by time-averaged (mean) values with fluctuating values superimposed upon them (37). In a statistically stationary (sometime, but misleading, termed 'steady') flow the mean value of each variable ϕ (i.e. u,v,w,P,h...etc) is given by:

$$\Phi = \frac{1}{t} \int_0^t \phi \, dt \qquad 2.6$$

$$\phi = \Phi + \phi' \qquad 2.7$$

Where Φ and ϕ' are the time-averaged and fluctuating component of the variable respectively.

Substituting for the instantaneous values of each variable in equations 2.1, 2.2 and 2.3, and time-averaging (38) yields the following equations which govern the mean motion of a 'steady' turbulent flow of uniform density:

(i) Continuity

$$\frac{\partial}{\partial x_j} (\rho U_i) = 0.0 \qquad 2.8$$

(ii) Momentum

$$\frac{\partial}{\partial x_j} (\rho U_i U_j) = \frac{\partial}{\partial x_j} \left[\mu \left(\frac{\partial U_i}{\partial x_j} + \frac{\partial U_j}{\partial x_i} \right) - \overline{\rho u_i' u_j'} \right]$$

$$- \frac{\partial P}{\partial x_i} + S_{b,i} \qquad 2.9$$

(iii) General scalar property

$$\frac{\partial}{\partial x_j} (\rho \Phi U_j) = \frac{\partial}{\partial x_j} \left[\frac{\mu}{\sigma_\Phi} \left(\frac{\partial \Phi}{\partial x_j} \right) - \overline{\rho \phi' u_j'} \right] + S_\Phi \qquad 2.10$$

Where U are the time-averaged velocity components,
P is the " " static pressure,
Φ is the " " general scalar property,
S_Φ is the " " source/sink of Φ
u′ is the fluctuating value of U, and
ϕ' is the " " of ϕ.

The additional terms appearing in equations (2.9-10) i.e. $(-\rho \acute{u}_i \acute{u}_j)$ and $(-\rho \acute{u}_j \acute{\phi})$ are called the Reynolds stress tensor and turbulent flux tensor respectively, while the equations themselves are often termed Reynolds equations. The main difficulty in solving these equations concerns the determination of the Reynolds tensors. It is not possible to compute their values directly as additional transport equations for the turbulent fluxes involve further unknown quantities. Therefore before any solution can be obtained they must be approximated in terms of a known or calculable quantities. These approximations are called turbulence models, and are the subject of the next section.

2.4 TURBULENCE MODELS

The Reynolds stress tensor constitutes an unknown term in the momentum equation (2.9) which has to be related to other, calculable turbulence and/or mean properties of the flow field in order that it may be determined. The necessary algebraic or differential equations collectively constitute a turbulence closure or model.

The first turbulence closure was introduced by Boussinesq, who suggested that it might be possible to replace the Reynolds shear stress by turbulent or 'eddy' viscosity (μ_t). Since then it has been the task of many workers to determine μ_t, and progress has advanced from merely formulating algebraic expressions to the more difficult problem of solving partial differential 'transport' equations involving turbulence quantities.

The basic requirements of a turbulence model are accuracy, wide applicability, economy and simplicity. A number of state-of-the-art reviews of turbulence modelling have been produced (see, for example, 38-42). They indicate the wide variety of models that are now available, and which lend themselves to several types of classification. Although there is no ideal classification scheme, the one suggested by Reynolds (43) and described below provides a systematic framework for discussing the various models.

2.4.1 The Classification of Turbulence Models

i) Zero equation models

The zero-equation models are those in which no partial differential, or transport, equations for turbulence quantities are used. They employed an algebraic expression based on empirical data, and often need to be varied for each flow situation. The Boussinesq eddy visosity formulation is an example of such models, in which the turbulent transport is related to the gradient of mean flow quantities. For example, in thin shear layers:

$$-\rho\overline{u_1'u_2'} = \mu_t \left(\frac{\partial U}{\partial x_2}\right) \qquad 2.11$$

$$-\rho\overline{u_2'\phi'} = \frac{\mu_t}{\sigma_t}\left(\frac{\partial \Phi}{\partial x_2}\right) \qquad 2.12$$

The mixing length hypothesis relates the turbulent viscosity to the local mean velocity gradient:

$$\mu_t = l_m^2 \left|\frac{\partial U}{\partial x_2}\right|$$

where l_m is the mixing length, and must be described over the flow field empirically.

ii) One equation models

Here a differential equation is solved for a suitable velocity scale of the turbulent motion, usually as such a scale, $\sqrt{K}$ is taken, where K is the kinetic energy of the turbulent motion. A corresponding turbulent length scale distribution must then be prescribed algebraically for each flow. The modelling proposal of Launder and Spalding (39) and others lead to the following equation for K, which is applicable only to flows or flow regions where the local turbulence Reynolds number, Re_t is sufficiently high.

$$\frac{\partial}{\partial x_j}(\rho K U_j) = \frac{\partial}{\partial x_j}\left(\frac{\mu_t}{\sigma_k}\frac{\partial K}{\partial x_j}\right) + G_k - \rho\varepsilon \qquad 2.14$$

and

$$G_k = \mu_t \left[\frac{\partial U_i}{\partial x_j}\left(\frac{\partial U_i}{\partial x_j} + \frac{\partial U_j}{\partial x_i}\right)\right] \qquad 2.15$$

where ε is the turbulence energy dissipation rate,

σ_k is Prandtl/Schmidt number for K and,

G_k is the generation term.

In such models, the dissipation rate is usually defined from:

$$\varepsilon = C' K^{\frac{3}{2}} / l \qquad 2.16$$

where C' is an empirical constant, and l is the dissipation length scale and must be prescribed empirically in a similar to that for l_m.

Two principal suggestions have been made to relate the turbulent stresses to the kinetic energy K (42). The first suggestion utilises eddy viscosity concept, and yields the so-called Kolmogorov-Prandtl expression:

$$\mu_t = C_D \rho K^{\frac{1}{2}} l \qquad 2.17$$

where C_D is an empirical constant.

The alternative proposal is due to Bradshaw etal (44), in which the K-equation is converted into a transport equation for the shear stress ($\rho \acute{u}_i \acute{u}_j$) by assuming a direct link between $\rho \acute{u}_i \acute{u}_j$ and K. They further assumed that the diffusion flux of K is proportional to a bulk velocity.

(iii) Two-equation models

Two equation models commonly solve a transport equation for a turbulence length scale parameter in addition to one for K. This overcomes the need to specify the length scale empirically, which is difficult in complex recirculating flows. In practice it proves to be more satisfactory to solve a transport equation for the energy dissipation rate (ε), rather than the dissipation length scale (l). The two variables related (45) by equation (2.16), and therefore l can be easily recovered if desired. By combining equation (2.16) and (2.17) the turbulent viscosity can be linked to K and ε. Thus

$$\mu_t = C_D \rho \frac{K^2}{\varepsilon} \qquad 2.18$$

Two-equation models are the simplest available means of calculating turbulent stresses in recirculating or separated flows. Where it is very difficult to prescribe the length scale distribution algebraically (46-48). The popular model which used the turbulence energy dissipation rate in place of the length scale equation is known as energy-dissipation or K-ε model of turbulence, see section 2.4.2.

iv) Stress equation models

The models which are based on the eddy viscosity/diffusivity concept are not valid under all circumstances. The main limitation of this approach is that the eddy viscosity and diffusivity are assumed to be isotropic; that is the same values are taken for the various $\overline{\rho u_i' u_j'}$'s and $\overline{\rho u_i' \phi'}$s. However in complex flows or flows with turbulence influenced by strong body forces acting in prefered directions, such as buoyancy forces, it is strictly anisotropic. The local state of turbulence is also characterized by one velocity scale, $\sqrt{K}$, and individual stresses are related to this scale. In reality, each stress component may develop in the flow quite differently.

In order to account for the different development of individual stress components, transport equations for all the components of $-\rho \overline{u_i' u_j'}$, and analogous equations for all the scalar fluxes $-\rho u_i \phi$, are necessary. These models are often called multi-equation models or second order closure-schemes (43). The differential equations for such models are complex, and have the general form:

$$\frac{D\left(\rho \overline{u_i' u_j'}\right)}{D_t} = \text{production + dissipation and redistriction} \qquad 2.19$$

There are, it should be noted, six such equations in a general three-dimensional flow, corresponding to each of the stress components. A variety of such models have been proposed by different investigators (41, 49-50).

v) Large-eddy simulations

In this approach three dimensional time-dependent numerical computations are performed for the large-eddy structure while a sub-grid effective viscosity is used for the small scale turbulence. The program of developing and explorating this approach was started in 1973 by a group at Stanford University with close co-operation from Nasa-Ames Laboratory. Considerable success has been achieved since that time, and a more detailed description can be found in (43).

2.4.2 Selection of Model for The Present Study

The zero-equation models are applicable to simple, two-dimensional thin shear flows (51), where the length scale may be easily prescribed empirically and the predominante mean velocity gradient does not change sign. The one-equation models solve a differential transport equation for K. Thus the effect of upstream history and free-stream turbulence may be taken into account. However, the problem of specifying the length scale distribution in complex flows remains. Such a model was used with considerable success by Launder and Ying (52) to predict the fully-developed flow in a square duct, but this is one of the few situations (other than two-dimensional thin shear layers) where sufficient knowledge of length scale distribution is available. Therefore, zero and one-equation models are not suitable for the present work; where the flow patterns are complex and a description of mixing length or length scale is difficult.

The multi-equation models appears, from the fundamental point of view, to be more accurate and 'universal', but they require much more computer time than the two-equation models, since there are more PDE's to be solved. The validation studies that have compared the two-equation models with stress transport models, such as that by Pope and Whitelaw (53), have shown that the predictions of the latter models display little improvement.

The two-equation model was therefore adopted for the present study principally because it is capable of handling complex recirculating flows without the need to prescribe a length scale, and

it uses much less computation time than do more complicated models. In the present study the 'K-ε' turbulence model was employed to predict two-and three-dimensional flows. An assessment of the model will be given later, but the nature of the differential equations used in this model will first be described more fully.

Energy-dissipation turbulence closure

The K-ε model was first put forward by Harlow and Nakayama (54), and a full account of the form used in the present work is given by Launder and Spalding (45). The fundamental supposition of this model is that the turbulence is adequately characterized by two quantities.

a) the kinetic energy of turbulence, K; and
b) the dissipation of turbulent kinetic energy, ε.

The transport equation for K is obtained via the equation of turbulent velocity fluctuation u_i'. The latter can be derived with the help of equation (2.7) by subtracting the time-average momentum equation (2.9) from the time-dependent momentum equation (2.2). The results are:

$$U_j \frac{\partial u_i'}{\partial x_j} = - u_j' \frac{\partial U_i}{\partial x_j} - \frac{\partial}{\partial x_j} (u_i' u_j' - \overline{u_i' u_j'}) - \frac{1}{\rho} \frac{\partial P'}{\partial x_i} + \nu \frac{\partial^2 u_i'}{\partial x_j^2} \qquad 2.20$$

where P' represent the fluctuating pressure. By multiplying equation (2.20) by u_i', and time averaging it yield the turbulent kinetic energy equation (45):

$$U_j \frac{\partial K}{\partial x_j} = - \overline{u_i' u_j'} \frac{\partial U_i}{\partial x_j} - \frac{\partial}{\partial x_j} \left(\frac{\overline{u_j' P'}}{\rho} + \overline{u_j' k'} - \nu \frac{\partial K}{\partial x_j} \right) - \varepsilon$$

I II III IV

2.21

where $K' = 0.5\ \overline{U_i'^2}$ and $\varepsilon = \nu\ \overline{(\frac{\partial u_i'}{\partial x_j})^2}$. According to Launder and Spalding (39) this equation expresses the fact that changes of kinetic energy will occur over a small element of fluid (I) as a result of an imbalance between the generation of K by the interaction of shear stresses with mean velocity gradients (II), diffusive transport by either pressure fluctuations, velocity fluctuations or molecular diffusion (III), and the destruction of K by viscous action (IV). The modelled form of the K equation (which has been given in equations 2.14-15) may be written in a three dimensional cartesian co-ordinate as follows (see figure 2.1):

$$\frac{\partial}{\partial x}(\rho UK) + \frac{\partial}{\partial y}(\rho VK) + \frac{\partial}{\partial z}(\rho WK)$$

$$= \frac{\partial}{\partial x}(\frac{\mu_t}{\sigma_k}\frac{\partial K}{\partial x}) + \frac{\partial}{\partial y}(\frac{\mu_t}{\sigma_k}\frac{\partial K}{\partial y}) + \frac{\partial}{\partial z}(\frac{\mu_t}{\sigma_k}\frac{\partial K}{\partial z}) + G_K - \rho\varepsilon \qquad 2.22$$

and

$$G_k = \mu_t \left[2\left((\frac{\partial U}{\partial x})^2 + (\frac{\partial V}{\partial y})^2 + (\frac{\partial W}{\partial z})^2\right) + (\frac{\partial U}{\partial y} + \frac{\partial V}{\partial x})^2\right.$$

$$\left. + (\frac{\partial U}{\partial z} + \frac{\partial W}{\partial x})^2 + (\frac{\partial V}{\partial z} + \frac{\partial W}{\partial y})^2\right] \qquad 2.23$$

An exact equation for ε can be derived by a similar procedure to that used above (54). The resulting equation is rather long and complicated, and it will suffice for the presence purposes to give the modelled form (45).

$$\frac{\partial}{\partial x}(\rho U\varepsilon) + \frac{\partial}{\partial y}(\rho V\varepsilon) + \frac{\partial}{\partial z}(\rho W\varepsilon)$$

$$= \frac{\partial}{\partial x}(\frac{\mu_t}{\sigma_\varepsilon}\frac{\partial \varepsilon}{\partial x}) + \frac{\partial}{\partial y}(\frac{\mu_t}{\sigma_\varepsilon}\frac{\partial \varepsilon}{\partial y}) + \frac{\partial}{\partial z}(\frac{\mu_t}{\sigma_\varepsilon}\frac{\partial \varepsilon}{\partial z})$$

$$+ \frac{\varepsilon}{K}(C_1 G_k - C_2 \rho\varepsilon) \qquad 2.24$$

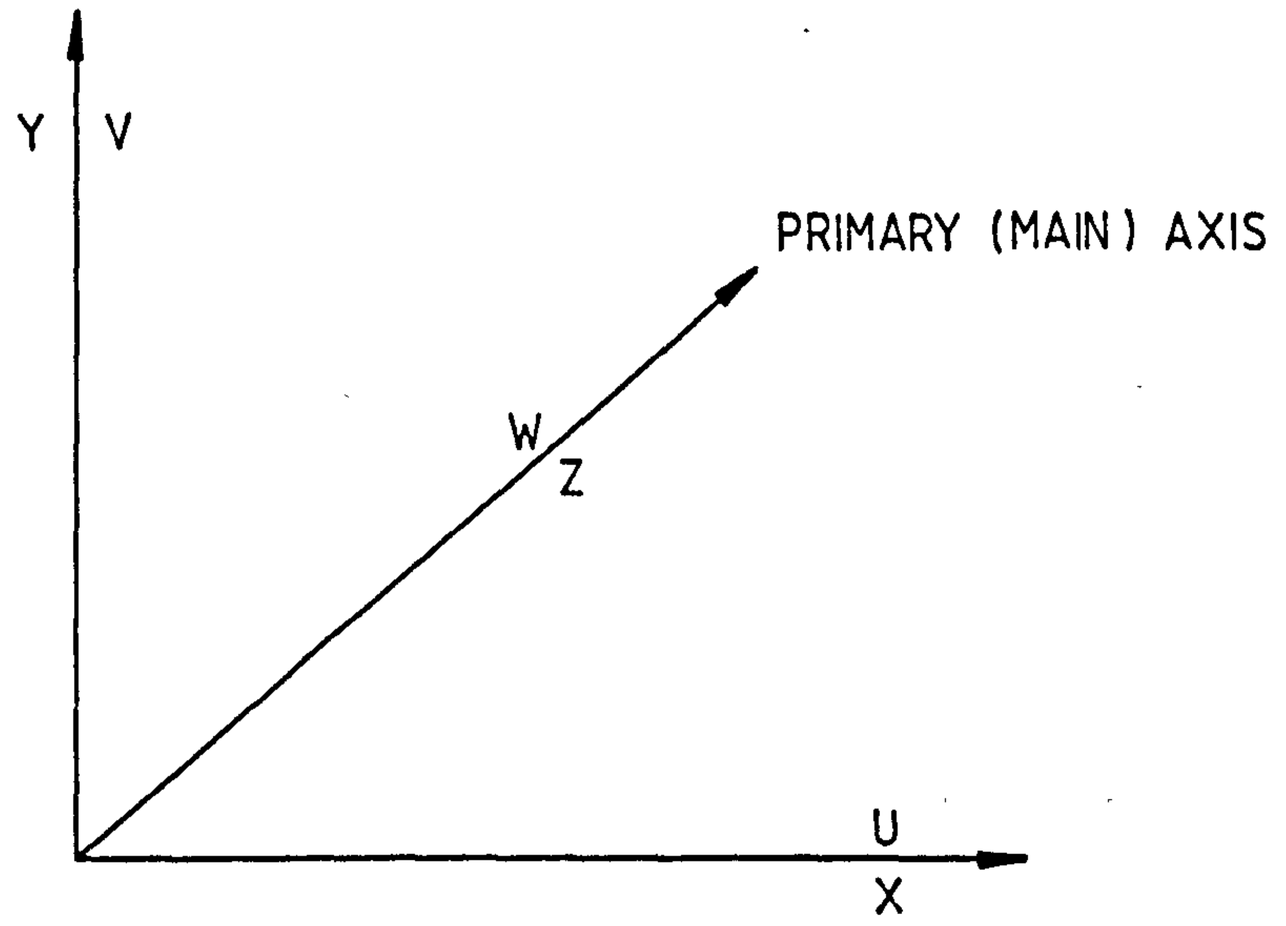

THREE DIMENSIONAL CARTESIAN COORDINATES (x, y, z)

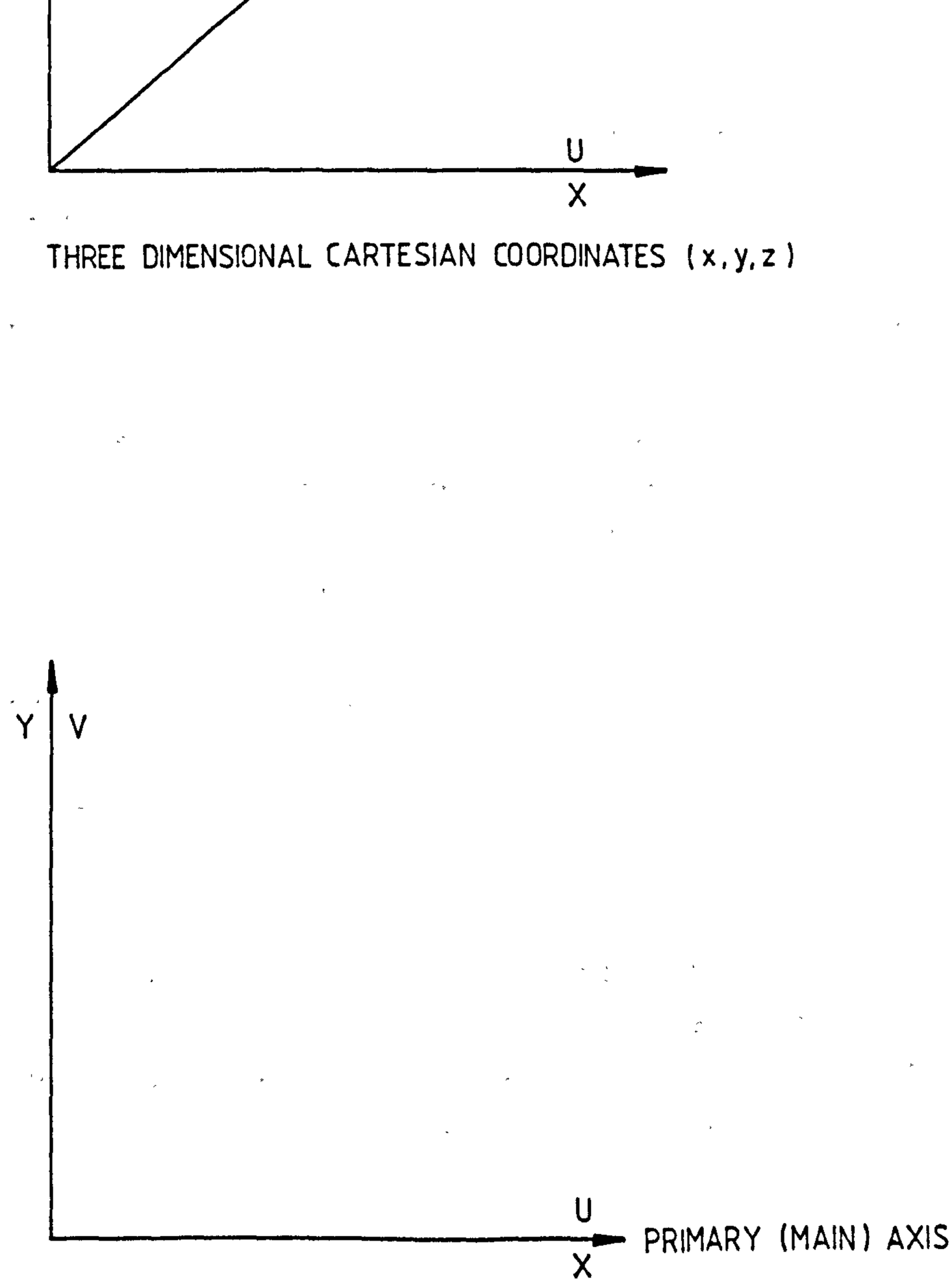

TWO DIMENSIONAL CARTESIAN COORDINATES (x, y)

Figure 2.1 : Coordinate systems

where C_1 and C_2 are empirical constants. The values of the turbulence model constants employed here are normally those adopted in the two-dimensional elliptic finite domain code of Pun and Spalding (34)*; the CHAMPION program.

C_1	C_2	C_D	σ_k	σ_ε
1.43	1.92	0.09	1.0	1.3

2.4.3 Assessment of K-ε turbulence model.

The K-ε turbulence closure has been used to compute numerous free and wall-bounded shear layers, and recirculating flows. Many investigators have obtained computations that were in good agreement with measurements (see, for example 12-17, 45,48,55-57). However, four special cases have been identified which are not predicted by the model without the inclusion of additional terms:

i) Buoyancy affected flows (58)
ii) Flows along curved walls (59)
iii) Flows with swirl (60)
iv) Axisymmetric free-jets (45)

of these four flows, only the first is directly related to the present study. However, the buoyancy effect has been accounted for by introducing additional terms into the momentum, K and ε equations (see table 2.2). Therefore the K-ε model has been adopted for the present work.

---

*Slightly different values are used in the developing duct-flow problem (chapter 6).

2.5 BOUNDARY CONDITIONS

2.5.1 General Remarks

The elliptic nature of the problem considered in the present study implied that the condition at any point in the flow can be influenced by other points. Therefore it is necessary to supply boundary conditions for the variables at all the boundaries of the flow domain, these boundaries could be one of the following:

i) A specified value of the variable or its gradient,
ii) A specified value of the flux of the variable.

The variables for which boundary conditions must be supplied are the velocity components (U,V,W), enthalpy (H) turbulence energy (K), and its dissipation (ε). The pressure (p) does not have to be prescribed, because of its interdependent nature with the velocity field.

For turbulent flow near an impermable solid boundary there are many numerical difficulties in using the simple approach to specify the velocity components to be zero at the surfaces as required by the 'no slip' condition. These will be discussed in the following section, and a practical method of overcoming them will then be outlined. However some of the other boundary conditions specified for the present study are summarised in table 2.1, and further details are given in subsequent chapters.

2.5.2 Turbulent Flows Near Walls (Wall Function)

i) General remarks

It has already been mentioned that the turbulence model employed in this study is only valid for flow region with high turbulence Reynolds number (Re_t). In the regions very near to a wall, the velocities tend to zero, and hence these are zones where the local Reynolds number is small and the viscous effects are dominant. If the exact momentum equations were to be solved in these regions then a large number of grid nodes would be needed. This would substantially increase the cost of the computations, due to the increase storage and

	Velocity Components			Enthalpy	Turbulent quantity	
	W	U	V	H	K	ε
Inlet*	W_{in}	0.0	0.0	H_{in}	K_{in}	ε_{in}
Outlet **	$\frac{dw}{dz} = 0.0$	0.0	0.0	$\frac{dH}{dz} = 0.0$	$\frac{dK}{dz} = 0.0$	$\frac{d\varepsilon}{dz} = 0.0$
Seymmetry*** & Free boundaries	$\frac{\partial\phi}{\partial n} = 0.0$, except in symmetry condition, the normal velocity equal to zero.					
Solid Walls	See sections (2.5.2) & (3.3)					

Table 2.1 Summary of boundary conditions.

* For two-dimensional flow there is a special treatment for the inlet velocity see section 4.3.1

** There is special treatment for flow in room see section (7.2.2)

*** See also section (3.3).

central processor requirements. Fortunately, very close to the wall, one-dimensional 'Couette flow' behaviour is observed. This offers an attractive approach of 'bridging over' the near-wall regions, via the introduction of 'wall functions'. These functions are often expressed in the form of algebraic equations. It is therefore possible to use these equations to connect the wall flux of momentum and scalar properties (K,ε and H), which are required for numerical computation, to the conditions at the outer-edge of the Couette layer.

ii) Wall function employed

The wall function adopted for this work is based on that used by Pun and Spalding (34) in their elliptic code, and which is described in full by Launder and Spalding (45). The form of these wall functions for each of the variables is outlined below:

a) Momentum flux

The variation of a resultant velocity in the near-wall region is assumed to follow a logarithmic law. For a smooth wall this law can be expressed in the form:

$$U^+ = \frac{U_p}{U_\tau} = \frac{1}{\kappa} \ln \left[E\, n^+\right] \qquad 2.25$$

where

$$U_p = \sqrt{U_1^2 + U_2^2} \qquad 2.26$$

$$U_\tau = \sqrt{\frac{\tau_w}{\rho}} \qquad 2.27$$

$$\text{and} \quad n^+ = \frac{\rho\, n_p\, U_\tau}{\mu_1} \qquad 2.28$$

Here U_1, U_2 are the velocity parallel to the wall at a distance n_p;

U_τ is the so-called friction velocity;

τ_w is the resultant shear stress;

n_p is the normal distance between the near-wall grid mode (P) and the wall, wherein P is located in the 'fully turbulent' region,

κ and E are empirical constants, (E = 9.0, κ = 0.4)

b) K and ε

The variation of K and ε in the constant stress layer near the wall may be deduced from the following assumptions:

1) The total (viscous plus turbulent) shear stress in this region is uniform.

2) The generation and dissipation of turbulence kinetic energy are in balance (local equilibrium).

3) The length scale varies according to $l = C_D \kappa n_p$.

The resulting expressions are:

$$\tau_w = \rho C_D^{\frac{1}{2}} K_p \qquad 2.29$$

The value of K_p is calculated from the transport equation for K, equation (2.22), with its diffussion to the wall set equal to zero thus:

$$\frac{\partial K}{\partial n} = 0.0 \qquad 2.30$$

The generation and dissipation terms (i.e. G_k and $\rho\varepsilon$) are then modified to be consistent with known results for near-wall flow (34), see section (3.7).

The length scale near a wall is assumed proportional to the distance from the wall as have been mentioned above, thus the dissipation rate can be expressed as:

$$\varepsilon = C_D^{\frac{3}{4}} K_p^{\frac{3}{2}} / n_p \kappa \qquad 2.31$$

c) Heat flux

The distribution of temperature is assumed to be anologous to that for velocity given by equation (2.25). It may be written in the form

$$T_p^+ = \sigma_t \, (U_p^+ + P_J) \qquad 2.32$$

where

T^+ may be written in terms of temperature near the wall (T), temperature at the wall (T_w), and local heat flux to the wall (q_w) as follows:

$$T^+ = \rho \, U_\tau \, C_p \, (T_w - T) / \, q_w'' \qquad 2.33$$

P_J in equation (2.32) represents the viscous sublayer 'resistance', which according to Jayatillaka (61) is given by

$$P_J = 9.0 \left[\frac{\sigma_l}{\sigma_t} - 1.0 \right] \Big/ \left[\frac{\sigma_l}{\sigma_t} \right]^{\frac{1}{4}} \qquad 2.34$$

and σ_l, σ_t being the laminar and turbulent Prandtl number respectively. Equation 2.33 is strictly valid for $\sigma_l \geq 0.5$.

2.6 A GENERAL FORM OF THE EQUATIONS TO BE SOLVED.

The equations to be solved could be expressed in the general form:

$$\frac{\partial}{\partial x}(\rho\Phi U) + \frac{\partial}{\partial y}(\rho\Phi V) + \frac{\partial}{\partial z}(\rho\Phi W)$$

Convection term

$$= \frac{\partial}{\partial x}\left(\Gamma_\Phi \frac{\partial \Phi}{\partial x}\right) + \frac{\partial}{\partial y}\left(\Gamma_\Phi \frac{\partial \Phi}{\partial y}\right) + \frac{\partial}{\partial z}\left(\Gamma_\Phi \frac{\partial \Phi}{\partial z}\right) + S_\Phi \qquad 2.35$$

Diffusion term Source term

The expressions for the diffusion coefficient Γ_Φ, and the source term, S_Φ, corresponding to each variable are given in table 2.2. The buoyancy source or production term in the K and ε transport equation is given by (12,60,62-64):

$$G_B = -\beta g \frac{\mu_t}{\sigma_t} \frac{\partial \theta}{\partial n} \qquad 2.36$$

where

θ is the excess temperature ($T-T_R$),

T_R is reference temperature,

β is coefficient of thermal expansion and,

g is the gravitational acceleration.

The effective viscosity μ_{eff} is defined by

$$\mu_{eff} = \mu_l + \mu_t \qquad 2.37$$

and the corresponding effective exchange coefficient for H is given by:

$$\Gamma_{h,eff} = \left(\frac{\mu_l}{\sigma_l} + \frac{\mu_t}{\sigma_t}\right) \qquad 2.38$$

Variable	ϕ	Γ_ϕ	S_ϕ
Continuity	1	0	0
x-direction momentum	U	μ_{eff}	$-\frac{\partial P}{\partial x} + \frac{\partial}{\partial x}\left(\mu_{eff}\frac{\partial U}{\partial x}\right) + \frac{\partial}{\partial y}\left(\mu_{eff}\frac{\partial V}{\partial x}\right) + \frac{\partial}{\partial z}\left(\mu_{eff}\frac{\partial W}{\partial x}\right)$
y-direction momentum	V	μ_{eff}	$-\frac{\partial P}{\partial y} + \frac{\partial}{\partial x}\left(\mu_{eff}\frac{\partial U}{\partial y}\right) + \frac{\partial}{\partial y}\left(\mu_{eff}\frac{\partial V}{\partial y}\right) + \frac{\partial}{\partial z}\left(\mu_{eff}\frac{\partial W}{\partial y}\right) + \rho\beta g\phi$
z-direction momentum	W	μ_{eff}	$-\frac{\partial P}{\partial z} + \frac{\partial}{\partial x}\left(\mu_{eff}\frac{\partial U}{\partial z}\right) + \frac{\partial}{\partial y}\left(\mu_{eff}\frac{\partial V}{\partial z}\right) + \frac{\partial}{\partial z}\left(\mu_{eff}\frac{\partial W}{\partial z}\right)$
Thermal energy	H	$\Gamma_{h,eff}$	S_h
Turbulence energy	K	$\frac{\mu_{eff}}{\sigma_k}$	$G_k - \rho\varepsilon + G_B$
Dissipation rate	ε	$\frac{\mu_{eff}}{\sigma_\varepsilon}$	$\frac{\varepsilon}{K}\left[C_1 (G_k + G_B) - C_2 \rho\varepsilon\right]$

Table 2.2 Exchange coefficient & source terms of Φ

CHAPTER 3

NUMERICAL SOLUTION PROCEDURE

3.0 NUMERICAL SOLUTION PROCEDURE

3.1 BACKGROUND

3.1.1 Numerical Techniques

This chapter describes the basic tool used for the calculations presented in this thesis; a numerical integration technique that, together with modern high speed computers, enables the differential equations described in chapter two to be solved. There are two main techniques currently employed : the 'finite-domain method' (FDM) and 'finite element method' (FEM). The main differences between these methods concerns the manner in which the discretized equations are derived. The FEM has the potential advantage of being able to readily handle complicated geometries. However a number of technical difficulties have been experienced in simulating fluid flow (as opposed to solid mechanics) problems, and these are fully discussed by Patankar (65). The FDM on the other hand, has been adopted in most of the studies in computational fluid dynamics (CFD) under-taken during the past few decades. Many of the latter have results from the efforts of Professor D.B. Spalding and his co-workers (at both the Imperial College and CHAM Limited), who have developed a series of finite-domain computer codes. Among these programs, the GENMIX and CHAMPION codes are concerned with two-dimensional parabolic and elliptic flow problems respectively. The more recent program suite is designed for two- or three- dimensional parabolic, hyperbolic or elliptic flow cases, and embodies commericially classified information (34).

In view of its wide acceptance and more advanced level of development for fluid flow problems, the FDM was adopted for the present study. The flow fields considered here are, in any case, all rectangular, and are therefore readily handled by the FDM. Consequently, this technique has been incorporated into a computer program called the ESCEAT (Elliptic Equation Solver for Convection and Heat Transfer) code, produced to handle three-dimensional elliptic flow cases. In developing this program the Cranfield team made use of their past experience in applying the CHAMPION code to two-dimensional mechanical ventilation problems (21,33). The ESCEAT code, in addition to its ability to handle more complex geometries, incorporates a number of improvement in the numerical solution procedure for the

finite-domain equations. Both the CHAMPION and ESCEAT codes have been employed in the present study in order to compute two- and three-dimensional elliptic flows respectively.

3.1.2 Outline of the Chapter

In the following sections, the basic approach, that has been used in formulating the finite domain analogues of the differential equations is first described. The manner in which the boundary conditions for these equations are inserted is then explained. Finally, the solution procedure and some related computational aspects are described.

3.2 FINITE-DOMAIN APPROXIMATION

3.2.1 Introduction

The starting point for the FDM is to derive finite-domain analogues to the governing differential equations. This is accomplished by dividing the flow domain into many small control volumes, and then integrating the PDE's over these cells to obtain an algebraic equation for each variable. Since the resulting finite-domain equations (FDE's) are non-linear and strongly interlinked it is necessary to employ an iterative procedure to solve them. A number of solution algorithms have been developed for this purpose, including MAC (66), SMAC (67), SIMPLE (68), SIMPLER (65, 69) and SIMPLEC (70). Both the SIMPLE and SIMPLEC algorithms (described in section (3.2.6)) have been used in the present study, although the latter was normally preferred. The SIMPLE procedure was adopted only for the three-dimensional laminar flow test cases (see chapter 5), which were carried out only in the development for the ESCEAT code. The iterative sequence used with both the CHAMPION and ESCEAT codes employed a line-by-line technique, together with either an 'overall continuity correction' or a 'block-adjustment' procedure used to ensure mass conservation (see section 3.4.3 and 3.4.4).

3.2.2 Computational Grid

The first step in the derivation of the FDE's is to divide the calculation domain completely into a set of non-overlapping control volumes. This produces a computational (grid that comprising a multi-(two or three) dimensional, rectangular, cartesian lattice of grid lines. The grid spacing may be non-uniform in some or all directions so as to allow the spacing to be made small in regions with steep gradients, such as near walls. The intersection of the grid lines form the so-called grid nodes, each of which is assumed to be enclosed in its own control volume. The control volume boundaries were taken to be mid-way between the grid nodes in the present work following (34).

Figure (3.1) shows a small portion of the grid, comprising a typical node P together with its nearest neighbours, N, S, E, W, D and U, as well as the relevant control volume (i.e., that volume enclosed by the solid lines). The boundaries of the control volume are labelled with the lower case version of the label for the neighbouring nodes (n,s,e,w,d and u).

3.2.3 The Staggered Grid

All scaler dependent variables are stored in the grid node just described while the velocity components are stored at staggered location coinciding with boundaries of the control volumes for the scalar variables. The adoption of a staggered grid ensures that the velocities lay between the pressures that induce them, and are directly available for calculating the convective fluxes of the scalar flow variables. The staggered location and control volume for the velocity components are shown in figures (3.2-3).

3.2.4 Finite-Domain Equations:

The finite domain equations will be developed below by integrating the governing differential equations over a finite control volume. In this subsection the general FDE for the transport of the general variable, Φ, is derived by integrating equation (2.35). The control volume and the grid nomenclature utilised in deriving these FDE's is

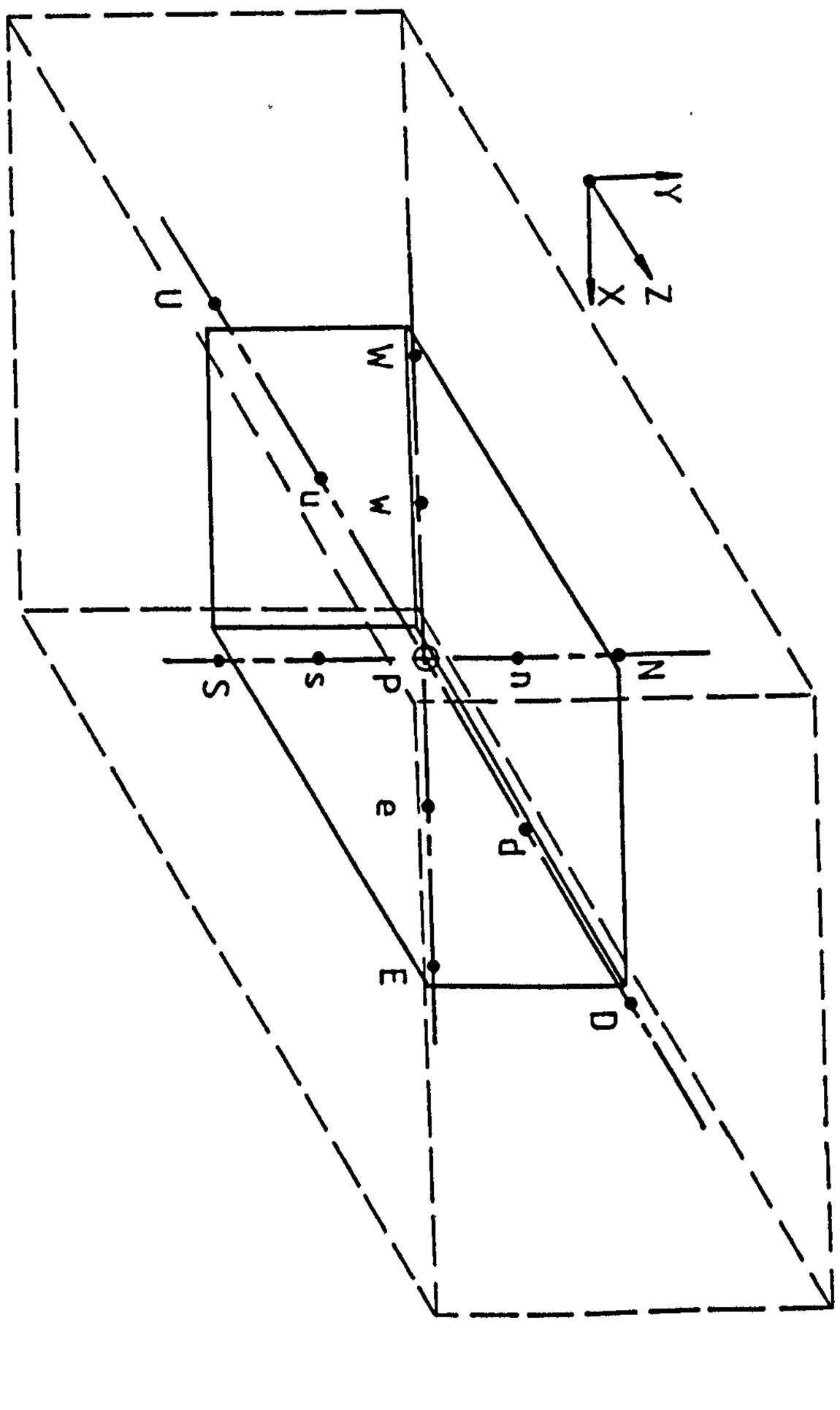

Fig. 3.1 : Illustration of a portion of the computational grid showing notation and control volume boundaries

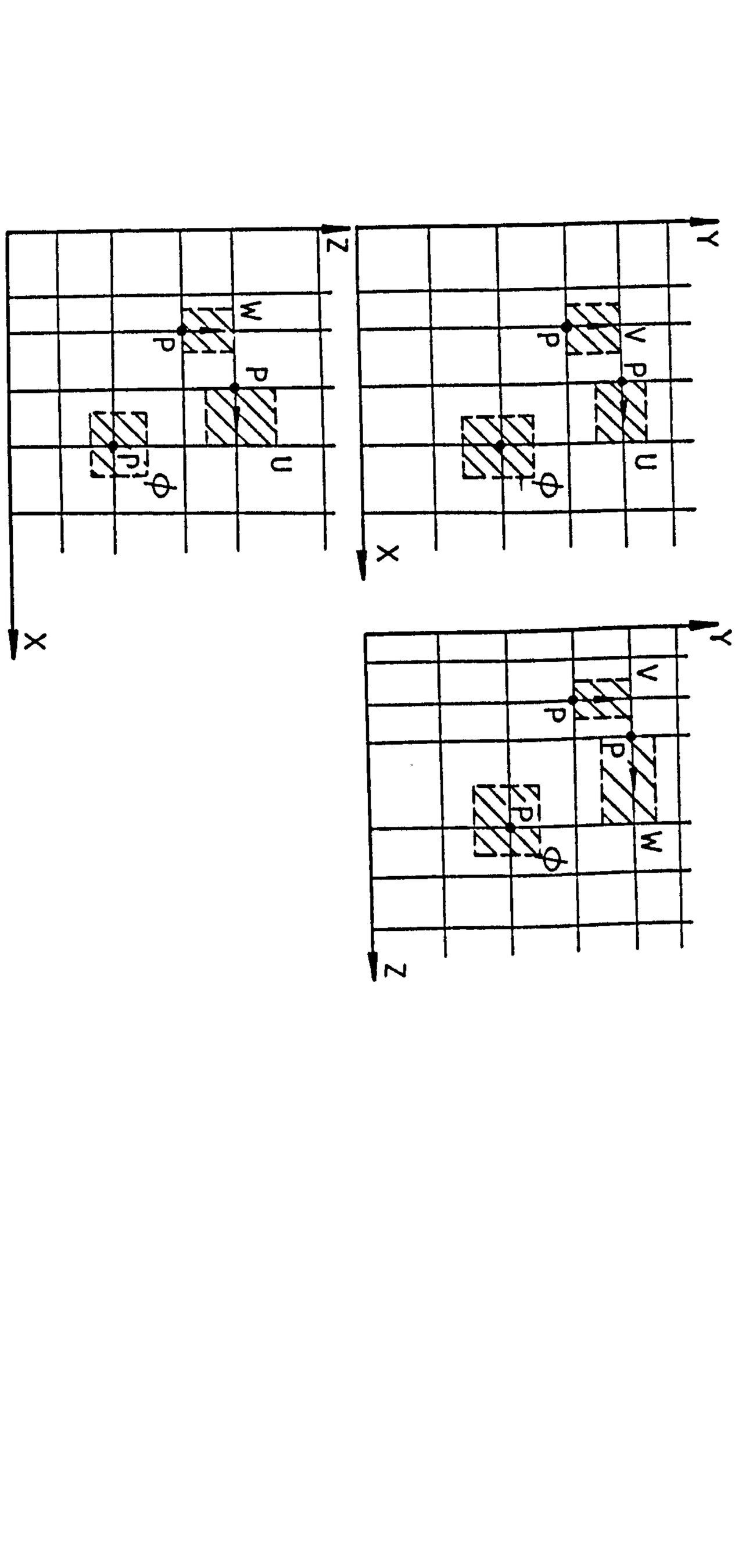

Fig. 3.2 :Location of variables and associated control volumes

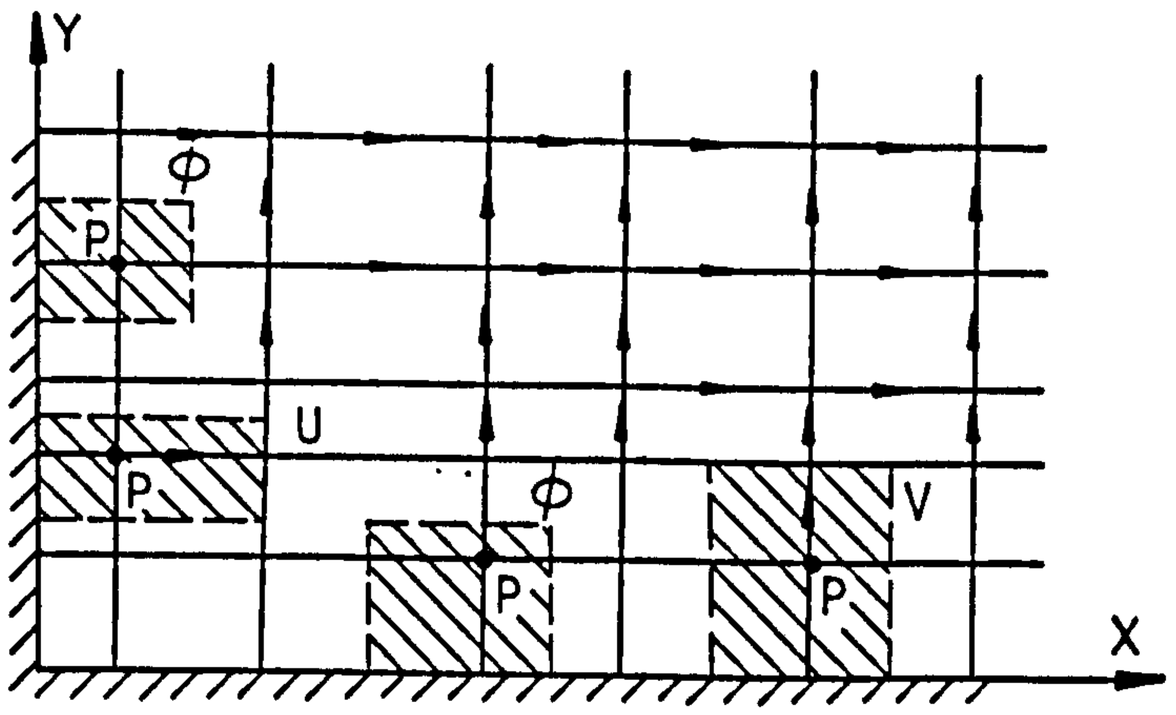

Fig. 3.3 : Illustration of arrangement of grid and variables locations at external boundaries.

given in figures (3.1-4). In the X-Y plane, the adjacent locations are described according to a north, south, east, west (N,S,E,W) system. In the direction of the main flow the adjacent locations are referred to as either upstream or downstream (U or D) subscripts.

The general differential equation (2.35) may be written in the form

$$\frac{d}{dx_j}(J_j) = S_\Phi \qquad 3.1$$

where J_j is the total flux in direction j, which defined as

$$J_j = \rho\Phi U_j - \Gamma_\Phi \frac{\partial\Phi}{\partial x_j} \qquad 3.2$$

The integration of equation (3.2) over the control volume gives:

$$J_e - J_w + J_n - J_s + J_d - J_u = S_\Phi .\Delta X.\Delta Y.\Delta Z \qquad 3.3$$

where J_e, J_w, J_n, J_s, J_d and J_u are the integrated total fluxes over the control volume faces. The source-term, S_Φ, may simply be written in quasi-linear form as:

$$S_\Phi = S_p + S'_p \Phi_p \qquad 3.4$$

where S_p and S'_p are determined from a suitable finite domain approximation of S_Φ expression for the particular variable Φ. Therefore equation (3.3) becomes:

$$J_e - J_w + J_n - J_s + J_d - J_u = (S_p + S'_p \Phi_p).\Delta X.\Delta Y.\Delta Z \qquad 3.5$$

The continuity approximation could be obtained from the general form of equation (3.5) as:

$$F_e - F_w + F_n - F_s + F_d - F_u = 0.0 \qquad 3.6$$

where F_e, F_w, F_n, F_s, F_d and F_u are the mass flow rate through the control volume faces.

$$\begin{aligned} F_e &= (\rho U)_e.\Delta Y.\Delta Z \\ F_w &= (\rho U)_w.\Delta Y.\Delta Z \\ F_n &= (\rho V)_n.\Delta X.\Delta Z \\ F_s &= (\rho V)_s.\Delta X.\Delta Z \\ F_d &= (\rho W)_d.\Delta X.\Delta Y \\ F_u &= (\rho W)_u.\Delta X.\Delta Y \end{aligned} \qquad 3.7$$

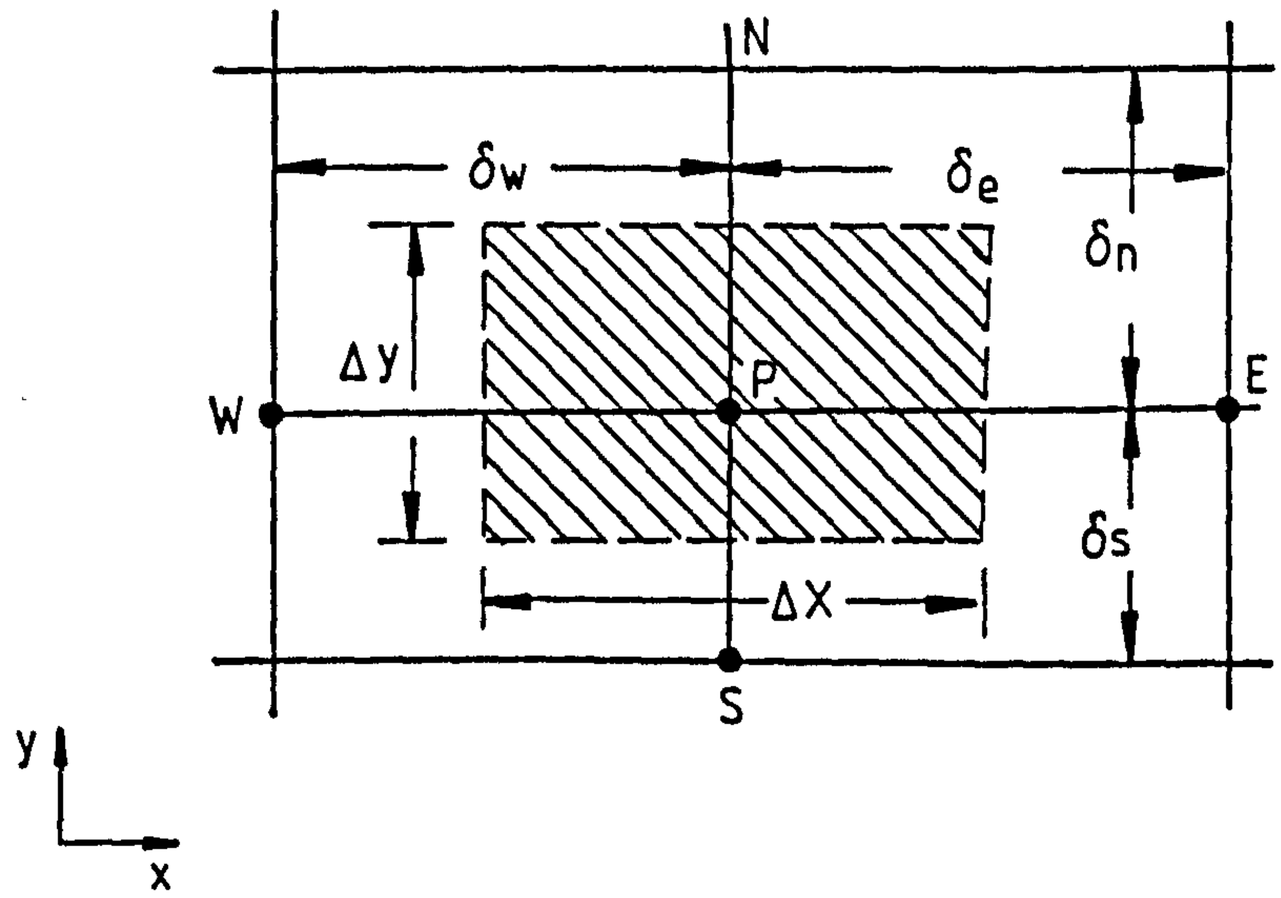

Fig. 3.4 : Typical notation for geometrical parameters of grid and control volumes.

Multiplying equation (3.6) by Φ_p and subtracting it from equation (3.5) result in:

$$(J_e - F_e \Phi_p) - (J_w - F_w \Phi_p) + (J_n - F_n \Phi_p) - (J_s - F_s \Phi_p) +$$

$$(J_d - F_d \Phi_p) - (J_u - F_u \Phi_p) = (S_p + S_p' \Phi_p)\ \Delta X.\Delta Y.\Delta Z. \qquad 3.8$$

Equation (3.8) is the finite-domain equivalent of equation (2.35). According to Patankar (65), the terms $(J_e - F_e \Phi_p)$ ... etc., can be replaced by:

$$\begin{aligned}
J_e - F_e \Phi_p &= a_E (\Phi_P - \Phi_E) \\
J_w - F_w \Phi_p &= a_W (\Phi_W - \Phi_P) \\
J_n - F_n \Phi_p &= a_N (\Phi_P - \Phi_N) \\
J_s - F_s \Phi_p &= a_S (\Phi_S - \Phi_P) \\
J_d - F_d \Phi_p &= a_D (\Phi_P - \Phi_D) \\
J_u - F_u \Phi_p &= a_U (\Phi_U - \Phi_P)
\end{aligned} \qquad 3.9$$

The substitution of relations (3.9) into equation (3.8) and rearranging gives:

$$a_P \Phi_P = \left(\sum_{E,W,N,S,D,U} a \Phi\right) + b \qquad 3.10$$

where

$$a_E = D_e\ B\ (|Pe|)_e + [[-F_e, o]]$$

$$a_W = D_w\ B\ (|Pe|)_w + [[\ F_w, o]]$$

$$a_N = D_n\ B\ (|Pe|)_n + [[-F_n, o]] \qquad 3.11$$

$$a_S = D_s\ B\ (|Pe|)_s + [[\ F_s, o]]$$

$$a_D = D_d\ B\ (|Pe|)_d + [[-F_d, o]]$$

$$a_U = D_u\ B\ (|Pe|)_u + [[\ F_u, o]]$$

$$a_p = \left(\sum_{E,W,N,S,D,U} a\right) - S_p' .\Delta X.\Delta Y.\Delta Z$$

$$b = S_p.\Delta X.\Delta Y.\Delta Z$$

The D's are the diffusion terms and they are defined as:

$$D_e = \Gamma_{\Phi,e} \quad \Delta Y.\Delta Z/(\delta x)_e$$

$$D_w = \Gamma_{\Phi,w} \quad \Delta Y.WZ/(\delta x)_w$$

$$D_n = \Gamma_{\Phi,n} \quad \Delta X.\Delta Z/(\delta y)_n$$

$$D_s = \Gamma_{\Phi,s} \quad \Delta X.\Delta Z/(\delta y)_s \qquad 3.12$$

$$D_d = \Gamma_{\Phi,d} \quad \Delta X.\Delta Y/(\delta Z)_d$$

$$D_u = \Gamma_{\Phi,u} \quad \Delta X.\Delta Y/(\delta Z)_u$$

$(Pe)_e$, $(Pe)_w$ ... etc. are the cell Peclet numbers at the control volume boundaries, which may be interpreted as ratio of the strength of the convention term to that of the diffusion term. These are defined by:

$$(Pe)_e = \frac{F_e}{D_e} = (\rho U\ \delta x/\Gamma_{\Phi,e})$$

$$(Pe)_w = \frac{F_w}{D_w} = (\rho U\ \delta x/\Gamma_{\Phi,w}) \qquad 3.13$$

$$(Pe)_n = \frac{F_n}{D_n} = (\rho V\ \delta y/\Gamma_{\Phi,n})$$

$$(Pe)_u = \frac{F_u}{D_u} = (\rho W\ \delta z/\Gamma_{\Phi,u})$$

The exchange coefficient Γ_Φ at the control volume faces may be written in the form:

$$\Gamma_{\Phi,e} = (\Gamma_{\Phi,p} + \Gamma_{\Phi,E})/2 \qquad 3.14$$

$$\Gamma_{\Phi,w} = (\Gamma_{\Phi,W} + \Gamma_{\Phi,P})/2$$

with similar expressions for $\Gamma_{\Phi,s}, \Gamma_{\Phi,n}, \Gamma_{\Phi,d}$ and $\Gamma_{\Phi,u}$. The operator [[A,B]] denotes the greater of A and B, and $B(|Pe|)$ is a function related to the choice of differencing scheme to be used in the derivation. Some alternative schemes are discussed in the next subsection.

Special attention needs to be paid to the momentum equations from the general equation (3.10). This is firstly due to the staggered storage location of the velocities and associated control volumes, whose boundaries are arranged in the manner of figures 3.2-3 , and secondly to the pressure gradient terms (see table 2.2). The resulting W-momentum, U-momentum and V-momentum equations have the form:

$$a_p W_p = (\sum_{E,W,N,S,D,U} a W) + b_m + A_d (P_P - P_D)$$

$$a_p U_p = (\sum_{E,W,N,S,D,U} a U) + b_m + A_e (P_P - P_E) \qquad 3.15$$

$$a_p V_p = (\sum_{E,W,N,S,D,U} a V) + b_m + A_n (P_P - P_N)$$

The pressure gradients, $A_e (P_P - P_E)$, $A_n (P_P - P_N)$ and $A_d (P_P - P_D)$ are acting in the x-, y- and z- directions respectively, where

$$A_d = \Delta X.\Delta Y$$
$$A_e = \Delta Y.\Delta Z \qquad 3.16$$
$$A_n = \Delta X.\Delta Z$$

The b_m's plus the pressure gradient terms are now equivalent to the b's in equation (3.10).

3.2.5 The Choice of Differencing Schemes

There are several differencing schemes available for use in deriving the FDE's from their PDE's. In order to illustrate some of these schemes and their relative merits, a steady one-dimensional situation in which only convection and diffusion terms exist will be considered. The governing differential equation (2.3) then reduced to:

$$\frac{d}{dx} (\rho U \Phi) = \frac{d}{dx} (\Gamma_\Phi \frac{d\Phi}{dx}) \qquad 3.17$$

Similarly the continuity equation becomes:

$$\frac{d}{dx} (\rho U) = 0.0 \qquad 3.18$$

The integration of equation 3.17 over the control volume in figure 3.5 yields

$$(\rho U\Phi)_e - (\rho U\Phi)_w = (\Gamma_\Phi \frac{d\Phi}{dx})_e - (\Gamma_\Phi \frac{d\Phi}{dx})_w \qquad 3.19$$

The manner in which the diffusion and convection terms are formulated at the control volume faces identifies the differencing scheme employed. Various alternative schemes are discussed below:

i) Central differencing scheme.

This scheme presumes a linear variation of Φ between grid nodes, and therefore the value of Φ at an interface is given by:

$$\Phi_e = 0.5\ (\Phi_E + \Phi_P) \qquad 3.20$$

$$\Phi_w = 0.5\ (\Phi_P + \Phi_W)$$

with diffusion terms in the form:

$$(\Gamma_\Phi \frac{d\Phi}{dx})_e = \Gamma_{\Phi,e}\ \frac{\Phi_E - \Phi_P}{\delta x_e} \qquad 3.21$$

$$(\Gamma_\Phi \frac{d\Phi}{dx})_w = \Gamma_{\Phi,w}\ \frac{\Phi_P - \Phi_W}{\delta x_w}$$

The substitution of equations 3.20 - 3.21 into equation 3.19 yields:

$$0.5(\rho U)_e\ (\Phi_E + \Phi_P) - 0.5(\rho U)_w\ (\Phi_P + \Phi_W) = \qquad 3.22$$

$$\Gamma_{\Phi,e}\ (\Phi_E - \Phi_P)/\delta x_e - \Gamma_{\Phi,w}\ (\Phi_P - \Phi_W)/\delta x_w$$

The finite domain form of equation 3.22 may be obtained by rearranging and using equation 3.18 to give:

$$a_P\ \Phi_P = a_E\ \Phi_E + a_W\ \Phi_W \qquad 3.23$$

where

$$a_E = D_e - 0.5F_e$$

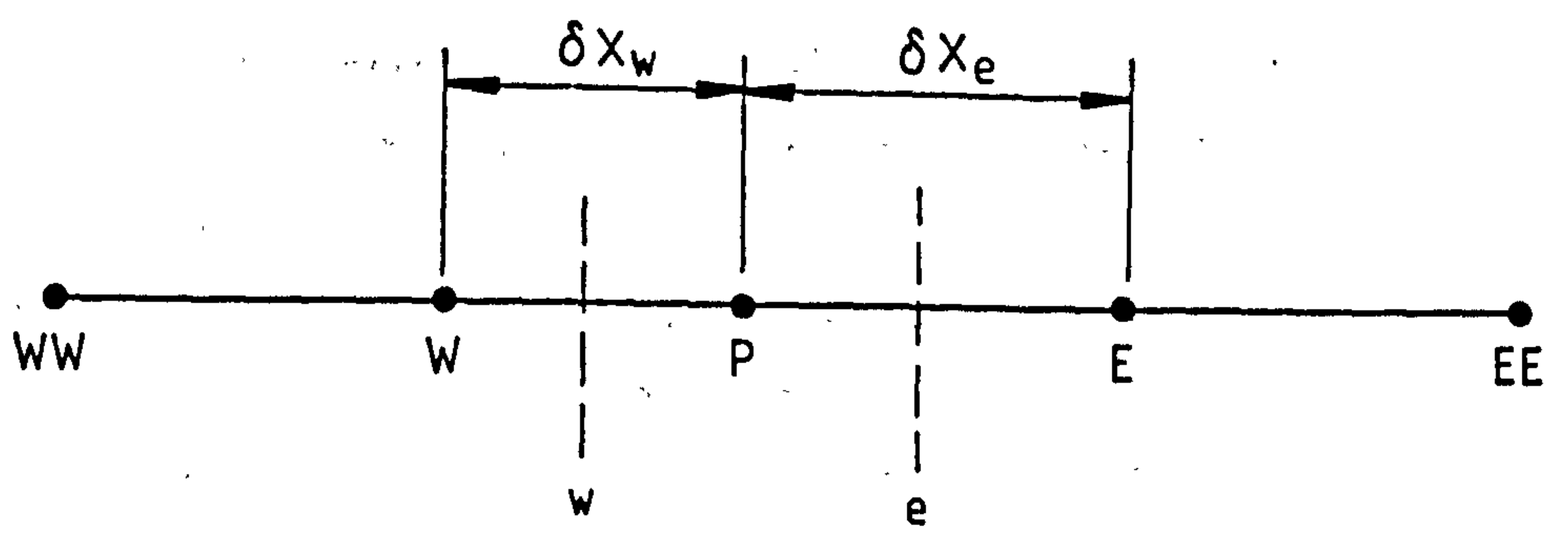

Figure 3.5 : One-dimensional grid [after Patankar (65)]

$$a_W = D_W + 0.5F_W$$
$$a_P = a_E + a_W$$

According to Patankar (65), Runchal (71) and others, this central differencing scheme works well when $-2<Pe<2$, but outside these limits the coefficients a_E, a_W and a_P become negative, and leading to physically unrealistic calculations. If an iterative method of solution is employed, instability may also occur (65, 71-72).

ii) Upwind differencing scheme

A well known remedy for the difficulties encountered in the central differencing scheme is the upwind scheme (65). In this scheme the diffusion term on the right of equation 3.19 retains its central difference formulation, while the convection term is calculated in different manner (65, 73). The interface value for Φ is assumed to be equal to the value of Φ at grid point on the upwind side of the face:

$$\Phi_e = \Phi_P \quad \text{if } F_e > 0 \qquad 3.24$$

$$\Phi_e = \Phi_E \quad \text{if } F_e < 0$$

with the value of Φ_W being similarily defined. The replacement of equation (3.20) by equation 3.24 gives rise to new coefficients in the finite domain equation (3.23), namely

$$a_E = D_e + [[-F_e, o]] \qquad 3.25$$

$$a_W = D_W + [[F_W, o]]$$

The predictions that are obtained with this scheme are stable at all Peclet numbers, in contrast to those of the central differencing scheme. It is also more accurate than the central differencing scheme when $|Pe|>2$, although it is slightly inferior at smaller values (65).

iii)Hybrid scheme

A hybrid differencing scheme was developed by Spalding (72), which employ the central difference formulation when $|Pe| \leqslant 2$, and the upwind one when $|Pe| > 2$. This implies that the coefficient a_E is given by:

$a_E = -F_e$ if $Pe < -2$;

$a_E = D_e - 0.5F_e$ if $-2 < Pe < 2$ and 3.26

$a_E = 0.0$ if $Pe > 2$

In a combined and more compact form, the coefficients a_E and a_W can be written as:

$$a_E = [[-F_e,\ D_e - \frac{F_e}{2}\ ,\ 0]] \qquad 3.27$$

$$a_W = [[F_w,\ D_w + \frac{F_w}{2}\ ,\ 0]]$$

Although this hybrid scheme is not in complete agreement with the exact result obtained by Spalding (72) for one dimensional convection-diffusion problem (see Figure 3.6), it nonetheless incorporates the best feature of the central and upwind schemes respectively.

iv) Power-law scheme

This scheme has been proposed by Patankar (65) as an improvement to the hybrid differencing scheme. He introduced it as 'a power-law' approximation to the exponential (i.e. exact) differencing scheme of Spalding (72). Patankar argued that the departure of the hybrid scheme from this exact solution rather large at $Pe = \pm 2$ (see Figure 3.6) and that was unrealistic to set the diffusion effect to zero as soon as $|Pe|$ exceeded 2. The coefficients in this scheme read:

$$a_E = D_e\ [[0,(1- 0.1\ |\frac{F_e}{D_e}|)^5]]\ + [[0, - F_e]] \qquad 3.28$$

$$a_W = D_w\ [[0,(1- 0.1\ |\frac{F_w}{D_w}|)^5]]\ + [[0, + F_w]]$$

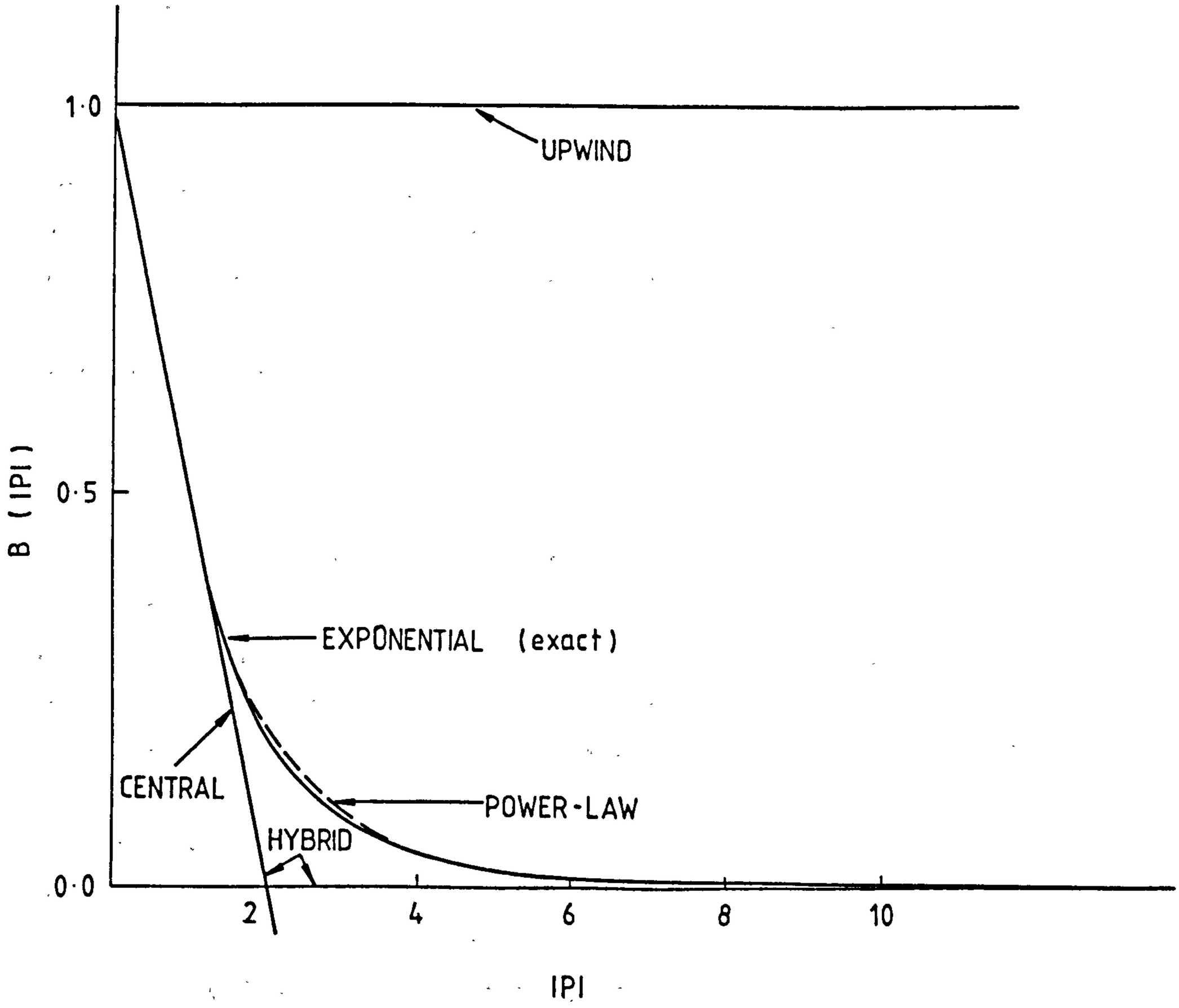

Figure 3.6 : The function B(|P|) for various schemes , [after Patankar (65)].

which means that;

$$a_E = -F_e \text{ if } Pe < -10,$$

$$a_E = D_e\,(1 - 0.1|\tfrac{F_e}{D_e}|)^5 - F_e \text{ if } -10 \leqslant Pe < 0,$$

$$a_E = D_e\,(1 - 0.1|\tfrac{F_e}{D_e}|)^5 \quad \text{if } 0 < Pe \leqslant 10, \text{ and} \qquad 3.29$$

$$a_E = 0.0 \quad \text{if } Pe > 10$$

The power-law scheme therefore extends the range of Peclet number over which simulation is reliable from ± 2 in the case of hybrid scheme to ± 10. Hence, it provides a good approximation to the exact expression (as shown in Figure (3.6)), while requiring less computational time than that needed for the exponential scheme.

v) Quadratic scheme

This scheme was proposed by Leonard (74) as an alternative form of discretization for the convective transport terms in the numerical simulation of convection-dominated flows. It has been found to reduce the numerical or 'false' diffusion (see section 4.3.6) arising from the upwind treatment (55, 75-76). However, it is less stable than either the hybrid or power-law schemes (76-78). The QUICK (Quadratic Upstream Interpolation for Convective Kinematics) scheme of Leonard employs a three-point upstream-weighted quadratic interpolation in which the control-volume surface values are obtained by fitting a parobala to the values of Φ at the three consecutive nodal positions. These are two nodes located on either side of the surface in question, plus the next node on the upstream side. Examples of quadratic interpolation expressions for a uniform grid spacing are given below, (see Figure 3.5):

$$\Phi_e = \begin{cases} \tfrac{1}{2}(\Phi_P + \Phi_E) - \tfrac{1}{8}(\Phi_W + \Phi_E - 2\Phi_P) & U_e > 0 \\ \tfrac{1}{2}(\Phi_P + \Phi_E) - \tfrac{1}{8}(\Phi_P + \Phi_{EE} - 2\Phi_E) & U_e < 0 \end{cases} \qquad 3.30$$

$$\Phi_w = \begin{cases} \tfrac{1}{2}(\Phi_P + \Phi_W) - \tfrac{1}{8}(\Phi_W + \Phi_E - 2\Phi_P) & U_w < 0 \\ \tfrac{1}{2}(\Phi_P + \Phi_W) - \tfrac{1}{8}(\Phi_{WW} + \Phi_P - 2\Phi_W) & U_w > 0 \end{cases}$$

The above formulation was found to require extra computational time per node over the previously mentioned schemes (76-77). However this penalty can be worthwhile if numerical accuracy is the most important factor, as may be the case in convection dominant recirculating flows (76).

The formulation of the scheme for a non-uniform staggered grid, and the way it was implemented for the present work, is detailed in Appendix A.

3.2.6 Assessment of Alternative Differencing Schemes

The choice of the previously mentioned schemes is essentially problem dependent. The factors that could be used in making such a choice are accuracy, economy (computational time), and stability. In term of accuracy and economy, these schemes may be listed in the following order:

	QUICK scheme	
increasing accuracy ↑	Power-law scheme	increasing computational time ↑
	Hybrid scheme	
	Upwind scheme	per node

However, the QUICK scheme is intrinsically, less stable than the others.

3.2.7 Pressure and Velocity Corrections

The momentum equations (3.15) allow a velocity field to be determined for a given or estimated pressure field, but unless the correct pressure field is employed, the resulting velocities will not satisfy the continuity equation. A solution based on a gussed pressure field P^* will therefore produce 'imperfect' velocities W^*, U^*, V^*. These 'starred' velocity components will result from the solution of the following equations.

$$a_P W_P^* = [\Sigma_{E,-,U} \; a W^*] + b + A_d (P_P^* - P_D^*)$$
$$a_P U_P^* = [\Sigma_{E,-,U} \; a U^*] + b + A_e (P_P^* - P_E^*) \qquad 3.31$$

$$a_P V_P^* = [\Sigma_{E,-,U} \; a V^*] + b + A_n (P_P^* - P_N^*)$$

The starred pressure P^* must be improved in such a way that the resulting starred velocities will progressivley get closer to those velocities that satisfy continuity. Correction quantities P', W', U', V' are now determined whose purpose is to bring continuity and momentum into balance,

$$\begin{aligned} P &= P^* + P' \quad ; \\ W &= W^* + W' \quad ; \\ U &= U^* + U' \quad ; \text{ and} \\ V &= V^* + V' \end{aligned} \qquad 3.32$$

The substitution of equations 3.32 into equation 3.31 and subtraction from 3.15, gives:

$$\begin{aligned} a_P W_P' &= [\Sigma_{E,-,U} \; a W'] + A_d (P_P' - P_D') \\ a_P U_P' &= [\Sigma_{E,-,U} \; a U'] + A_e (P_P' - P_E') \\ a_P V_P' &= [\Sigma_{E,-,U} \; a V'] + A_n (P_P' - P_N') \end{aligned} \qquad 3.33$$

In the popular SIMPLE algorithm of Patankar and Spalding (68), the terms $\Sigma \; a W'$, $\Sigma \; a U'$ and $\Sigma \; a V'$ in the above equation set are neglected. However in the more recent SIMPLEC algorithm of Doormaal and Raithby (70) terms of the form $\Sigma \; a W_p'$, $\Sigma \; a U_p'$ and $\Sigma \; a V_p'$ are subtracted from both sides of equation 3.33 to yield:

$$\begin{aligned} [a_P - \Sigma_{E,-,U} \; a] W_p' &= \underline{\Sigma_{E,-,U} a (W' - W_p')} + A_d (P_P' - P_D') \\ [a_P - \Sigma_{E,-,U} \; a] U_p' &= \underline{\Sigma_{E,-,U} a (U' - U_p')} + A_e (P_P' - P_E') \\ [a_P - \Sigma_{E,-,U} \; a] V_p' &= \underline{\Sigma_{E,-,U} a (V' - V_p')} + A_n (P_P' - P_N') \end{aligned} \qquad 3.34$$

where it is the underlined terms that are neglected in this approach.

Equation 3.33 and 3.34 then become:

$$\begin{aligned} W_p' &= d_d (P_P' - P_D') \\ U_p' &= d_e (P_P' - P_E') \\ V_p' &= d_n (P_P' - P_N') \end{aligned} \qquad 3.35$$

where for the SIMPLE algorith:

$$d_d = \frac{A_d}{a_p} \; , \; d_e = \frac{A_e}{a_p} \; , \; d_n = \frac{A_n}{a_p} \qquad 3.36$$

and for its SIMPLEC counterpart:

$$d_d = \frac{A_d}{a_p - \sum_{E,-,U} a} \; d_e = \frac{A_e}{a_p - \sum_{E,-,U} a} \; , \; d_n = \frac{A_n}{a_p - \sum_{E,-,U} a} \qquad 3.37$$

The substitution of equations 3.35 into equation 3.32 yields:

$$W_p = W_p^* + d_d \, (P_P' - P_D') \; , \; U_p = U_p^* + d_e \, (P_P' - P_E') \qquad 3.38$$

$$V_p = V_p^* + d_n \, (P_P' - P_N')$$

The substitution of equation 3.38 into the continuity equation (3.6), and rearranging, then yields the desired equation for the pressure correction, P':

$$a_p \, P_p' = [\sum_{E,-,U} a \, P'] + b \qquad 3.39$$

where

$$a_E = (\rho \, A \, d)_e \; , \; a_W = (\rho \, A \, d)_w \; , \; a_N = (\rho \, A \, d)_n ,$$

$$a_S = (\rho \, A \, d)_s \; , \; a_D = (\rho \, A \, d)_d \; \text{ and } \; a_U = (\rho \, A \, d)_u$$

Here the densities can be calculated by interpolating between the values at the surrounding grid nodes.

The term b in equation 3.39 is defined as;

$$b = (\rho WA)_u - (\rho WA)_d + (\rho UA)_W - (\rho UA)_e + (\rho VA)_s - (\rho VA)_n \qquad 3.40$$

and has the significant of a mass balance on the control volume based on the preliminary velocity field. The purpose of the pressure correction equation (3.39) is to reduce this mass source to zero. Since the mass-source and pressure corrections tend to zero as the velocities and pressures approach those that satisfy the continuity equation, the final solution will be independent of the terms neglected from equations (3.33) and (3.34) in the SIMPLE and SIMPLEC algorithms respectively (68, 70). However, while the SIMPLEC

approximation removes the need to under-relax the pressure (see section 3.5.2), a practice that improves the convergence rate, it may also be regarded as a more consistent approximation (70). This is because equation (3.34) becomes exact when the diffusion and convection of momentum are small compared with the pressure gradiant and source terms. Equation (3.39) is similar form to equation (3.10) and may be solved in the same manner. The resulting solution is then used to adjust the velocities and pressure via the procedure outline above.

3.3 INCORPORATION OF BOUNDARY CONDITIONS

The boundary conditions appropriate to the present set of problems were outlined in section (2.5). The incorporation of these conditions into the finite-domaine equations will now be discussed.

3.3.1 Situations Where Φ is Prescribed

This condition particularly applies to the velocities at inlet plane and at the walls, as well to the distribution of scalar variables in incoming flow. In this situation no special action is required apart from specifying the Φ distribution at all grid nodes in the entry plane of the solution domain.

3.3.2 Situation Where the Flux of Φ is Prescribed

This condition applies to all variables at the symmetry plane (apart from the normal velocity) and to the enthalpy at adiabatic walls; in all cases the convection and diffusion fluxes are both zero. These fluxes are represented in finite-domain by the flux coefficients defined by equations (3.10). In order to get a particular flux to zero, all that is required is to get the appropriate coefficient equal to zero. For example, if the boundary in question coincides with n face of the adjoining control volume, the A_N coefficient in the FDE for that volume is set to zero.

3.3.3 Situation Where the Gradient Φ is Prescribed

This situation applied to all variables at free boundary planes and to all variables (apart from the parallel velocities) at outlet opening. This is simply done by deducing the value of the variable at the outflow plane from the adjacent upstream plane (for example in z-direction, $\Phi_D = \Phi_P$ for an outlet/Free plane).

3.3.4 Situation Where a Wall-function is Prescribed

It was explained earlier in section (2.5.2) that for a turbulent flow the various flow properties immediately adjacent to a wall are commonly calculated from a 'wall functions'. The practice adopted for the incorporation of the wall function for each variable into the FDE's are described below.

i) Velocity components

The requirement here is to correct the tangential velocity components in question for the wall shear stress, which represents the flux of momentum traversing the adjacent momentum control volume boundary. When the flow is laminar, the standard FDE performs this function, but for turbulent flow it is necessary to calculate the shear stress from the 'logarithmic law' equation (2.25). Taking, for example, a wall lying in the X-Z plane (see Figure (3.7.a)) the required shear stresses may be introduced into the FDE by first breaking the link between the node on the wall (N) and the adjacent grid node (P), (i.e. putting $a_N = 0.0$) and then modifying the source terms in the FDE. If the point P is within the turbulent region ($Y^+ > 11.5$) the latter source term may be obtained by rearranging equation (2.2 5) to yield a formula for the resultant shear stress τ_w, which for the X-Z directions leads to:

$$\tau_{w,z} = \kappa C_D^{\frac{1}{4}} \rho W_p K_p / Ln (Ey^+) \qquad 3.41$$

$$\tau_{w,x} = \kappa C_D^{\frac{1}{4}} \rho U_p K_p / Ln (Ey^+)$$

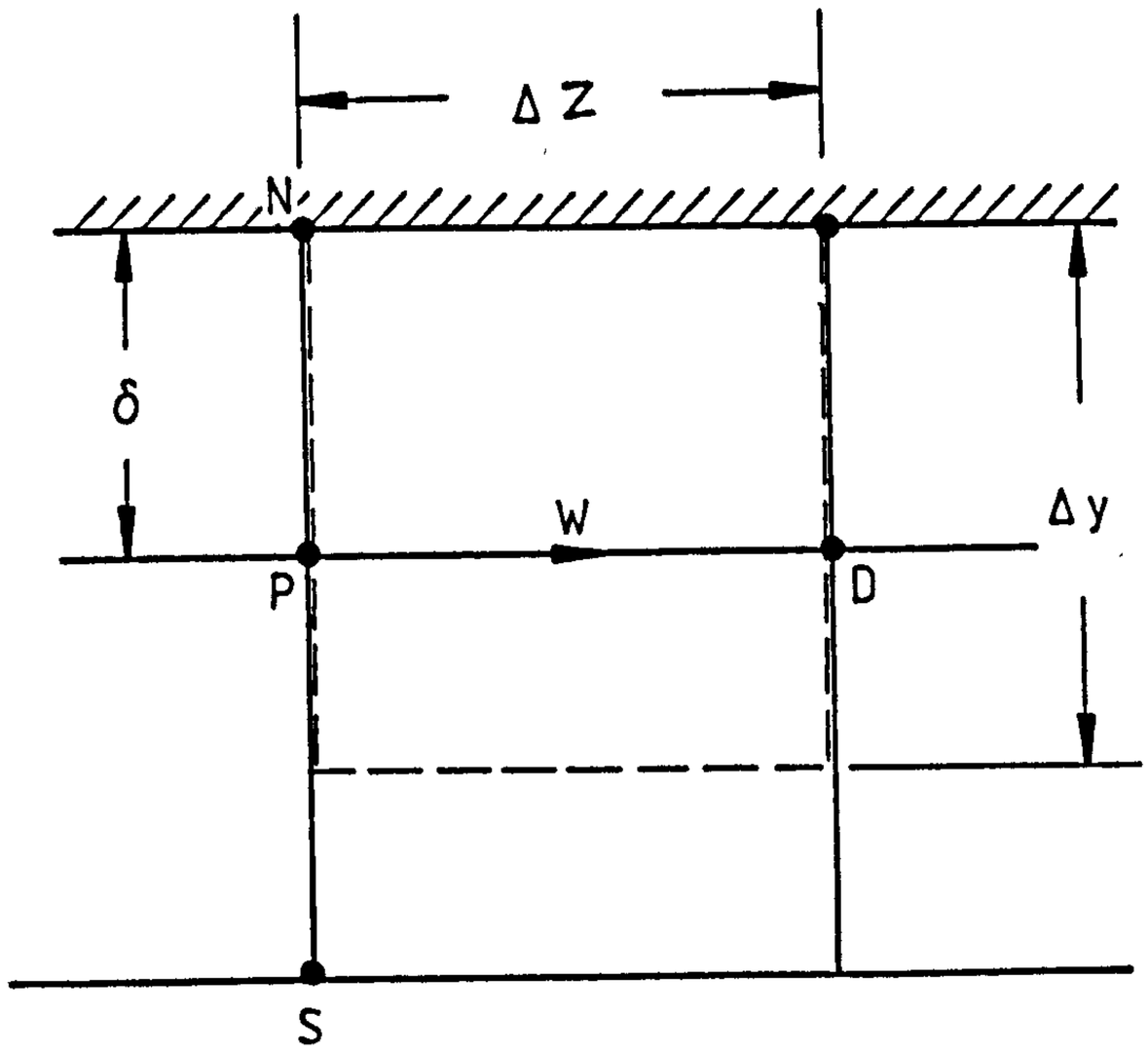

(a)

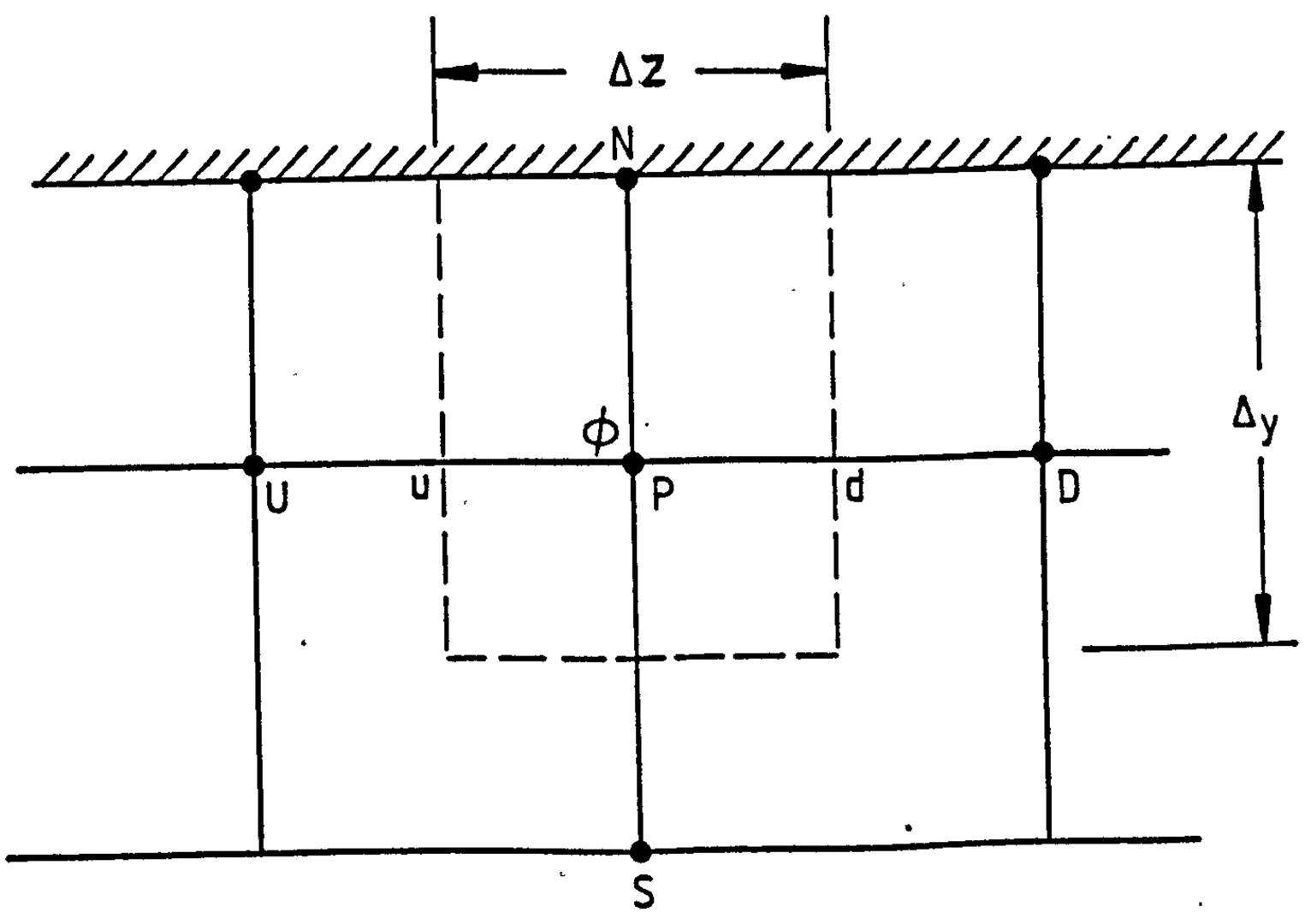

(b)

Figure 3.7 : Boundary control volumes for W and Φ .

where

$$y^+ = C_D^{\frac{1}{4}} \rho K_p^{\frac{1}{2}} \delta/\mu_l \qquad 3.42$$

However, if the point P is within the viscous (strictly 'linear') sublayer (i.e. $y^+ < 11.5$), then the wall shear stress simply be evaluated from:

$$\tau_{w,z} = \mu_l W_p/\delta \qquad 3.43$$

$$\tau_{w,x} = \mu_l U_p/\delta$$

Equations (3.41) and (3.43) constitute a simple two-layer model for the viscous sublayer. Although more elaborate models are possible, this simple approach will normally yield good results for practical purposes.

Pun and Spalding (34) recommend that the appropriate form of τ_w obtained from either of these expressions be inserted into the FDE via the source terms, for both tangential velocities, as follows

$$S_p' = S_p' - \tau_{w,z} \cdot A_n/W_p \qquad 3.44$$

$$S_p' = S_p' - \tau_{w,x} \cdot A_n/U_p$$

It should be noted that no special treatment is required for the velocity component normal to the wall.

ii) Turbulence kinetic energy

In addition to specifying zero normal gradient of K at the wall by setting the relevant flux coefficient to zero (i.e. $a_N = 0.0$, Figure 3.7b), it is also necessary to modify the terms describing the generation and dissipation rates to account for their steep near-wall variations. According to Pun and Spalding (34) these source terms are best expressed using the wall shear stress as follows:

$$S_K = G_K - \rho\varepsilon$$

$$= \tau_w \frac{\partial U_R}{\partial y} - \frac{C_D \rho^2 K^2}{\mu_t} \qquad 3.45$$

$$= \tau_w \frac{\partial U_R}{\partial y} - \frac{C_D \rho^2 K^2}{\tau_w} \cdot \frac{\partial U_R}{\partial y}$$

The integration of S_K over the control volume yields

$$\iiint S_K \, dV = S_p + S_p' K_p \qquad 3.46$$

with

$$S_p = \tau_w \cdot U_{Rs} \cdot A_n$$

and

$$S_p' = -C_D \rho^2 K_p U_{Rs} \cdot A_n/\tau_w \qquad 3.47$$

where

$$U_{Rs} = \sqrt{W_s^2 + U_s^2}$$

and

$$\tau_w = \sqrt{\tau_{w,z}^2 + \tau_{w,x}^2} \qquad 3.48$$

iii) Turbulent dissipation rates

The practice for this variable is to replace the finite-domain equation at the near-wall node by the log law-based relation given by equation (2.31), thus:

$$\varepsilon_p = C_D^{\frac{3}{4}} K_p . K_p^{\frac{1}{2}}/\kappa\delta \qquad 3.49$$

Pun & Spalding (34) and Patankar (65) recommend that this value be incorporated into the FDE via the source terms in the following manner:

$$S_p = \xi \varepsilon_p \qquad 3.50$$

$$S_p' = -\xi$$

Where ξ is a large number ($\simeq 10^{30}$) so that the other terms in the discretization equation (3.10) becomes negligible, i.e.

$$S_p + S_p' \Phi_p = 0.0 \qquad 3.51$$

and
$$\Phi_p = -\frac{S_p}{S_p'} = \frac{\xi\, \varepsilon_p}{\xi} = \varepsilon_p$$

iv) Heat flux

The enthalpy boundary condition can be introduced into the thermal energy FDE through a heat flux, q", from equation (2.33). This can also be written in terms of the wall shear stress following the practice of Pan & Spalding (34):

$$st = \frac{-q_w''}{\rho(H_P - H_N)U_{RP}} = \frac{|\tau_w|/\rho U^2_{RP}}{\sigma_t\ (1+P_J\sqrt{\frac{|\tau_w|}{\rho U_{RP}}})} \qquad 3.52$$

Another variant of this approach was adopted for the two-dimensional offset flow following (45)

$$st = \frac{-q_w''}{\rho(H_P - H_N)\ U_{RP}} = \frac{KC_D^{\frac{1}{4}}\ K_P^{\frac{1}{2}}}{\sigma_t\ [Ln\ (Ey^+) + P_J].U_{RP}} \qquad 3.53$$

The Jayatellaka P-function in this case is given by:

$$P_J = \frac{\pi/4}{\sin(\pi/4)}\left(\frac{26.0}{K}\right)^{\frac{1}{2}}\left(\frac{\sigma_l}{\sigma_t} - 1\right)\left(\frac{\sigma_t}{\sigma_l}\right)^{\frac{1}{4}}$$

The FDE coefficient a_N is first set to zero (see Figure 3.76), and the heat flux is then incorporated into the FDE by way of the source terms:

$$S_p = S_p + |St|\ \rho\ U_{RP}\ A_n\ H_N \qquad 3.54$$

$$S_p' = S_p' - |St|\ \rho\ U_{RP}\ A_n$$

3.4 SOLUTION OF FDE's

3.4.1 The Task

Section 3.2 illustrates how the partial differential equations, which describe a three-dimensional flow field, can be approximated by a set of algebraic equations (i.e. equations 3.10 & 3.15). These equations represent sets for the variables W, U, V, P', K, ε, H and any other scalar variables of interest, each comprising as many equations as there are grid nodes in the field. Since there are simultaneities and non-linearities both within and between sets, the equations have been solved using the SIMPLE iterative procedure of Patankar and Spalding (68). The procedure has been adopted in the following manner:

i) For the two-dimensional reattaching jet: a combination of 'line-by-line' iteration with a 'block' adjustment also applied in a line-by-line manner; see section 4.3.5

ii) For the three-dimensional laminar flow test cases: a line-by-line iteration; see section 5.2

iii) For the three-dimensional developing duct flow: a combination of line-by-line iteration with an overall continuity correction.

iv) For three-dimensional ventilated room problem: a combination of line-by-line iteration with a 'block' adjustment applied in a plane-by-plane manner.

Details will be given below, but first the essence of the method will be described.

The FDE's for nodes lying along a particular grid line can be expressed as:

$$\Phi_i = A_i \phi_{i+1} + B_i \Phi_{i-1} + C_i \qquad (3.55)$$

where

i denote the position along a particular line (i=2,n-1), and

n is the number of the grid points on the line.

With regard to the general finite-domain equation (3.10) for a particular Y-direction line, the quantities in equation 3.55 become

$$\Phi_i = \Phi_p \quad ; \quad \phi_{i+1} = \Phi_N \quad ; \quad \phi_{i-1} = \Phi_S$$

$$A_i = \frac{a_N}{a_p} \quad ; \quad B_i = \frac{a_S}{a_p} \qquad \text{and}$$

$$C_i = \frac{a_W \Phi_W + a_E \Phi_E + a_D \Phi_D + a_U \Phi_U + b}{a_p} \qquad 3.56$$

Equations 3.55 for nodes on the line are solved simultaneously by a matrix-inversion procedure, to yield all the Φ's along that line. The tri-diagonal matrix algorithm (TDMA) described in the next section, which has been adopted by Pun and Spalding (34) in the CHAMPION code, was also used in the present work. The algorithm is based on an elimination procedure that employs successive substitution to solve the elliptic FDE sets.

3.4.2 The Tri-Diagonal Matrix Algorithm (TDMA)

The TDMA enables the solution of a set of simultaneous, linear, algebraic equations which relate the value of Φ at adjacent points along a line in the form:

$$\Phi_i = A_i' \Phi_{i+1} + B_i' \qquad 3.57$$

which is a simpler form of equation (3.55). The transformed

coefficients A_i and B_i are given by the recurrence relations:-

$$A_i' = A_i/(1 - A_{i-1}' B_i)$$

$$B_i' = (C_i + B_{i-1}' B_i)/(1 - A_{i-1}' B_i) \qquad 3.58$$

Solution is then obtained by successive substitution; starting the recurrence with the coefficients having the values

$$A_1' = A_1 = B_1' = B_1 = 0.0 \qquad 3.59$$

3.4.3 The Block-adjustment Procedure

The block-adjustment procedure is used in an effort to speed convergence by taking better account of plane-to-plane (or for two-dimensional case line-by-line) interaction. Here the overall requirement for conservation of Φ is employed to yield adjustments $\delta\Phi$ which are uniform in each plane or line but vary between them. These adjustments are applied in such a way that all the adjusted planes or lines satisfy the overall conservation requirement. In order to achieve this, equation 3.10 is first rewritten in the form

$$A^P_{ijk}\,\Phi_{ijk} = A^E_{ijk}\,\Phi_{i+1,jk} + A^W_{ijk}\,\Phi_{i-1,jk} + A^N_{ijk}\,\Phi_{i,j+1,k} + A^S_{ijk}\,\Phi_{i,j-1,k} + A^D_{ijk}\,\Phi_{ij,k+1} + A^U_{ijk}\,\Phi_{ij,k-1} + Bijk \qquad 3.60$$

Where the i,j,k denote positions in the x,y and z directions respectively. If the approximate solution produced by TDMA line iteration is denoted by $\bar{\Phi}_{ijk}$, then a uniform increment $\delta\Phi$ is added to the interior nodes on each plane or line of constant k or i (excluding the boundary Φ's). This yields the following equations which must be satisfied:

$$\sum_i \sum_j A^P_{ijk}\,(\bar{\Phi}_{ijk} + \delta\Phi_k) = \sum_i \sum_j \left[A^E_{ijk}\,\bar{\Phi}_{i+1,jk} + \right.$$

$$A^W_{ijk}\ \bar{\Phi}_{i-1,jk} + A^N_{ijk}\ \bar{\Phi}_{i,j+1,k} + A^S_{ijk}\ \bar{\Phi}_{i,j-1,k} + A^D_{ikj}\ \bar{\Phi}_{ij,k+1}$$

$$+ A^U_{ijk}\ \bar{\Phi}_{ij,k-1} + B_{ijk}\Big] \ + \sum_i \sum_j \Big[A^E_{ijk} + A^W_{ijk} + A^S_{ijk} + A^N_{ijk}\Big]\ \delta\Phi_k$$

$$+ \sum_i \sum_j A^D_{ijk}\ \delta\Phi_{k+1} + \sum_i \sum_j A^U_{ijk}\ \delta\Phi_{k-1} \qquad 3.61$$

This produces, after further manipulation, the following equation for the $\delta\Phi$'S:

$$D_k\ \delta\Phi_k = A_k\ \delta\Phi_{k+1} + B_k\ \delta\Phi_{k-1} + C_k \quad ; \qquad 3.62$$

where

$$A_K = \sum_i \sum_j A^D_{ijk} \quad ; \quad B_K = \sum_i \sum_j A^U_{ijk} \quad ;$$

$$C_k = \sum_i \sum_j \Big[A^E_{ijk}\ \bar{\Phi}_{i+1,jk} + A^W_{ijk}\ \bar{\Phi}_{i-1,jk} + A^N_{ijk}\ \bar{\Phi}_{i,j+1,k}$$

$$+ A^S_{ijk}\ \bar{\Phi}_{i,j-1,k} + A^D_{ijk}\ \bar{\Phi}_{ij,k+1} + A^U_{ijk}\ \bar{\Phi}_{ij,k-1}$$

$$+ B_{ijk} - A^P_{ijk}\ \bar{\Phi}_{ijk}\Big]$$

and $D_k = \sum_i \sum_j A^P_{ijk} - \Big[A^E_{ijk} - A^W_{ijk} - A^N_{ijk} - A^S_{ijk}\Big]$

Equation (3.62) has the form of equation (3.55) and so can be solved by the TDMA with the increments ($\delta\Phi$'S) set to zero at boundaries. When the coefficient C_k (the sum of the residuals sources of equations (3.62) for a particular plane) is zero, $\delta\Phi_k$ will also be zero.

3.4.4 Overall Continuity Correction

The use of the overall continuity correction with the developing duct-flow problem was to ensure that, the true mass-flow rates pass each section along the duct. This could be achieved (following Patankar & Spalding (68), Pratap & Spalding (79) and Pun & Spalding (34)), by adjusting the streamwise velocity component to give the correct flow-rate, and the field pressure to satisfy the momentum

balance. According to Patankar and Spalding (68), a gussed pressure gradient, denoted by $(\partial p/\partial z)^*$ may be used to obtain the primary velocity w_p^* subjected to its boundary conditions. The gussed mass flow-rate, is given by:

$$M^* = \Sigma\rho\ \Delta x.\Delta y\ W_p^* \qquad 3.63$$

which will, in general be different from the true one (M) that can be computed directly from the inlet boundary conditions. This difference can be used to obtain corrected values for $\partial p/\partial z$,

$$\left(\frac{\partial p}{\partial z}\right) = \left(\frac{\partial p}{\partial z}\right)^* + \left(\frac{\partial p}{\partial z}\right)' \qquad 3.64$$

where $\left(\frac{\partial p}{\partial z}\right)'$ is the correction for $\left(\frac{\partial p}{\partial z}\right)^*$

The correct velocity can then be related to W_p^* using:

$$W_p = W_p^* + A_d \left(\frac{\partial p}{\partial z}\right)' \qquad 3.65$$

The required solution is:

$$\Sigma\rho\ \Delta x.\Delta y.W_p = M \qquad 3.66$$

and therefore substituting equation (3.65) for W_p yields:

$$\Sigma\rho.\Delta x.\Delta y\ [W_p^* + A_d \left(\frac{dp}{\partial z}\right)'] = M \qquad 3.67$$

Further manipulation of equation (3.67) leads to:

$$\left(\frac{\partial p}{\partial z}\right)' = \frac{M - M^*}{\Sigma\rho.\Delta x.\Delta y.A_d} \qquad 3.68$$

This will permit both W_p and $\partial p/\partial z$ to be found from equations (3.65) and (3.64).

The way in which these two alternative adjustment procedures were introduced into the solution procedure is described in section (6.3.2).

3.5 SOME NUMERICAL ASPECTS

3.5.1 Assessment of Convergence

During the computation the numerical process is monitored through the assessment of residual terms. A residual of any variable Φ at node P is defined from equation 3.10, by:

$$R_\Phi = a_p \Phi_p - \sum_{E,\ldots,U} a\Phi + b \qquad 3.69$$

For a given grid, the solution that produces sifficiently small residuals for all the variable solved everywhere in the field is regarded as a converged one. In order to facilitate monitoring, the residuals are suitably normalized, so that they are all of comparable magnitudes for the different variables considered, i.e.

$$\frac{\sum_{\text{FOR ALL FIELD}} |R_\Phi|}{R_{\phi,\text{REF}}} \leqslant \lambda \qquad 3.70$$

where λ is a convergence criteria, and $R_{\phi,ref}$ is some reference value specified relative to an appropriate property at entrance of the flow. The value of λ adopted for the present study was typically less than 0.005. The residual source for pressure correction equation was defined as the mass balance on the relevant control volume, i.e. b in equation 3.40.

3.5.2 Numerical Stability

The non-linear and strong inter-linkage characteristics of the FDE's, coupled with the use of an iterative solution procedure, lead to the possibility that numerical instability may develop. These instabilities usually lead to an imbalance in the conservation of the variable Φ on a local and overall basis, and hence to the oscillation of their calculated values over successive iterations. Such oscillations are particularly prevalent in the case of the buoyant flow, and when the QUICK differencing scheme is employed. Other factors which may also provoke instabilities include poor

specification of initial fields, inappropriate choice of under-relaxation factors and unsuitably linearisation of the source terms. The following measures were adopted in order to suppress such instabilities.

i) Initialization

Specifying realistic initial field values for the variables can be an important factor in ensuring both fast convergence and stability. In the two-dimensional reattaching jet case a free jet profile was adjusted so as to provide realistic initial guesses for the flow field (see section 4.3.3). The wall-jet profile analysis of Hammond (29-30) was used to initialise the field values for the variables with the three-dimensional ventilated room problem, prior to the first initial run. However, for subsequent runs, the results of previous computation were used to initialise the field values for all the variables and this procedure reduced the number for iterations needed to obtain a converge solution.

ii) Under-relaxation

Under relaxation promotes stability by carrying forward from one iteration to the next a value $\Phi_{p_{new}}$ which is a weighted mean of the value $\Phi_{p_{old}}$ from the previous iteration. Thus;

$$\frac{a_p}{\alpha_\phi} \Phi_{p_{new}} = \sum_{E,..,U} a \Phi + b(1 - \alpha_\phi) \frac{a_p}{\alpha_\phi} \Phi_{p_{old}}$$

or

$$\Phi_{new} = \alpha_\phi \Phi^* + (1 - \alpha_\phi) \Phi_{old} \qquad 3.71$$

where

$0 < \alpha_\phi < 1$ implies under-relaxation, and
$\alpha_\phi = 1$ implies no relaxation.

In this study α_ϕ was assigned values between 0.3 and 1.0 depending on the variables in question and the choice of solution algorithm. The

values of α adopted for each of the variables are listed in Table (3.1). However, in the case of buoyant flow the stability has been enhanced through the use of the inertial relaxation method of Ideriah (63). This method can be explained by re-writing equation (3.10) in an equivalent form (63):

$$\Phi_p = \frac{\sum_{E,\ldots,U} a_\Phi + b + \Phi_{p\ old}\ I}{a_p + I} \qquad 3.72$$

where Φ stands for the V component of the velocity

I is the relaxation factor which is given by:

$$I = \alpha_I\ \rho\ g\ \beta\ (T_p - T_R)\ /\sqrt{g\ \beta\ T_r\ L} \qquad 3.73$$

Here L is a geometrical length and α_I is a constant. In the present work α_I was given a value of 0.2 following the recommendation of Ideriah (63).

	W	U	V	H	K	ε	P	μ
	Relaxation factors							
SIMPLE	0.30	0.30	0.30	1.00	0.50	0.50	0.50	0.50
SIMPLEC	0.55	0.55	0.55	1.00	0.50	0.50	1.00	0.50

Table 3.1 Values of relaxation factors employed

iii) Linearisation of the source terms

The source terms of the FDE's may produce divergent solutions if they are not properly linearised. In the bucyant flow, for example, the temperature gradient in the source terms of K and ε equations may lead to unrealistic (negative) values for these variables if the linearisation is handled improperly. In the present work, therefore,

in addition to the use of the linearization practice employed in the CHAMPION code by Pun & Spalding (34), an extra measure was introduced to help obtain a converge solution. This involved specifying the source terms in the following way:

$$S_p = [[SA, 0.0]] \cdot \Phi_p$$

$$S_p' = -[[- SA, 0.0]] \qquad 3.74$$

$$\text{and} \quad SA = \frac{TERM}{\Phi_p}$$

where TERM is the buoyant part of the source term in K or ε equations, which can be either positive or negative.

3.5.3 Accuracy of the Solution

The following factors may influence the accuracy of the predicted results:

i) The degree to which the solution satisfy the FDE's

This can be assessed by ensuring that the residual sources for each variable have been reduced to an acceptable level. In this study, the iterative procedure was continued until the residual sources were less than the limit specified by equation (3.70).

ii) The degree to which the solution depends on the grid arrangement.

This results from discretized errors, which are a consequence of representing the continuous distribution of Φ in terms of values at the discrete grid nodes of the finite-domain mesh, and then interpolating between them. These errors can be reduced by increasing the grid fineness to an acceptable level. It is also desirable to use a non-uniform grid, with nodes concentrated in regions of high property gradients, such as those near walls. Evidence of the

existence or otherwise of such errors may be obtained from grid refinement tests, in which the number of grid nodes is systematically increased until changes in the solution become smaller than an acceptable tolerance. Since Φ_p is calculated as a weighted mean of the Φ's at adjacent nodes, smearing of the profile may occur in a situation where a steep gradient in ϕ occurs, such as in strongly recirculating flows. This leads to 'false diffusion' (55, 56, 74, 75), which can be minimised by keeping the cell Peclet number in these regions small. This could be achieved by:

a) identifying regions with high levels of effective diffusivity induced by false duffusion using an approach such as that suggested by McGurick et al (55) (which will be discussed in section 4.3.6).

b) refining the grid in these regions and/or

c) employing a differencing scheme, such as the QUICK scheme, which reduces these errors.

CHAPTER 4

COMPUTATION OF TWO-DIMENSIONAL JET REATTACHMENT

4.0 COMPUTATION OF TWO-DIMENSIONAL JET REATTACHMENT

4.1 INTRODUCTION

4.1.1 Background

The air-conditioning of a room serves several purposes: to remove or supply heat in order to maintain a comfortable temperature level and to supply the room with a given amount of fresh air. However, in the present economic climate with the relatively high price of land in urban areas, multi-storey buildings are common. In such buildings room height is at a premium, and is therefore restricted. To provide a controlled air supply to rooms, during winter and summer conditions, ceiling air diffuser systems have been used, but these leave only a small space between the inlet and the head of the occupant. This may lead to velocities in the occupation zone exceeding the threshold of 0.127 - 0.254 ms^{-1} normally required for human comfort (3,82). Similarly, a cooled jet stream issuing from small-aspect-ratio rectangular grilles mounted at high level in a side-wall will tend to arc downwards due to cold 'dumping' effects (2 - 4). Thus, the jet trajectory may enter the occupation zone, and again give rise to an undesirable level of air-movement (3). In order to prevent these uncomfortable conditions, the use of continuous linear diffusers has been suggested (2,83). One such device discharges an air jet adjacent to, but offset from, the ceiling. The jet entrains ambient air at its 'free' boundary, while air entrainment near the ceiling is restricted by the presence of the ceiling itself. This results in a reduction of static pressure in the region bounded by the jet and the ceiling. Consequently the jet curves towards the ceiling, and attaches to it forming a sub-atmospheric pressure, 'recirculation bubble' (84-90): see figure (4.1). Downstream of the attachment position the flow behaves in a similar manner to that of a plane turbulent wall-jet (86-87).

The phenomenon which causes the attachment has been referred to as the Coanda effect by several workers (84-90). However, Bradshaw (91) has noted that this is but one of three physical phenomona which have been associated with Coanda. The other two phenomena are:

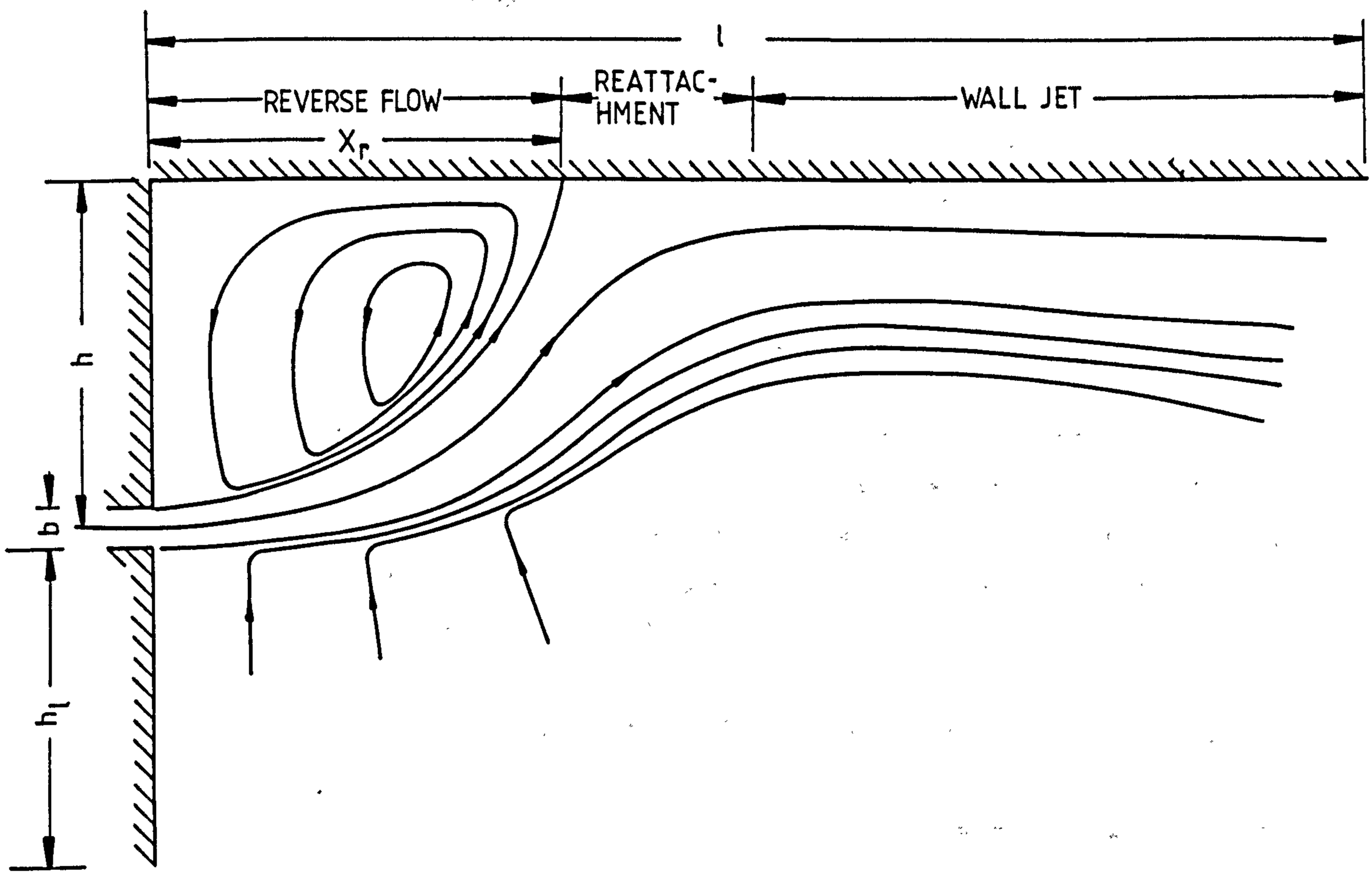

Fig. 4.1 : Two-dimensional jet reattaching to an offset solid boundary [adopted from Borque and Newman (84)] .

1) the inviscid flow effects whereby a jet, initially tangential to a curved surface, remains attached to the surface; the so-called "teapot effect"(91); and

2) the more complex viscous effect whereby a jet attached to a convex surface grows more rapidly than the corresponding wall-jet on a flat plate for which Bradshaw (91) has suggested the term Coanda effect should be reserved.

The phenomenon associated with the attaching jet, considered here, will therefore be referred to as the 'Chilowsky effect' following Metral and Zerner (92) who noted its use by Lafay in 1929, Hammond etal (93), and Omere (94).

4.1.2 The Aim of the Present Contribution

Much attention has been focused on the development of theoretical models to predict the jet characteristics of unbounded flows, but the effect of jet-boundary interaction has received less attention (87-88). The most commonly encountered problems of jet boundary interaction could be classified as (87):

1) wall-jets, where fluid is discharged along a solid boundary.

2) impinging-jets, where the discharge is aimed towards the boundary, and

3) offset jets, where the fluid is discharged parallel but at some distance from the boundary, and eventually attached to it.

Buoyancy effects, orientation of supply terminal and threedimensional effects, are additional factors which may further complicate a particular jet-boundary interaction problem.

The present contribution is concerned with the numerical simulation of a non-buoyant two-dimensional turbulent jet, discharging parallel to and offset from a solid boundary. It's purpose is to examine the flow field and heat transfer induced by such phenomenon.

4.2 LITERATURE REVIEW

4.2.1 Introduction

The behaviour of jets subjected to the Chilowsky effect have been investigated by several workers (83-95). These flows are of great importance in many practical applications, including air movement in rooms (1,3,4,82,94), the design of fluidic control elements, combustion and flow control mechanism (95), boundary layer control via blowing (96), fluid amplification devices (97), and flow speration in industrial heat transfer apparatus (86). The flow field induced by the Chilowsky effect may be divided into three regions (87): the reversed flow region, the reattachment region, and the wall-jet region, as shown in figure (4.1).

The main aim of the present study is to highlight the nature of a turbulent jet reattached to an offset parallel wall using computational modelling. Nevertheless, this survey will also embrace numerical work on other separated and reattaching turbulent flows, such as those created by an abrupt pipe expansion and a rearward-facing step. These are considered because the two situations have much in common from a numerical point of view, and they also represent a good test of the ability of the K-ε turbulence model to handle elliptic flow situations. The survey is consequently divided into two parts dealing firstly with turbulent offset jets, and secondly with numerical studies related to separated and reattaching turbulent flows.

4.2.2 Turbulent Offset Jets

Studies related to these flows can be catagorized into two groups: those concerned with flow field charactristics and momentum transfer, and those on heat/mass transfer. Both categories are considered below.

(i) Flow field characteristics and momentum transfer

Borque and Newman (84) were among the first to investigate the velocity and pressure field induced by two dimensional reattaching jets. They developed a theoretical model in which the problem was simplified by assuming that the velocity distribution is not directly affected by the presence of the solid boundary. Thus, the velocity field is calculated from similarity solution for two dimensional turbulent free-jets. This implies a zero pressure gradiant along the jet trajectory. The radius of curvature of the jet centre-line and the pressure inside the recirculation region were assumed constant. This model which is only valid for the pre-attachment or reversed flow region, yield reasonable predictions of the reattachment line location along the boundary. However, the use of the free-jet profile, together with the assumption of constant values for the radius of curvature and the base pressure, are not borne-out by Borque and Newman's own experimentatal data. Nevertheless, the assumption of a constant radius of curvature has been used to develop subsequent jet-boundary interaction models. Sawyer (89) employed it with a control volume approach, and obtained a solution that gave the reattachment line as a function of offset distance. The solution required the adoption of a value for the spread parameter of the curved jet that was greater than for a plane free-jet. Sawyer (90) later showed, using a first-order mixing length model, that different entrainment rates at the two edges of the jet does not substantially change the velocity profile shape from that of a free-jet. Despite the asymmetry in entrainment at the two edges, the total entrainment was found to be independent of curvature.

An experimental investigation of two-dimensional jet reattachment phenmenon carried out by Schwartzbach (97) suggests that the curved reattaching jet behaves in similar manner to plane free-jets, except that the spread rate and turbulence intensity are greatly increased (by about 75% in each case compared to free-jet data). Schwartzbach also used a volume flow rate balance in the reattachment region in an effort to evaluate the effect of jet curvature on entrainment along external and internal boundaries of the jet. He concluded that, although curvature may have some influence on the entrainment, this influence is not as simple as that suggested by Sawyer (90).

Hoch and Jiji (87) recently developed integral/entrainment methods to predict the velocity and pressure field in and around a two-dimensional jet discharging parallel to, and offset from, an adjacent solid boundary in the presence of co-flowing free-stream. In this model, the pressure and local radius of curvature in the reversed flow region were considered as variable to be determined from the solution. Agreement between their theoretical predictions and experimental data support the assertion that the entrainment mechanism in an offset jet is not influenced by the pressure field. However the model is restricted to rather limited range of values for the dimensionless offset high and free stream velocity ($Hr \leqslant 12.0$ and $u_\infty \leqslant 0.3$ respectively). Outside this range the modelling assumptions are not valid, and agreement with experimental data is poor.

(ii) Heat and mass transfer

Studies of heat/mass transfer beneath two-dimensional offset jets have been undertaken by several investigators (86,88,94). Kumada et al (86) carried out experimental measurements using the sublimation of nuphthalene to obtain mass transfer data, which may be converted to heat transfer rate via one of the heat/mass transfer analogies. They concluded that the flow development of an offset jet depends on the shape of the recirculation zone or 'bubble' induced by separation and reattachment. They found that a change in the bubble shape occurred when the ratio of offset distance to nozzle height exceeded 6.5. Moreover they suggested that the flow field down-stream of the reattachment point behaves like that of a classical plane wall-jet. On the basis of these results they developed several empirical formulaes to enable calculation of the maximum Sherwood number (Sh_{max}) in the reattachment region, the mean (surface-averaged) Sherwood number in the separation bubble region, and the local Sherwood number distribution over the region of reattached wall-jet. Their data indicates that the position of Sh_{max} occurs at a position rather close to the nozzle than the point of maximum pressure, normally regarded as being the reattachment point.

Omere (94) carried out an experimental study of the Chilowsky effect at Cranfield, for which a cooled offset air jet was ejected from a linear slot parallel to an adiabatic flat ceiling plate,

subsequently attached to it. The air jet (at ≃ 0°C) issued into quiescent ambient surroundings, and its temperature field was mapped using a 15 cm x 19 cm field view laser-stimulated Mach-Zchnder interferometer. Omere also made measurements of the mean (time-averaged) velocity distribution employing pitot-tube traverses. He found that the transverse-velocity and temperature profiles were near similar in the wall-jet region.

More recently Hoch and Jiji (88) conducted a theoretical and experimental study of the thermal characteristics of two-dimensional heated turbulent jets discharging parallel to, but offset from an adiabetic solid boundary. Their theoretical model was based on an integral formulation of the basic conservation laws, and utilises their previous flow field solutions (87) for this essentially non-buoyant jet. The model provides an analytic solution for the temperature distribution on the assumption that, due to efficient mixing, the temperature inside the recirculation region was uniform, and that the temperature profile in the reverse region of the jet could be represented by a Gaussian function. They concluded that the variation in the offset ratio (in the range $0 < Hr < 8.7$) has a noticeable influence on the adiabatic surface temperature in the recirculation region, but that this influence diminishes progressively downstream. On the basis of comparisons between their theoretical analysis and measurements Hoch and Jiji (88) argued that, although their model is adequate for the prediction of the thermal field it may not satisfactorily describe jet flow characteristics.

4.2.3 Numerical Investigations of Separated and Reattached Turbulent Flows

Nearly all the recent numerical studies of separated turbulent flows using the FDM have focused attention on that created by an abrupt pipe expansion (48,57,98-102), or that behind a rearward facing step (78, 102-103). These investigations involved computing the flow field pattern and the convective heat transfer, using either 'standard' or extended version of the K-ε turbulence model, together with a suitable computer program to solving the elliptic differential equations that govern such flows. Chieng and Launder (57) computed the flow field and heat transfer beneath the separated region created

by an abrupt pipe expansion. They used the standard K-ε turbulence closure, but with a modified wall function for evaluating the mean generation and dissipation rate terms in the K-equation. This model that was based on the idea that, beyond the viscous sublayer the turbulent length scale is universal, increasing linearly with distance from the wall, and that the sublayer Reynolds number is universal constant (as postulated by Spalding (104)). Their predicted Nusselt number distributions agree well with available experimental data for an expansion ratio (D/d) of 1.85, although a systematic difference was evident for ratio of 2.3, except at high Reynold numbers. They attributed this discrepancy to an incorrectly predicted reattachment line and to departures from axial symmetry in the experimental studies. They predicted the location of the maximum heat transfer rate to occure at about one step height [0.5 (D-d)] upstream of the reattachment point, and indicated that none of the various assumptions implied by the modified wall functions had any significant effect on this location. However, they argued that it is a matter of conjecture whether differences arose from near-wall turbulence modelling, or from inherent asymmetries or periodicities in the flow. They therefore recommended that new experiments be carried out, in which details of the flow field and heat transfer are simultaneously recorded. They suggested that these measurements should include turbulence correlations as well as mean-flow properties.

Johnson and Launder (98) have continued the above research (57) and drew attention to a coding error in the computer program used by Chieng and Launder. The corrected version gave heat transfer distributions which were 20-30% lower than those previously predicted, thereby increasing the disagreement with measurements. They concluded that their modified wall functions were still unsatisfactory for separated flows. In order to remedy this situation they derive a formula in which the sublayer Reynold number (Re_v) was effectively a function of the dimensionless change in total shear stress across the viscous layer. This was accomplished by introducing a new parameter which was equal to the ratio of the rate of turbulence energy diffusion into viscosity affected sublayer to the turbulence energy rate in the sublayer. The resulting variation in Re_v gave a satisfactory agreement with the measured Nusselt number distribution.

Amano (48) has extended the model of Chieng and Launder (57) by evaluating the corresponding terms in the ε-equation from the local variations in turbulence quantities with the near-wall region. He argued that ε near the wall is an order of magnitude larger than in the fully-turbulent core and reaches its maximum at the wall. He used his modified wall functions together with standard K-ε turbulence model to study the heat transfer for the abrupt pipe expansion geometry (57). A hybrid differencing scheme was employed to solve the full Reynold's (or time-averaged Navier-Stokes) equations. Amano's predictions show an improvement in the magnitude of the peak Nusselt number of about 20% compared to those of Chieng and Launder (57), but with little change in the location of this maximum. He noted that the location of the peak displayed good agreement with the experimental data for an expansion ratio of 1.85. However, a difference of four step heights between the predicted and measured location of the heat transfer peak was observed with an expansion ratio of 2.33.

Amano etal (99) conducted both experimental and numerical studies of the abrupt pipe expansion, but with expansion ratios of 1.7, 2.56 and 5.13. These investigations laid emphasis on the heat transfer in the separation region. The standard K-ε turbulence model, together with a fourth order differencing scheme, were adopted for the numerical study [which is also reported by Amano (100)]. However a refinement to the wall function of Amano (48) was employed, which utilized a three-layer model of the near-wall region. These three layers were the viscous sublayer ($o<y^+<5$), a buffer zone ($5<y^+<30$), and the fully turbulent zone ($30<y^+<400$). They noticed that the predictions given by Amano's two-zone model (48) agreed better with the experimental data for lower Reynolds numbers than for higher ones. In contrast, the three-zone model yields results which agree relatively well with the experimental data over a wide range of Reynold's numbers. They concluded that the treatment of the near-wall region is not very important for relatively low Reynold's numbers ($Re < 5 \times 10^4$), but is significant at higher values. The location of the maximum heat transfer rate was predicted in good agreement with experiment by both the two-and three-layer wall functions. Amano et al (99) observed that the simple K-ε turbulence model gave relatively good agreement with experiments provided that improved differencing schemes and near-wall modelling were adopted.

The flow behind a rearward-facing step at low to moderate Reynold's numbers was investigated by Gooray etal (101). They calculated the momentum and temperature fields numericlaly using the standard K-ε turbulence model, but using variable turbulent Prandtl number (Pr_t) distribution for the near wall region. However, the main contribution of their study was an assessment of the influence of the prescribed inlet profiles. They concluded that reasonably accurate predictions of the heat transfer coefficient for turbulent recirculating flows downstream of a step can be made using the standard K-ε model provided that the approach profiles are properly simulated.

Gooray et al (78) employed modified numerical procedure which utilized the quadratic differencing scheme of Leonard (74) to predict the above flow. They also used generalized expression for C_D and Pr_t in order to account for the effects of streamline curvature and the wall-damped pressure-strain interaction. Their procedure consists of a sequence of two computational passes (or sweeps); in the first one the modified K-ε turbulence model is used for the entire flow field, while in the second pass this modified model is used up to the reattachment line and then a low Reynolds number version is employed for the rest of the field. The two pass procedure can only be used for cases where a reliable prediction of the attachment can be made with the standard K-ε model. In spite of this restriction, Gooray et al (78) argued that with the variable turbulent exchange coefficient the two-pass procedure can be used for the engineering calculation of heat transfer coefficients for the rearward-facing steps and related configurations.

More recently, Hackman etal (103) reported numerical study of two-dimensional steady, incompressible flow over rearward-facing steps, under both laminar and turbulent conditions. Both hybrid and mixed skew/hybrid differencing schemes were employed in this study, together with the standard K-ε turbulence model in the turbulent case. The problem was solved using two different co-ordinate systems:- cartesian and curvilinear. The author's attention was focused on obtaining accurate solutios to the differential equations in order to

asses the actual source of discrepancies that have previously occured between prediction and observation. These have been attributed in earlier studies to inadequacies in the K-ε turbulence model. The study highlights the importance of accurately specifying the inlet profiles and the turbulence energy term near solid boundaries. They argued that their results gave significantly better agreement with measurement than some previous studies of this geometry using the same turbulence model. They concluded that the improved computations were mainly due to the better numerical accuracy of the differencing schemes. In order to assess the adequency of a turbulence model properly, they advocated that extream care must be taken to avoid confounding the error in such models with that due to the numerical solution error.

The overall conclusion that may be drawn from the above numerical studies is that, the standard K-ε turbulence model is capable of producing reliable predictions for turbulent recirculating flows provided that numerical errors are reduced or eliminated. This may be achieved by using differencing schemes that minimise false diffusion, and accurate inlet profiles. Obviously experimental data adapted for validation purposes must be reliable.

4.2.4 Conclusion

The theoretical models for two-dimensional offset jets reviewed in the previous section, were based on simple mass, momentum and heat balances along the curved path of the jet. This approach has been employed with extensive assumptions, about the shape of the mean velocity profile, the jet spread rate, the pressure gradient along the curved jet, its radius of curvature and entrainment rate. These were made in order to make corrections to the flow field characteristics of the plane free-jet. However, the validity of most of these assumptions is limited to the reverse flow region, and a restricted range of offset heights. On the other hand, there appears to be no high-level numerical studies of the offset jet geometry reported in the literature, and therefore the present investigation was undertaken to fill this gap.

4.3 SOLUTION PROCEDURE

The governing equations for offset jet flows have been solved numerically in the present study, employing the CHAMPION finite-domain code for two-dimensional elliptic (recirculating) flows. The general, three-dimensional formulation of these equations and their finite-domain counterparts were described in detail in chapters 2 and 3 respectively. The major problem-specific changes to the code are discussed below.

4.3.1 Boundary Conditions

The flow boundaries used for the offset jet geometry illustrated in figure (4.2) were as follows (see also sections 2.5 and 3.3).

i) Flow inlet

-U component: the presence of a strong pressure gradient over the jet inlet induces a non-uniform profile. This has been simulated using the practice adopted by Khan et al (105) who argued that the profile must be consistent with a constant total pressure condition. The computation was started assuming zero static pressure at the inlet region, and the total pressure was then calculated from a constant jet velocity (U_J):

$$P_{tot} = \frac{1}{2} \rho U_J^2 \qquad 4.1$$

The static pressure distribution over the inlet region computed at each subsequent iterations was then used to calculate the velocity profile within the jet region via the following relation:

$$P_{tot} = P_n + \rho u_n^2$$

$$\text{or} \quad u_n = \sqrt{\frac{1}{\rho} (0.5\rho U_J^2 - P_n)} \qquad 4.2$$

where P_n and U_n are the nodal values of the static pressure and the non-uniform velocity within the jet inlet region respectively. The

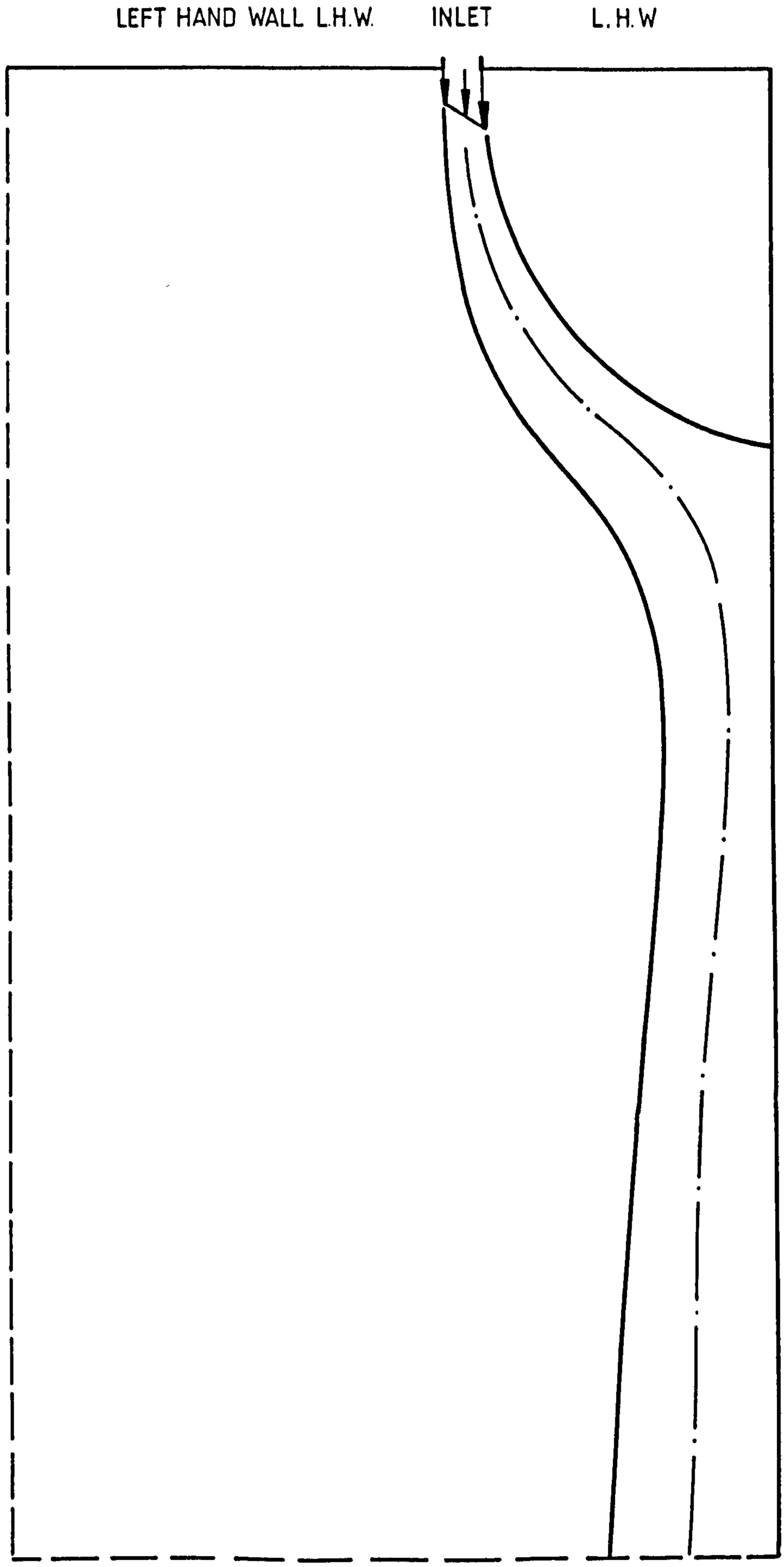

Figure 4.2 : Flow geometry considered .

BOTTOM FREE BOUNDARY (B F B)

values of U_n were corrected at each iteration in order to satisfy the original mass flow through the jet inlet using:

$$U_n \Big|_i = \frac{\rho U_J A_J}{\sum_n \rho U_n A_n} U_n \Big| i-1 \qquad 4.3$$

Here i represents the present iteration, and A_J and A_n are the total and the nodal area of the jet inlet respectively.

- Enthalpy (H): a uniform profile was specified by simply assigning a fixed value of all grid nodes across the nozzle inlet.

- Kinetic energy: a uniform profile has been assumed which is given by the following equation,

$$K_{in} = C_k U_J^2 \qquad 4.4$$

where C_k is a constant, which was given the value of 0.00387 (Hammond, 106). The inlet turbulence intensity was not provided by any of the experimental data reviewed in section 4.2.2.

- Energy dissipation rate: a uniform profile was adopted with a fixed value determined from the following formula.

$$\varepsilon_{in} = K_{in}^{\frac{3}{2}} / b.C_\varepsilon \qquad 4.5$$

where b is the width of the inlet nozzle and C_ε is a constant = 0.03 (Hammond, 106). The inlet value for ε was again not available from previous experimental studies, so the above value was chosen which is compatible with inlet value for K.

ii) Walls

The boundary conditions at the top and left hand walls for all the variables have been described in section 3.3.

iii) Exit and lower free boundarieds

A zero gradient was assumed for all the variables, except for V at the exit planes and H at the lower free boundaries which were specified as follows:

$$V = 0.0 \qquad 4.6$$

H see section 4.4.2 and table 4.3.

In order to ensure that these assumptions had no significant influence on the predictions in the vicinity of the recirculation zone, the position of both boundaries was progressively moved downstream and downward respectively until this zone became unaffected by the boundary locations. These locations were then adopted for further computations.

4.3.2 Computational Grid

Computations for the offset jet geometry have been performed for the following range of offset ratio (Hr): $3.5 \leqslant Hr < 32.5$. A typical computational grid distribution is shown in Figure 4.3, where the grid expansion in both directions is evident. In the X-direction the expansion starts from the left hand wall (LHW) and then proceeds downstream until the exit plane. In the Y-direction a uniform grid distribution was adopted for the jet inlet nozzle. This grid was then expanded from the bottom lip of the nozzle downward towards the lower free boundary (LFB). It was also expanded upwards as far as half the offset distance, from where the grid spacing was decreased up to the top wall. This arrangement was employed in order to cluster the grid nodes together in regions where the flow properties vary rapidly, such as close to the jet 'axis' and near the walls. The total number of grid lines and their expansion factors in both direction were calculated from formulae derived from grid independent tests (details

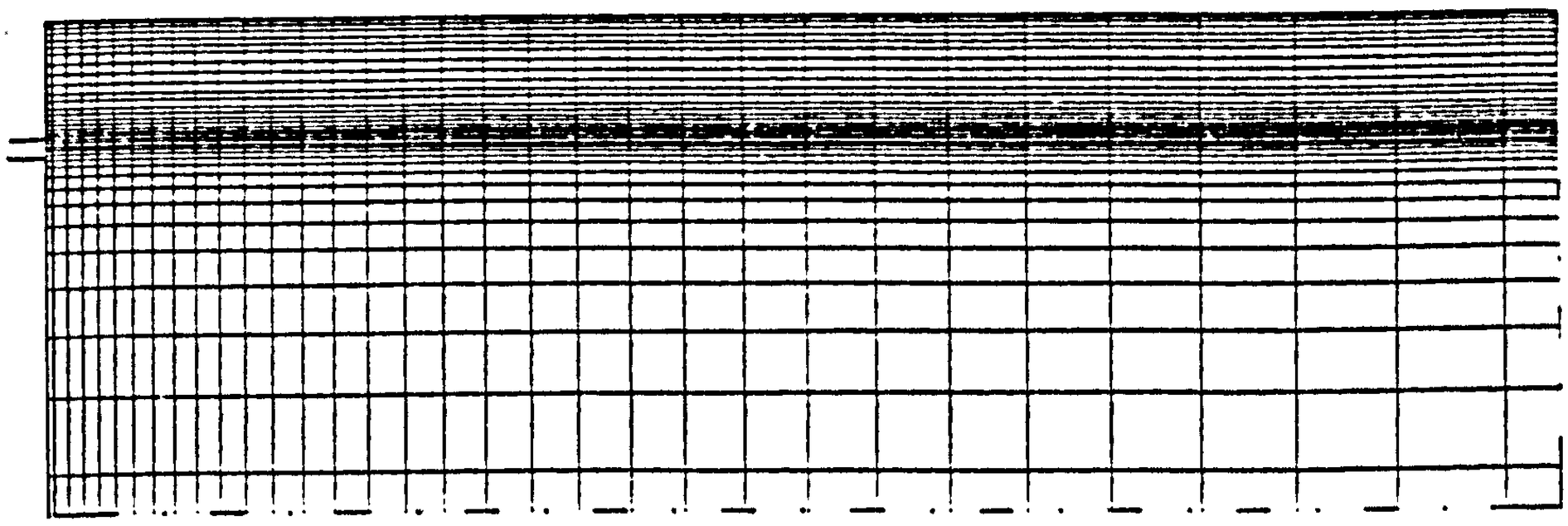

(a)

(b)

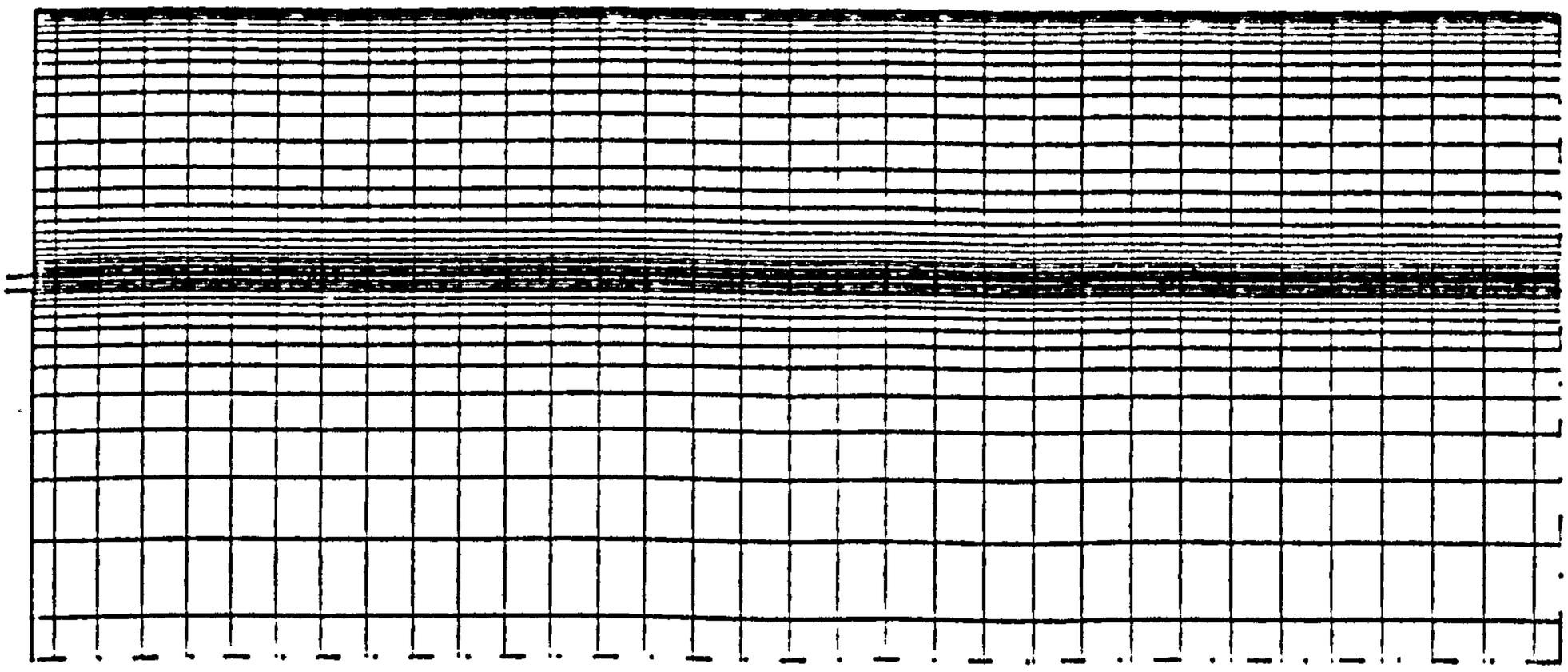

Figure 4.3 : Typical grid distribution for offset jet ,
a) Hr=6.5 and b) Hr=20.0 .

of which are given in section 4.3.6). These expressions yield a nodal network that ensures grid-independent solutions for each offset ratio, and they are given below.

The generation of a nodal network for a given offset ratio requires the knowledge of the ceiling plate length (L), and the length of the lower-left-hand wall. In the present contribution L was obtained on the basis of experimental recommendation (84,86), L (= 3.8 X_r) where X_r is the reattachment length. Kumada et al (86) have proposed the following relations for X_r:

$$X_r = 3.7\, h\, Hr^{-0.36} \qquad Hr < 6.5 \text{ , and}$$
$$X_r = 2.3\, h\, Hr^{-0.125} \qquad Hr > 6.5 \qquad (4.7)$$

The length of the boundary surface below the nozzle (h_1), on the other hand, was estimated from:

$$h_1 = 0.27L \qquad (4.8)$$

The value given by this expression was found, by trial-and-error, to be sufficient to eliminate the effect of the lower free boundary on the final solution. The grid distribution in both directions (Y and X) was then obtained as follows:

i) Y-direction

- <u>At jet inlet nozzle</u>

A uniform grid distribution was used in this region and was obtained from:

$$Y_s = b/N_b \qquad (4.9)$$

where Y_s is the distance between two adjacent grid lines lying in the X-direction and N_b is the total number of grids in this region. N_b was given a value of 5 in the present computations.

- Below the lower lip of the jet inlet nozzle

An expansion factor F_y = 1.3 was used to generate an expanding grid in this region. The required number of grid lines in the region was estimated using the following expression:

$$N_y = Ln\left[(H_y\ (F_y-1.0) + Y_s)/\ Y_s\right] / Ln(F_y) \qquad 4.10$$

where H_y represents the length of the surface (h_1 in figure 4.1).

- Above the jet inlet nozzle

The expansion factor used in this region is given by

$$F_y = 0.809 - 0.258\ Ln\ (Hr) - 5.120 \times 10^{-2}\ (Ln(Hr))^2 + 3.820 \times 10^{-3}\ (Ln\ (Hr))^3. \qquad 4.11$$

It was previously mentioned that the grid in this region was expanded up to half of the offset distance, and then contracted up to the ceiling plate. In order to obtain this grid distribution equation 4.10 was employed, but with the value of F_y given by equation 4.11 and H_y set equal to 0.5h.

The total number of the grid nodes in the Y-direction, was then obtained by summing the grid nodes for the three regions: the jet inlet region, and those regions above and below the jet inlet nozzle.

ii) X-direction

The total number of the grid lines in this direction (N_x) was calculated from:

$$N_x = \ln\left[(L\ (F_x - 1.0) + X_s)/X_s\right]/\ln\ (F_x) + 1.0 \qquad 4.12$$

where F_x is the expansion factor which given by:

$$F_x = 1.132 - 8.250 \times 10^{-3}\ Hr - 3.770 \times 10^{-4}\ Hr^2 + 3.442 \times 10^{-5}\ Hr^3 - 5.7971^{-6}\ Hr^4 \qquad 4.13$$

and, X_s is the distance between the first and second nodes in the region. The latter was used as a base value from which to expand the grid, and was given by :

$$X_s = 2.450 \times 10^{-3} - 6.680 \times 10^{-2} \times X_r + 1.917\, X_r^2 - 1.188\, X_r^3 + 89.519\, X_r^4 - 314.801\, X_r^5 \qquad 4.14$$

4.3.3 Initialization of the Dependent Variables.

Field values for the dependent variables must be assumed in order to start the iterative procedure that is employed to solve the governing equations. The impact and importance of these assumptions on the solution were discussed in section 3.5. In the offset jet study, the initial distribution of the dependent variables was based on plane free-jet data. Experiments suggest (106) for the following relations:

- Centreline velocity decay

$$\frac{U_m}{U_J} = 1 \quad \text{for} \quad \frac{x}{D} < 5.86$$

$$\frac{U_m}{U_J} = 2.42 \left(\frac{x}{D}\right)^{-0.5} \quad \text{for} \quad \frac{x}{D} > 5.86 \qquad 4.15$$

The velocity profile may be approximated by (107):

$$\frac{U}{U_m} = \exp\left[-0.693 \left(\frac{y}{b_u}\right)^2\right] \qquad 4.16$$

while the jet spread may be obtained from:

$$\frac{b_u}{D} \simeq 0.108 \left(\frac{x}{D}\right) \quad \text{and} \quad \delta \simeq 2.4\, b_u \qquad 4.17$$

Here U is local mean velocity, b_u is the velocity 'half width' (defined as the distance between the jet centreline and the point where the local velocity is half the maximum), and δ is half the jet thickness.

The field values for the V-component was assumed to be a small fraction of the value of the corresponding U-component. The distribution of both these components were arranged to follow a curved jet trajectory up to the reattachment line given by equation (4.7); see Figure 4.4.

- Turbulence quantities

The initial distribution of the turbulence quantities were found from the following equations (106-107).

$$K = K_{in} \quad 2.64 \Big/ \sqrt{(X/b)} \qquad 4.18$$

$$\mu_t = 0.037 \ \rho U_m \ b_u \qquad 4.19$$

$$\varepsilon = C_D \ \rho \ K^2 \Big/ \ \mu_t \qquad 4.20$$

These distributions were assumed constant in the cross-stream direction.

The above approach was found to reduce the computational time required to obtain a converged solution by ≈ 10% compared with a uniform distribution - originally adopted by Pun and Spalding (34) for the CHAMPION code. More importantly, it was found to prevent the possibility of divergence, especially for large offset ratios (Hr >10.0).

4.3.4 The Choice of Differencing Scheme

Numerical diffusion, or false diffusion, is known to accompany first-order upwind-differencing schemes that are used to approximate the convection terms in the FDE's for turbulent recirculating flows (55,75,108-111). These errors arise because the velocity vector is significantly skewed to the numerical mesh in recirculation zone (65,111). Recently, Leonard (74) proposed the QUICK-scheme (see section 3.2.5) in an attempt to reduce false diffusion, and several workers have been shown that it produces greater numerical accuracy for both laminar and turbulent recirculating flows (75,76,78,81,110). This scheme has therefore been adopted for the present study in order

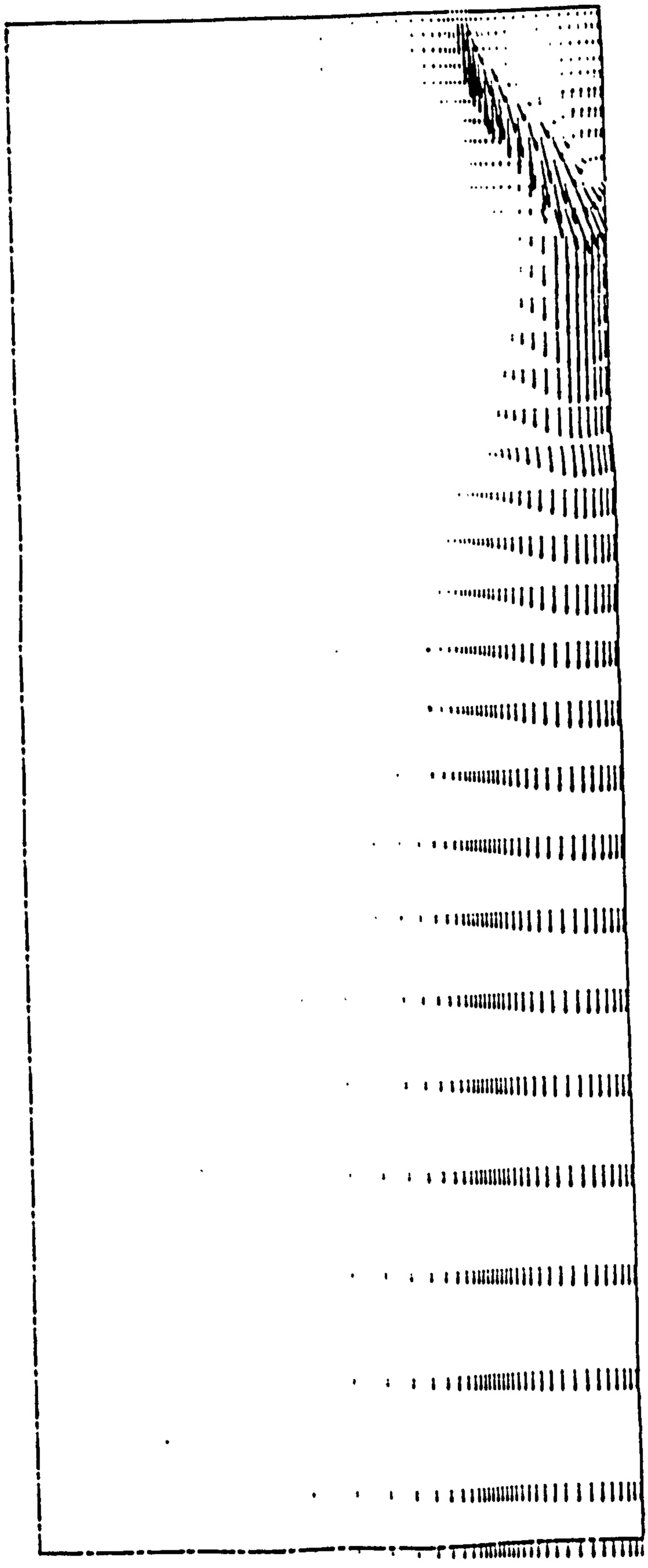

Fig. 4.4 : Vector profiles implied by the intial distribution chosen for the veolcity components .

to reduce the numerical diffusion errors. It should be mentioned that the QUICK scheme was only used in the solution of the momentum equations, while a power-law scheme was employed in the calculation of the thermal energy and turbulence transport equations. This approach was first employed by Leschziner and Rodi (110), who concluded that the solution of the K and ε equations is insentive to the choice of differencing scheme. They argued that, in the regions bordering a recirculation zone, the source terms will dominate convective transport.

4.3.5 The Solution Sequence

The solution procedure adopted here is similar to the SIMPLE algorith of Patankar and Spalding (68) [more recently described by Patankar (65)] except that:

i) This algorithm was replaced by SIMPLEC in order to speed-up convergence;

ii) All variables were solved in a line-by-line manner advocated by Pun and Spalding (34); and

iii) A two- dimensional block adjustment procedure also applied in a line-by-line manner was employed to ensure continuity.

The sequence in which the FDE's were solved was as follows:

a) The variables were initialized
b) A line was selected.
c) The convection, diffusion and source terms for a chosen variable (Φ) were evaluated for all nodes on the line.
d) The FDE's were solved using the TDMA.
e) The block-adjustment coefficients were calculated.
f) Steps b-e were repeated for all variables (Φ's), except P'.
g) U^* and V^* (obtained from step d) were then employed to calculate the coefficients in the pressure-correction equation.
h) The pressure corection equation was solved using the TDMA.
i) The resulting pressure correction was then employed to update the pressure and velocity components.

j) An adjacent line was selected and the sequence of steps c-i was repeated.

k) The cycle of step b-j represents one iteration at the end of each of these iterations the block-adjustment equation was solved using TDMA.

l) The increment $\delta\phi$ were then added to the corresponding Φ's on each line.

m) Steps b-l were finally repeated until a converged solution was obtained.

4.3.6 Grid Independent Solution

A grid independence test was performed by refining the nodal network in two regions, namely the recirculation and reattached regions. The methods used to assess the grid independence of the present computations are similar to those developed by McQuirk and Rodi (56), and by De Vahl Davis and Mallinson (108). These tests were performed over nearly the whole range of offset heights considered in the present study ($3.0 < Hr < 32.5$), although only the results for Hr = 6.5 and 32.4 are presented here. The two methods are explained below.

i) McQuirk and Rodi's method.

McQuirk and Rodi (56) devised a method for identifying those flow regions which are likely to contain significant false diffusion errors. It enables the magnitude of these errors to be determined, and the influence they have on the local flow variables. A detailed description of this approach may be found in McQuirk etal (109), but the main step in the method was as follows:

1) A converged solution of the FDE's for a given grid distribution was obtained using the current (i.e. QUICK) differencing scheme.

2) The magnitude of the convection, diffusion and source/sink at each grid node were then calculated using central differencing together with the converged solution values for the relevant variables (Φ's). This gave rise to an out-of-balance residual (T_r), which represented the false or numerical diffusion error.

3) Cross-stream profiles for the three transport terms, and the out-of-balance residual were then plotted for selected axial stations. This enabled the magnitude of T_r to be examined to see whether they constituted an important term in the local balance of the relevant differential equation. If this residual was large at a particular location, then this indicated that the grid spacing needed refinement in this locality.

4) A new solution was then obtained with refined grid, and again a check was made for large values of T_r. This sequence was repeated until a grid with acceptably small values for T_r was obtained.

This method has been used to guide the selection of a suitable grid for the present study. Refined grid solution for two offset ratios (H_r of 6.5 and 32.4) are illustrated in figure 4.5-10. In these figures the various terms in the U- momentum equation are plotted as cross-stream profile at selected axial stations. Each term in these figures has been normalized using $\rho U_J^2/b$. The four profiles in each plot reflect the net convection, the net diffusion, the source/sink term, and the resulting out-of-balance residuals. The locations for these profiles were chosen to represent the recirculation region (Figures 4.5,4.8), the reattachment region (figures 4.6,4.9), and the wall-jet region (Figures 4.7,4.10). In figures 4.5-4.7 (which represent a relatively small offset ratio of 6.5) a grid of 34 x 36 nodes in X and Y direction has been used. It is clear that the vlaue of T_r is small everywhere and is smaller than the other terms, except in the near-slot area of the recirculation zone (Figure 4.5(a) and (b)). This was anticipated as the velocity vector make an angle with computational grid and false diffusion is therefore greatest. The out-of-balance residual decreases downstream, and falls to negligible values in the wall-jet region.

Figures 4.8-4.10 show the balance profiles for larger offset ratio of 32.4 for which a 39 x 48 nodal network was employed. The above remarks about the value of T_r also apply to this geometry.

The values of T_r within the recirculation regions (station (a) and (b) of figures 4.5 and 4.8) for both ratios were found to be large relative to other regions and unresponsive to further grid refinement.

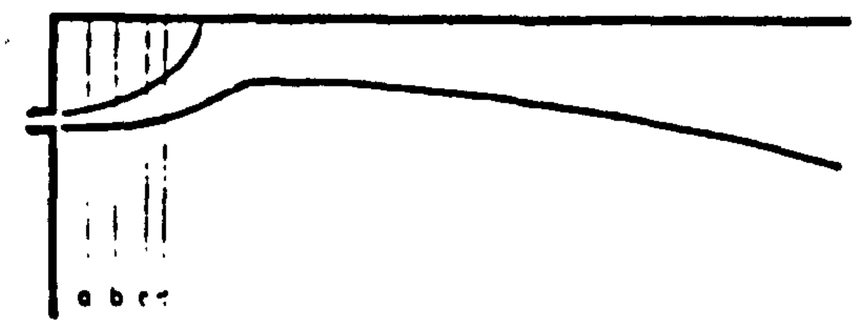

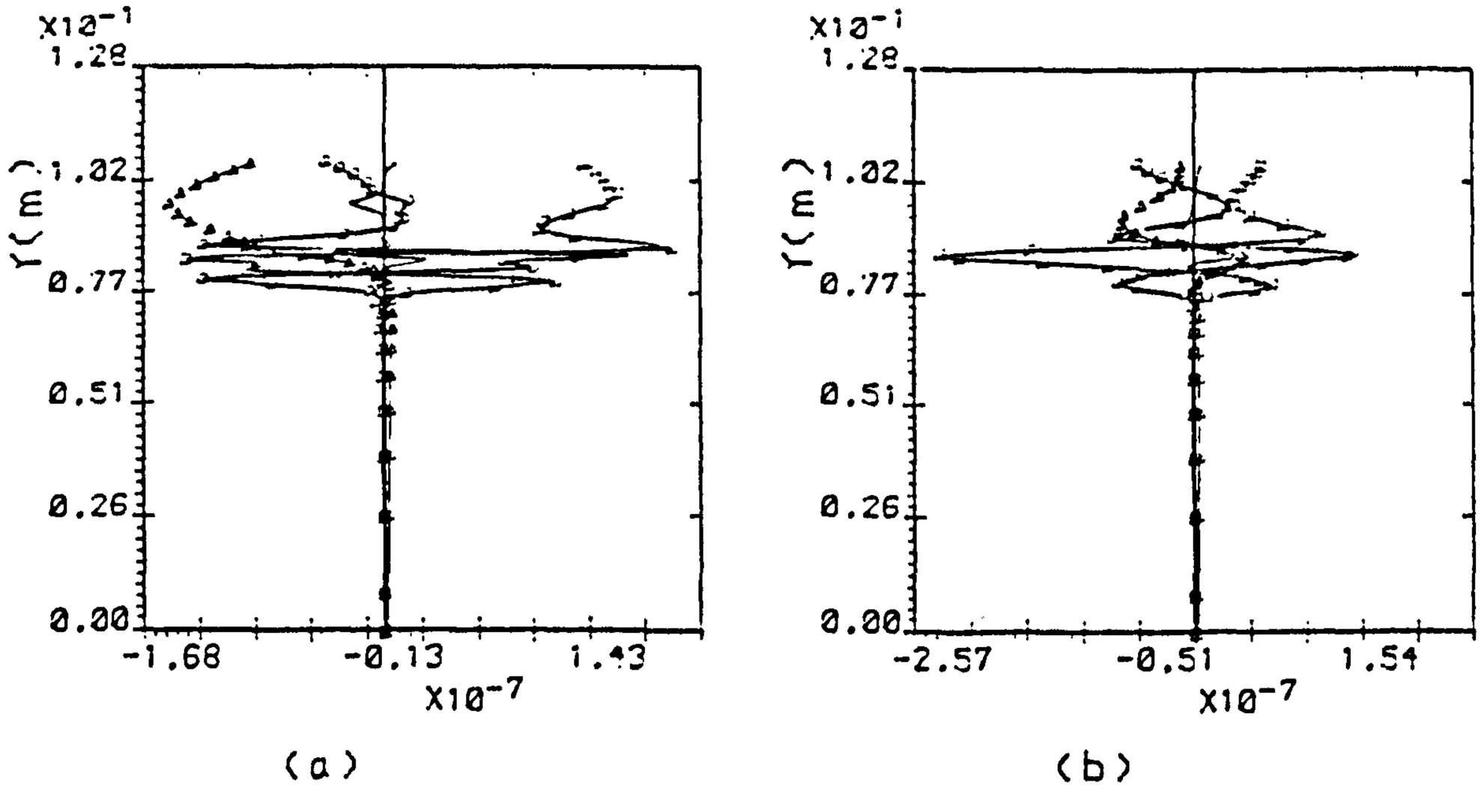

o net diffusion , □ net convection , △ source term , — Tr

Fig. 4.5 : The balance of U-momentum eqt. at the recirculation region for Hr=6.5 ,
(a) x/b=2.4 , (b) x/b=4.2 , (c) x/b=6.3 , (d) x/b=7.4

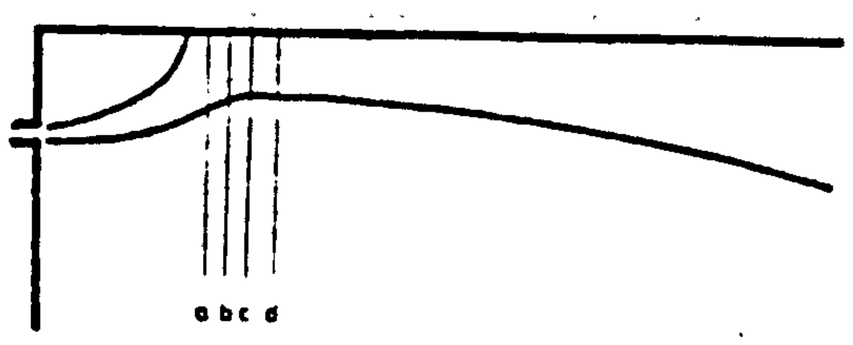

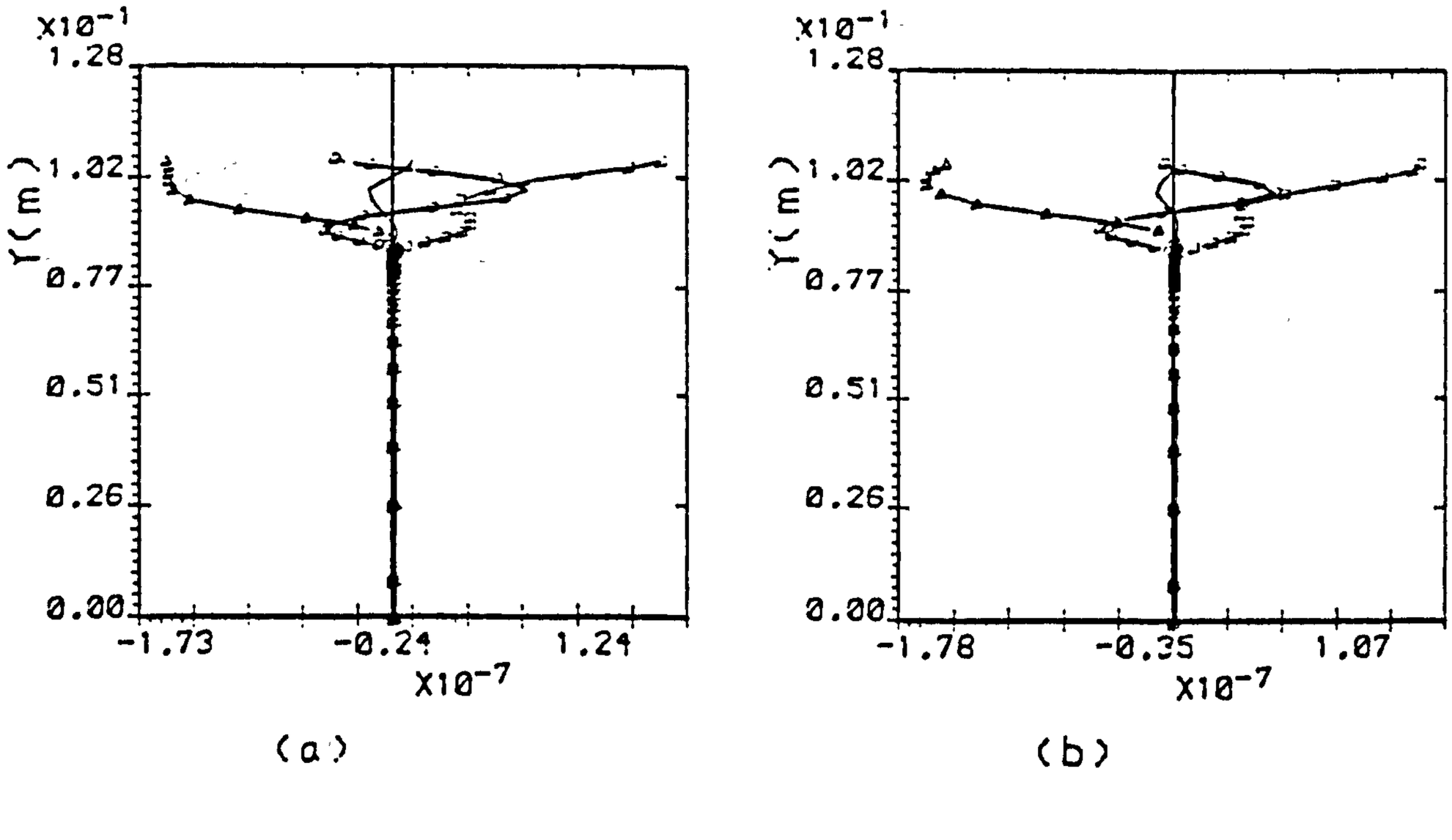

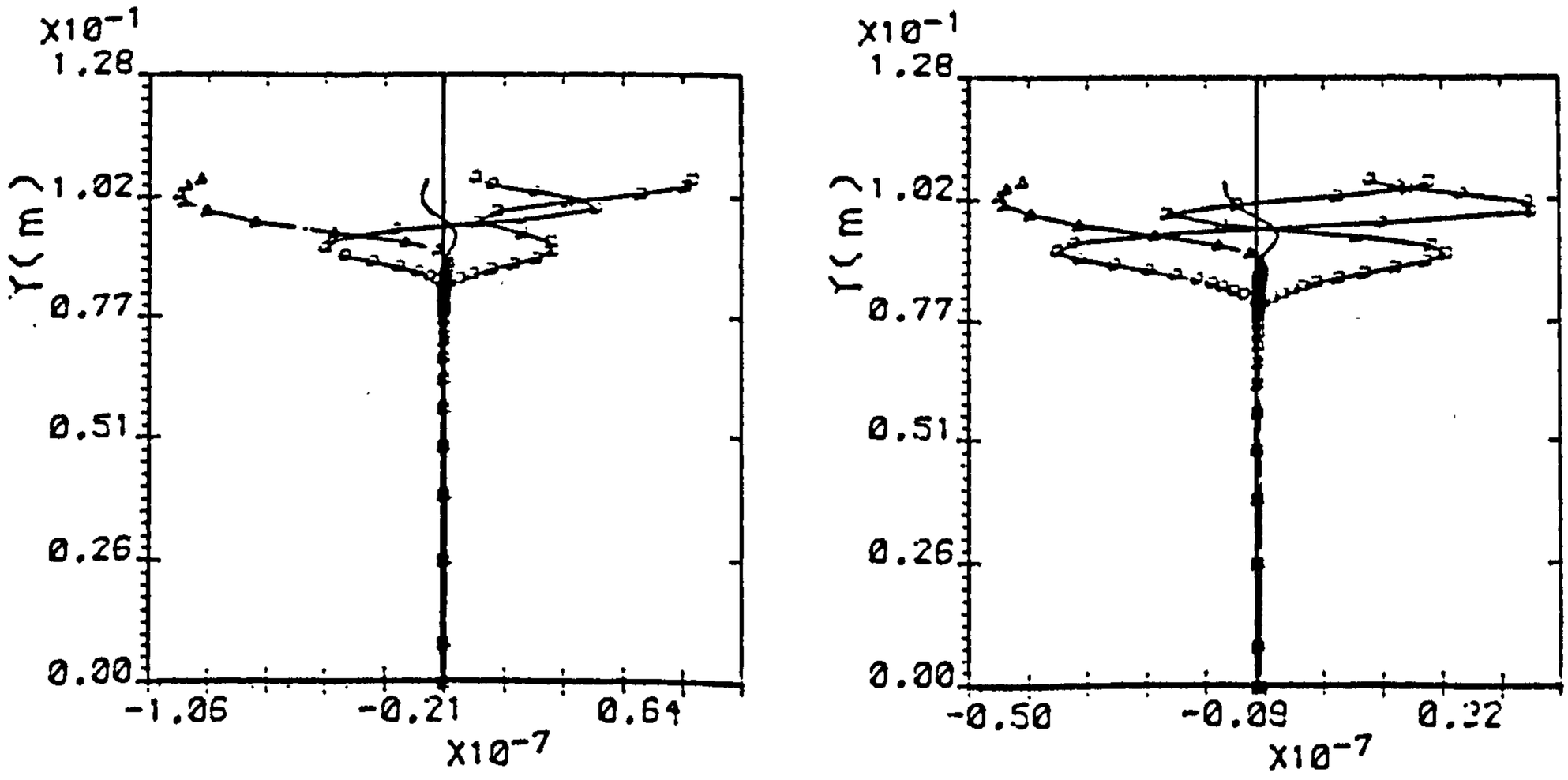

o net diffusion , □ net convection , △ source term ,— Tr

Fig. 4.6 : The balance of U-momentum eqt. at the reattachment region for Hr=6.5 ,
(a) x/b=11.5 ,(b) x/b=13.1 ,(c) x/b=14.7 ,(d) x/b=16.5

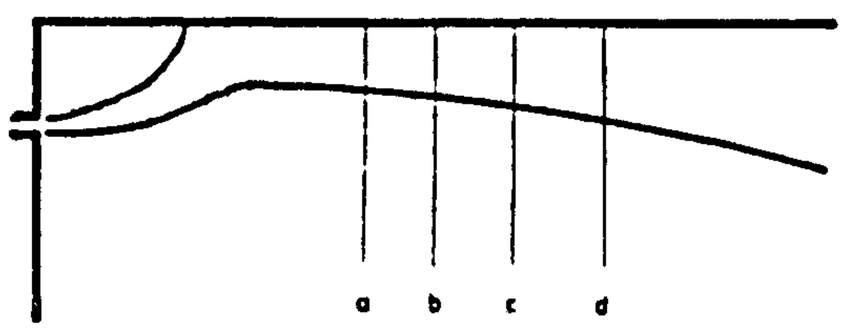

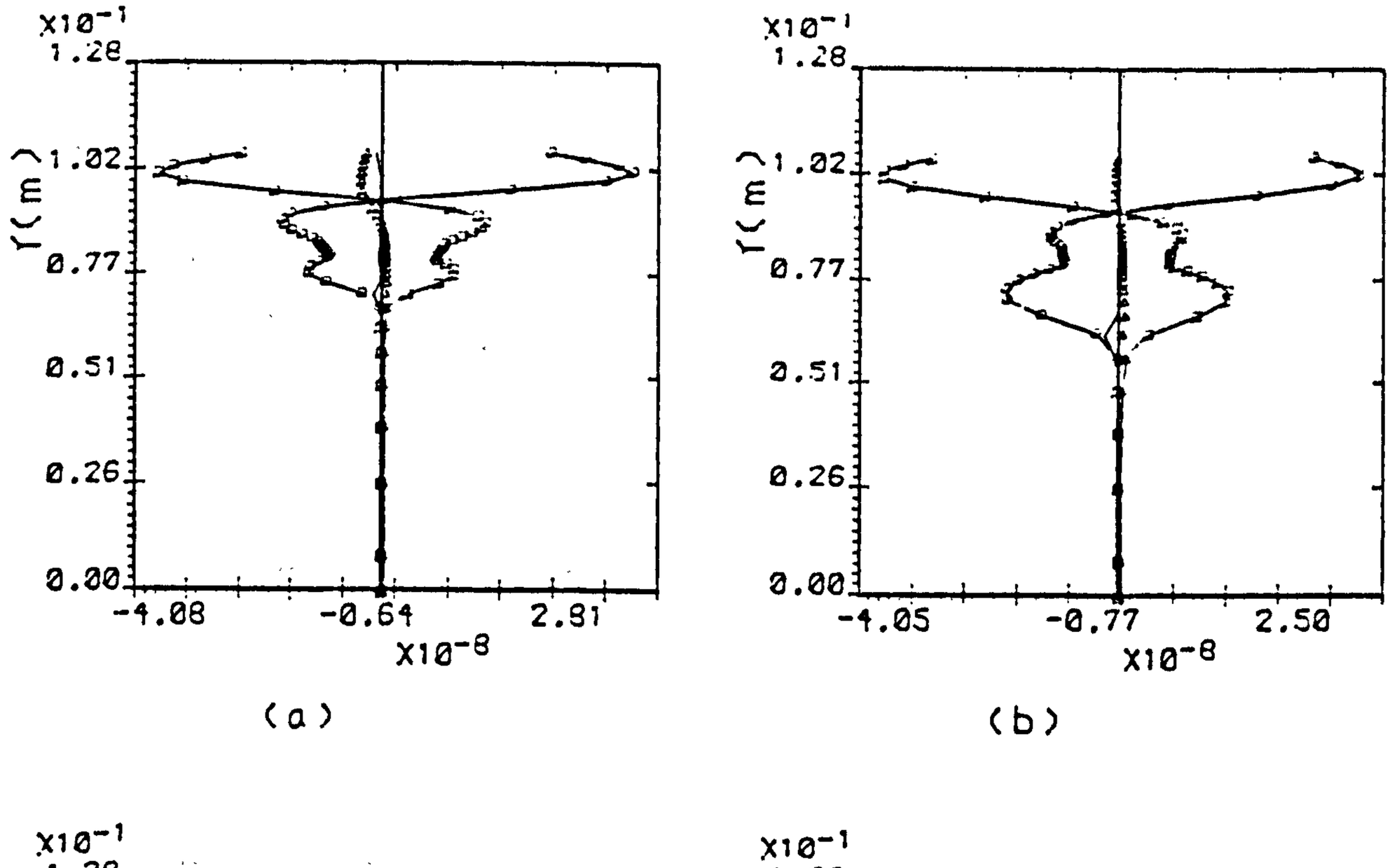

o net diffusion , □ net convection , Δ source term , ___ Tr

Fig. 4.7 : The balance of U-momentum eqt. at the wall-jet region for Hr=6.5 ,
(a) x/b=22.5 ,(b) x/b=27.3 ,(c) x/b=32.8 ,(d) x/b=39.1

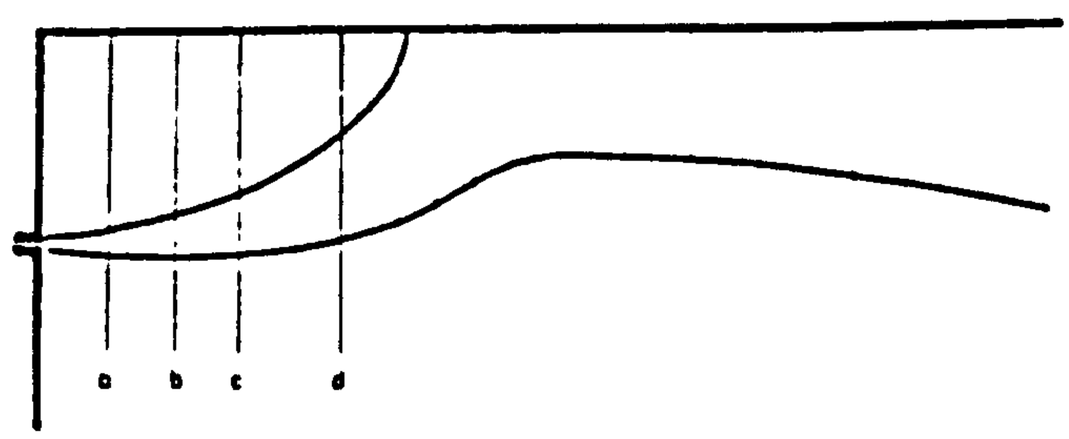

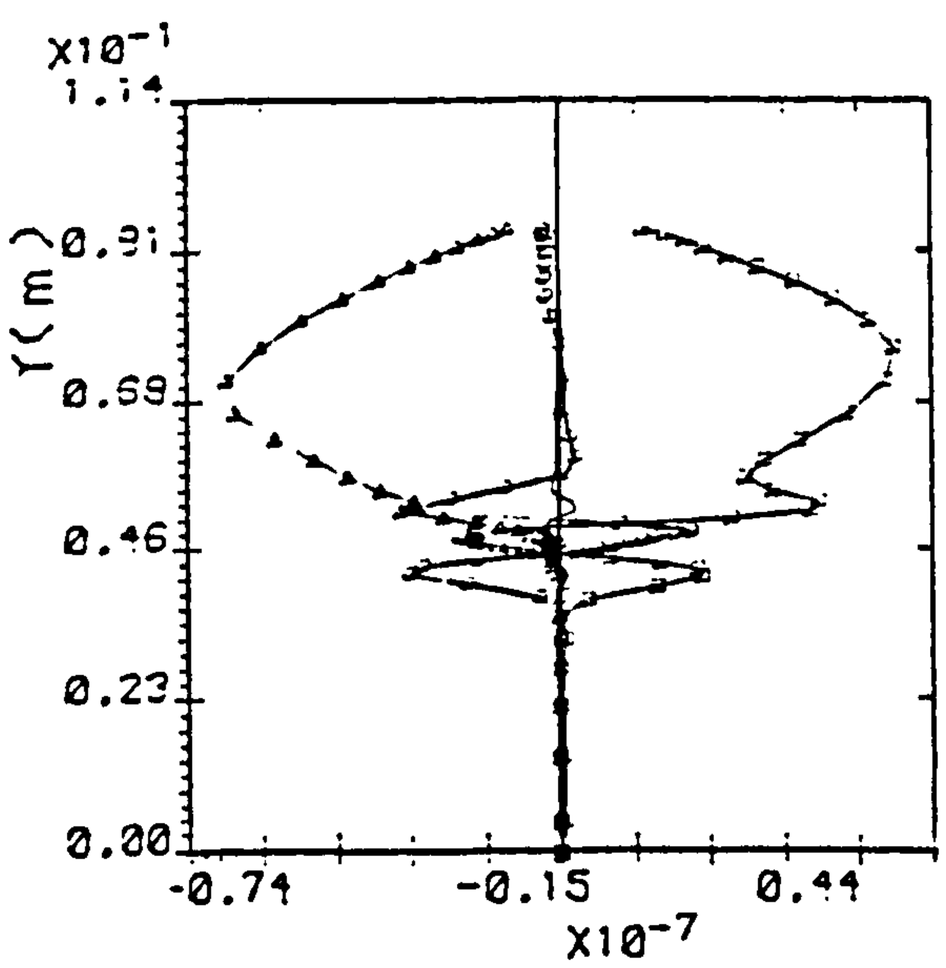

(a)

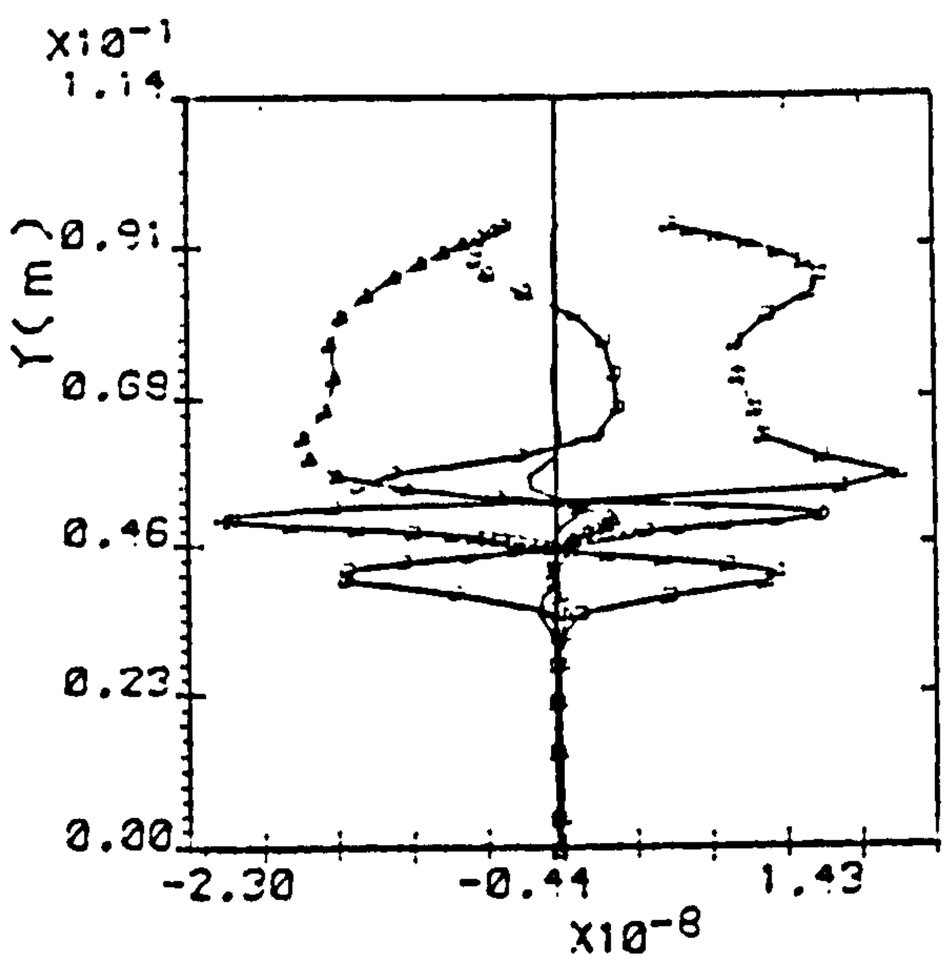

(b)

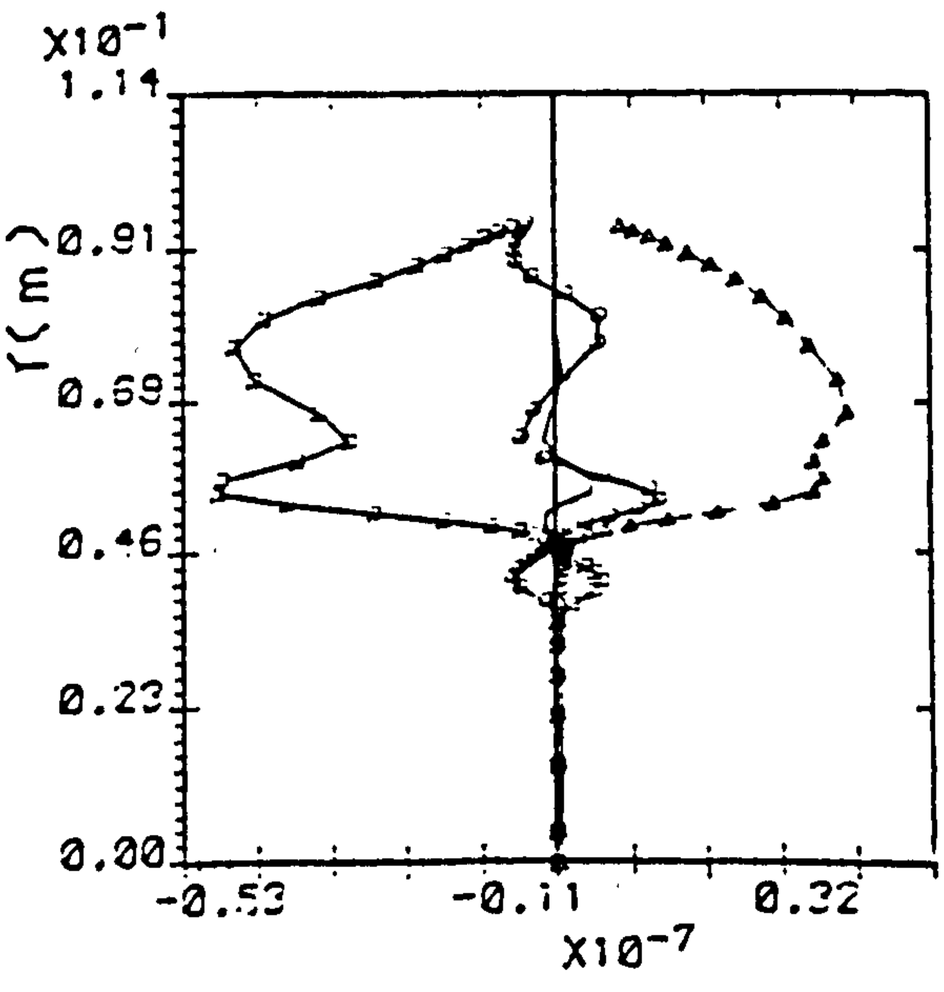

(c)

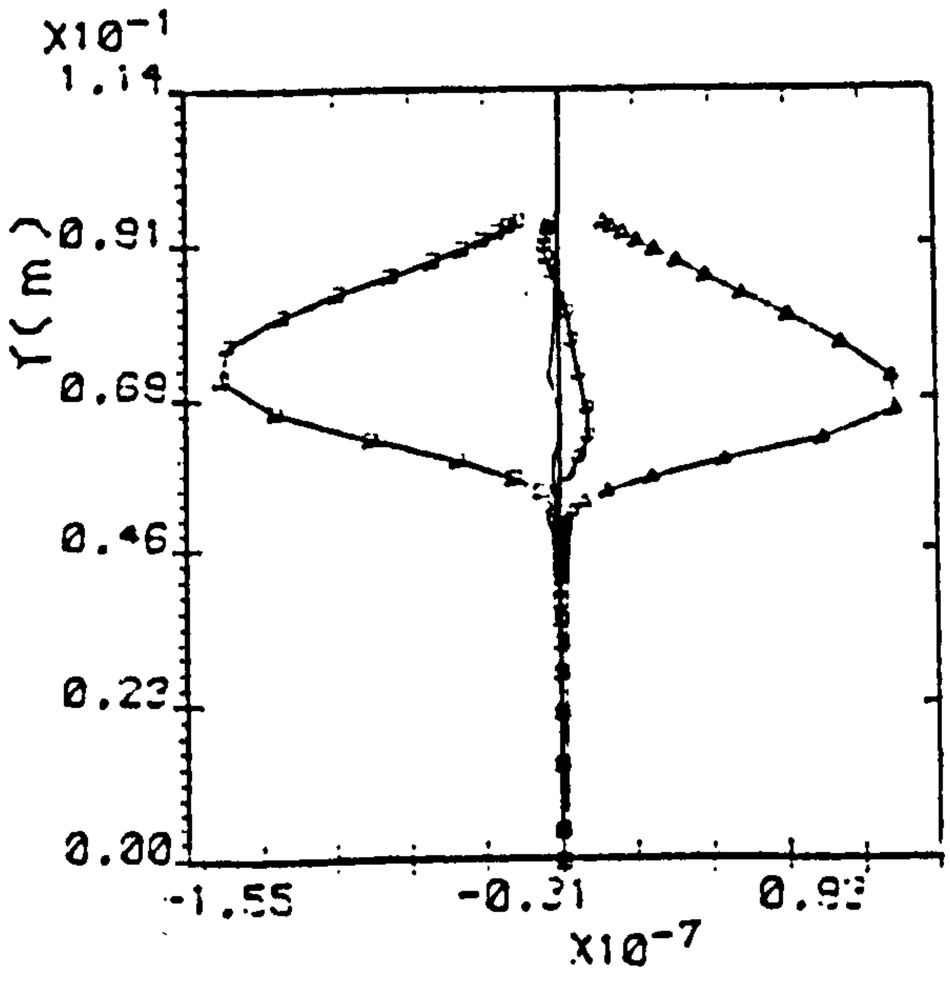

(d)

o net diffusion , □ net convection , Δ source term , ___ Tr

Fig. 4.8 : The balance of U-momentum eqt. at the recirculation region for Hr=32.4 ,
(a) x/b=8.5 ,(b) x/b=15.3 ,(c) x/b=22.2 ,(d) x/b=32.4

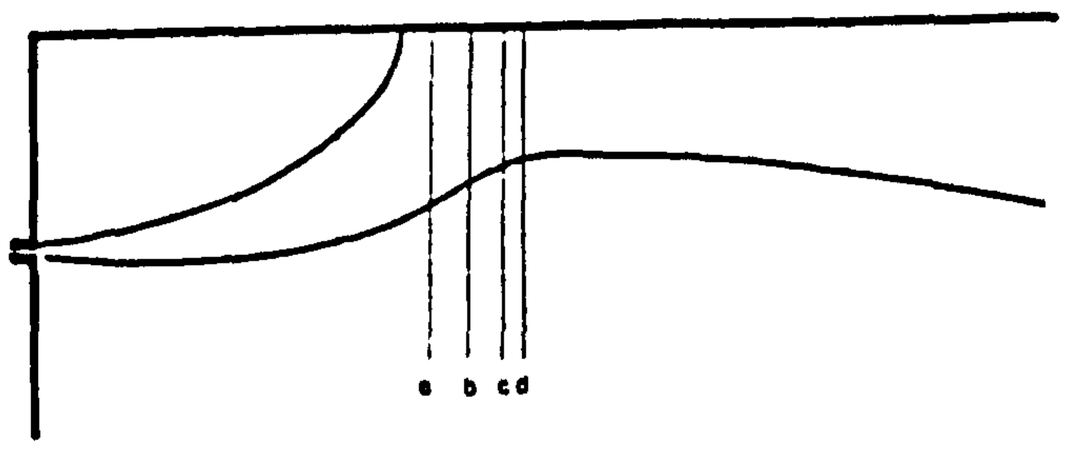

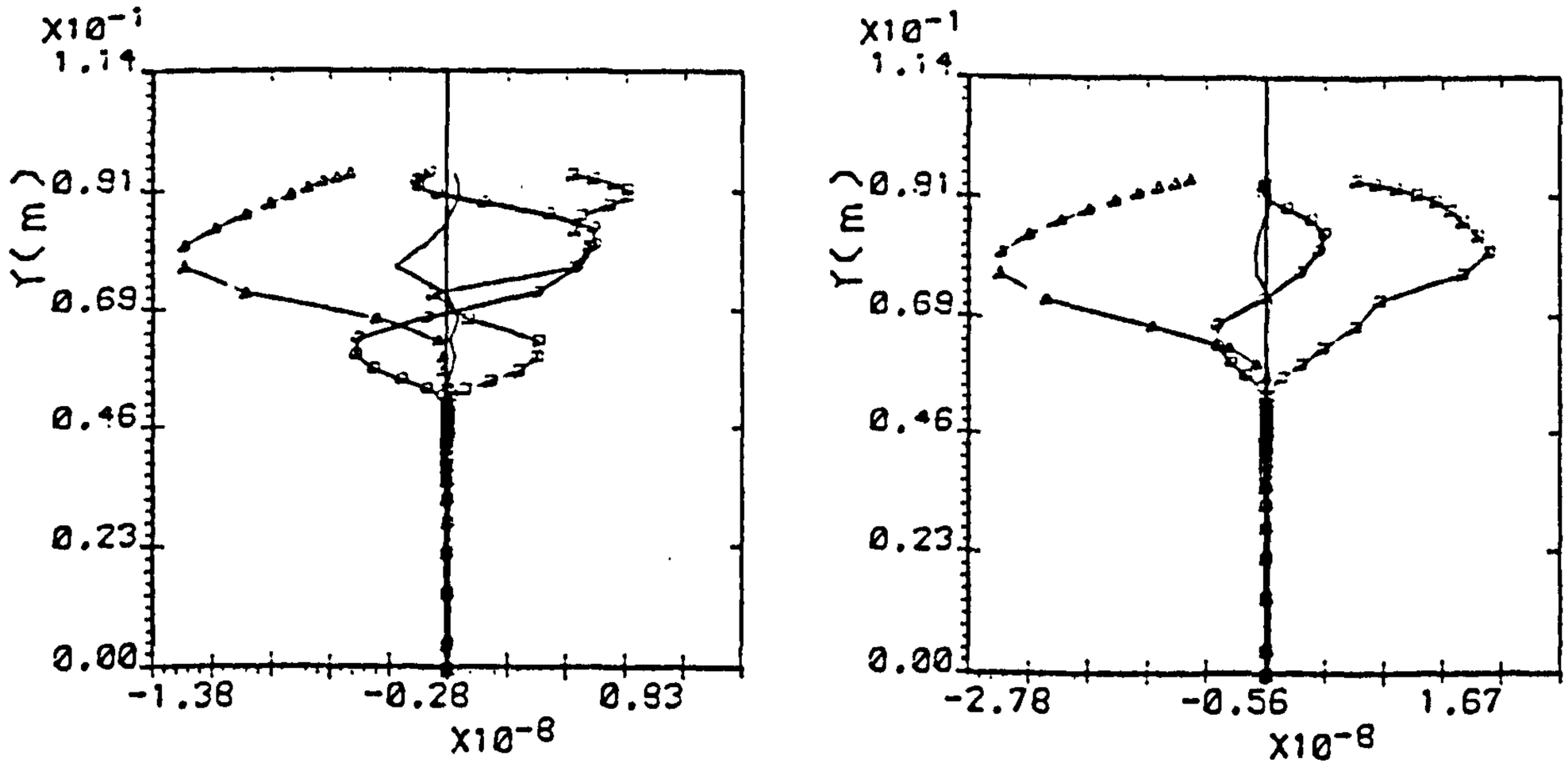

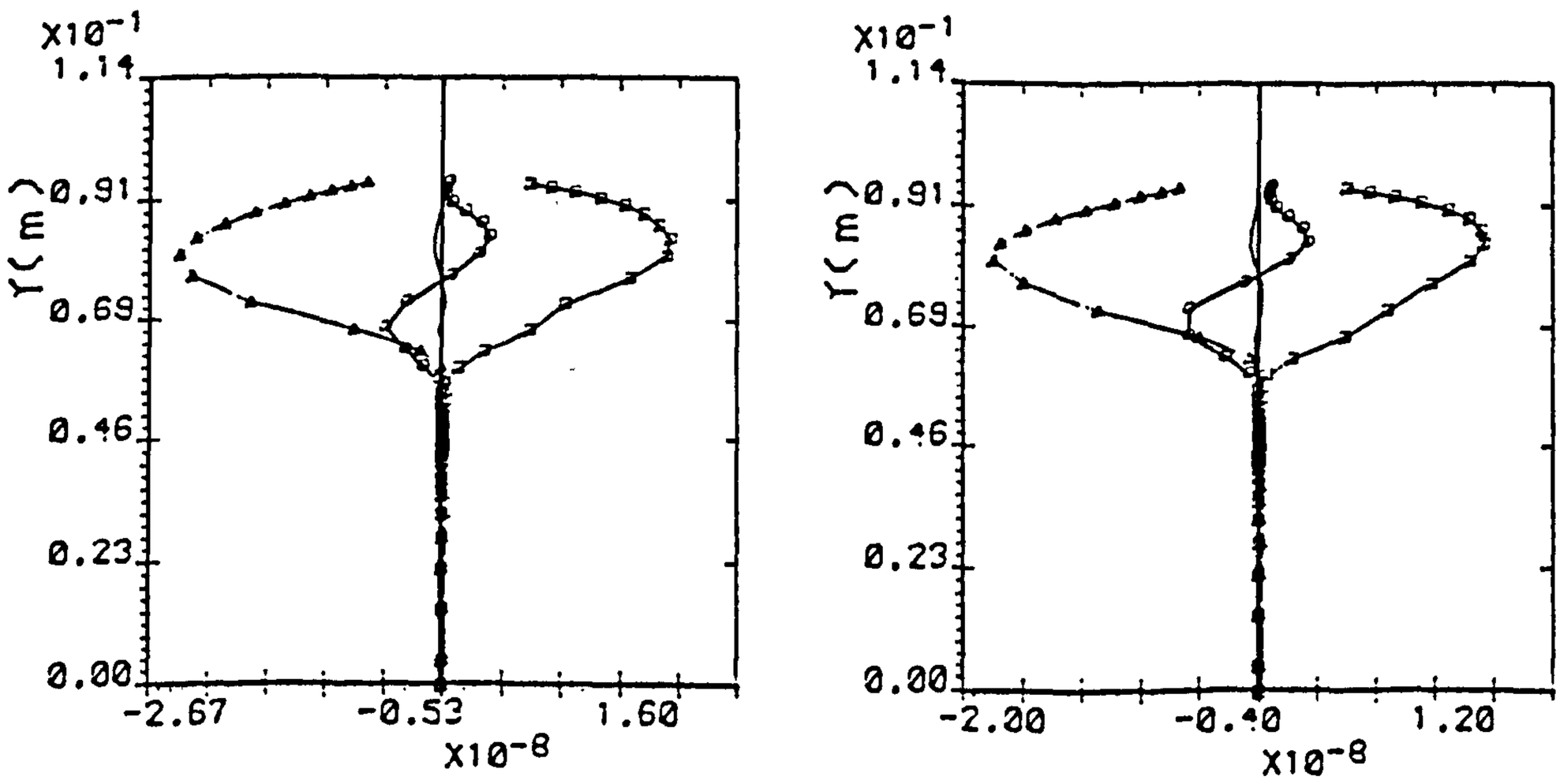

o net diffusion , □ net convection , Δ source term , — Tr

Fig. 4.9 : The balance of U-momentum eqt. at the reattachment region for Hr=32.4 ,
(a) x/b=42.7 ,(b) x/b=46.2 ,(c) x/b=49.6 ,(d) x/b=53.1

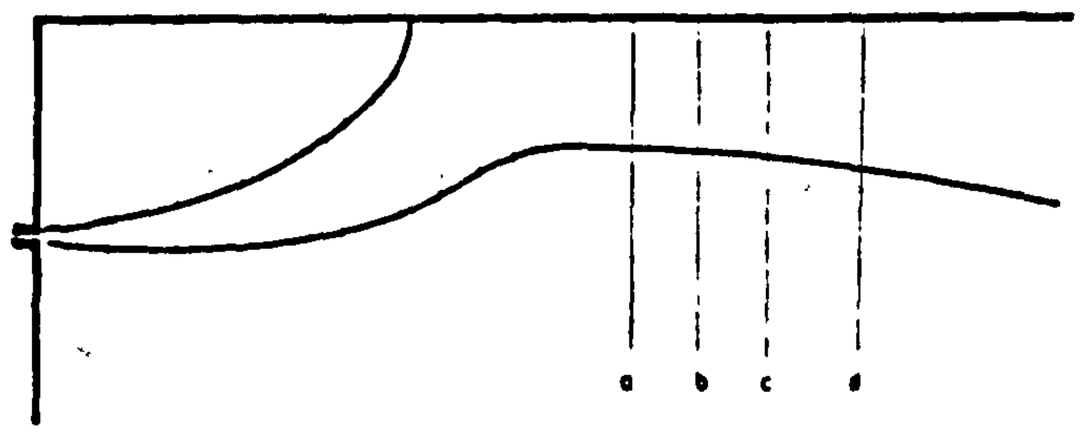

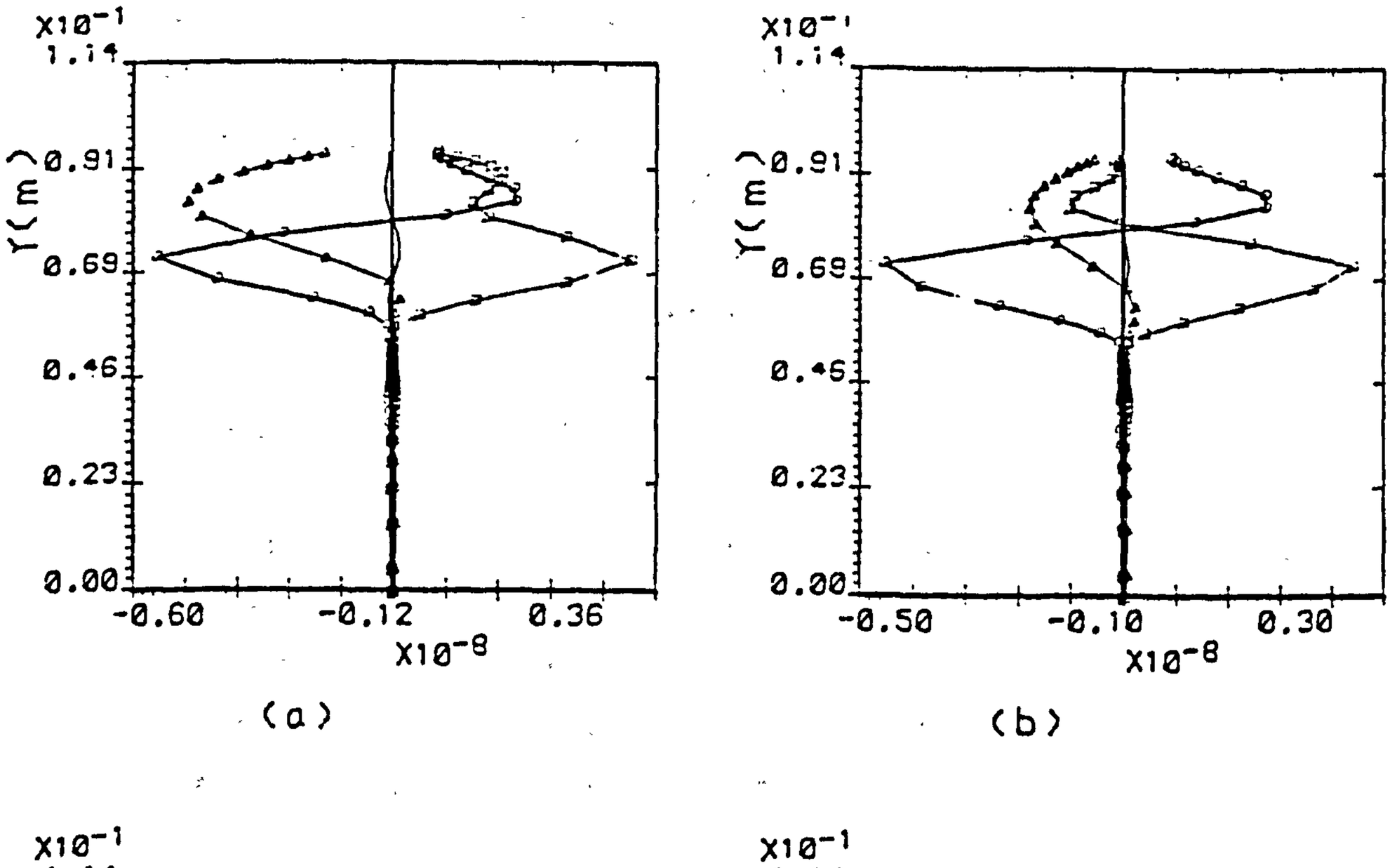

o net diffusion , □ net convection , Δ source term , ___ Tr

Fig. 4.10 : The balance of U-momentum eqt. at the wall-jet region for Hr=32.4 ,
(a) x/b=63.4 ,(b) x/b=66.9 ,(c) x/b=77.2 ,(d) x/b=80.7

However their effect on the solution will be discussed in the next section.

The momentum balance obtained above was also useful in gaining understanding of the development of the flow. Figures 4.5-4.10 show that diffusion and convection terms were dominant along the jet trajectory prior to reattachment. However, in the upper part of recircualtion region and in the reattachment region, the pressure gradient plays an important part, together with diffusion term, in balancing convection. This relatively large pressure gradient is of course responsible for inducing flow reattachement. In the wall-jet region the net diffusion becomes a more significant term and is balanced by convection, while the pressure gradient progressively falls to negligible in this region.

(ii) Numerical diffusion formula

False diffusion arises when the flow cuts across a grid at an angle, and when there is a non-zero gradient of the dependent variable in the direction normal to the flow (65,111). An approximate expression for false diffusion in a two-dimensional situation has been devised by de Vahl Davis and Mallinson (108):

$$\Gamma_{false} = \frac{\rho U_R \, \Delta X \, \Delta Y \, \sin(2\theta)}{4 \, (\Delta Y . \sin^3 \theta + \Delta X \cos^3 \theta)} \qquad 4.27$$

where U_R is the resultant velocity; θ is the angle between velocity vector and the X-axis, ΔX and ΔY are the cell dimensions. It can be readily seen from this expression that no false diffusion present when the resultant velocity is parallel to either of the grid-line directions. Conversily, false diffusion reaches a maximum when the flow direction makes an angle of 45 degrees with the grid lines (65). Nevertheless, Raithby (112) has argued that it might be possible to accept large errors from upwind differencing approximation, provided that these errors were sufficiently masked by the real diffusion

within the flow. This implies that $\Gamma_{false} << \Gamma$, where Γ is the effective viscosity of the fluid. Therefore, the above equation has been used to assess the significance of the false diffusion coefficient in the offset jet recirculation zone (see Figure 4.5 and 4.8). The false diffusion coefficient within the recirculation region for an offset distance of Hr = 6.5 is plotted in Figure 4.11, where it is normalised by the effective viscosity. The maximum false diffusion occured as previously identified in the near-slot area stations a, b, and its value decreased as the flow became more parallel to the grid lines. However, the values are small over the whole region, being of the order of 10^{-4}. This low level of false diffusion gave confidence in the use of the present refined grid.

The grid network required for a wide range of offset ratios was studied (see table 4.1), using the above methods, as was mentioned in Section 4.3.2. Computations with 34 x 36 nodal network in which five FDE's were solved needed about 550 iterations to obtain a converged solution. This required approximately 40 minutes of computing time on the DEC VAX 11/782 computer.

Hr		3.5	5.6	6.0	8.70	10.0	16.5	20.0	22.0	24.5	32.4
Grids in X & Y	X	32	29	30	28	36	38	34	30	30	39
	Y	33	35	35	38	40	43	45	44	46	48

Table 4.1 Grid nodes in X and Y direction for the geometry considered.

4.4 COMPARISON WITH EXPERIMENTAL DATA

The present computations of the two-dimensional turbulent offset jet have been compared with the experimental data of Borque and Newman (84), Kumada etal (86), Hoch and Jiji (87-88), Sawyer (89), Omere (94), and Shchwartzbach (97). The boundaries of the solution domain were therefore, arranged to simulate the test conditions employed by these researchers. Comparisons were undertaken for both the flow field properties annd surface heat/mass transfer rates, depending on

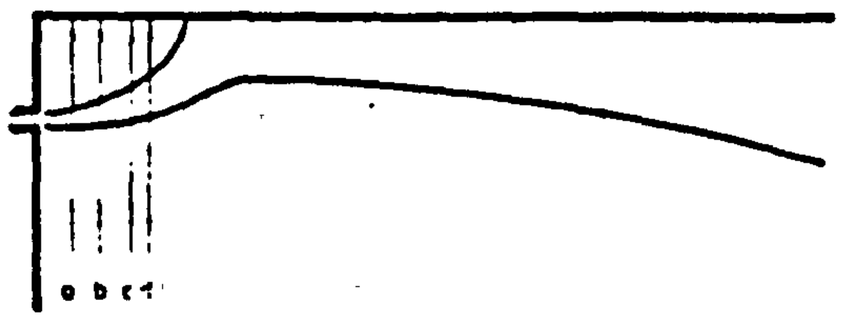

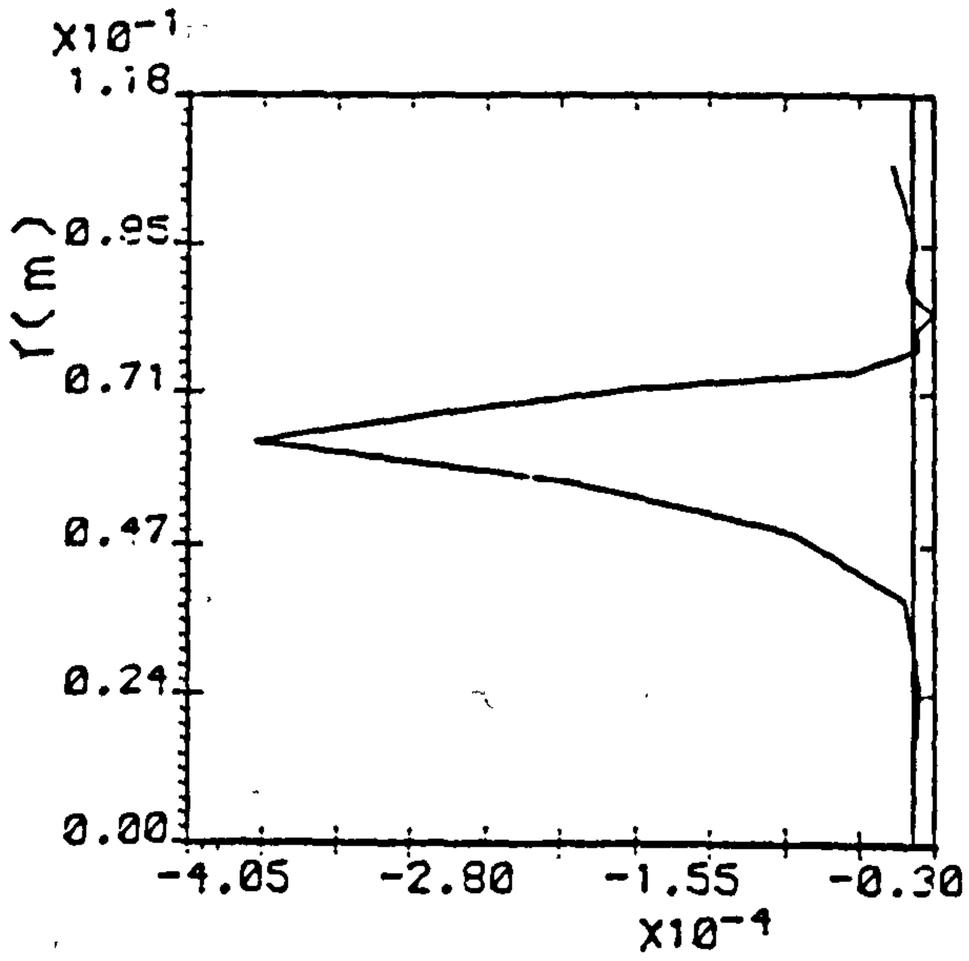

(a)

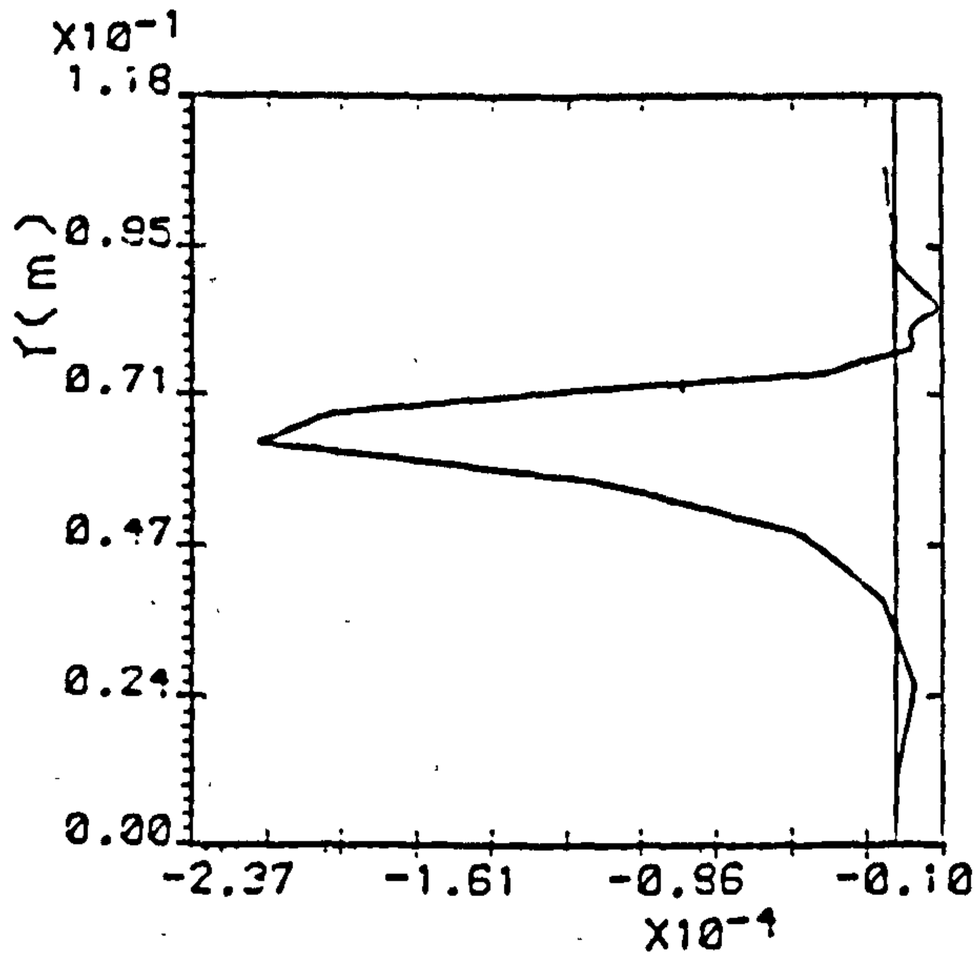

(b)

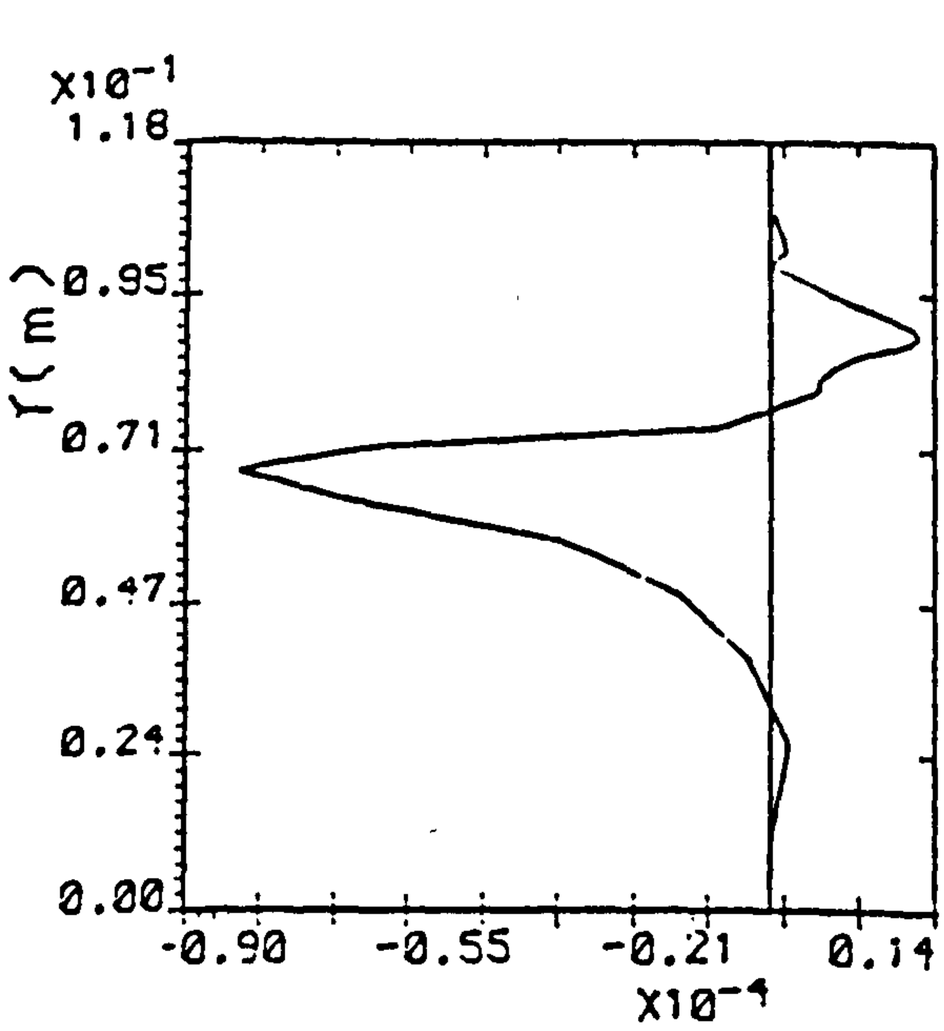

(c)

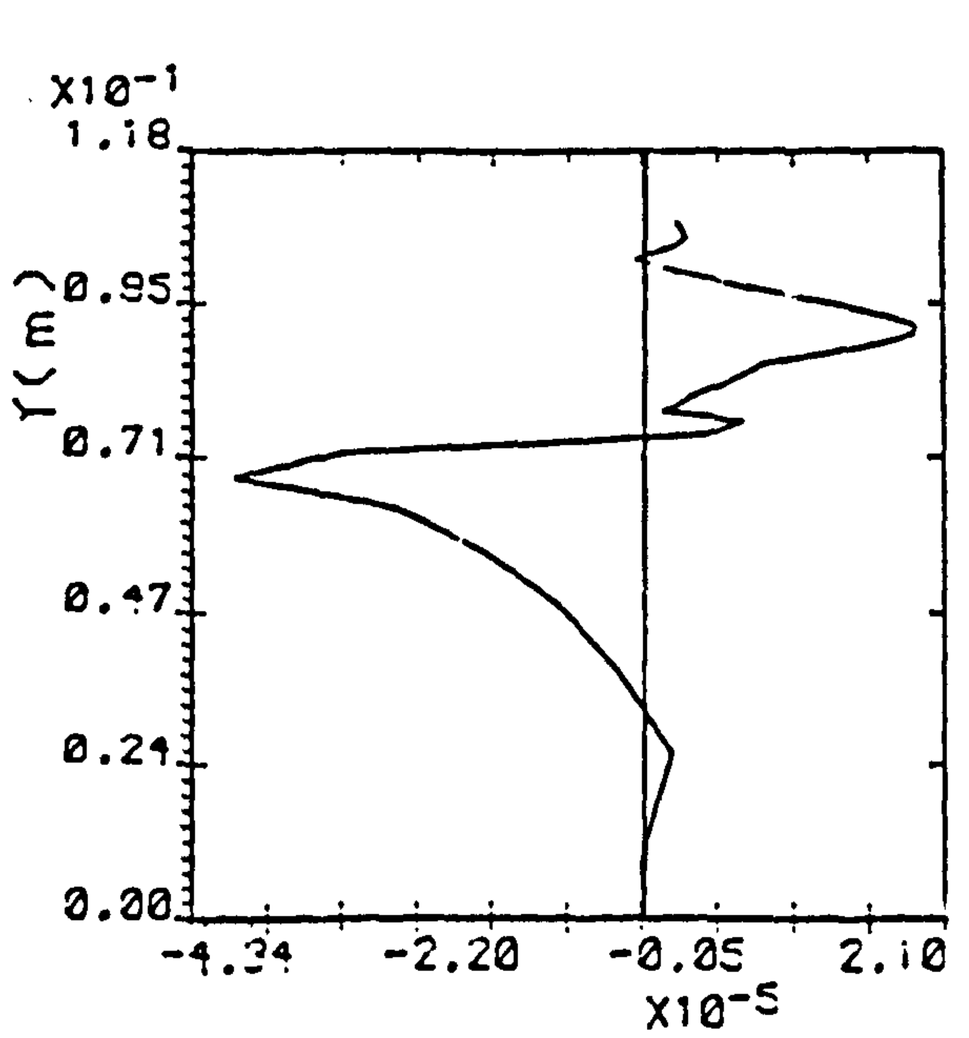

(d)

Fig. 4.11 : The normlised false diffusion profiles at the recirculation region for Hr=6.5 ,
(a) x/b=2.4 , (b) x/b=4.2 , (c) x/b=6.3 , (d) x/b=7.4

the available experimental data from each study. The dimensions of the flow domain and the slot Reynolds number investigated by the experiments are detailed in Table 4.2.

4.4.1 Flow Field

This section presents some general characteristics of offset jet flows in order to provide a clear description of this flow. These include computed velocity vectors and profiles, the streamwise velocity decay, surface pressure distribution and the jet trajectory.

The flow pattern is presented in figure 4.12-17 for different offset ratios in term of velocity vectors and velocity profiles (which are proportional to the local resultant and X-direction velocity component respectively). These figures illustrate the three regions associated with offset jet flows and the shape of the jet inlet profile. In particular, the vectors show how the jet curves

Reference	b (mm)	Hr	Re
Borque & Newman (84)	1.524	32.4	$8.485\ 10^3$
Kumada etal (86)	4.00	3.5	$\approx 10^4$
		6.5	
		24.5	
Hoch & Jiji (87-88)	6.600	5.7	8.8×10^3
		8.7	
Sawyer (89)	4.520	5.62	9.5×10^4
Omere (94)	4.000	10.0	
		20.0	$2.7\ 10^3$
		30.0	
Schwartzbach (97)	3.000	6.0	10^4
		22.0	

Table 4.2 The offset jet geometries considered and their Reynolds number.

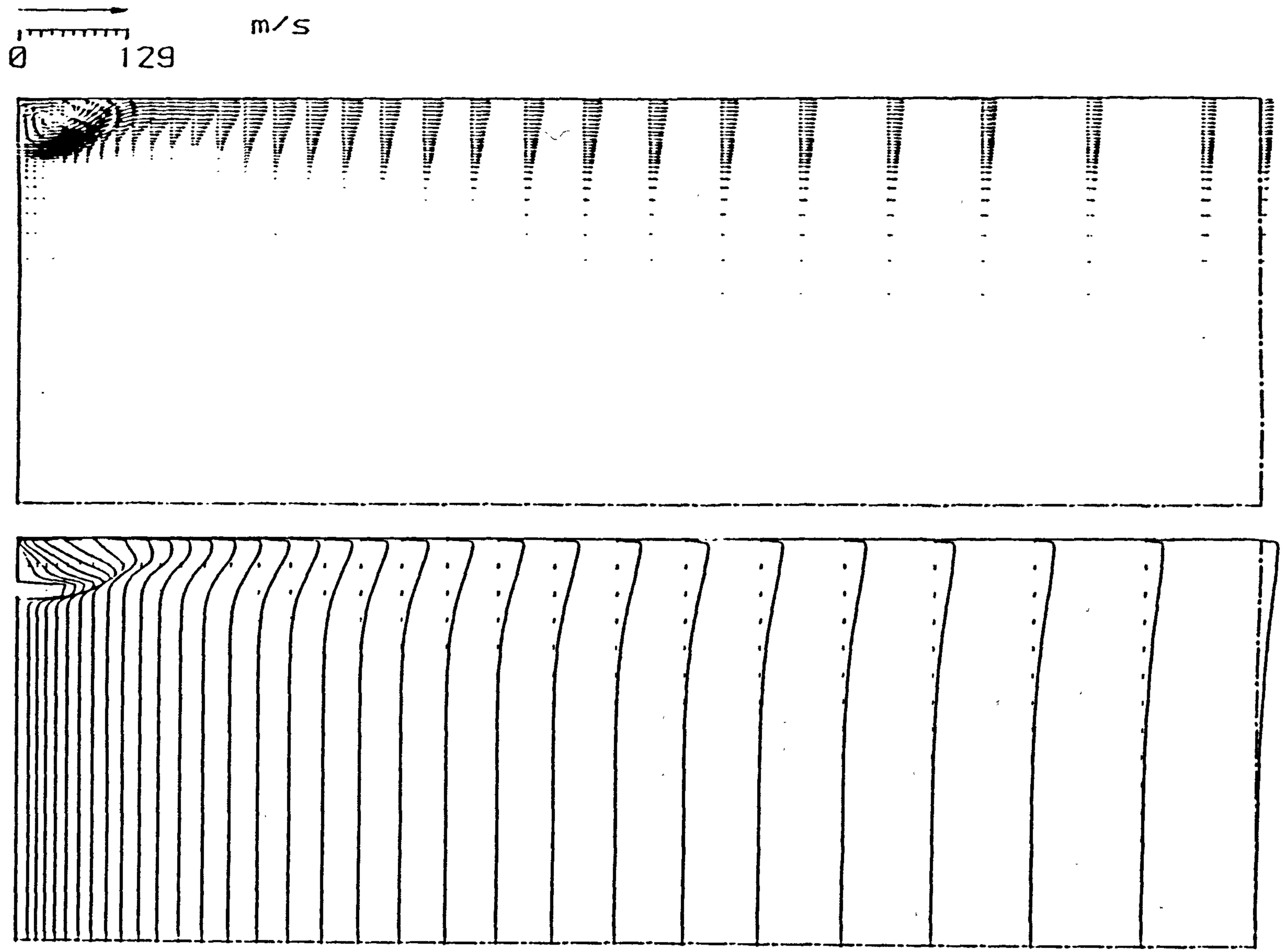

Figure 4.12 : Offset jet velocity vectors and profiles for Hr=3.5 .

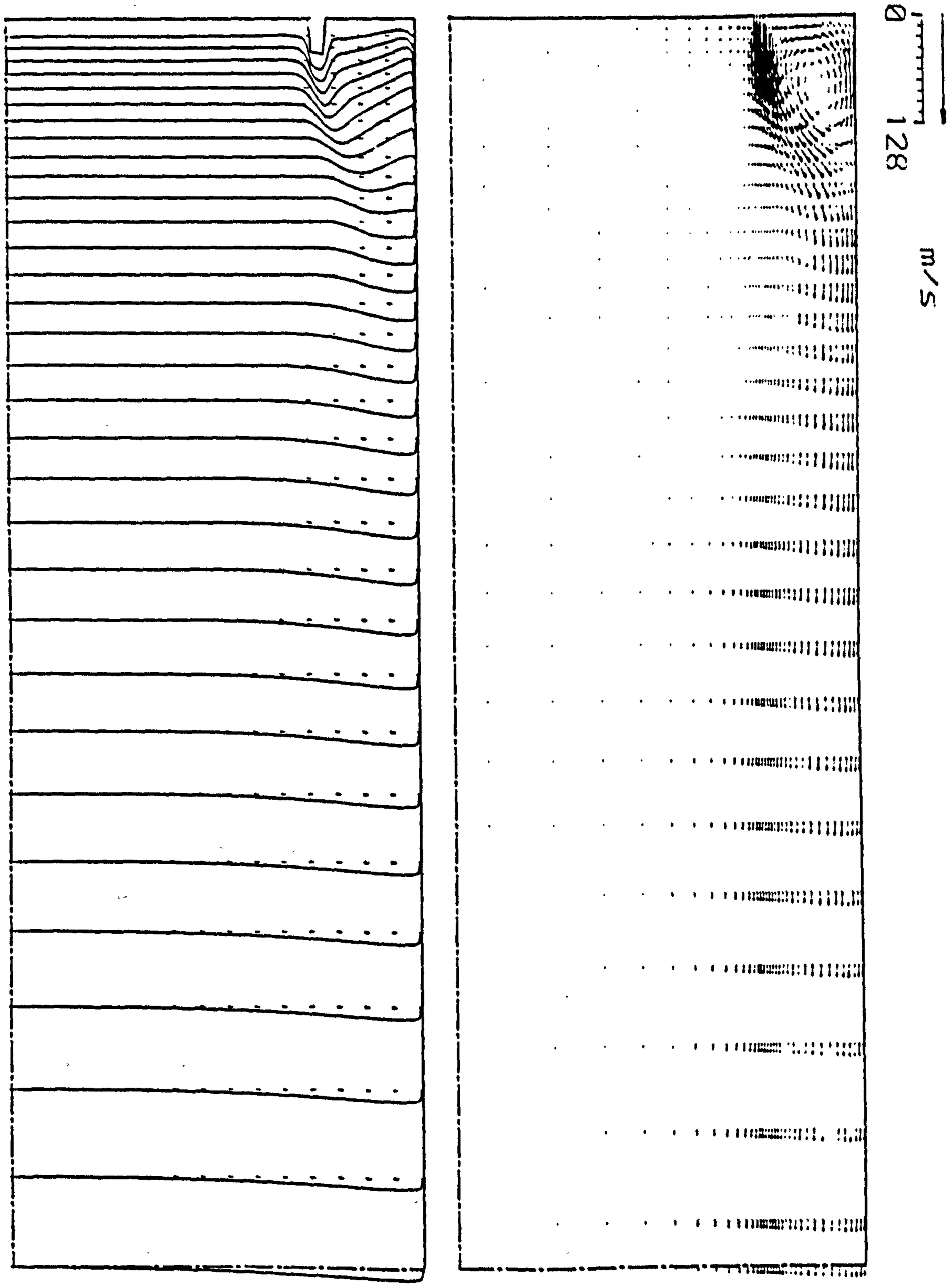

Figure 4.13 : Offset jet velocity vectors and profiles for Hr=6.5 .

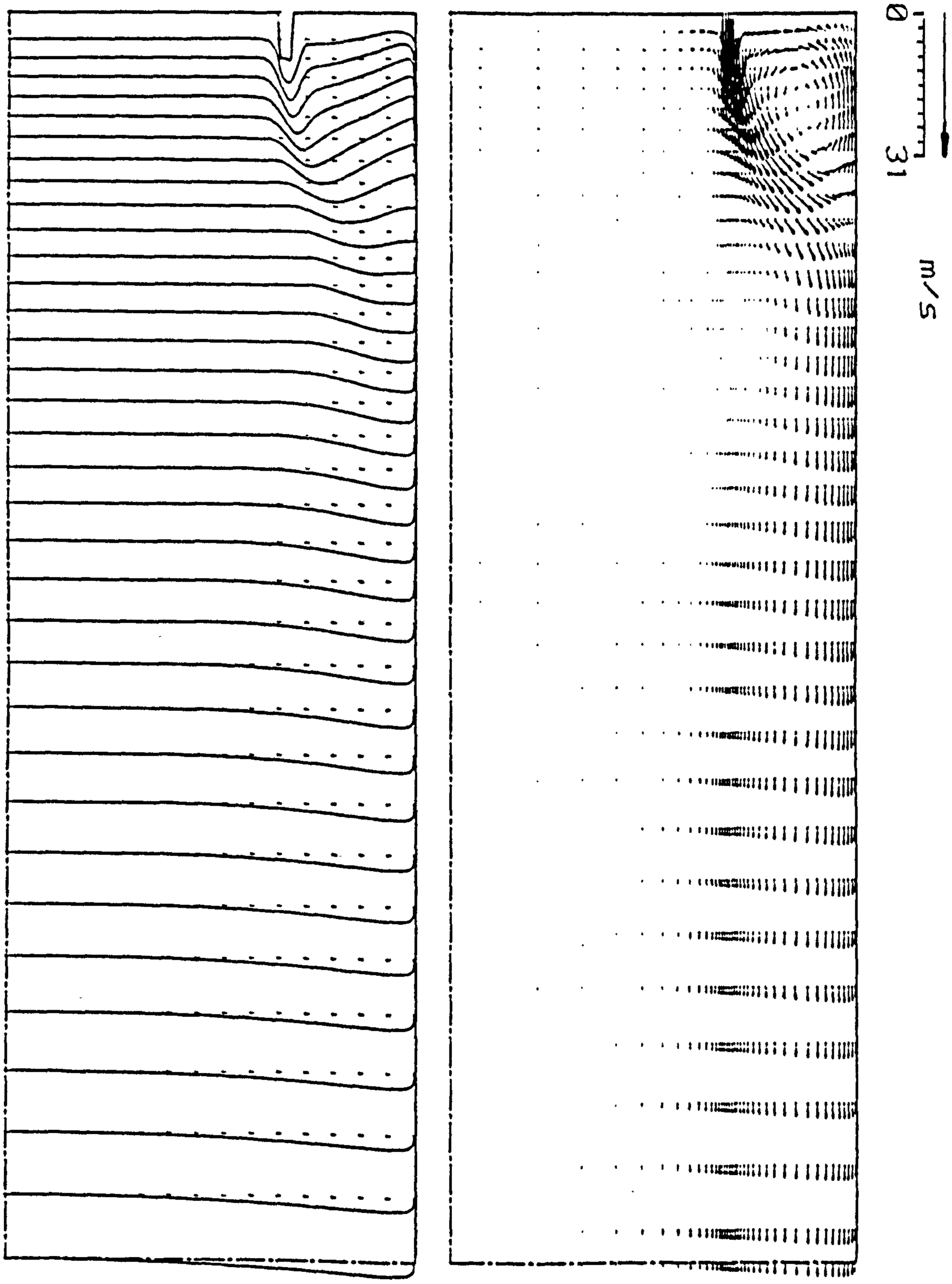

Figure 4.14 : Offset jet velocity vectors and profiles for Hr=10.0 .

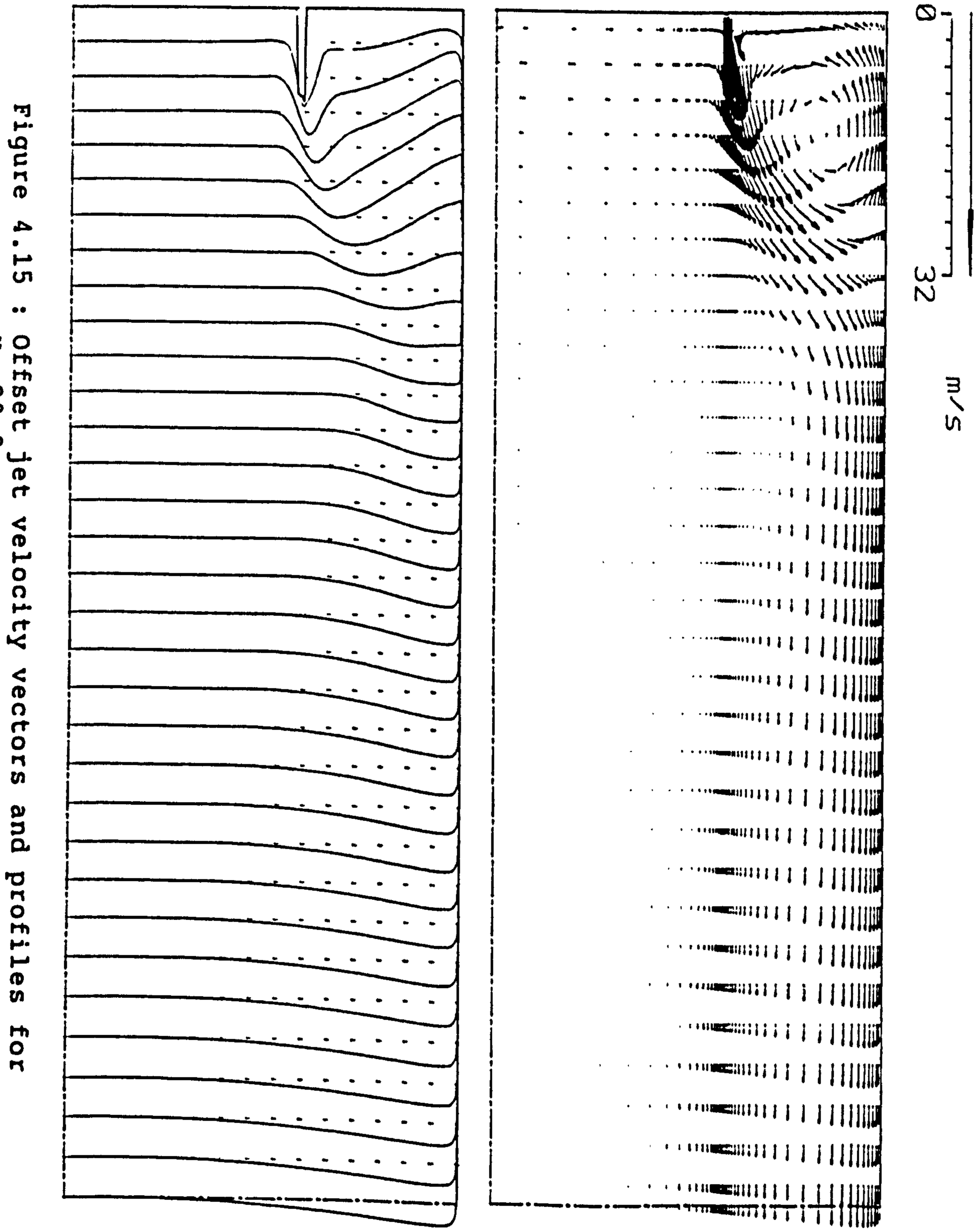

Figure 4.15 : Offset jet velocity vectors and profiles for Hr=20.0 .

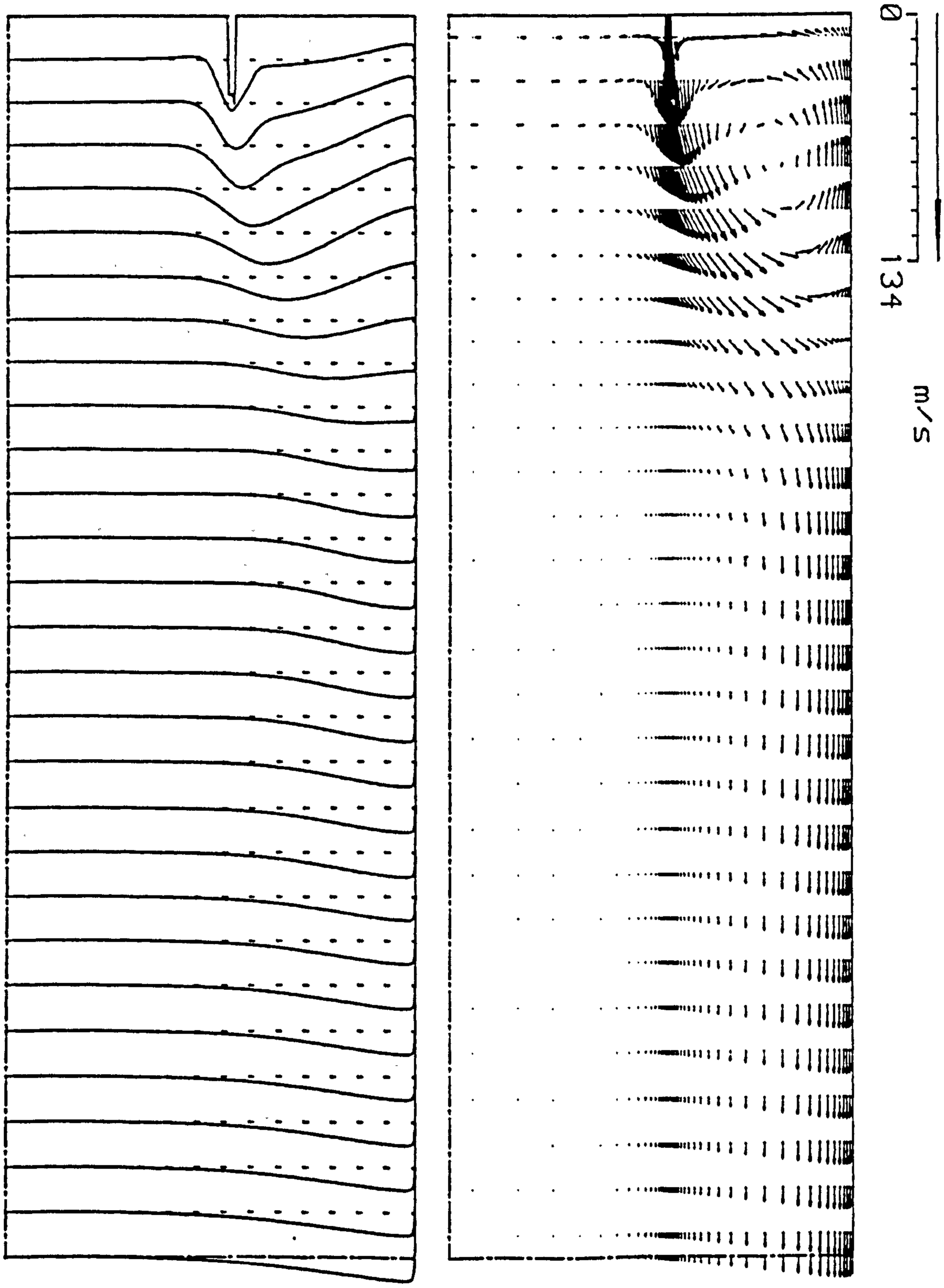

Figure 4.16 : Offset jet velocity vectors and profiles for Hr=24.5 .

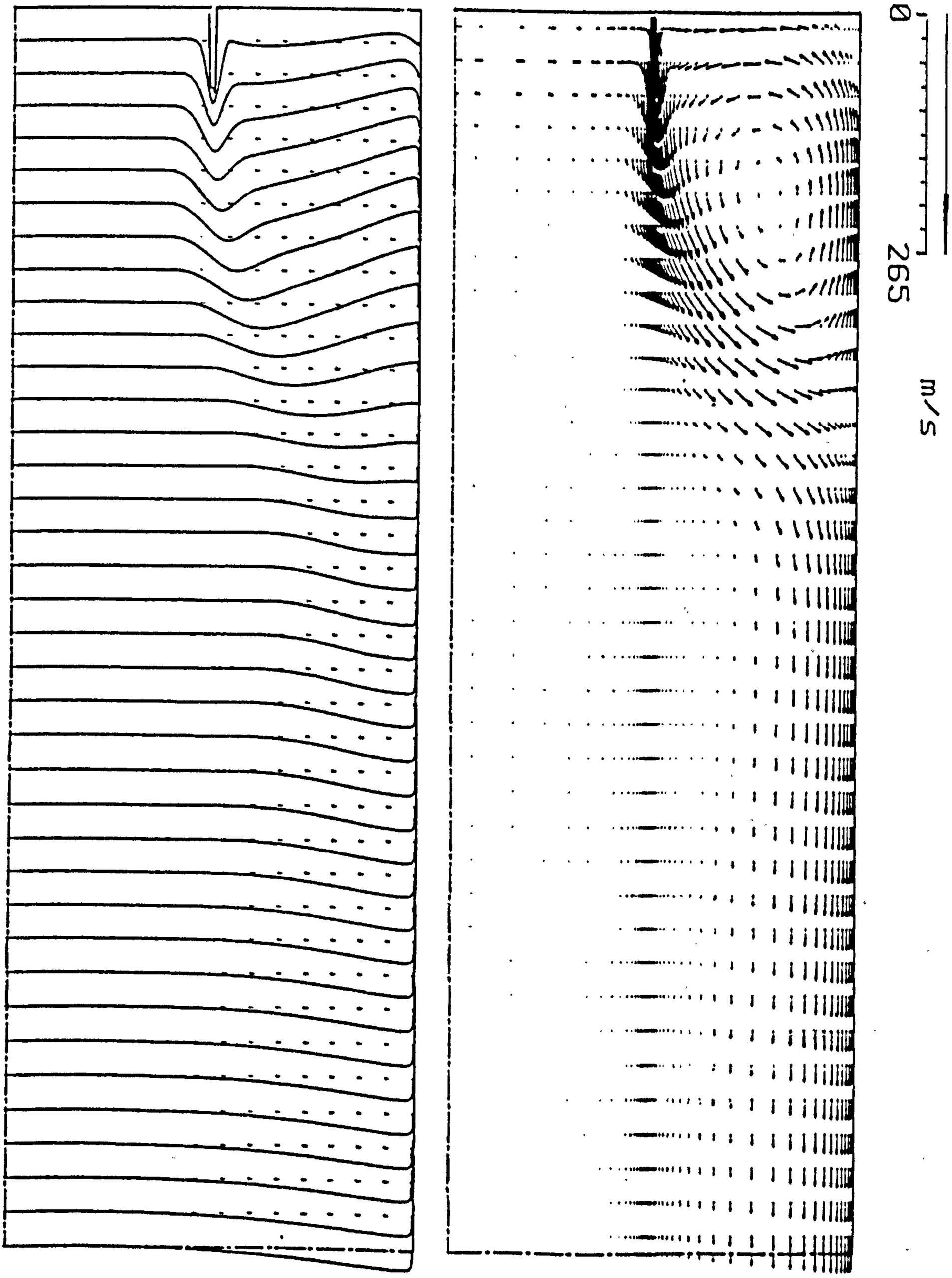

Figure 4.17 : Offset jet velocity vectors and profiles for Hr=32.4 .

upwards towards the ceiling plate, due to the creation of the sub-atmospheric pressure region, as it moves downstream. It then attaches to the ceiling forming a wall-jet flow. It also displays the small values of the velocities in the heart of the recirculation zone, as well as the region above the B.F.B.

The distribution of static pressure along the ceiling, plotted in terms of the pressure coefficient CPS = $2(P_s - P_{ref})/\rho U_o^2$, is shown in figures 4.18-21 for four offset distances (Hr = 3.5, 6.5, 24.5 and 32.4). Comparisons are made with the experimental data of Kumada etal (86) and Borque and Newman (84). It is clear from these figures that the present study computational procedure predicts the static pressure profiles in reasonably agreement with experimental data, although the location of the reattachment line (roughly the point of maximum pressure) was under-predicted. These pressure peaks were under predicted by about 0.3 - 0.34 of the offset ratios in the four cases examined.

In figures (4.22-23) the decay of the maximum axial velocity is presented and compared with experimental results of Hoch and Jiji (87) for offset ratios of 5.7 and 8.7 respectively. The two points along each curve where the slope changes sign corresponding, approximately, to the end of the recirculation and reattachment regions. The comparison show a reasonable agreement with the experimental data in the wall-jet region, while there is some discrepancy evident in the other two regions. The main cause of these discrepancies may be attributed to the underprediction of the reattachment distance (presumably due to inadequancies in the turbulence modelling), and to the uncertainties associated with experimental measurements in the two regions.

Computations of the maximum axial velocity decay in the wall-jet region for Hr = 3.5 and 6.5 are plotted in Figures 4.24-25 along with the corresponding experimental data of Kumada etal (86). The two Figures show good agreement with the experimental data, except close to the reattachment region. A similar comparison is made in figure 4.26 for the data of Schwartzbach (97) with offset ratios of 6.0 and 22.0. Again the agreement is seen to be reasonable in this region.

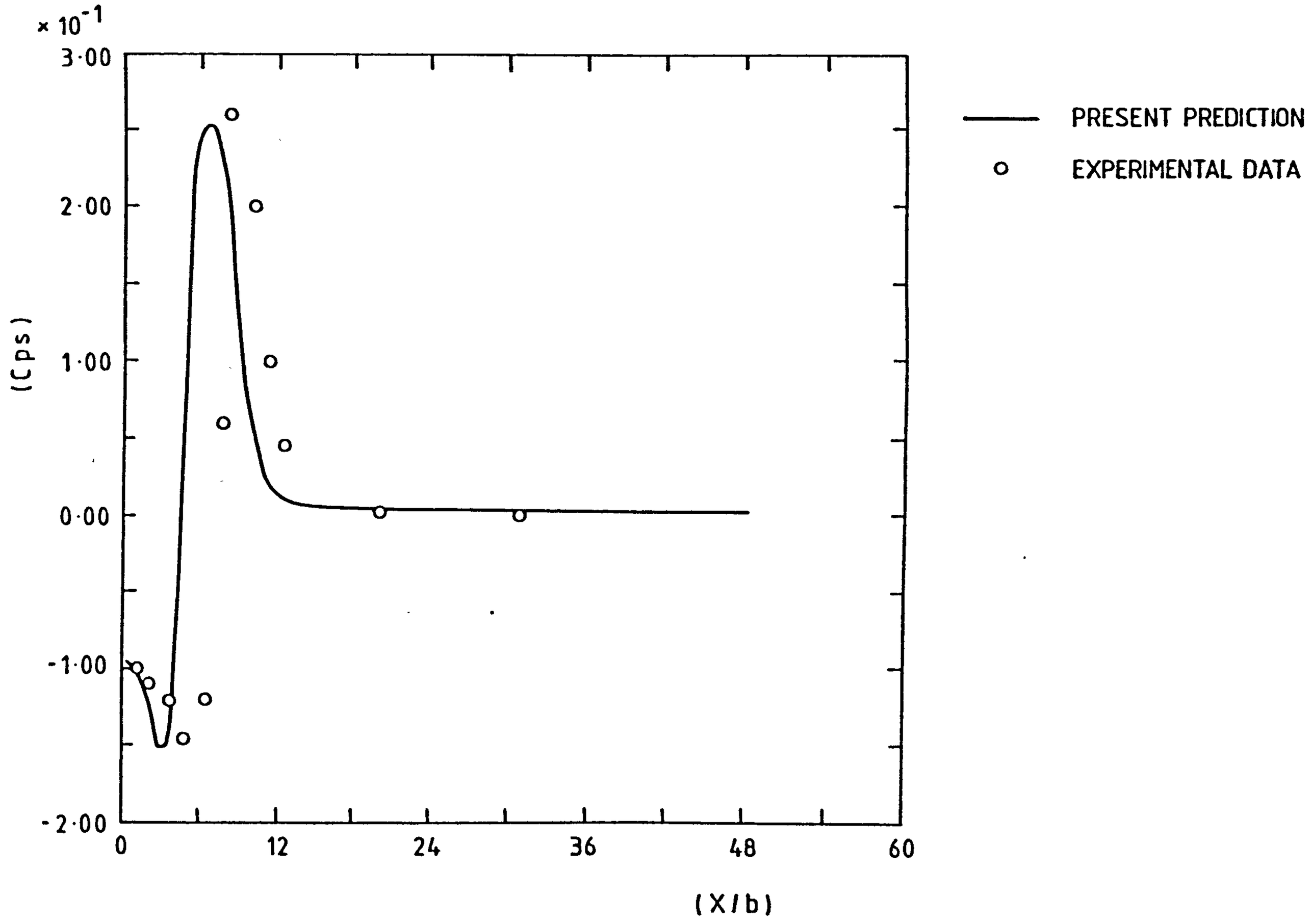

Figure 4.18 : Static pressure distribution on the top wall for offset air jet ,Hr=3.5 , [Data from Kumada etal (86)] .

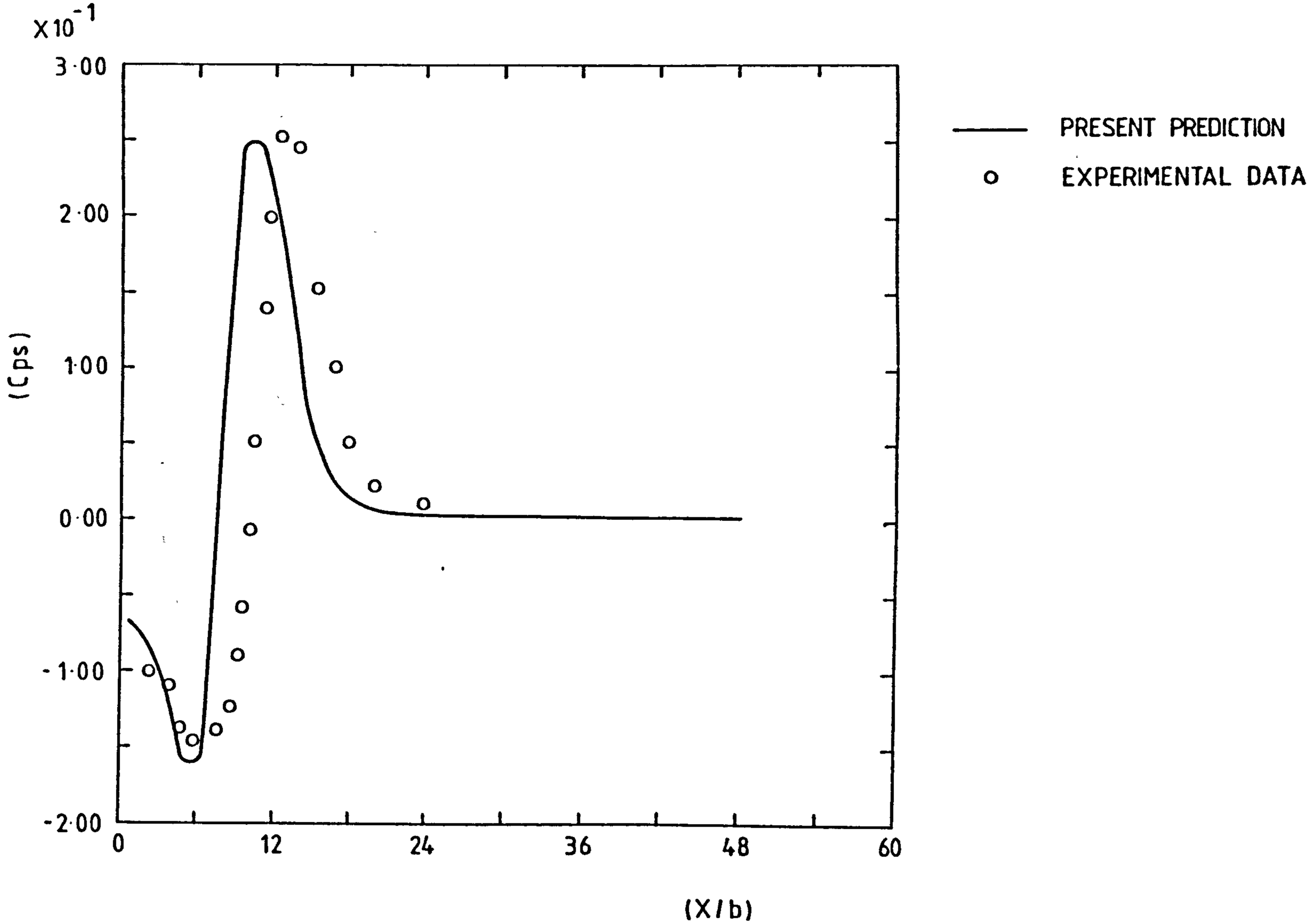

Figure 4.19 : Static pressure distribution on the top wall for offset air jet ,Hr=6.5 , [Data from Kumada etal (86)] .

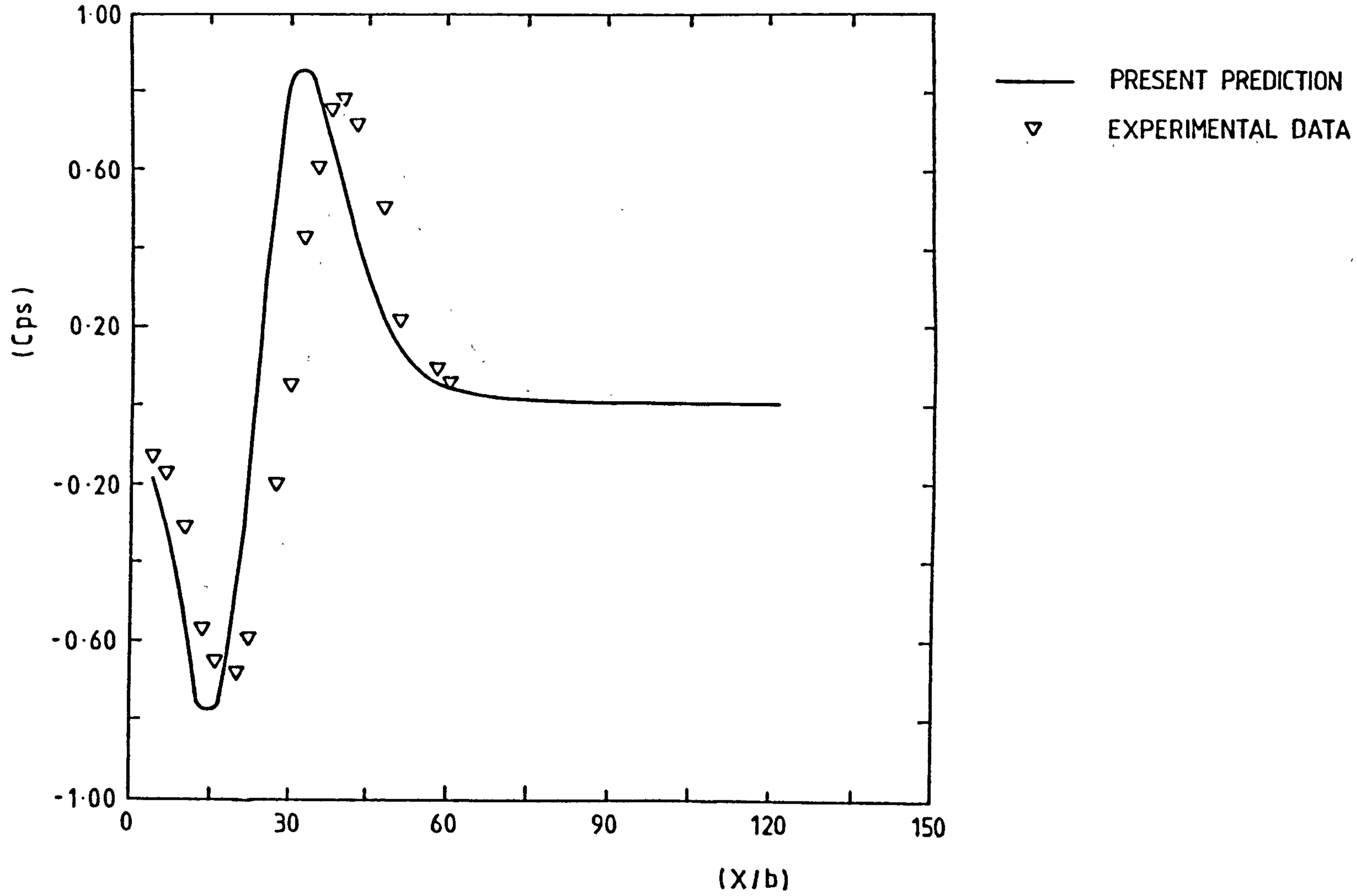

Figure 4.20 : Static pressure distribution on the top wall for offset air jet ,Hr=24.5 , [Data from Kumada etal (86)] .

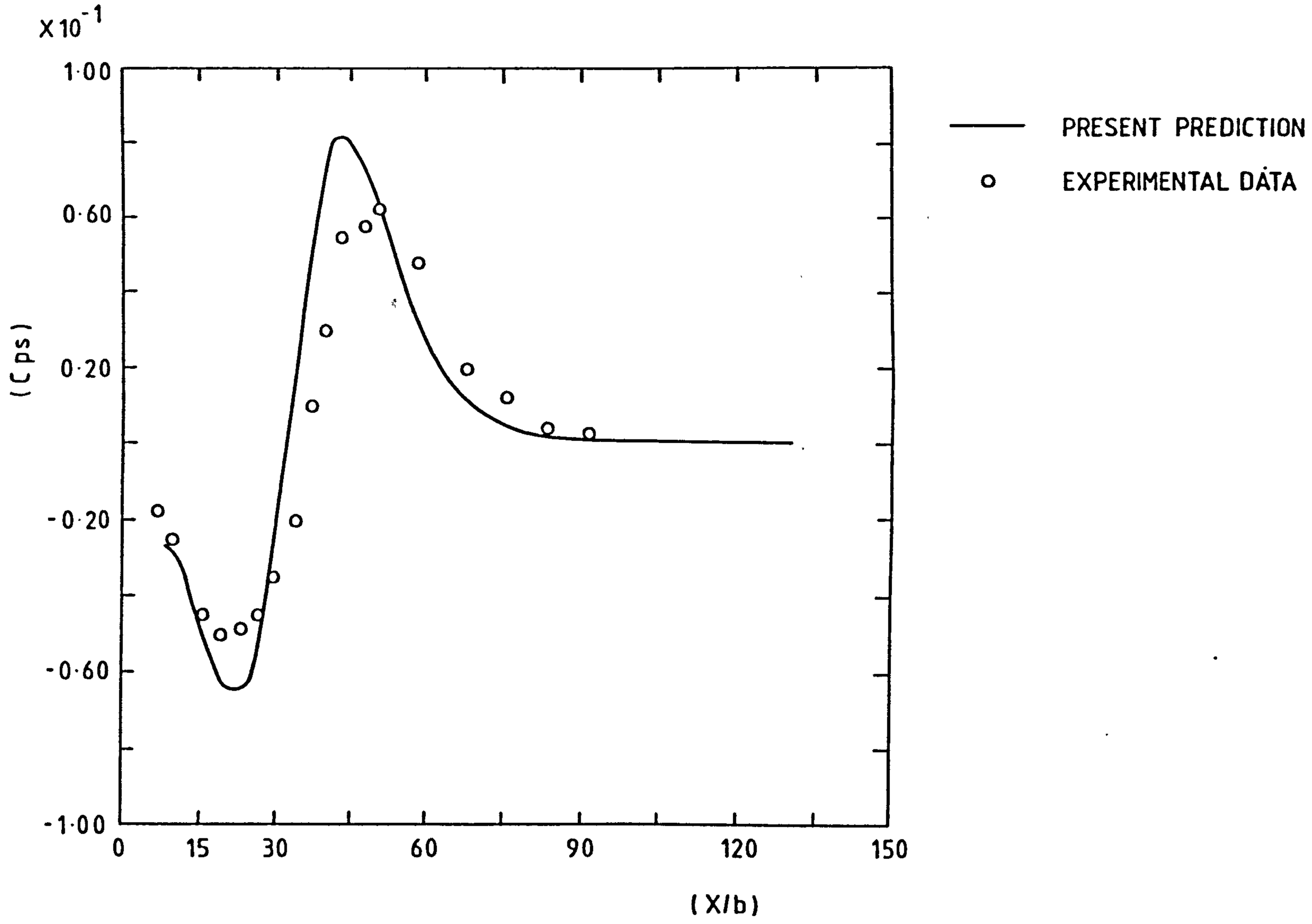

Figure 4.21 : Static pressure distribution on the top wall for offset air jet ,Hr=32.4 , [Data from Borque and Newman (84)] .

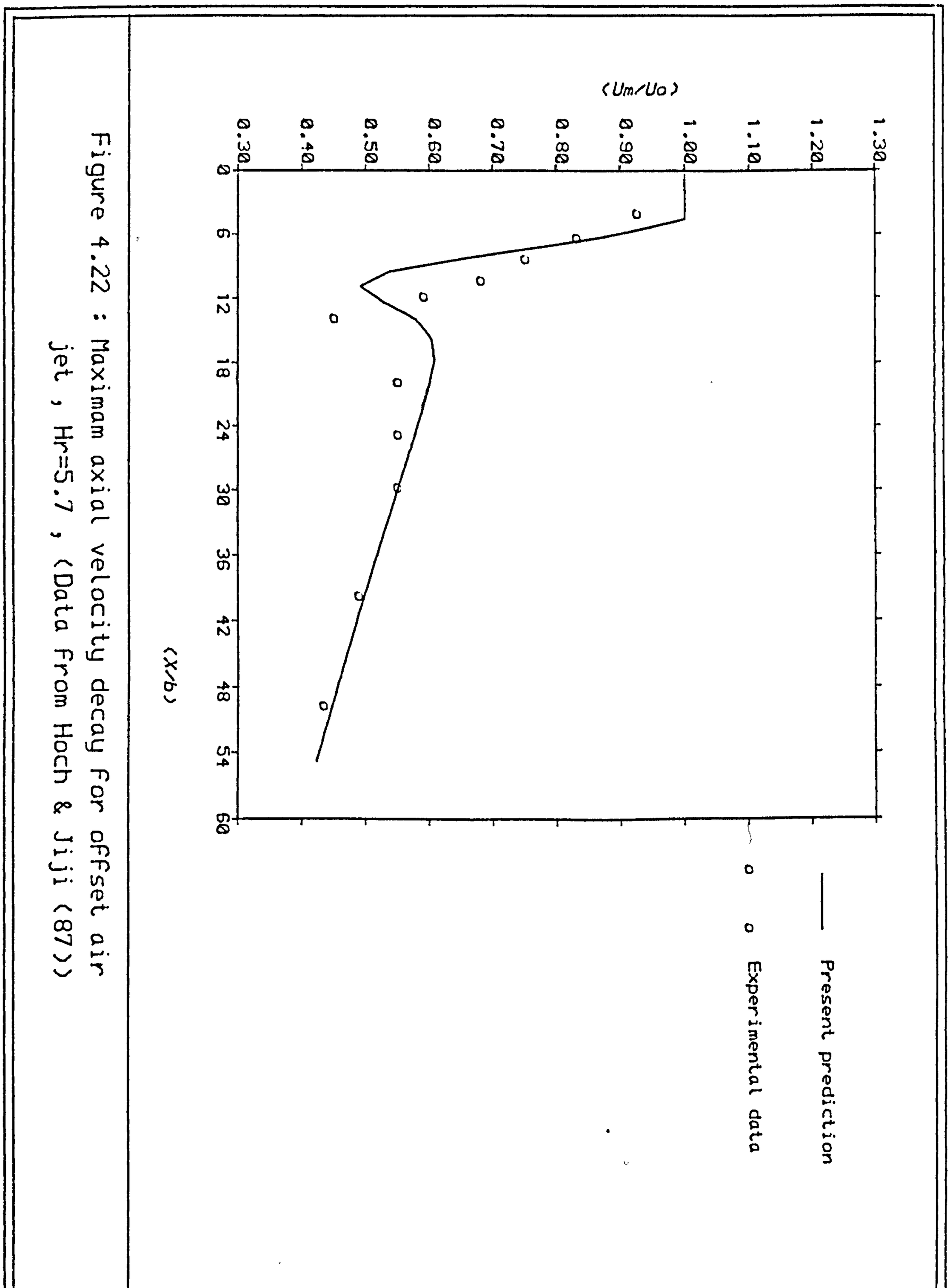

Figure 4.22 : Maximam axial velocity decay for offset air jet , Hr=5.7 , (Data From Hoch & Jiji (87))

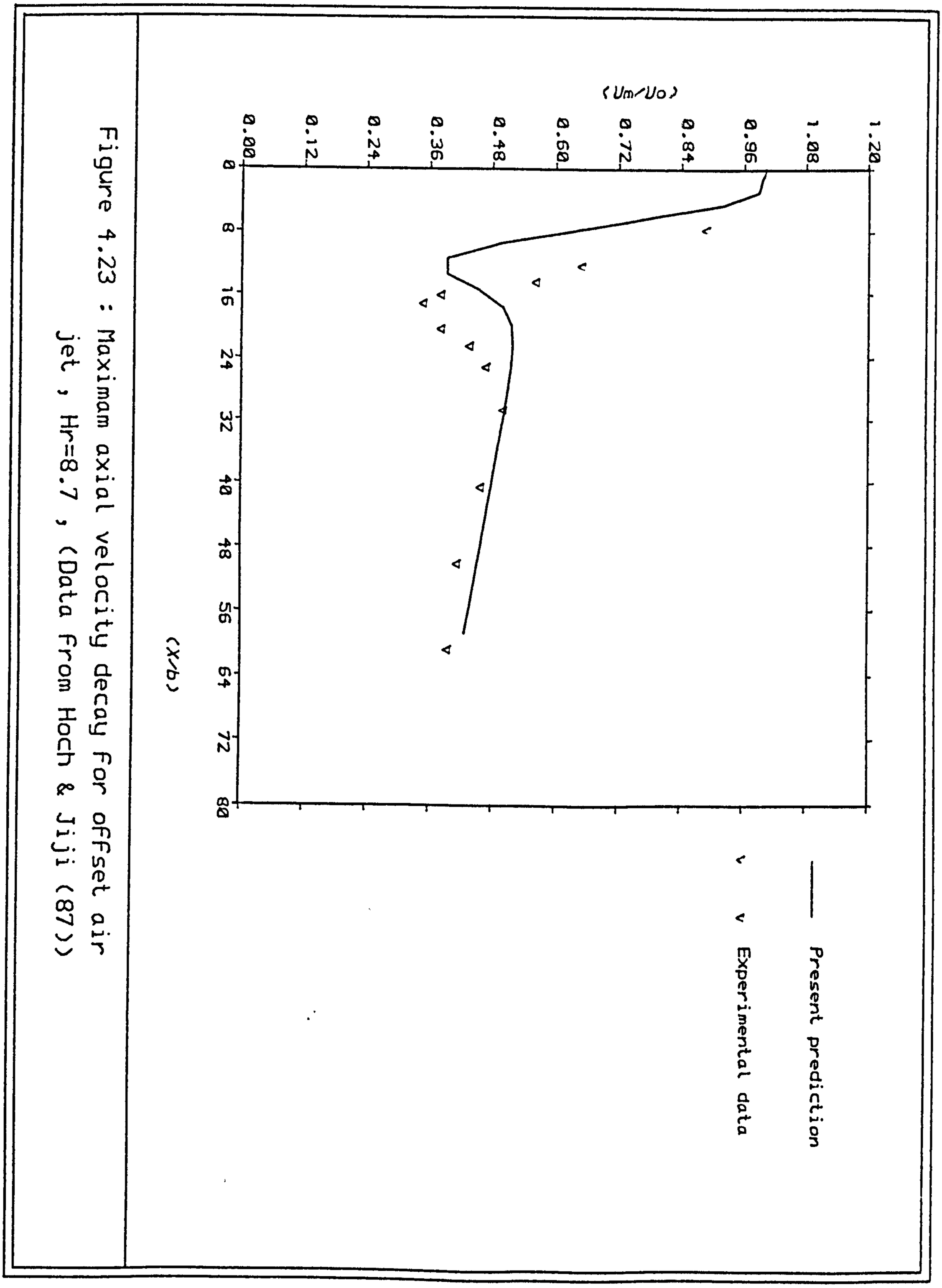

Figure 4.23 : Maximam axial velocity decay for offset air jet , Hr=8.7 , (Data from Hoch & Jiji (87))

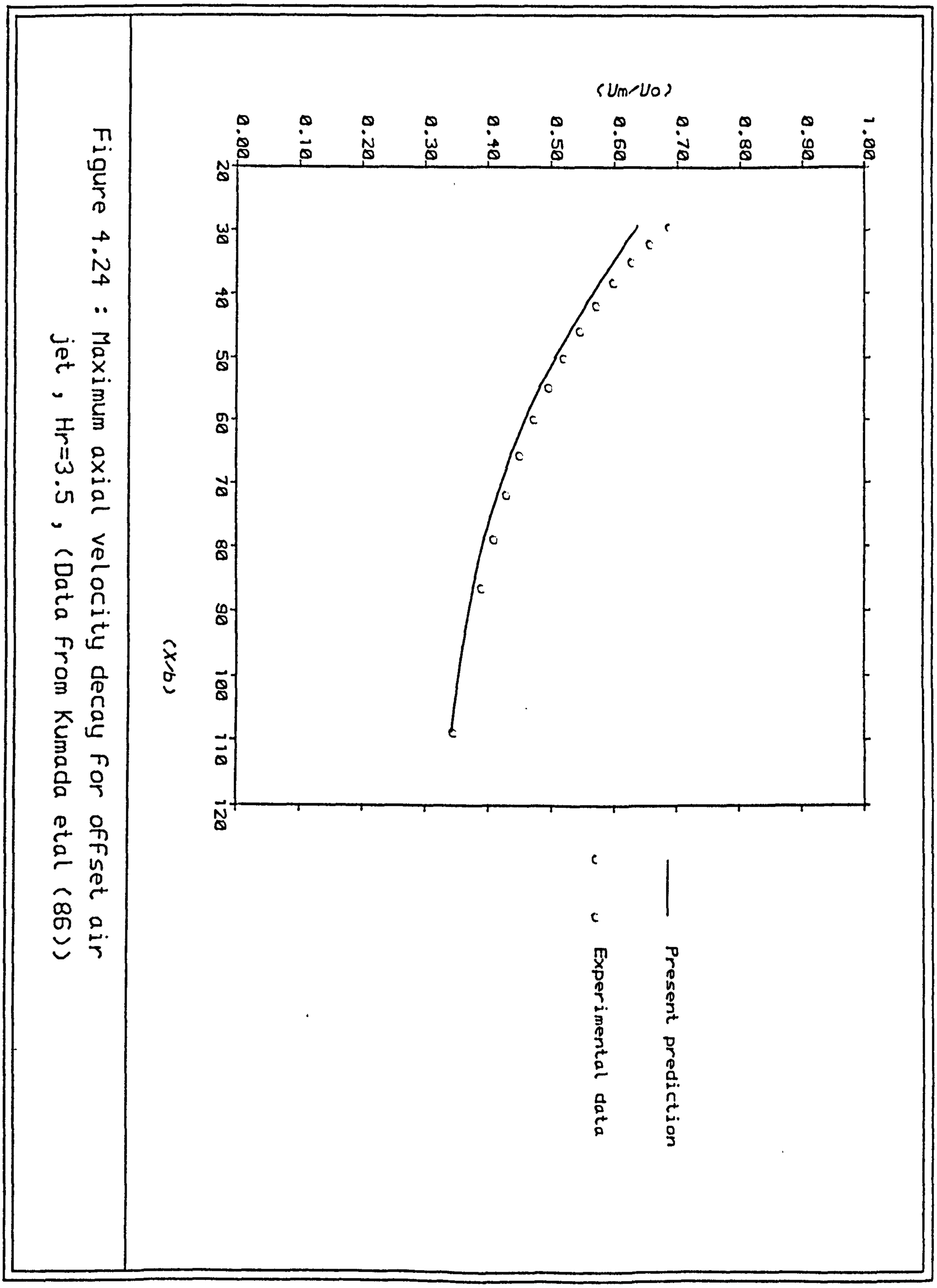

Figure 4.24 : Maximum axial velocity decay For offset air jet , Hr=3.5 , (Data From Kumada etal (86))

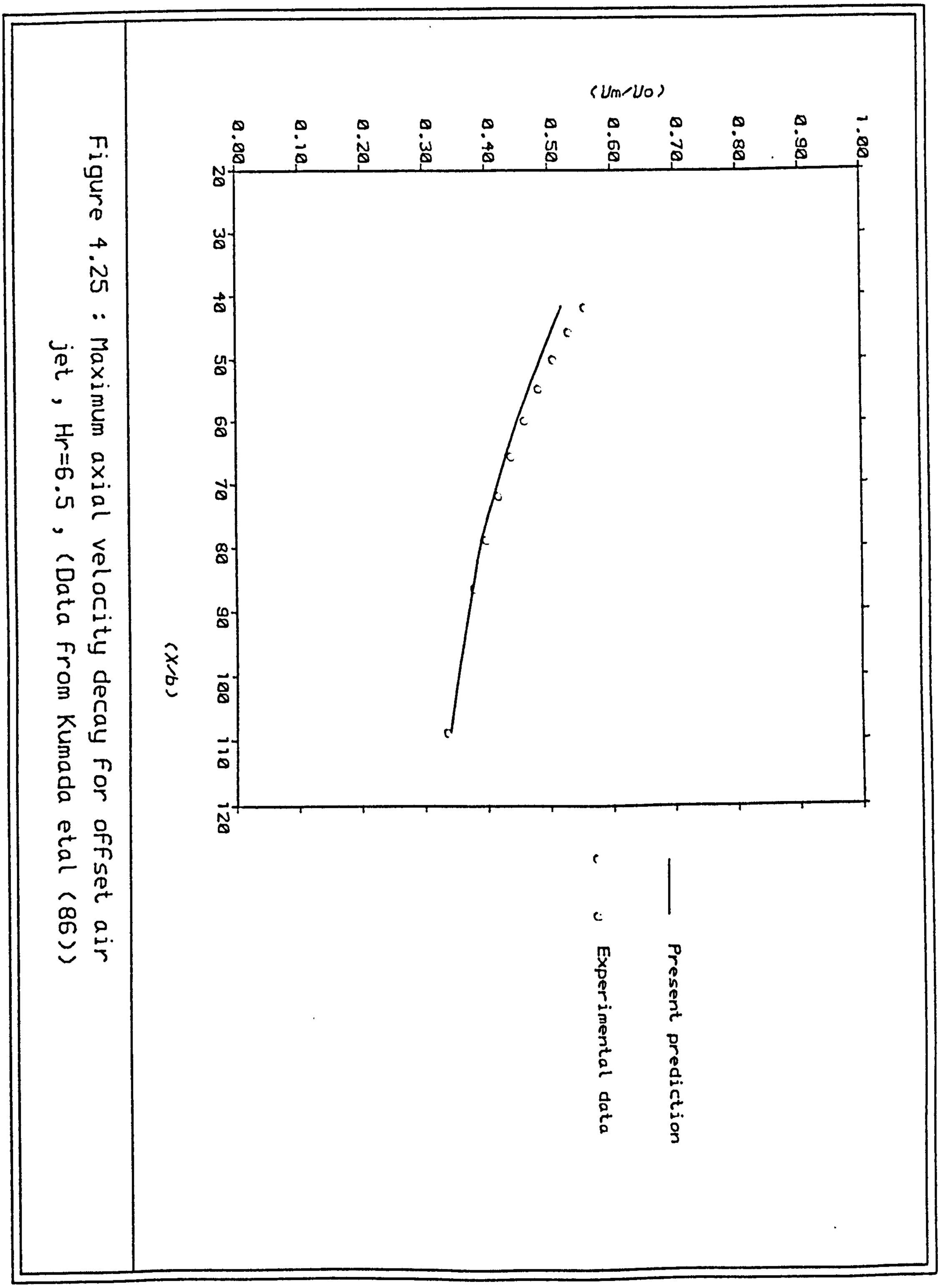

Figure 4.25 : Maximum axial velocity decay for offset air jet , Hr=6.5 , (Data From Kumada etal (86))

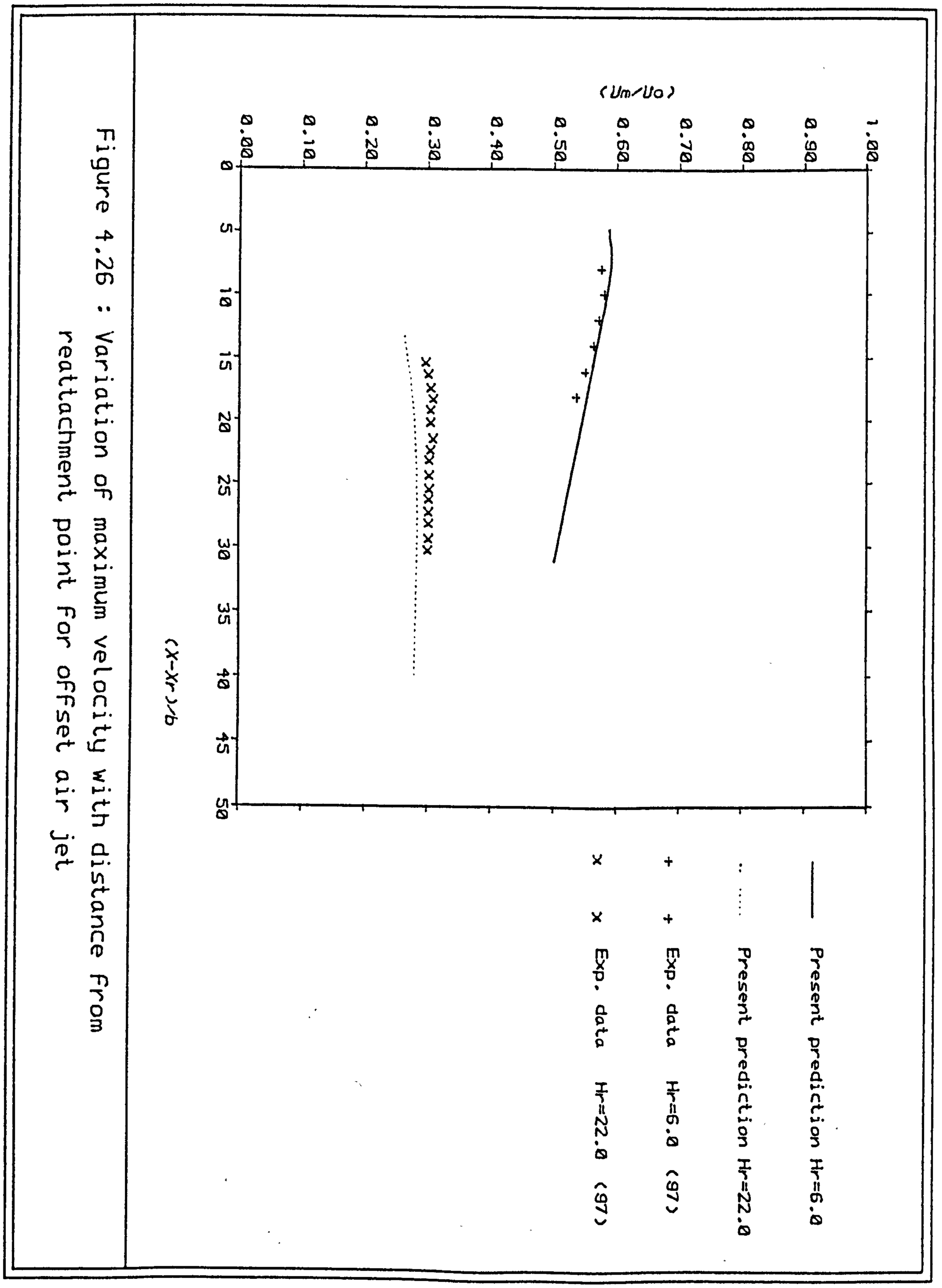

Figure 4.26 : Variation of maximum velocity with distance from reattachment point for offset air jet

The streamwise velocity distribution across the recirculation region is shown in Figure 4.27 for an offset distance Hr = 5.62 and a downstream distance x/b = 7.33. The computed distribution is compared with experimental data of Sawyer (89). The velocity were normalised using the jet inlet velocity U_o, while the vertical distance was non-dimensionalised using the offset height. The comparison shows approximately consistent displacement between the two profiles, which could again be attributed to those factors which led to the under-prediciton of the separation zone. Cross-stream velocity profiles at different axial stations in the wall-jet region are represented in Figures 4.28-30 for three offset ratio (Hr = 10, 20 and 30). Here the velocity was normalised using the local maximum value of each station and the vertical distance by the velocity half width distance (Y_h). Comparison is made between the computed profiles, the experimental data of Omere (94), and an analytical profile of Hammond (106). The predictions show a satisfactory agreement with both the data and the analytical solution.

The measured jet trajectory of Hoch and Jiji (87) and Kumada etal (86) for the recirculation and wall jet regions is compared with the computed results in Figures 4.31-33. The half width and the axial distance were normalised by the jet width in these Figures. Agreement between the computation and data in the recirculation zone is reasonable (see Figure 4.31), and the observed discrepancies are within the uncertainty associated with the measured data. The comparison in Figure 4.32-33 show only a small differencies in the trends of the computed and measured distributions. These are mainly apparent close to the reattachment region, and very good agreement may be observed further downstream.

4.4.2 Thermal Field

There is few experimental data sets available in the literature on the temperature field and surface heat transfer characteristics of turbulent, offset jet flows (see section 4.2.2). In this section the results of the present computational procedure are compared with selected heat/mass transfer data obtained by Hoch and Jiji (88), Omere (94) and Kumada etal (86). The thermal boundary condition that have been used to simulate the experimental conditions studied by these

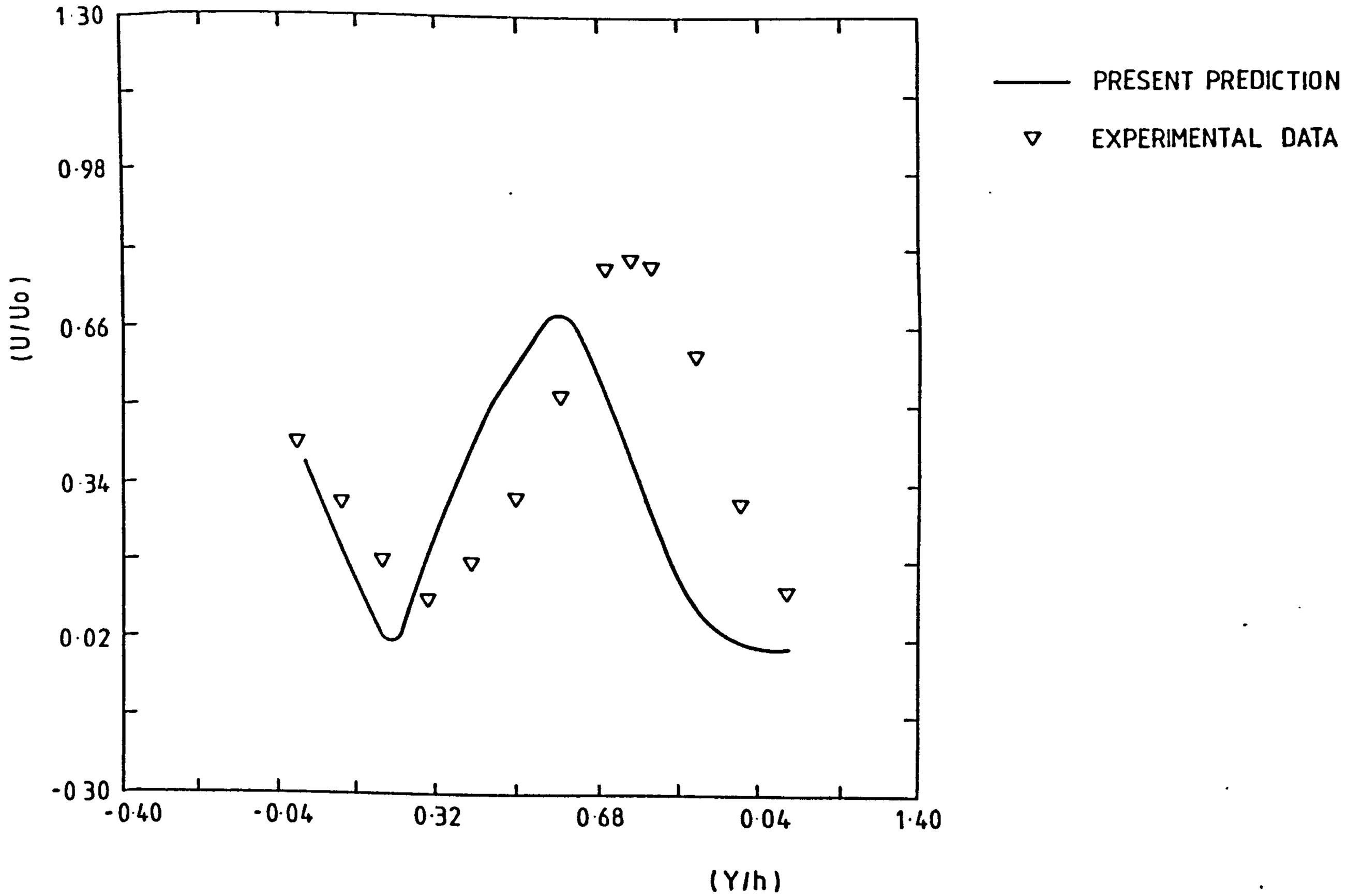

Figure 4.27 : Velocity profile at x/b=7.33 for offset air jet ,Hr=5.62 , [Data from Sawyer (89)] .

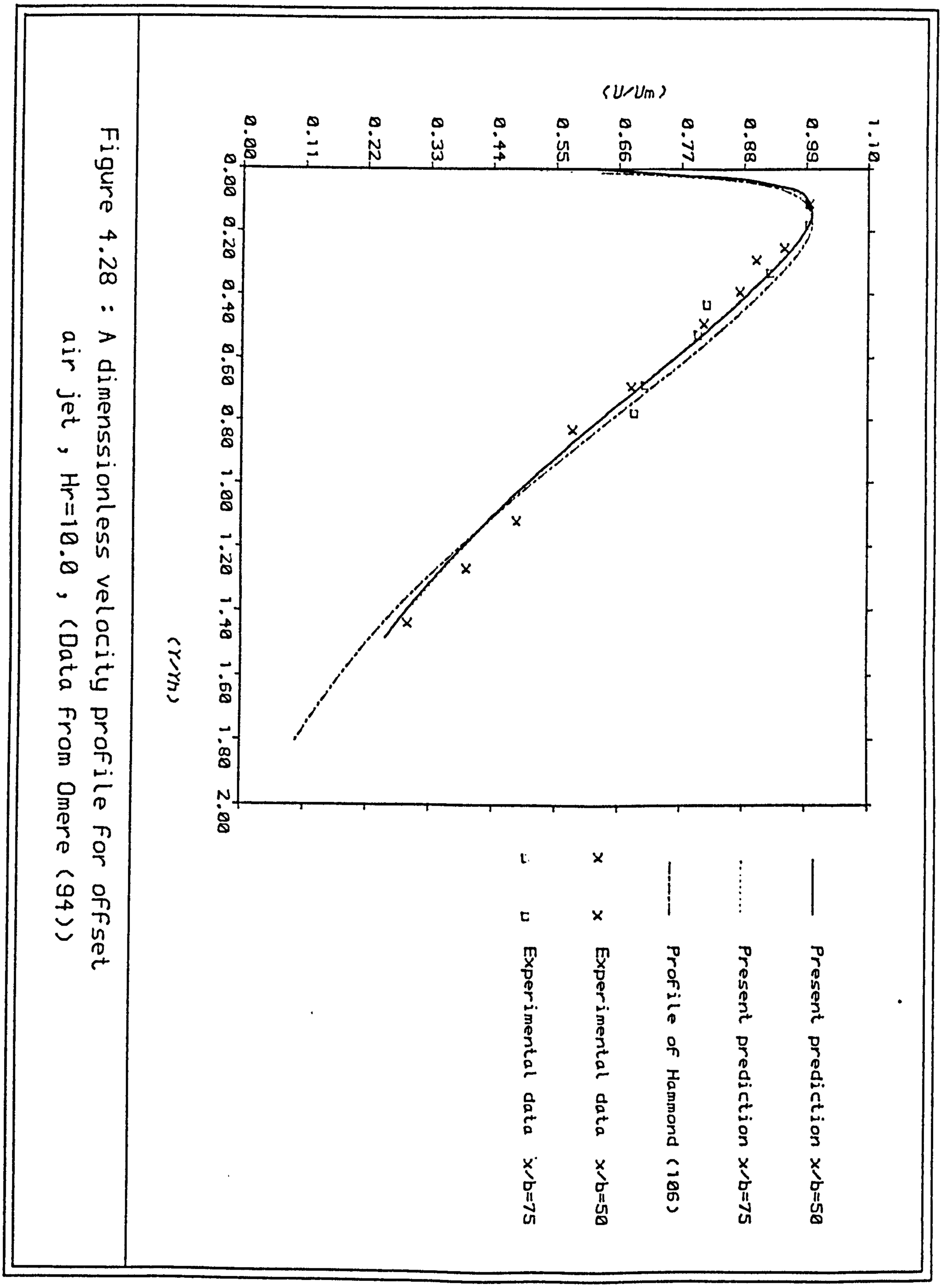

Figure 4.28 : A dimenssionless velocity profile for offset air jet , Hr=10.0 , (Data from Omere (94))

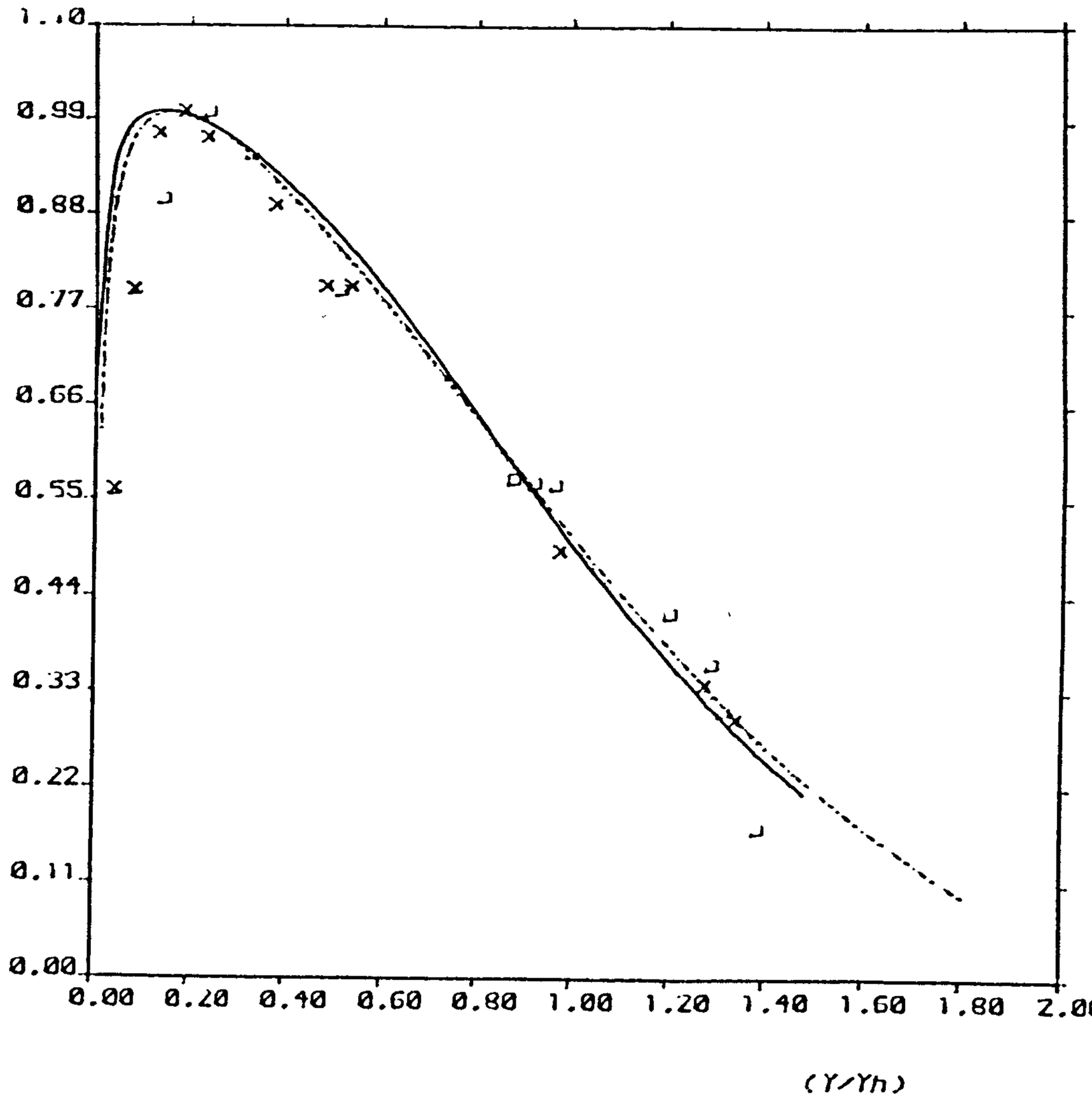

Figure 4.29 : A dimenssionless velocity profile for offset air jet , Hr=20.0 , (Data from Omere (94))

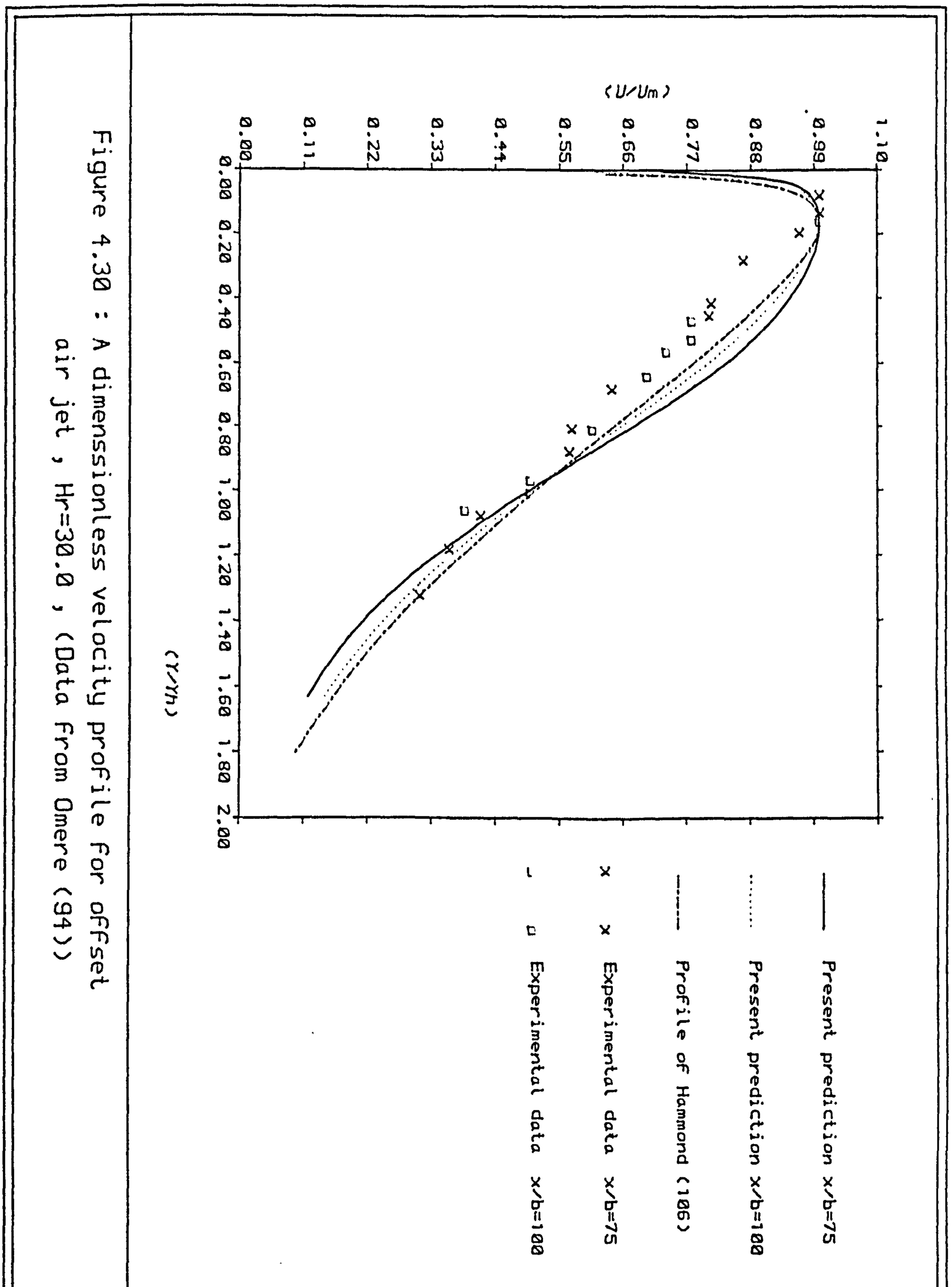

Figure 4.30 : A dimenssionless velocity profile for offset air jet , Hr=30.0 , (Data From Omere (94))

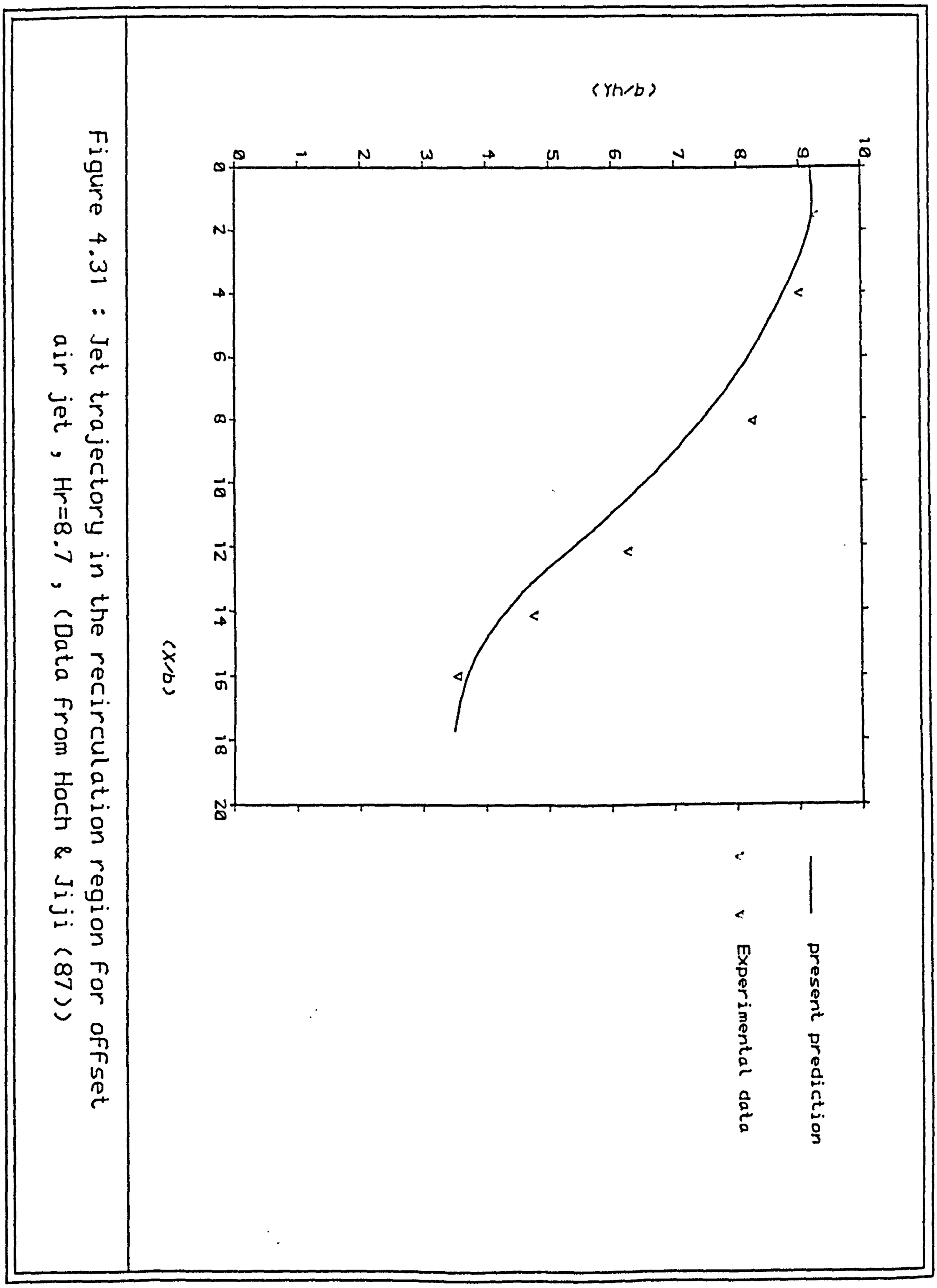

Figure 4.31 : Jet trajectory in the recirculation region for offset air jet , Hr=8.7 , (Data From Hoch & Jiji (87))

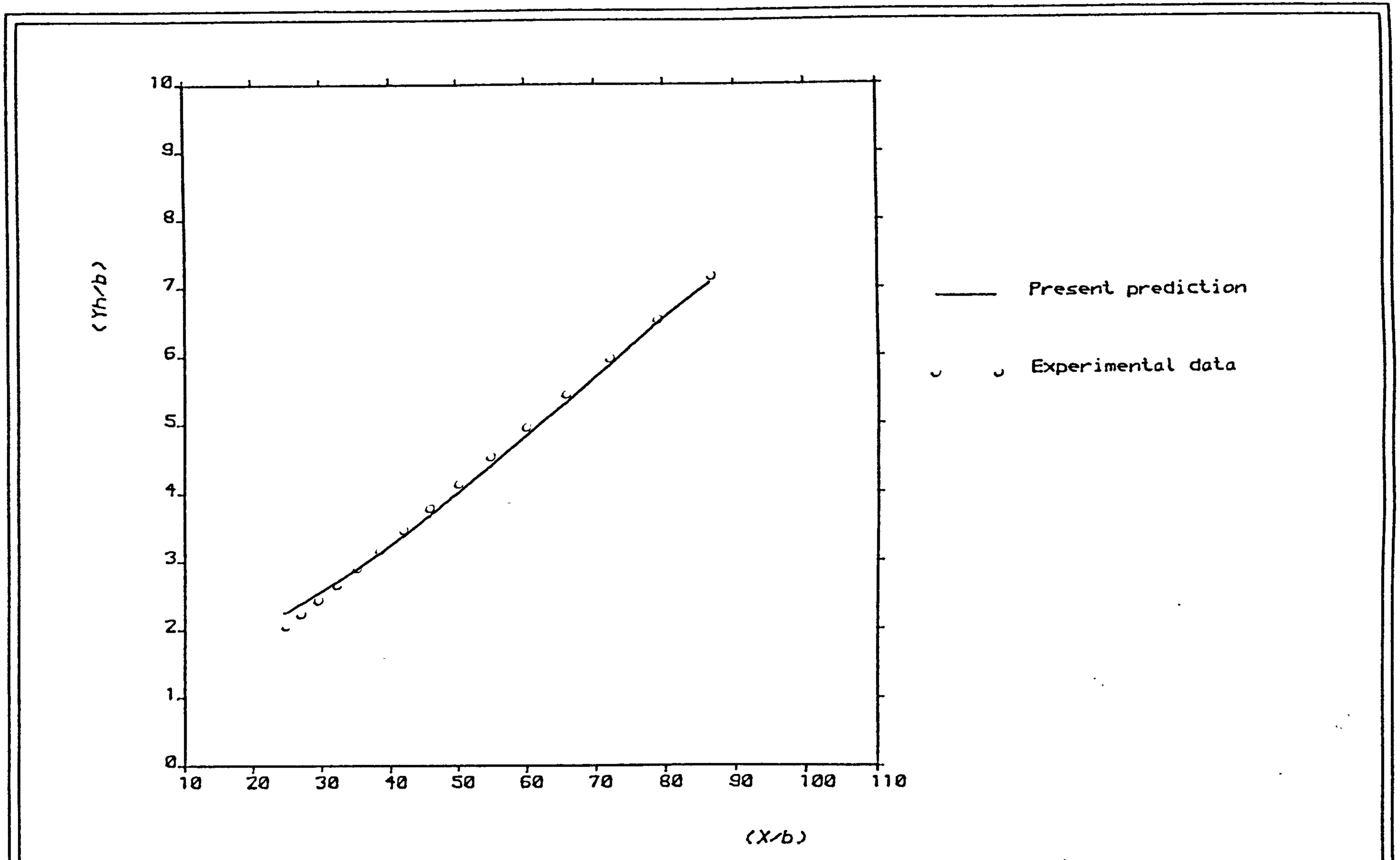

Figure 4.32 : Jet trajectory in the wall-jet region for offset air jet ,Hr=3.5 , (Data From Kumada etal (86))

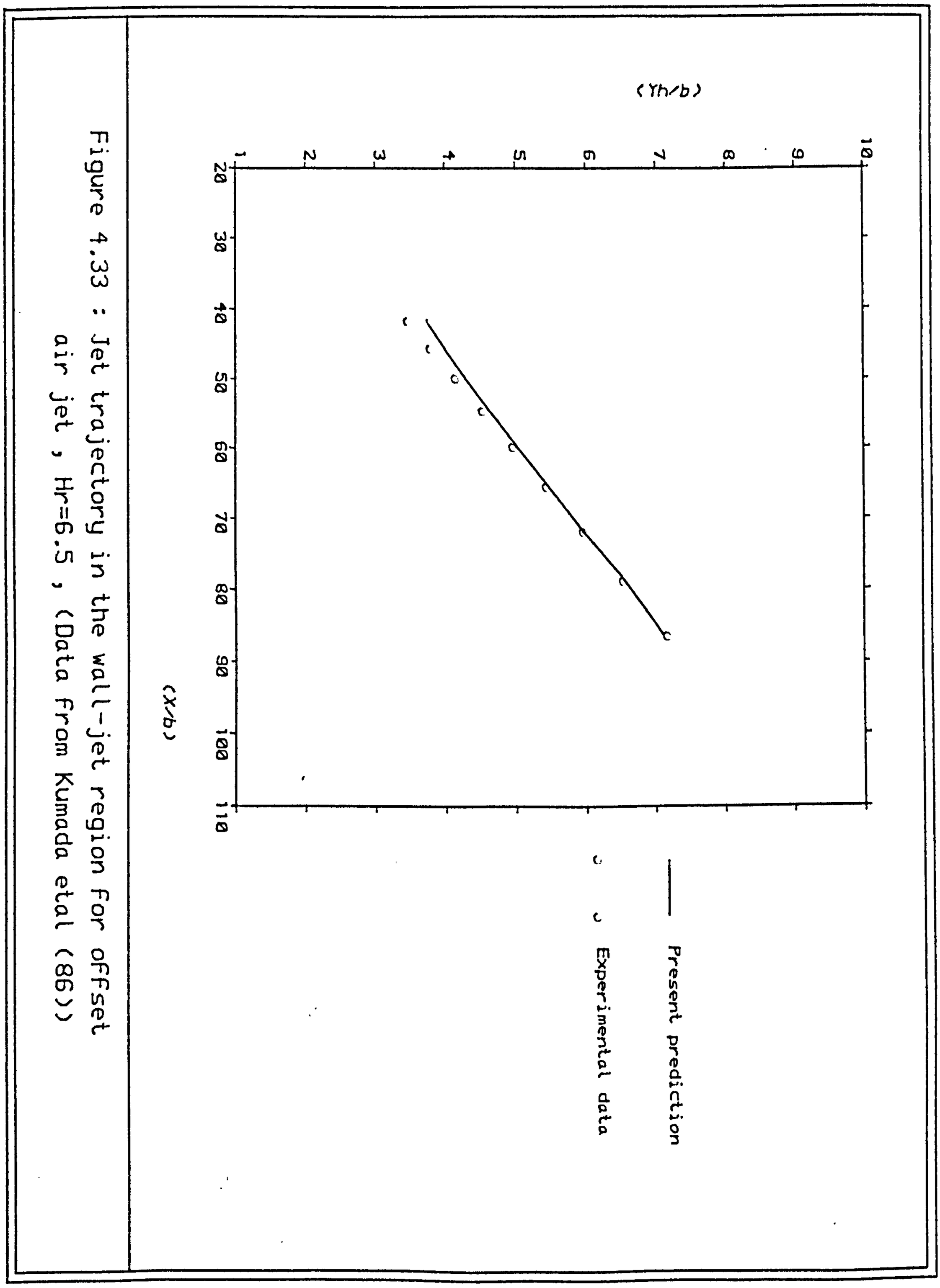

Figure 4.33 : Jet trajectory in the wall-jet region for offset air jet , Hr=6.5 , (Data from Kumada etal (86))

Experimentors (Ref)	Inlet temp (T_{in})	Top-wall temp (T_{TW})	B.F.B temp T_{BFB}	L.H.W temp T_{LHW}
Hoch & Jiji (88)	324 K (Hot jet)	$\frac{dT}{dy} = 0.0$ [adiabatic wall]	293 K	$\frac{dT}{dx} = 0.0$
Omer (94)	274 K	$\frac{dT}{dy} = 0.0$ (adiabatic wall)	291 K	"
Kumada etal (86)	293 K	284 K (cooled plate)	293 K	"

Table 4.3 Offset jet thermal boundary conditions used in the present computations.

researchers are listed in Table 4.3. The predicted temperature profile in the wall-jet region at different downstream stations is presented in figures 4.34-35 for an offset ratios, Hr of 8.7, 10, and 20. These are compared with the measurements of Hoch and Jiji (88) and Omere (94) who, following the experimental practice, normalise the local temperature using the maximum value and the vertical distance using the thermal half width. The Figures display reasonable good agreement with the data for the three offset ratios, given the scatter of the data especially near the B.F.B. (see Figure 4.35).

The computations of the local Sherwood number distribution on the top surface are compared in Figure 4.36-37 with the data of Kumada etal (86) for two offset ratios (Hr = 6.5 and 24.5). The maximum Sherwood number position (roughly corresponding to the reattachment line) can be seen to be under predicted and its simply because of the dependency of the thermal calculation on those of the flow field. Nevertheless the present computation of the Sherwood number peak appears reasonable in comparison with those of Amano (48) and Chieng and Launder (57) for the turbulent pipe expansion problem; see Figure 4.58. (Both studies have used the standard k-ε model, but with modified wall function see section 4.2.3.). Both these earlier studies predicte the peak to occur about four step heights (defined as (D-d)/2) upstream of the experimental one. In the present study, however, this location is predicted to be approximately 0.4 - 0.6 offset distance (Hr) upstream the experimental data. This may be attributed to those factors which led to the under prediction of the reattachment point, namely inadequencies in the present state-of-the-art in turbulence modelling.

4.4.3 Closure

The foregoing comparisons demonstrate that the present computational procedure yields generally good results for jet reattaching flows. The downstream distributions of static pressure, peak velocity, and jet trajectory were reasonably well predicted in the wall-jet region, although some discrepancies were apparent in the recirculation and reattachment regions. Here the location of the attachment line is underpredicted. The differences between the

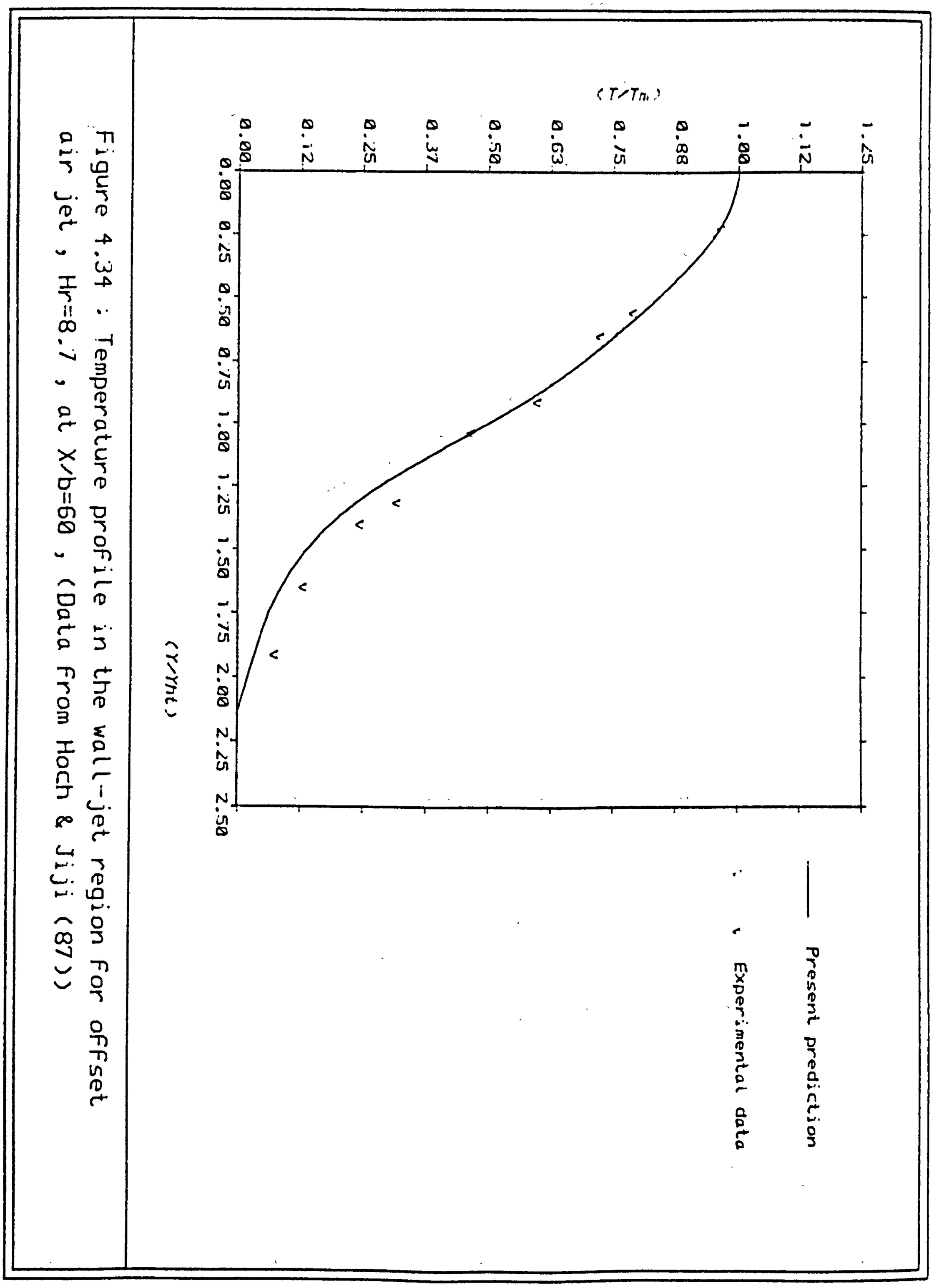

Figure 4.34 : Temperature profile in the wall-jet region For offset air jet , Hr=8.7 , at X/b=60 , (Data from Hoch & Jiji (87))

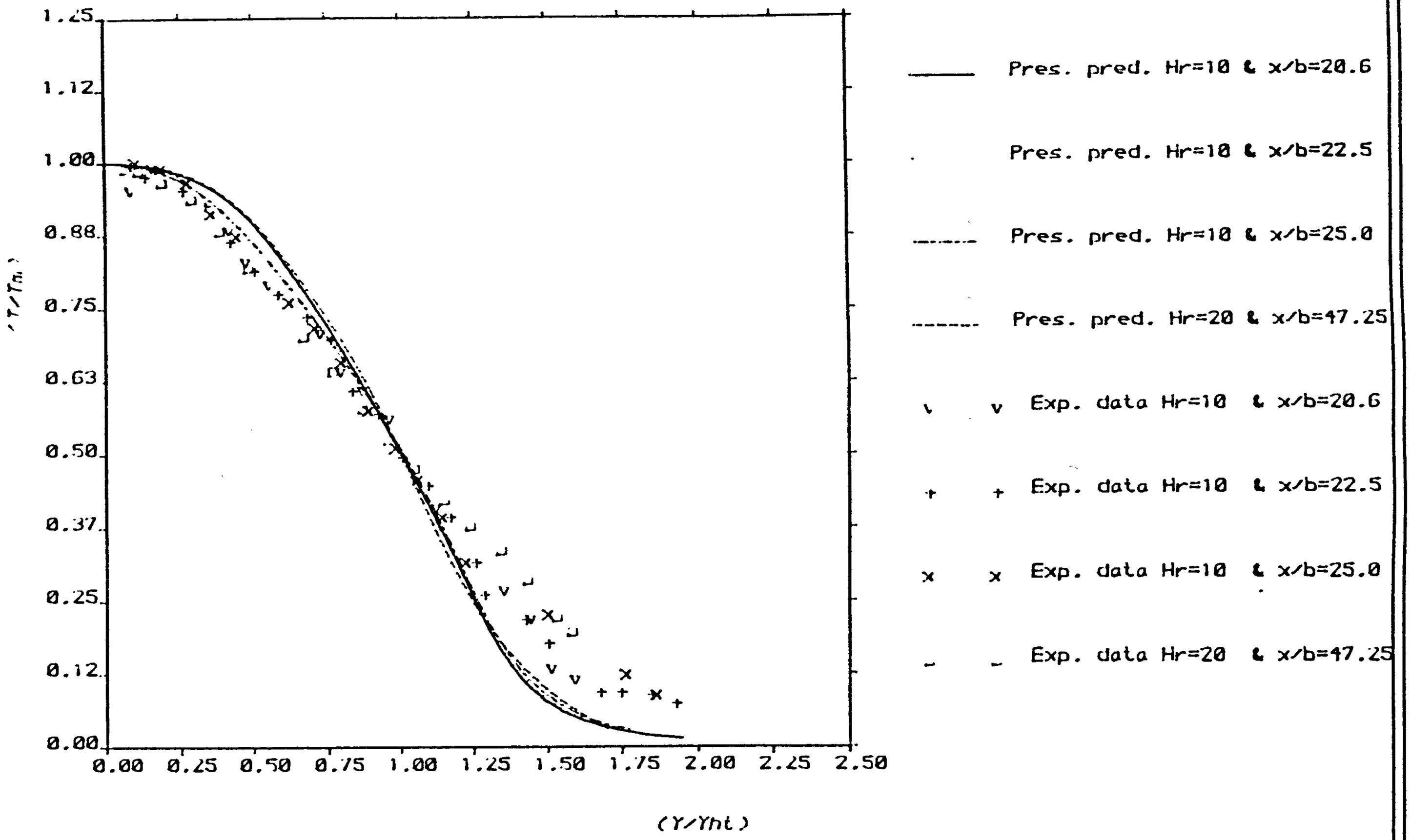

Figure 4.35 : A dimenssionless temperature profile for offset air jet , Hr=10.0,20.0 , (Data From Omere (94))

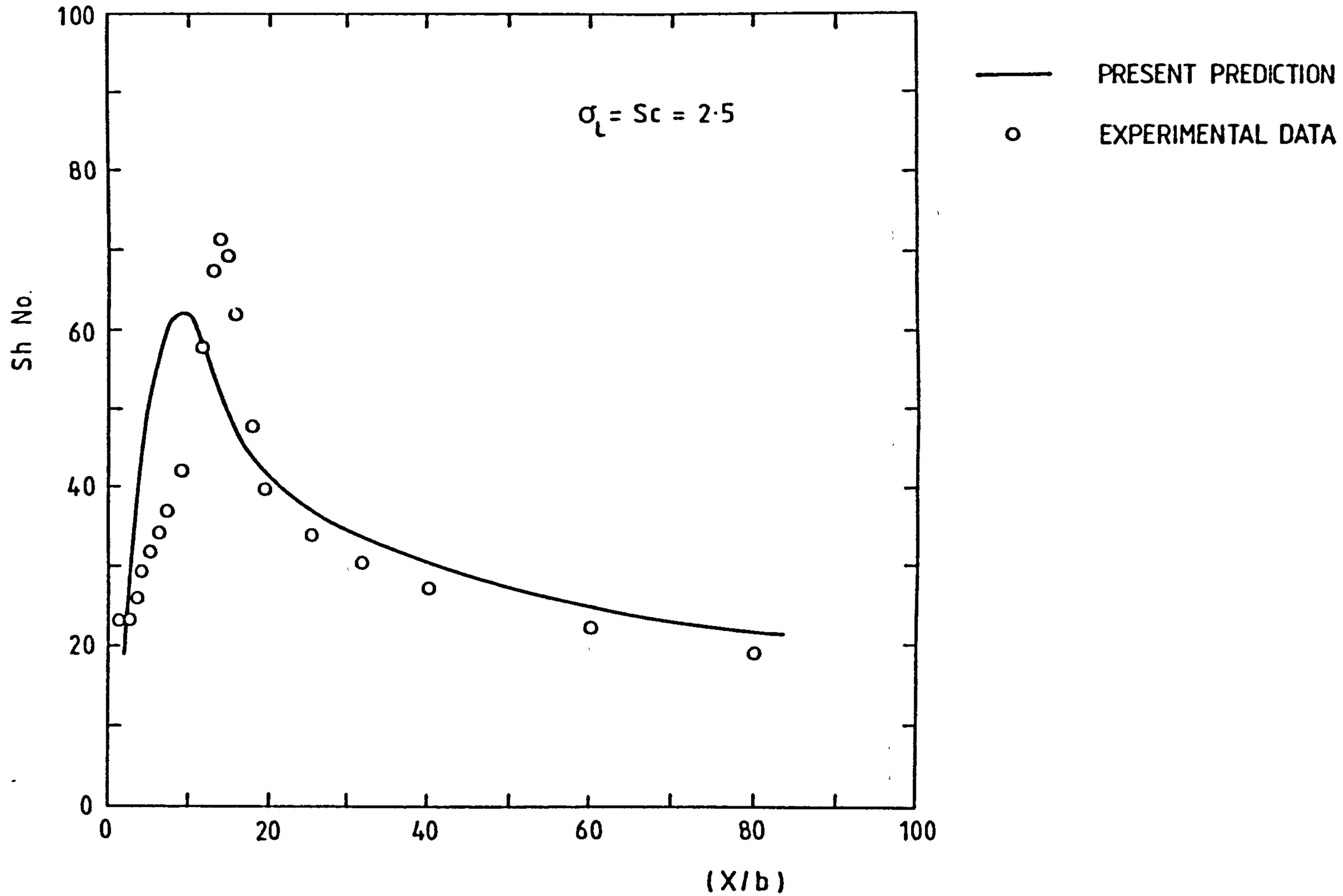

Fig. 4.36 : Local Sherwood number distribution on the top surface for offset air jet ,Hr=6.5 , [Data from Kumada etal (86)].

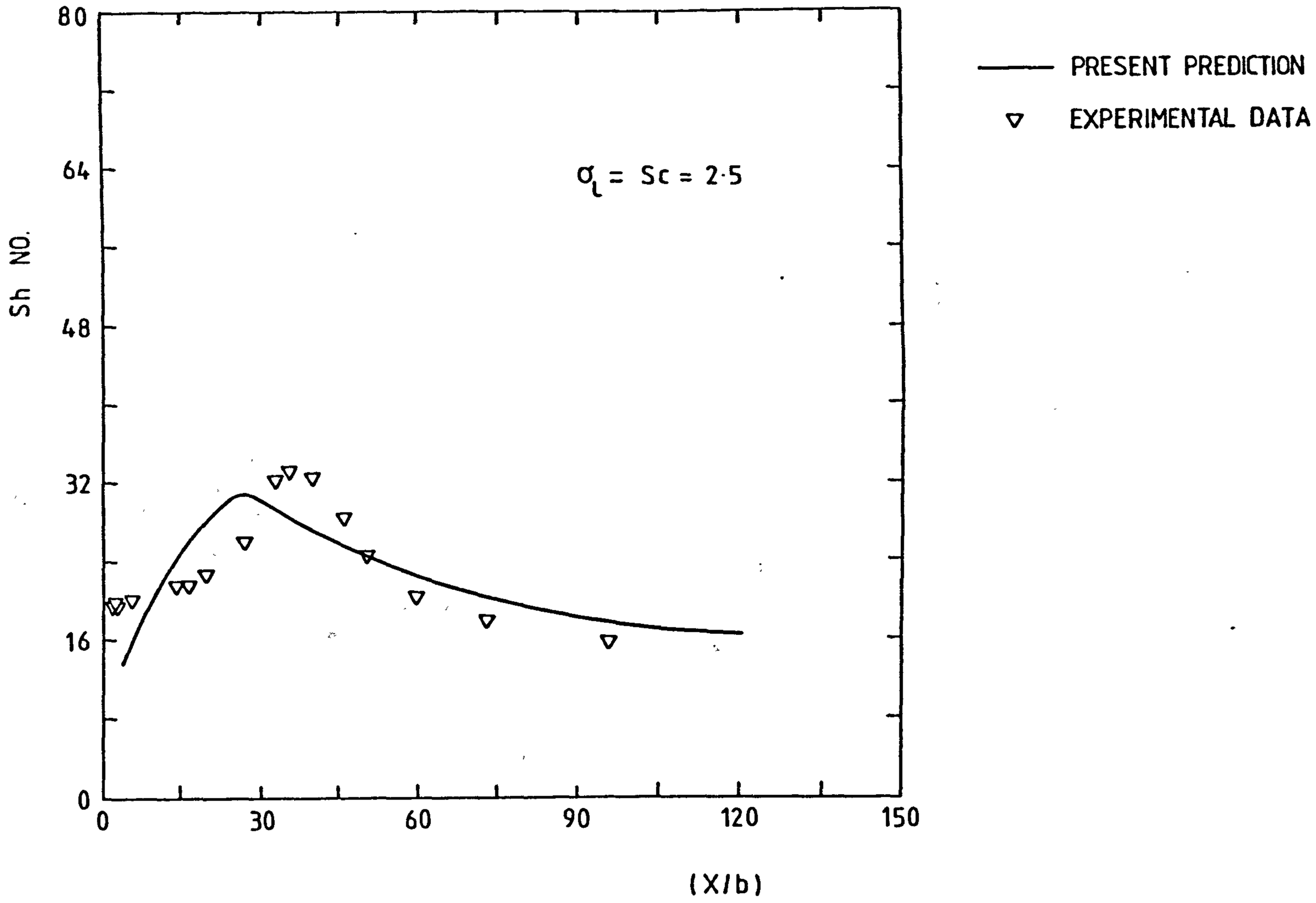

Fig. 4.37 : Local Sherwood number distribution on the top surface for offset air jet ,Hr=24.5 , [Data from Kumada etal (86)].

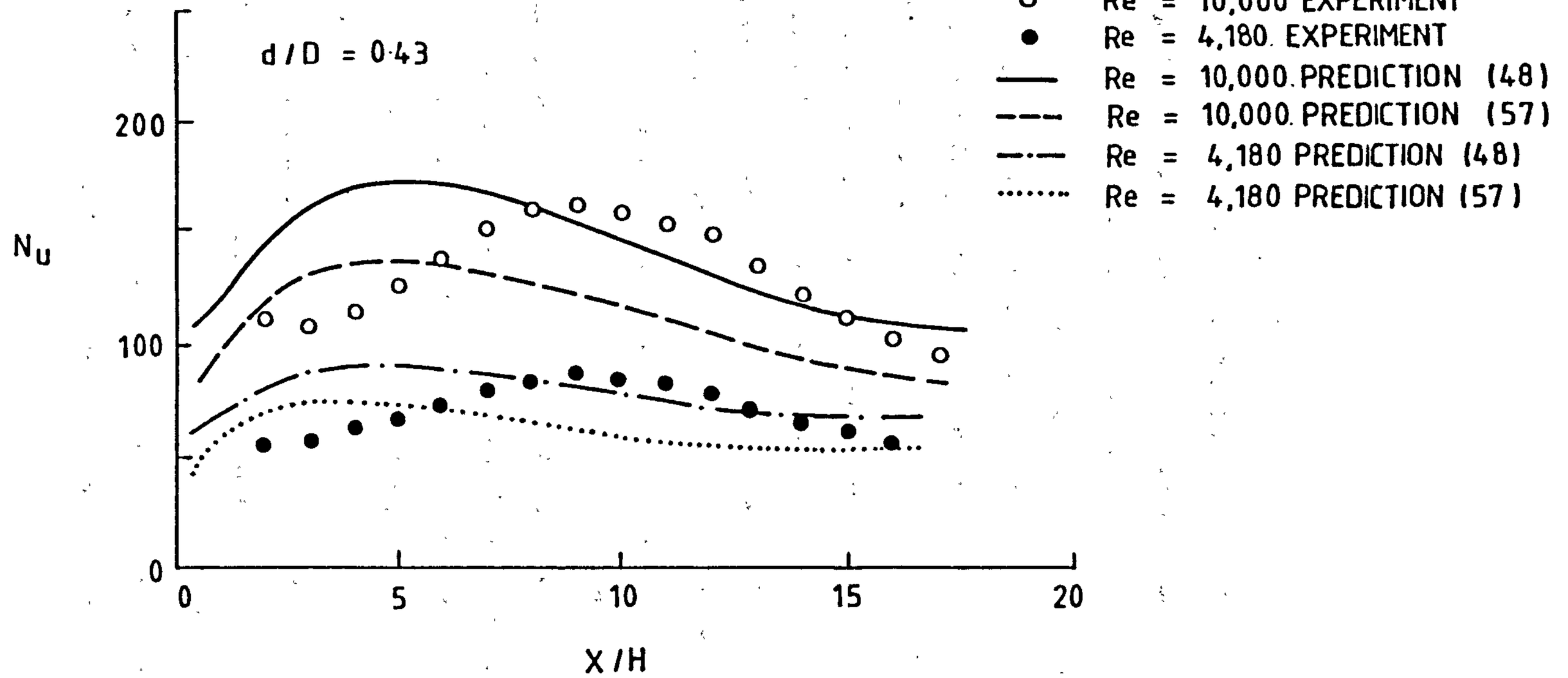

Fig. 4.38 : Nusselt number distribution along the pipe for d/D=0.43. [After Amano (48)].

present computations and measurement may be attributed to the assumptions regarding the approach profiles, the limitations of the K-ε turbulence model in recirculating flows, and to the usual uncertainties associated with experimental data.

4.5 CONCLUDING REMARKS

A numerical study has been undertaken to investigate the fluid flow and heat transfer induced by two-dimensional offset jets over a wide range of offset ratios (3.5 - 32.4). Such jets often govern the flow and thermal comfort within mechanically-ventilated rooms employing 'linear' diffusers. The relevant equations have been solved using finite-domain technique with aid of the CHAMPION computer program of Pun and Spalding (34) for two-dimensional elliptic flows. The standard K-ε model of turbulence was employed, together with a (QUICK) differencing scheme of Leonard (74) and the SIMPLEC algorith of Van Dourmaal and Raithby (70). Grid independent tests based on the methods developed by McGuirk and Rodi (56) and de Vahl Davis and Mallinson (108) were carried out in order to evaluate the grid refinement needed in regions of large false diffusion. A grid generation procedure was subsequently developed to provide computational meshes that were grid independent for each geometry considered. The computed results have been compared with experimental data for both the flow and thermal fields taken from several sources. These display reasonable agreement between computed and measured properties. The accuracy of these predictions are dependent on the proper specification of the approach (jet inlet) profiles and the adequancy of the turbulence model adopted, including the wall functions. Nevertheless, the present computations appears reasonable in view of the limited accuracy of measurements, and the uncertainties inherent in turbulent flow calculations.

CHAPTER 5

THREE-DIMENSIONAL FLOW COMPUTATIONAL CASE STUDIES

5.0 THREE-DIMENSIONAL FLOW COMPUTATIONAL CASE STUDIES

5.1 INTRODUCTION

The class of convective flows which are steady, recirculating, turbulent and three-dimensional are found in many processes of engineering importance. These include combustion processes in furnaces and combustors, developing flow in ducts, mechanically-ventilated enclosure, and in several other industrial and environmental situations. The analytical solution of such problems has been impossible due to their inherent complexity. The experimental techniques on the other hand, at either full or reduced scale, can be very expensive, particularly if comprehensive data sets are required. Recently, the computer had made the mathematical modelling of such processes feasible. However, to model these processes the basic equations of the flow, heat transfer and chemical reaction, as well as their coupling, must be solved for the three-dimensional flow domain.

The purpose of this chapter is twofold; firstly to present the solution sequence for the three-dimensional finite-domain computation procedure which has been incorporated into the ESCEAT computer code, and secondly to verify its computations for some relatively simple three-dimensional test cases. The latter validation was accomplished by comparing the ESCEAT code 'predictions' with the measurements and predictions of previous workers.

5.2 SOLUTION OF THE FINITE-DOMAIN EQUATIONS

The finite-domain form of the equations to be solved has been described in Chapter 3. The SIMPLE procedure (see section 3.2.6) was adopted in solving these equation in preference to SIMPLEC for reasons given in section 3.2.1. The method employed an alternating direction version of the TDMA algorithm described in section 3.4.2. This algorithm has been used, following the procedure adopted by Caretto et al (113) and Hjertager and Magnussen (114), successively in each of the three-co-ordinate directions. During each sweep the variables along a line under consideration are regarded as unknown, while those on the surrounding lines are known from the previous iteration or the initial guess. This means that each variable at a point has

connection with two neighbouring points along the line being considered. Each variable (except the pressure correction P′) is solved in sequence on this line, before the next line is considered. The overall solution cycle commences with a sweep of all lines lying in one direction (the Y-direction say), and then, using this solution as the best current estimate, a solution along grid lines in a second direction (the X-direction say) is obtained. The final sweep in the iteration cycle undertaken is for the lines in third direction with the last sweep solution being used as the best current estimate. Hence, the triple sweep procedure consists of the three following steps:

$$1)\ A_P \Phi_P^1 = A_N \Phi_N^1 + A_S \Phi_S^1 + [A_E \Phi_E + A_W \Phi_W + A_D \Phi_D + A_U \Phi_U + S_\Phi] \qquad 5.1$$

where the expression in the brackets is regarded as known, using the currently available values for Φ_E, Φ_W, Φ_U and Φ_D along the four neighbouring grid lines. The superscript 1 denotes values obtained after the first sweep.

2) Having solved equation 5.1 using the TDMA along all Y-direction lines, a second sweep is made along all X-direction lines to solve equation of the form:

$$A_P \Phi_P^2 = A_E \Phi_E^2 + A_W \Phi_W^2 + [A_N \Phi_N^1 + A_S \Phi_S^1 + A_U \Phi_U^1 + S_\Phi] \quad 5.2$$

3) The third sweep is carried out along all the lines in Z-direction in order to solve an equation of the form:

$$A_P \Phi_P^* = A_D \Phi_D^* + A_U \Phi_U^* + [A_N \Phi_N^2 + A_S \Phi_S^2 + A_W \Phi_W^2 + A_E \Phi_E^2 + S_\Phi] \quad 5.3$$

One triple sweep is performed for the velocity components and all other Φ's in a line-by-line manners, subsequently the pressure correction (P') is solved by sweeping the flow domain, also in a line by line manner, for each of the three co-ordinate direction in order to adjust the velocities and pressure.

The complete solution sequence adopted for the ESCEAT code proceeds by the iterative repetition of the following steps:

a) Variables are initialized.
b) The finite-domain equation coefficients are evaluated.
c) The direction of the first sweep is considered.
d) A line in this direction is then visited.
e) The FDE's are solved by TDMA (for all the variables except P').
f) Step e is repeated for all the lines (in a plane-by-plane manner) over the whole flow field.
g) Steps c-f are then repeated for the second, and finally the third sweep direction.
h) U^*,V^* and W^* are used to calculate the coefficients in pressure correction equation.
i) The P' equation is solved using the TDMA.
j) The resulting pressure correction is used to update the velocity components and pressure in the manner indicated by equations (3.32).
k) Steps h-j are repeated in a manner similar to that of steps g and h.
l) The cycle of steps (b-l) represents one iteration, and this cycle is repeated until a converged solution is obtained.

5.3 THE TEST CASES

The ESCEAT code currently utilises conventional three-dimensional cartesian coordinates, which restrict its use to rectangular geometries. However, more complicated geometries could be handled if a suitable coordinate transformation was to be incorporated. Two simple test cases were chosen for the initial validation of the code. Both were of the steady laminar flow type; the first case being through rectangular sudden expansion, while the other was flow in a cavity with moving wall. These were selected in order to enable comparisons with the computations of Hjertager and Magnussen (114).

5.3.1 Flow Through a Sudden Channel Expansion

This flow consists of a retarding central jet - with adjacent regions of recirculating fluid. The flow geometry was studied experimentally by Durst et al (115), and is illustrated in figure 5.1. It consists of the sudden expansion of the flow from a small channel into a larger one, both of which have confining side-walls. The experimental inlet profile for the streamwise velocity component was adopted for the present computations, while the other two components were set to zero. The remaining boundary conditions were simulated by prescribing zero normal and tangential velocity components at the walls and zero velocity gradients at the exit. The implementation of such boundary conditions followed the procedure described in section (3.3.), although no wall functions are required for laminar flow situation. A hybrid differencing scheme was employed for these compution. A nodal network of 9x13x11 grid were used to discretizel the space in X-, Y- and Z-direction respectively. This coarse mesh was essentially chosen for storage and economic reasons, and in order to match the location of the available experimental data sets with the grid expansion practice adopted here.

The streamwise velocity vectors and profiles along the symmetry plane of the flow field are shown in figure 5.2. The computed cross-stream velocity profiles and the axial velocity decay through the sudden expansion are plotted in Figures 5.3 - 5.6. These are presented for a Reynolds number (based on inlet channel height and peak velocity) of 56 along with the corresponding experimental data of Durst et al (115) and predictions of Hjertager and Magnussen (114). It can be seen that the present computation are in good agreement with the experimental data. In general they exhibit rather better agreement with this data than do the predictions of Hjertager and Magnussen (114), mainly due to the use of a 9x13x11 grid instead of the 9x9x9 grid used by the latter researchers.

5.3.2 Three-dimensional Cavity with Moving Lid

A constant-property fluid inside a three-dimensional cavity will be induced to circulate in laminar motion by the action of a steadily moving lid. The flow geometry and the boundary conditions simulated in the present study are depicted in figure 5.7. The dimensions of

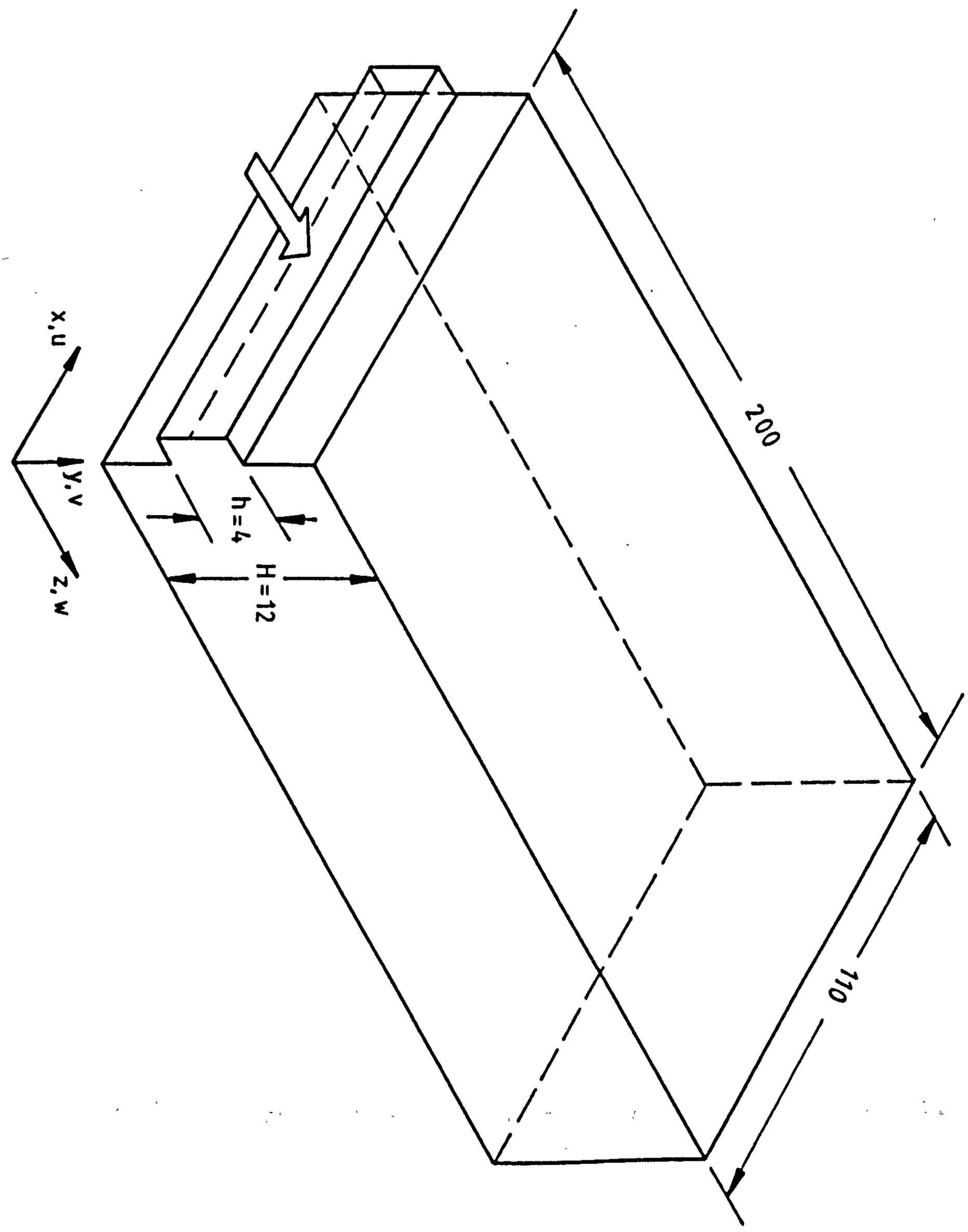

Figure 5.1 : Sudden expansion geometry for the test rig of Durst etal (115) :dimension in (cm)

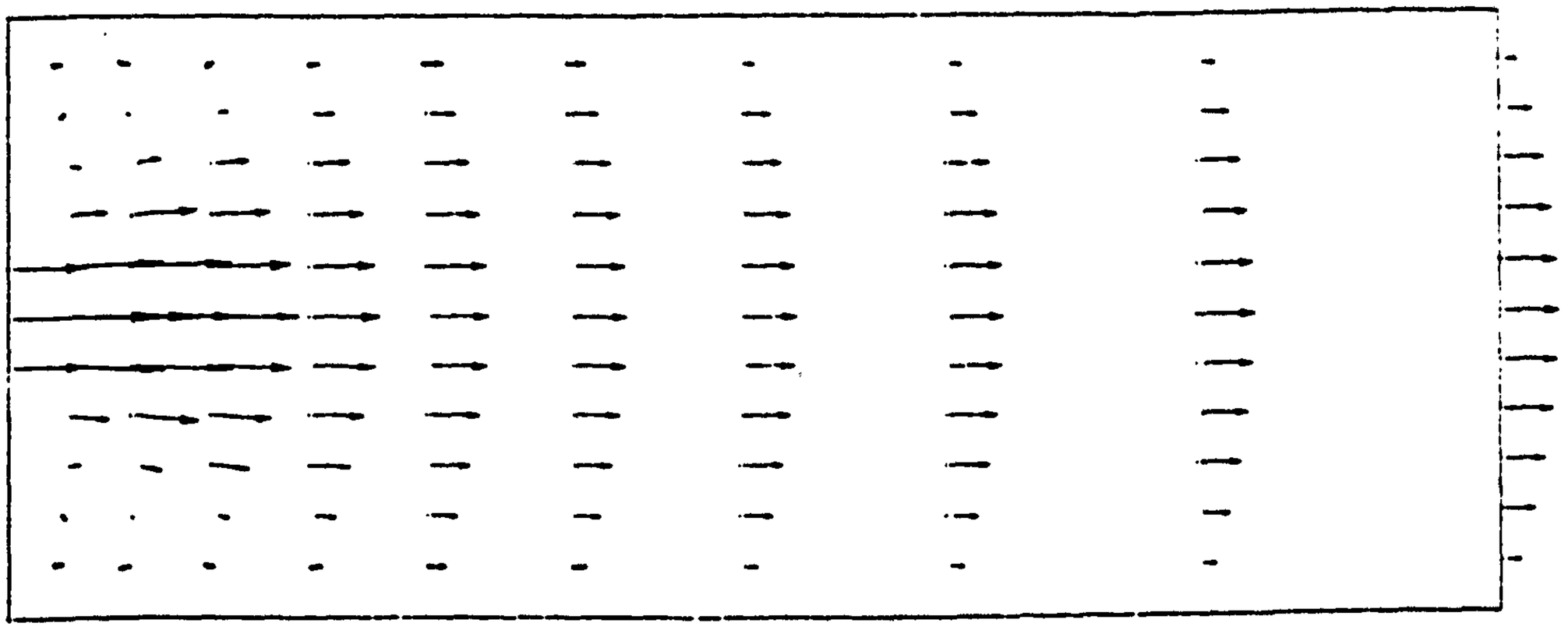

Fig. 5.2 : Velocity vectotrs and stream-wise velocity profiles for flow through a sudden expansion .

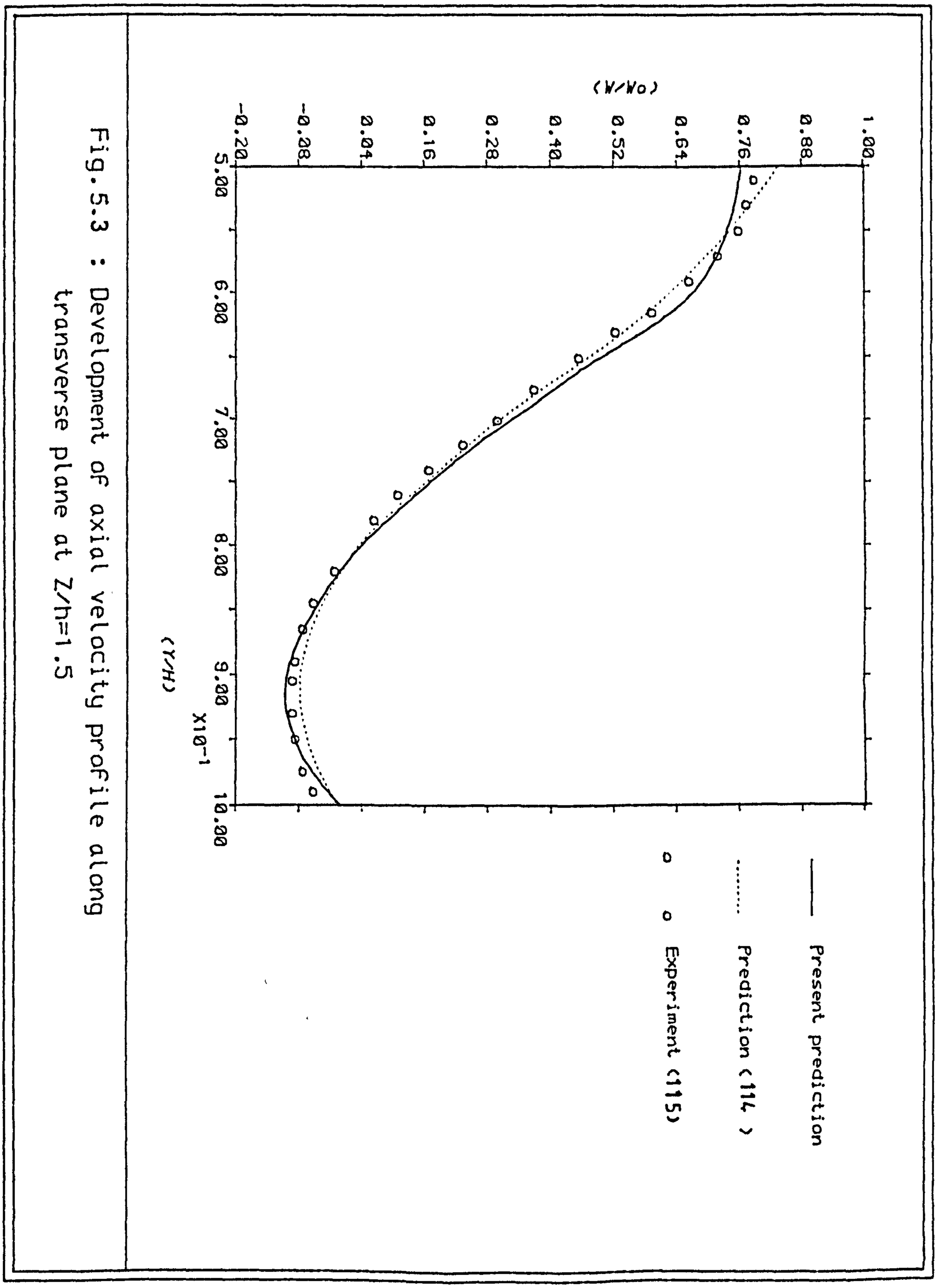

Fig.5.3 : Development of axial velocity profile along transverse plane at Z/h=1.5

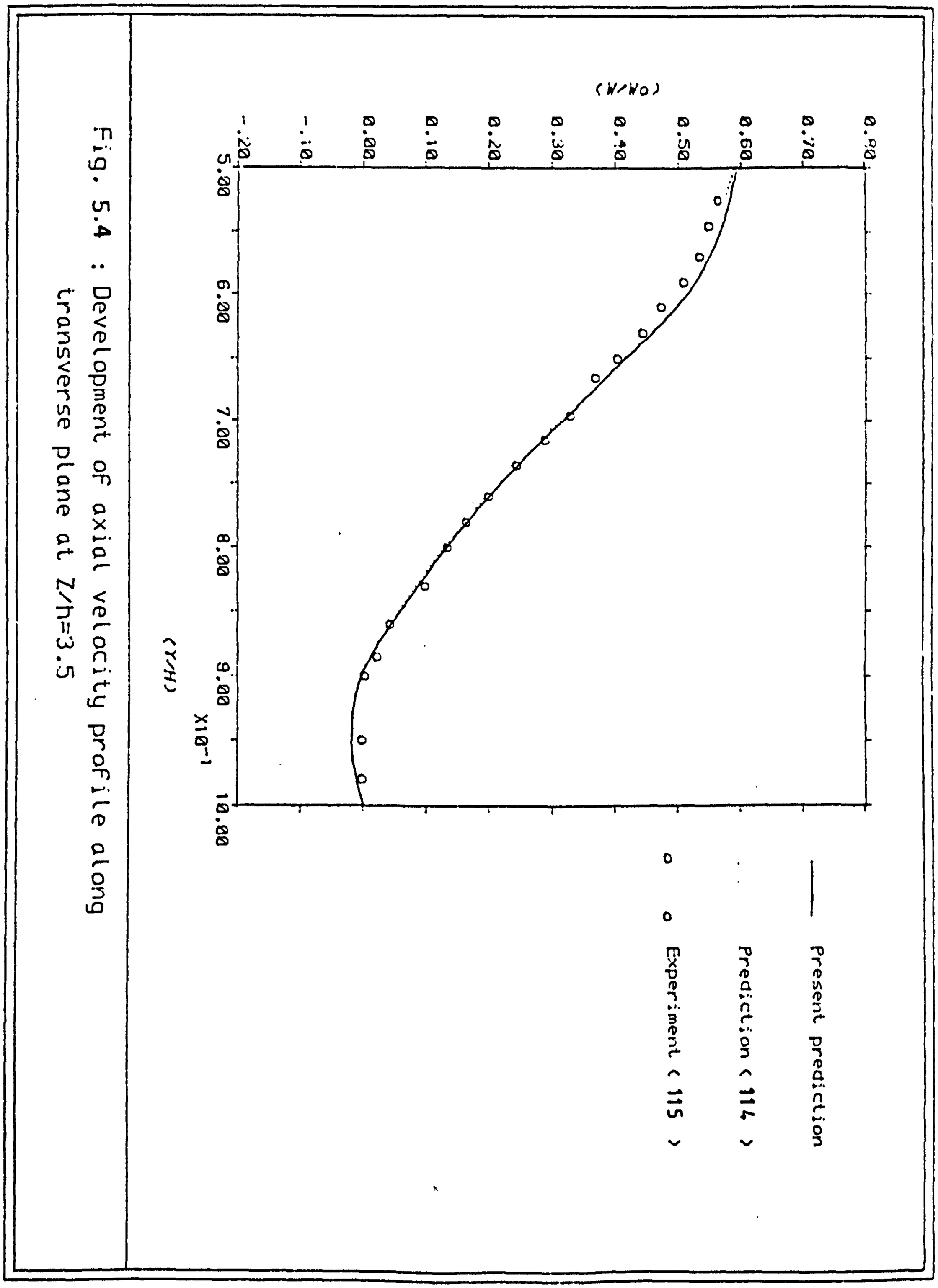

Fig. 5.4 : Development of axial velocity profile along transverse plane at Z/h=3.5

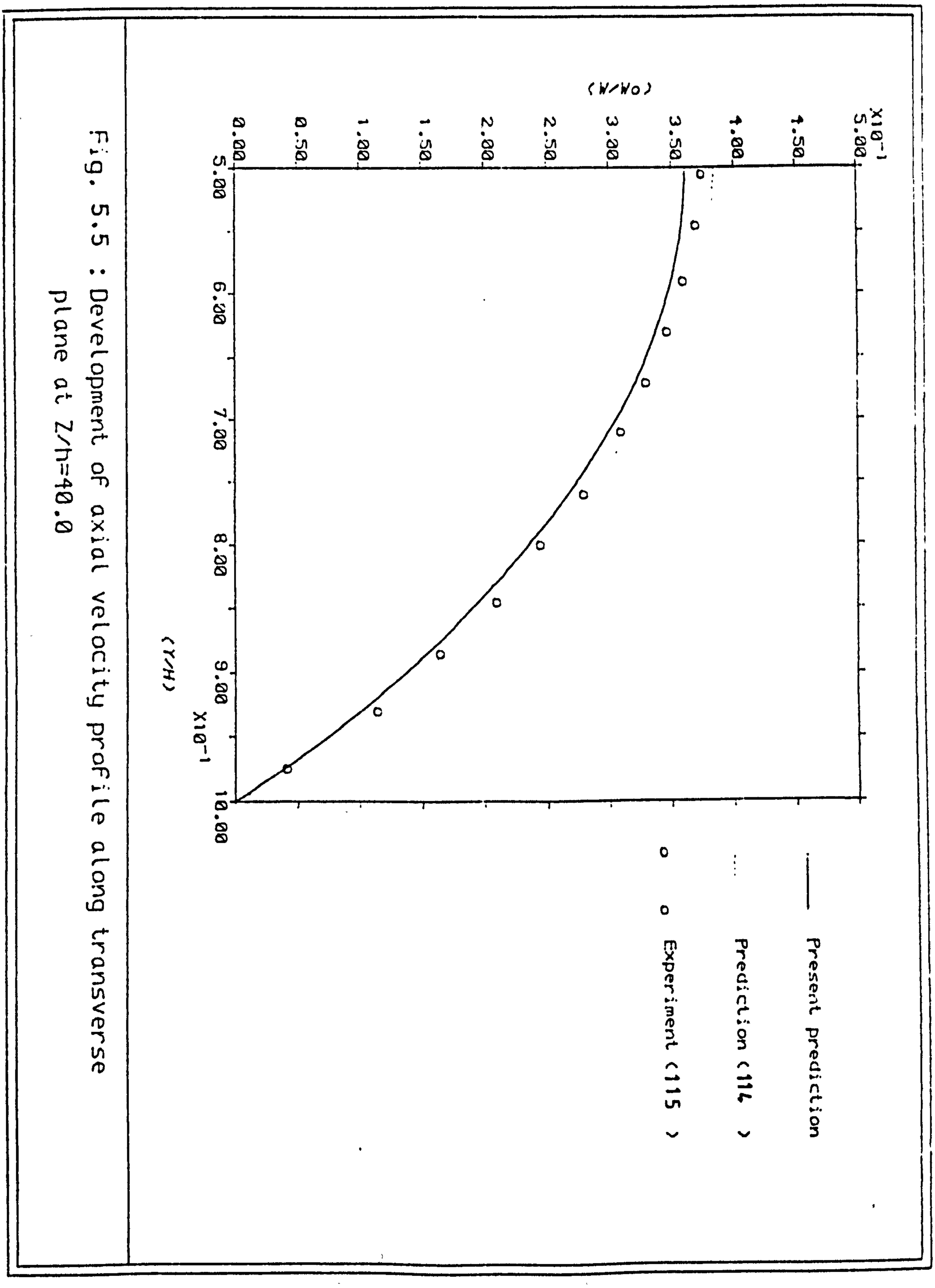

Fig. 5.5 : Development of axial velocity profile along transverse plane at Z/h=40.0

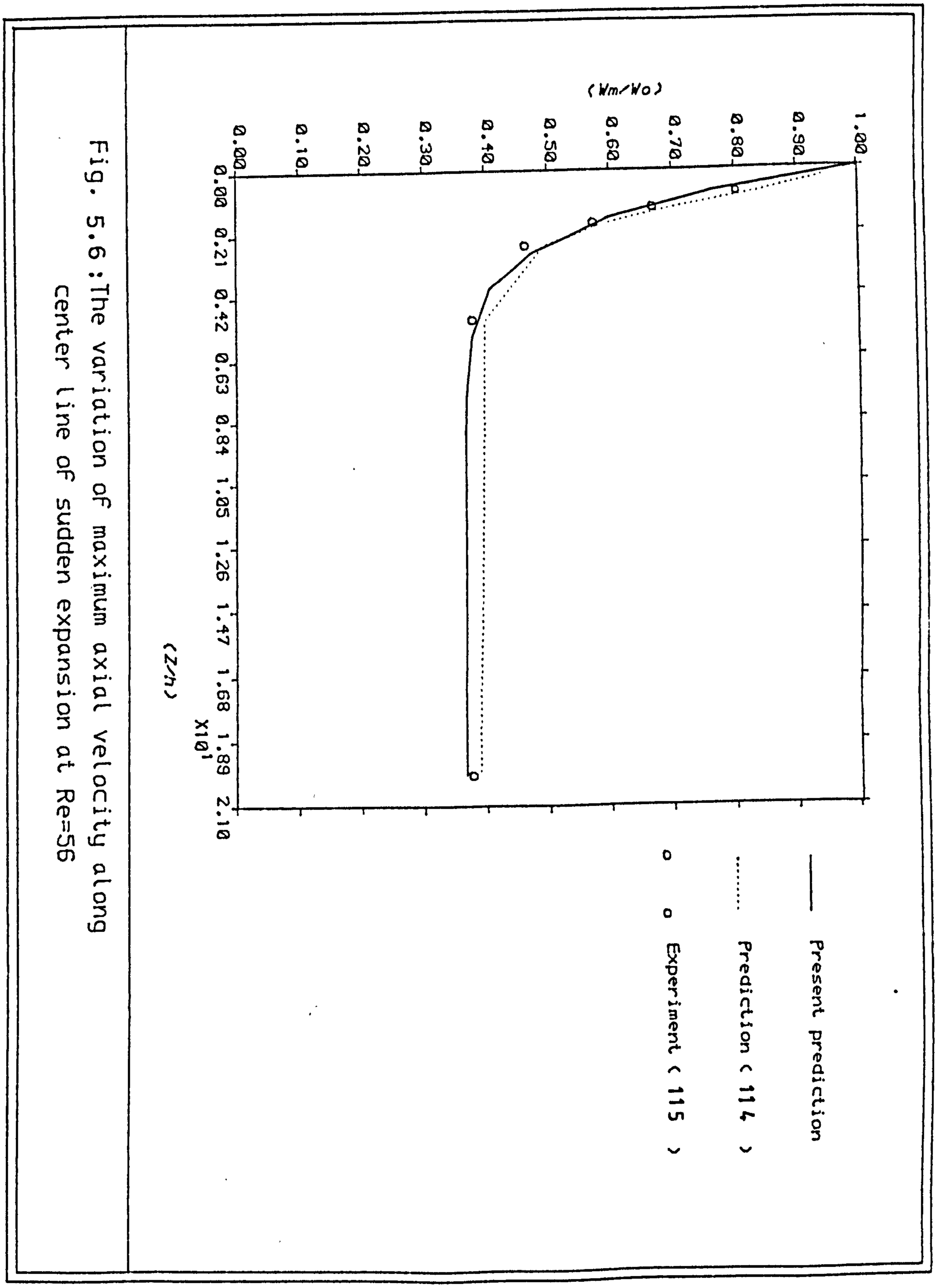

Fig. 5.6 : The variation of maximum axial velocity along center line of sudden expansion at Re=56

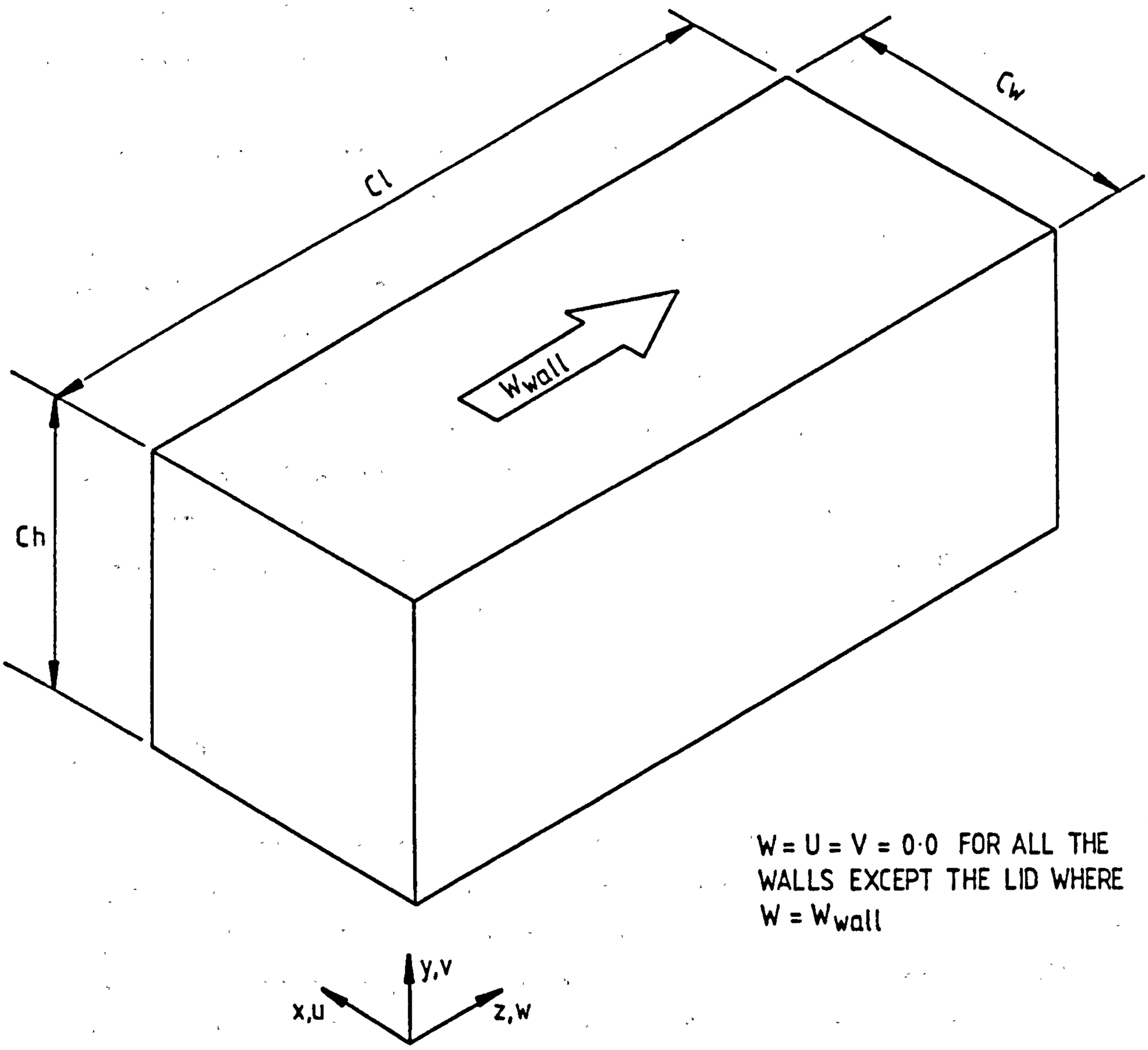

Figure 5.7 : The geometry of the three-dimensional cavity flow with a moving lid simulated by Hjertager and Magnussen (114) .

the cavity were Cw/Ch = 1.0, Ch/Cl = 0.2, while Re based on the wall velocity and cavity height (Ch) was 100.0. The hybrid differencing scheme was again used in the calculation with a 9x9x9 grid of uniform distribution. This rather coarse mesh was used for economic reasons, and also coincide with that adopted by Hjertager and Magnussen (114).

The velocity vectors and profiles at the Y-Z plane where X/Cw = 0.5 are presented in Figure 5.8, while the corresponding streamwise velocity distribution at different longitudnal positions are given in Figures 5.9 - 5.12. The distribution of the cross-flow velocity (the vertical or V-componet) along the cavity is shown in figures 5.13 - 5.14 at an X-Z plane close to the lid, where Y/Cl = 0.175. These are presented for two X-stations located at, X/Cw = 0.5 and 0.07 respectively. The predictions of Hjertager and Magnussen (114) are also shown in these figures (ie 5.9 - 5.14) for comparison purposes. It can be seen that the agreement between the two sets of computions are good bearing in mind that these were obtained using two different codes.

5.4 CLOSURE

Two laminar flow cases, namely; flow through sudden rectangular expansion and flow in three-dimensional rectangular cavity with moving lid, have been simulated using the ESCEAT computer code. These relatively simple geometries were chosen for the purpose of initially verifying the code. In the version of the program used here, the SIMPLE algorith was employed to solve the FDE's formulated using the hybrid differencing scheme. The computation were compared with measurements, and with the prediction of previous workers. These comparisons show that the ESCEAT code simulation were in good agreement with the earlier results for both test cases. The present computations took about from 230-450 seconds on the DEC VAX/782 computer. This is a rather low cost if the expense of a comparable experimental study is taken into account.

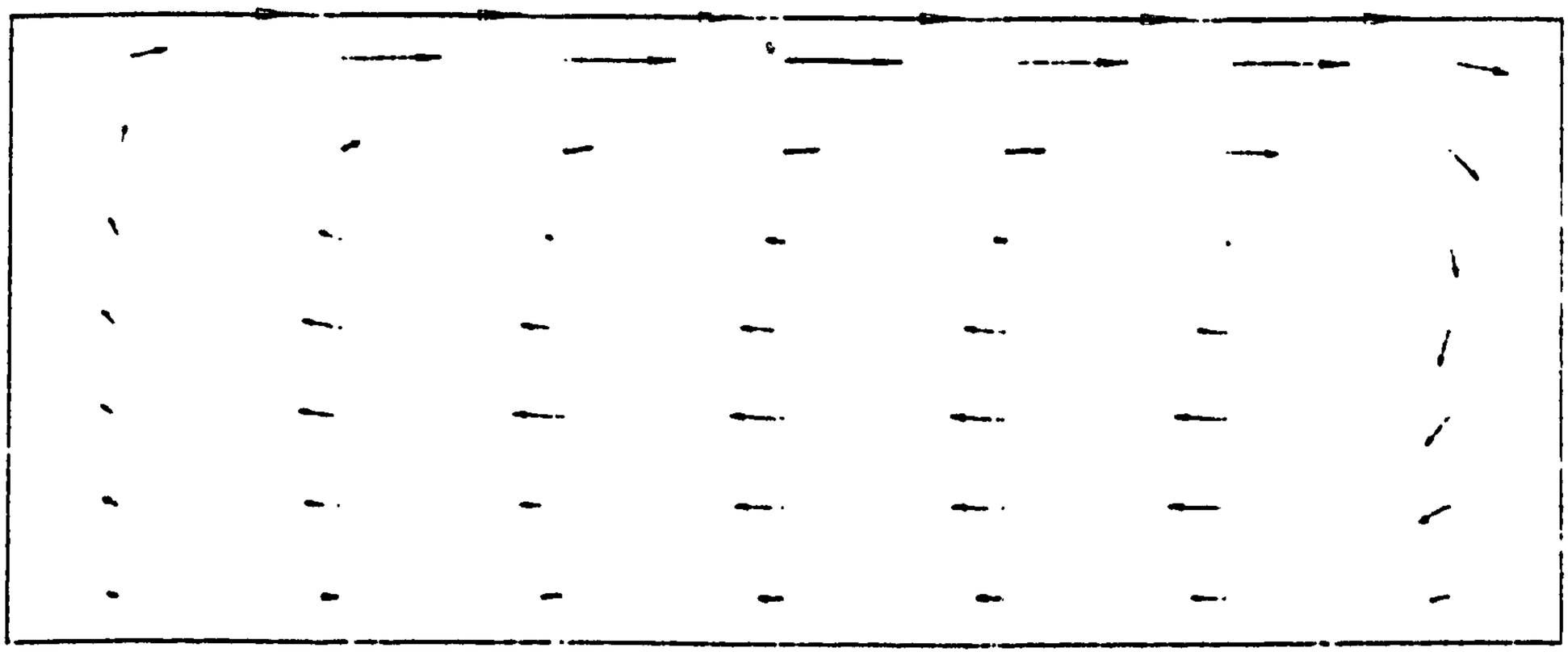

Fig. 5.8 : Velocity vectors and stream-wise velocity profiles in rectangular 3-D cavity with moving wall .

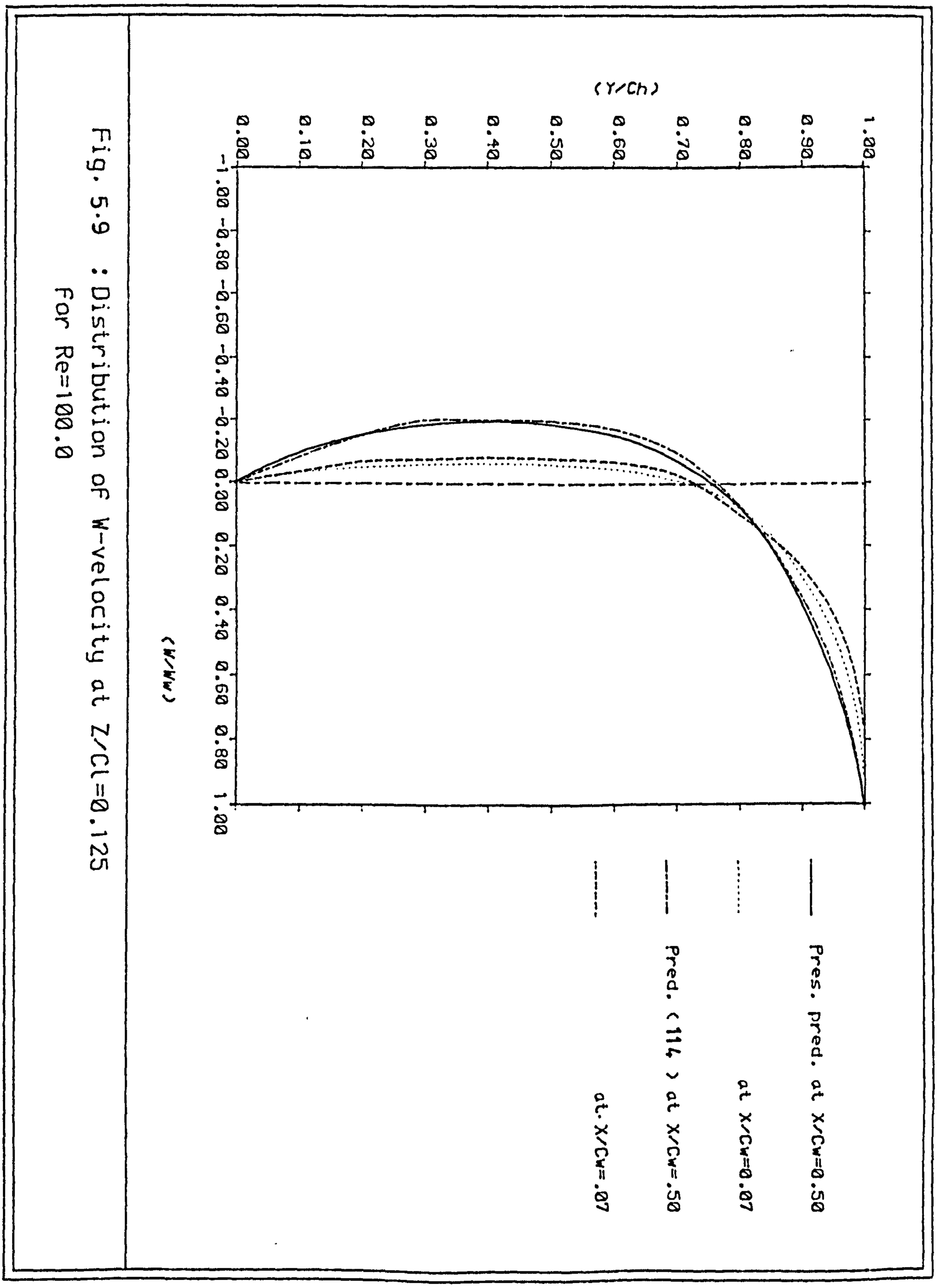

Fig. 5.9 : Distribution of W-velocity at Z/Cl=0.125
For Re=100.0

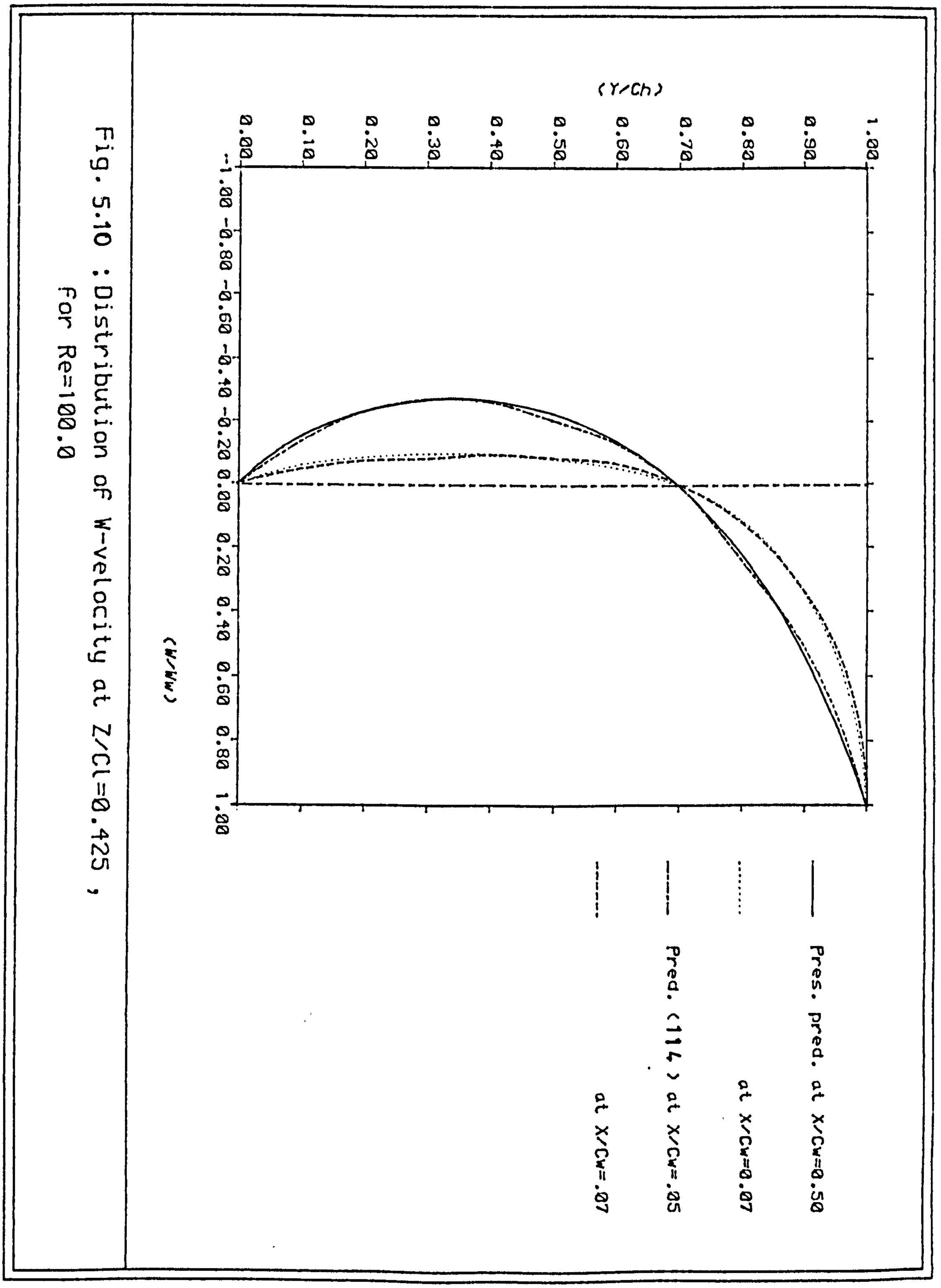

Fig. 5.10 : Distribution of W-velocity at Z/Cl=0.425 , For Re=100.0

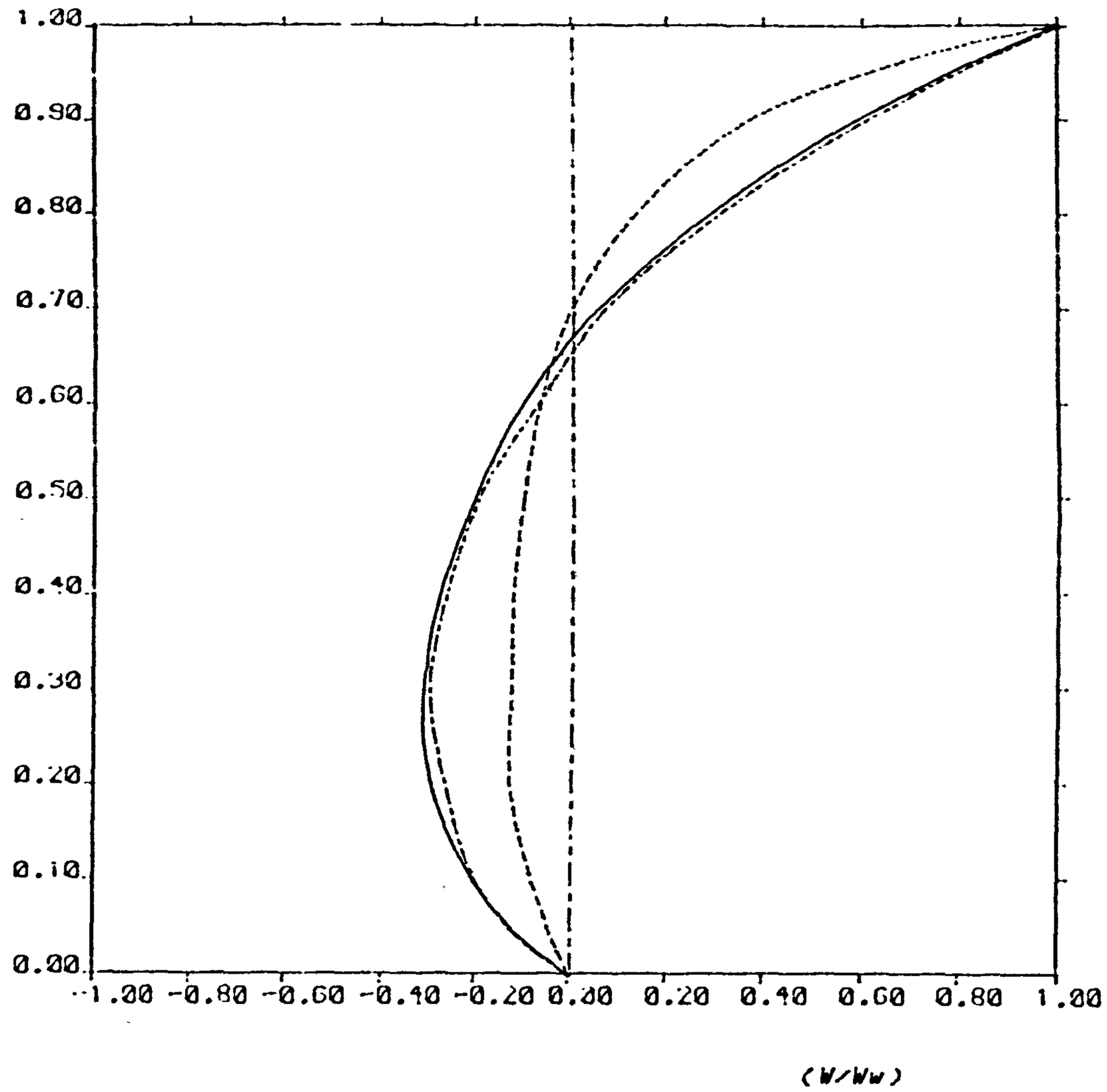

Fig. 5.11 : Distribution of W-velocity at Z/cl=0.725 ,
For Re=100.0

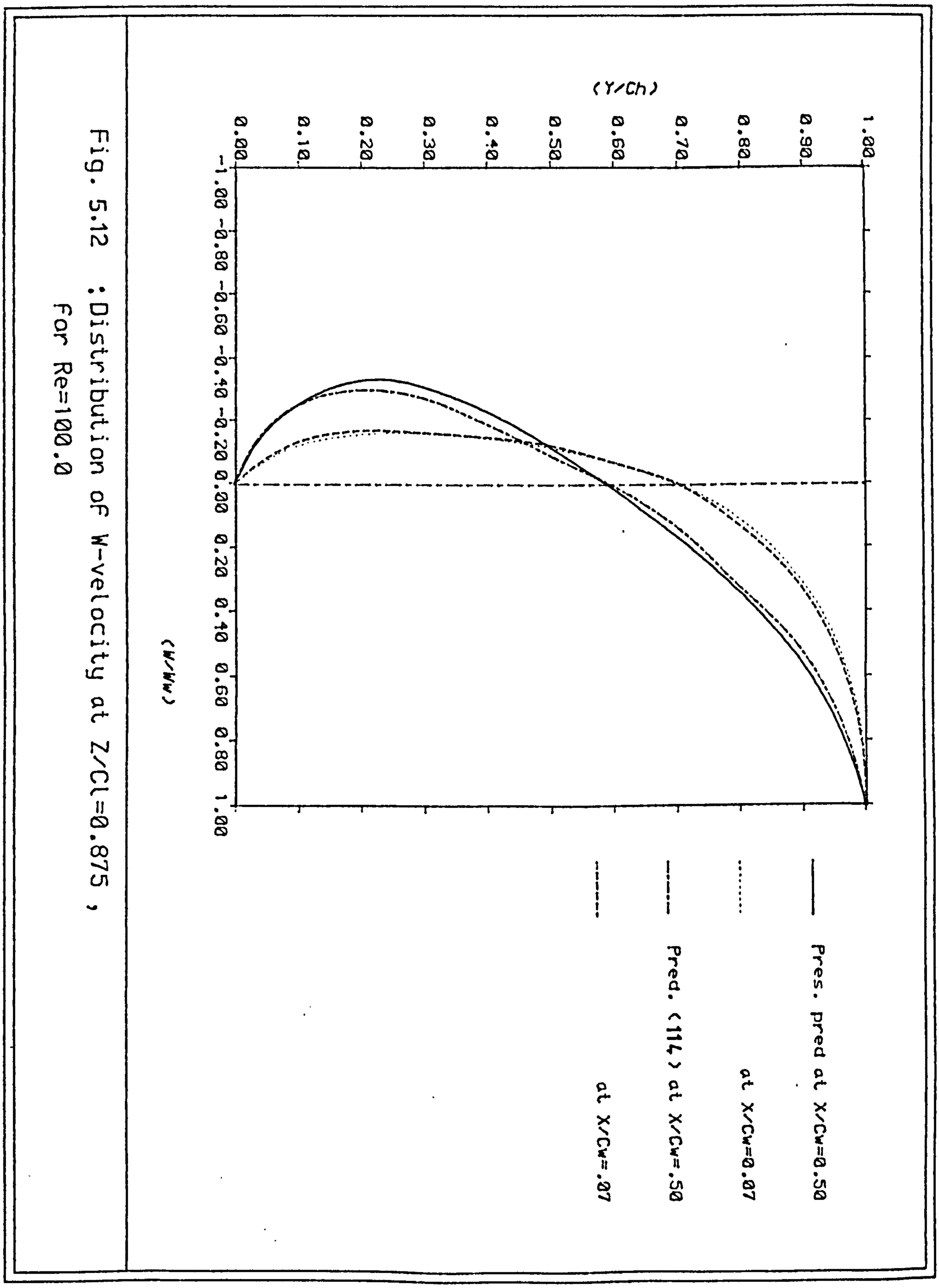

Fig. 5.12 : Distribution of W-velocity at Z/Cl=0.875 , For Re=100.0

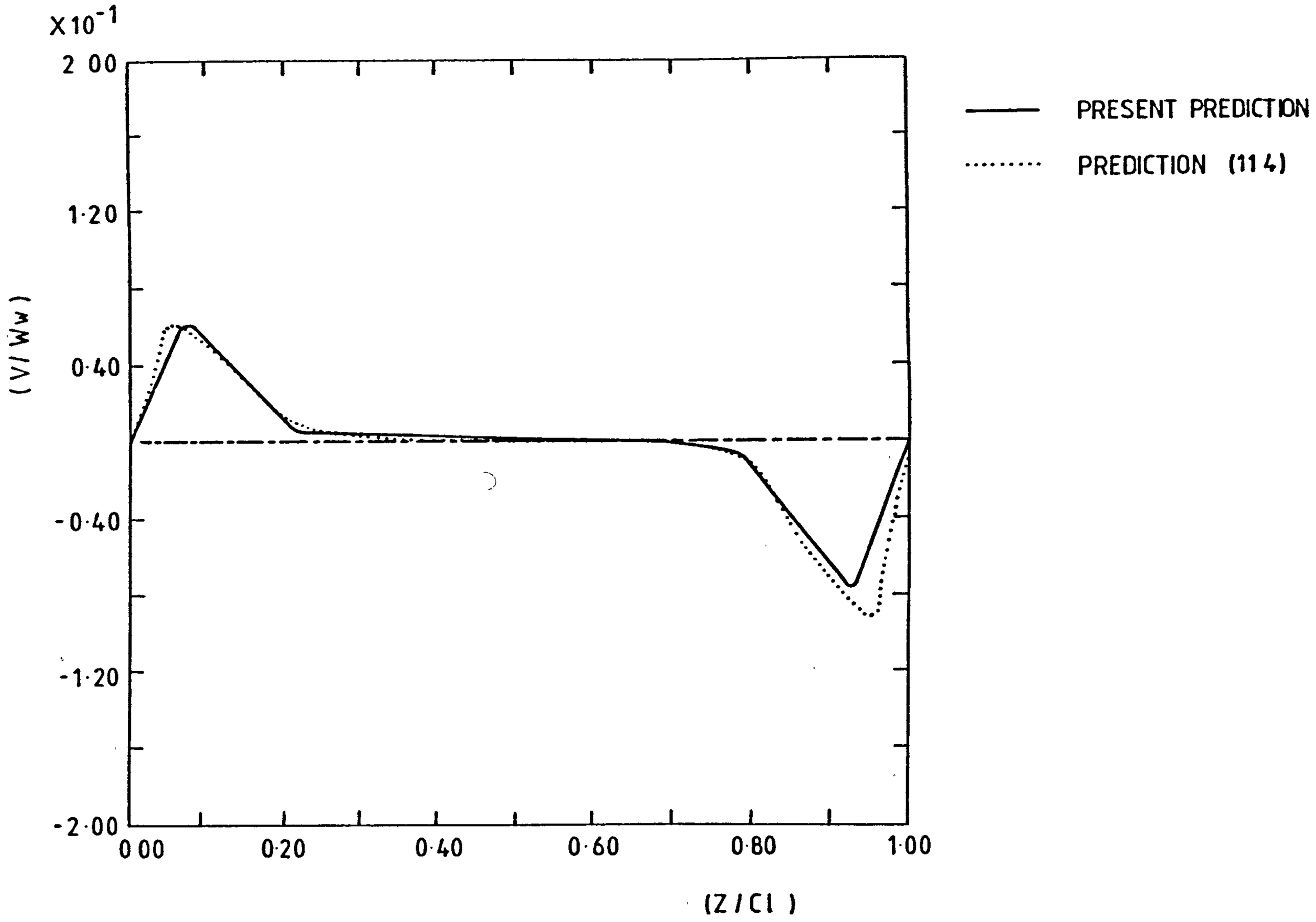

Figure 5.13 : Distribution of V-velocity at x/Cw=0.07 , Y/Ch=0.715 for Re=100.0 .

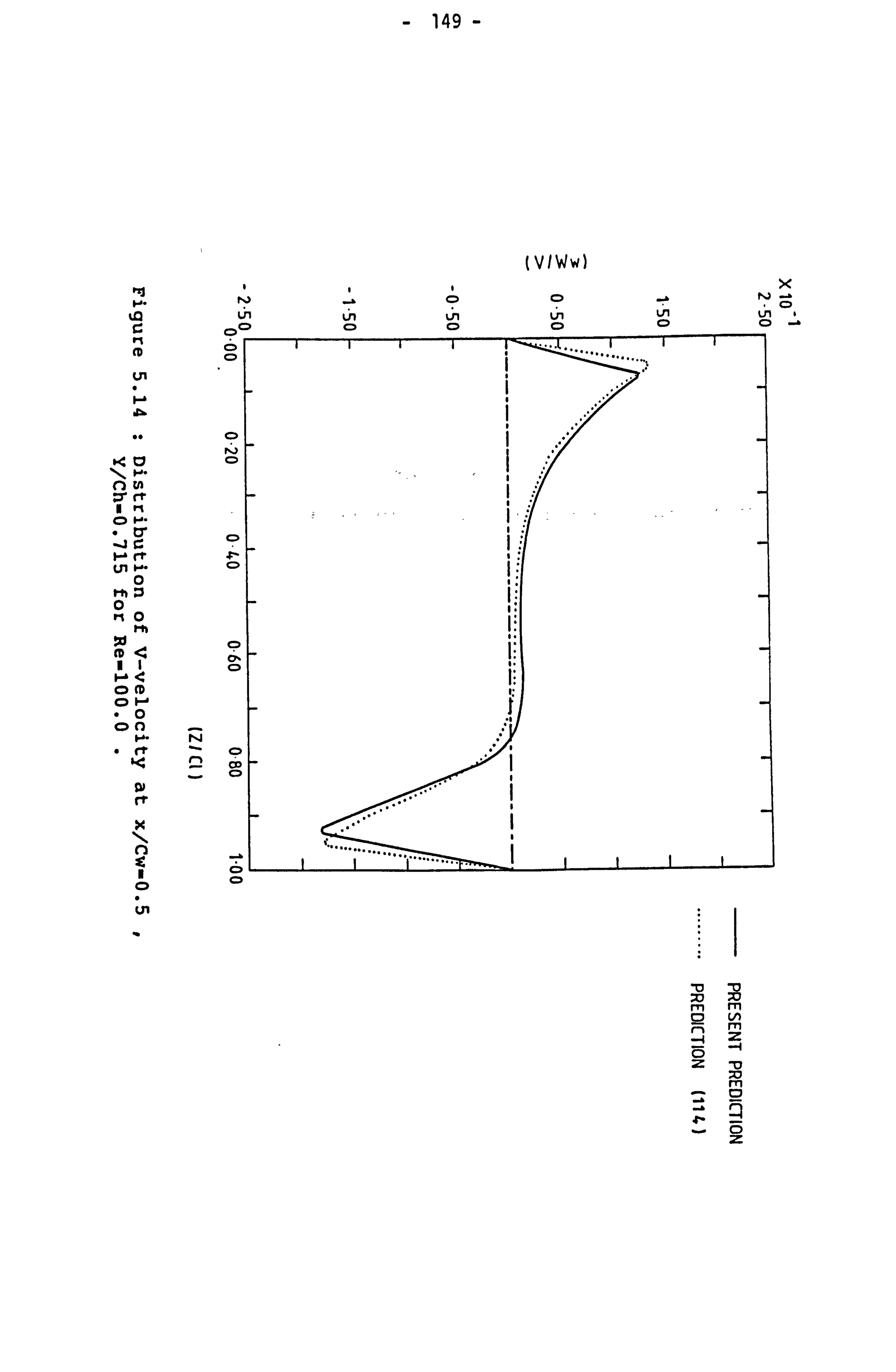

Figure 5.14 : Distribution of V-velocity at x/Cw=0.5 , Y/Ch=0.715 for Re=100.0 .

CHAPTER 6

COMPUTATION OF THREE-DIMENSIONAL TURBULENT DEVELOPING SQUARE DUCT FLOW

6.0 COMPUTATION OF THREE-DIMENSIONAL TURBULENT DEVELOPING SQUARE DUCT FLOW

6.1 INTRODUCTION

6.1.1 General Remarks

Turbulent flow in ducts of non-circular cross-section are often encountered in practical applications such as heat exchangers, nuclear reactor channels, turbomachinery, ventilation and air conditioning systems. A significant feature of the flow is the presence of 'secondary' motion in planes perpendicular to the streamwise directions; the primary motion. These are generated by Reynold stress gradients, and are typically about 2 per cent of the mean axial velocity (116-123). Although this value appears small, it exerts a strong influence on both overall and local properties of the flow (117-121, 123). In a square duct these secondary flow manifests itself in the form of two cells, centred about each of the corner bisectors (see figure 6.1). These grow laterally as the flow develops, and their influence is eventually felt across the entire duct cross-section (117,124). Thus, with a constant heat flux at the wall, these cells may induce hot spots in the corner region due to the convection of energy from the main stream and the generation of regions of locally low flow velocities (122,124). While the presence of the secondary motion can be readily detected, its accurate measurement is difficult (118-120). The problem lies in the fact that the secondary velocities are only a few per cent of the primary velocity, and therefore any distortion of the flow pattern caused by the measuring device can have a significant effect on the data obtained. For these reasons, there is an important need to be able to simulate the flow and thermal development within non-circular ducts.

6.1.2 Previous Work

There exists a considerable number of experimental investigations on turbulent flow in straight non-circular ducts.

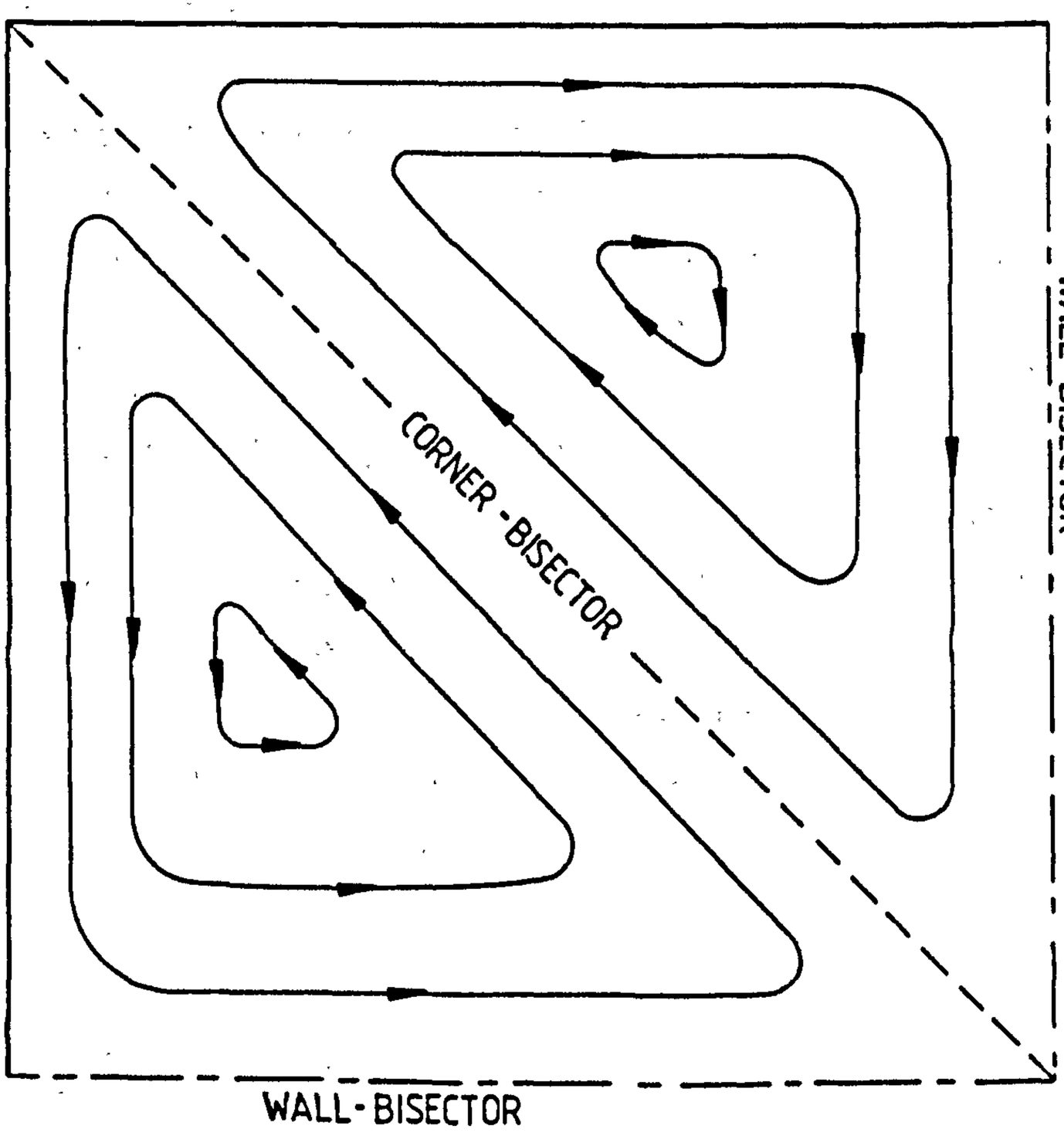

Figure 6.1 : Secondary flow within the quadrant of a square duct .

However, only a few of these investigations are concerned with the secondary motion, its origin and its effect on various global and local flow properties. The numerical analysis of the secondary motion, on the other hand, has been attempted by several workers. These attempts show some variation both in the manner in which the secondary flow, generated by the Reynolds stress gradients, is simulated, and in the way of solving the relevant differential equations. The experimental and numerical studies that have been concerned with secondary motion in straight square duct-flow are discussed below.

i) Experimental work

Measurements of developing turbulent flow in square ducts have been reported by Brundrett and Baines (116), Melling and Whitelaw (117), Launder and Ying (120), Po (121), Gessner and Emery (122) and Gessner et al (123). Brundrett and Baines (116) have presented a comprehensive description of turbulent flow in a square duct. They measured the six Reynolds stress components in the fully developed regions, and used these measurements to examine the magnitude of the terms in a streamwise vorticity equation. In a steady incompressible flow, the equation for the streamwise vorticity, Ω_1, has the form, neglecting gradients with respect to the streamwise direction (see Brundrett and Bains (116) and Demuren and Rodi (119)):

$$A_1 = A_2 - A_3 + A_4 \qquad 6.1$$

where

$$A_1 = \rho V \frac{\partial \Omega_1}{\partial y} + \rho U \frac{\partial \Omega_1}{\partial x} \quad ,$$

$$A_2 = \frac{\partial^2}{\partial y \partial x} (\overline{\rho u^2} - \overline{\rho v^2}) \quad ,$$

$$A_3 = \left(\frac{\partial^2}{\partial x^2} - \frac{\partial^2}{\partial y^2} \right) \overline{\rho v u} \quad ,$$

$$A_4 = \mu\left(\frac{\partial^2 \Omega_1}{\partial y^2} + \frac{\partial^2 \Omega_1}{\partial x^2}\right) ,$$

and $$\Omega_1 = \frac{\partial V}{\partial x} - \frac{\partial U}{\partial y}$$

The term A_1 represents the convection of streamwise vorticity by the mean motion. The terms A_2 and A_3 express the influence of the turbulent stress on the production or destruction of this vorticity, and A_4 the damping by the action of viscosity. However, in the evaluation of these terms Brundrett and Bains found that, of the two turbulent stress terms, only A_2 was significant and was balanced by the convection and viscous damping terms A_1 and A_4. They concluded that the streamwise vorticity is mainly produced via A_2 and convected via A_1 to regions where it is destroyed via A_4. Demuren and Rodi (119) reconsidered experimental work of several authors including that of Brundrett and Bains (116) and reached an alternative conclusion. They argued that the two production terms, the first (A_2) involving the difference between the turbulent normal stresses $(\overline{u^2} - \overline{v^2})$ and the second (A_3) involving the turbulent shear stress $\overline{vu}$, are of the same order of magnitude, but of opposite sign. They also suggested that these two terms are much larger than all the other terms, and that the difference $(A_2 - A_3)$ between them is of the same order of magnitude as the convection term. Demuren and Rodi (119) therefore, concluded that it is the <u>difference</u> between the two production terms that derive the secondary motion.

Melling and Whitelaw (117) obtained measurements of the developing flow in a square duct at various cross-sections up to about thirty-eight hydraulic diameters (D_h) downstream from the inlet plane, at which the flow is nearly fully-developed. The mean velocity and turbulent intensity distribution were measured within the developing flow region, while the secondary velocity components and five of the six corresponding Reynolds stresses were measured at the last, fully-developed flow measurement station. These results confirmed the qualitative features of turbulent flow through a square duct indicated by the earlier data of Brundrett and Bains (116). However, it has

also indicated some quantitative differences between the two sets of data. Melling and Whitelaw (117) argued that the disagreement reflected difficulties associated with making measurements in this flow configuration.

Various aspects of developing square duct-flow have been reported by Po (121), Gessner and Emery (122) and Gessner et al (123), all used the same experimental facililty at the University of Washington. These measurements were conducted at a number of cross-sections up to an axial location of about 84 hydraulic diameters from the inlet plane. The data indicated that the streamwise velocity at the centre-line (relative to the 'bulk', or cross-stream averaged velocity) increased monotonically up to about 40 D_h, where it reached a maximum. Its value decreased further downstream until about 70 D_h, beyond which it was practically constant. However, the Reynolds stresses measurements displayed a fall between the stations at 40 and 84 D_h of about 10-20%. Such a decrease, in the absence of any other measurements between or beyond these stations suggests that the flow may not have been quite fully-developed (119).

It is clear from the experimental studies discussed above that there are considerable difficulties in making measurements of the secondary flow properties in a square duct. The experimental uncertainty associated with this data is therefore even greater than normal. This must be borne in mind when comparisons are make below between the ESCEAT code predictions for developing square duct-flow and measurememts. The main cause of the generation of secondary motion is the Reynolds stress gradients (given by the terms A_2 and A_3 in equation 6.1). Consequently, both terms must be modelled accurately in order to simulate the secondary flow realistically.

ii) Numerical studies

Several attempts to analyse the nature of the turbulent flow in non-circular duct-flow have been reported. Due to the complex nature of the secondary motion in these flows, various ways of modelling the

Reynolds stresses have been tested. Some of these studies are described below.

Launder and Ying (52) were the first to model the secondary flow in straight non-circular duct. They simulated the Reynolds stresses ($\overline{u^2} - \overline{v^2}$) and $\overline{vu}$, by simplifying the transport equations for these stresses derived by Hanjalic and Launder (126) for their Reynolds stress turbulence model. Algebraic expressions for the secondary flow components were obtained from the full Reynolds stress transport equations by neglecting the convection and diffusion terms (assuming local equilibrium), and all the gradients of the secondary velocity components. The primary stress components such as $\overline{wv}$ and $\overline{wu}$ were obtained using the Prandtl-Kolmogorov eddy viscosity model (39). The turbulence quantities were obtained by solving a transport equation for turbulent kinetic energy and using a Buleev's algebraic formula (127) to determine the distribution of the length scale. The model (which will be denoted hereafter as the L-Y model for brevity) was then applied to calculate the fully-developed flow in a square duct, using the two-dimensional elliptic procedure of Gosman et al (36) in order to solve five coupled non-linear equations for the variables (W, V, U, K and T). This approach was used to compute the secondary flow profiles, their effect on the cross-stream distribution of primary velocity (W) and turbulent kinetic energy (K) as well as the heat-flux around the perimeter of the duct. Comparisons were made with the data of Brundrett and Baines (116) and Launder and Ying (52). Agreement between the predicted and measured secondary velocities for rough and smooth ducts was good except for the position nearest to the wall. Launder and Ying (52) argued that the discrepancy observed at the latter position could be attributed to measuring device (probe) interference. Computations of the cross-stream primary velocity (W) distribution displayed good agreement with measurements, although the cross-stream contours of K displayed a lower level than those from the data of Brundrett and Baines (116). Launder and Ying (52) made a comparison of wall shear stresses with and without the secondary flow and from this they conclude that the secondary motion is responsible for increasing the

friction factor by about 10 per cent. However, the computed friction factors were found to be lower than the measurement, and Launder and Ying attributed to the use of the Buleeve's formula in calculating the length scale distribution. The prediction of the heat flux around the periphery of the duct showed good agreement with the data (116) but those of stanton number showed lower levels than measurement and it is attributed again to Buleeve's formula.

Emery et al (124) and Gessner and Emery (128) have applied a modified version of the L-Y model to calculate the developing flow in square ducts, with and without heat transfer respectively. The main alteration involved the introduction of a three-dimensional algebraic length-scale distribution. The computations were made using an explicit (Dufort-Frankel) differencing scheme for solving the axial momentum equation, and a direct matrix solver for the cross-stream direction. The computed local wall shear stress profile displayed relatively good agreement with the measurement at Reynolds number (Re) > 50,000 provided that, one of the empirical constants (the so-called anisotropy coefficient (128)) in the model was given a value approximately 20 per cent less than its counterpart in the L-Y model. However it was found, that such values led to the under-estimate of the local wall shear stress in the vicinity of the wall-bisector for $Re \lesssim 50,000$. A slight increase in this value led to an agreement, which was comparable to that obtained by Tatchell (129) using the 'standard' K-ε model. The accuracy of Gessner and Emery predictions of the fully-developed flow values for the friction factor and the axial variation of the primary velocity (W) were found to be Reynolds number dependent. Agreement with the experiment was found to be reasonably good at high values of Re ($\simeq$ 250,000), while a discrepancy was observed at lower values. This was attributed to the neglect of the diffusion and convection transport effects in what is effectively an algebraic stress model, and to the length scale formula adopted. The latter was 'fine tuned' using data obtained at high Re conditions. Gessner and Emery (128) found that their computed secondary flow profiles were sensitive to grid spacing in the cross-flow directions, and to the axial step length. The level of agreement of such profiles

with measurements in the corner-bisector was found to be comparable to predictions with the full Reynold stress model. However, on the wall-bisector the computations were well below the measured data, especially at axial location of $z = 40\, D_h$. However, because their model neglected the near-wall pressure strain effect, the observed anisotropy between $\overline{v^2}$ and $\overline{u^2}$ was not well predicted.

Noat and Rodi (130) developed a turbulence model by simplifying the more recent Reynolds stress model of Launder et al (41). This led to an algebraic stress model in which only the transport equations for K and ε are required to be solved. The simplified model was obtained by neglecting the diffusion and convection terms in the full Reynolds stress equation as in the L-Y model, while the shear stresses $\overline{wv}$ and $\overline{wu}$ in the longitudinal (z-direction) momentum equation were modelled via an eddy viscosity. However, the effect of the secondary velocity gradients, which were neglected in the L-Y model, was retained by Noat and Rodi via the eddy viscosity part in the algebraic stress relations. They found that the neglect of these terms led to unbounded growth of the secondary motion, and hence to numerical instability. The resulting set of equations were solved using a modified version of the three-dimensional parabolic finite-domaine procedure of Patankar and Spalding (68). The model (which will be denoted hearafter as the N-R model for brevity) was used to calculate three-dimensional open and closed channel flow, and three-dimensional developed flow in a square duct. In the latter case, their computation of the primary velocity contours showed good agreement with the measurement of Launder and Ying (120), although the bulging of these contours toward the corner appeared to be rather over-predicted. the model was also found to over-predict the secondary motion near the corner and to under-predict it near the symmetry plane. It was able to simulate the wall shear stress in reasonable agreement with experiments.

Demuren and Rodi (119) have refined the N-R model by calculating the Reynolds stresses $\overline{v^2}$, $\overline{u^2}$ and $\overline{vu}$ via algebraic expressions, rather than using the eddy viscosity approximation originally employed by

Noat and Rodi (130). Several variants of the model were examined, including an algebraic stress treatment of the primary shear stresses $\overline{wv}$ and $\overline{wu}$, and alternative wall corrections in the pressure-strain model. The variants of the model (will be denoted hearafter as the D-R model for brevity) together with the N-R model, were applied to developing and fully-developed flow in a square duct at various Reynolds numbers. A forward-marching numerical procedure for three-dimensional parabolic flows developed by Patankar and Spalding (68) was used to solve the resulting set of equations. The computations were compared with several experimental data sets, and both models were found to satisfactorily predict the flow development of the primary velocity along the duct axis. The Reynolds number dependence of the solutions was again mainfested in the streamwise shifting of the maximum value of the centreline velocity, in good agreement with the experiment. The distributions of the primary velocity (W) along the wall-and corner-bisectors were predicted very well by both models, except in the near-wall region where small differences were noticed between the computations of the two models. The secondary velocities along the wall bisector were under-predicted by their model at measurement stations corresponding to z = 40 and 84 D_h. In contrast, the N-R model over-predicted these velocities at the first station, but produced about the right level at the second. In the corner-bisector, the N-R model over-predicted the secondary velocity, while the D-R model under-predicted them. The predictions of the turbulence quantities, such as cross-stream kinetic energy and shear stress profiles, along the wall-bisector showed good agreement with measurements with both turbulence closures. However, some discrepancies were observed in the corner-bisector, especially near the wall region. Nevertheless, Demuren and Rodi (119) have produced the correct level for the turbulent kinetic energy in the vicinity of the wall (in the fully-developed part of the flow), by employing the variant of the model that calculates the primary shear stresses ($\overline{wv}$ and $\overline{wu}$) via algebraic expression rather than the eddy viscosity approximation. They demonstrated that the magnitude of K in the vicinity of the wall is thereby improved. In effect this procedure is equivalent to altering the value of the eddy viscosity coefficient,

C_D, usually taken as 0.09 in the 'standard' K-ε turbulence model. The use of the latter value, effectively ignores the damping of the normal fluctuations due to the presence of the wall (119).

Recently, Nakayama et al (131) reported numerical study for three-dimensional developing turbulent flow in a square duct. They used the standard K-ε turbulence model and an extended version of the L-Y model. The extension included the retention of the axial derivatives for the stress components associated with the primary flow velocity functions. They solved the resulting set of equations using a fully elliptic numerical scheme, based on the pressure correction procedure of Patankar and Spalding (68). They compared their computations with the experimental data of Melling and Whitelaw (117) and concluded that the L-Y model yielded realistic predictions of the mean flow development. However, they observed that it fails to provide reasonable estimations of the cross-planar stress components ($\overline{v^2}$, $\overline{u^2}$). They also suggested that the value of the anisotropy coefficient that was recommended by Launder and Ying (52) would lead to an under-estimation of ($\overline{u^2} - \overline{v^2}$) by about 10 per cent.

The above review of numerical studies of developing turbulent flow in square ducts indicated that there are two main approaches to the simulation of the secondary motion in such geometries. These are full Reynolds stress models, such as those of Launder and Hanjalic (126) and Launder et al (41), and algebraic stress models developed originally by Launder and Ying (52) and Noat and Rodi (130). The main differences between the latter two models are:

i) The terms involving secondary velocity gradients in the stresses $\overline{v^2}$, $\overline{u^2}$ and $\overline{vu}$ were neglected in the L-Y model. In the N-R model these terms were approximated by products of an isotropic eddy viscosity and the corresponding secondary velocity gradients.

ii) The N-R model accounts for the near-wall effects on the turbulence quantities by a special wall proximity correction to the

pressure strain correlation. This effect was neglected in the L-Y model.

The N-R model, including its variants was found to simulate reasonably the difference between the normal stresses $\overline{u^2} - \overline{v^2}$, while the L-Y model and its variants produce much smaller values than those observed experimentally. Furthermore, the N-R model was found to reproduce reasonably well the correct dependency of the flow on the Reynolds number whereas the anisotroy constant in the L-Y model need to be tuned to produce the right behaviour over the full range of Reynolds numbers.

6.1.3 The Objectives of the Present Study

The previous sections indicated the industrial importance of turbulent flow in a square duct, and the difficulty associated with measurement of its secondary flow properties. It was also noted that several earlier attempts have been made at the numerical simulation of this flow. Nevertheless, it remains a good test case for verifying the fully-elliptic three-dimensional calculation procedure described in Chapter 5 (the ESCEAT code), which may then be used to compute more complex turbulent flows. In any case, the square duct-flow represents a flow situation that is commonly found in ventilation and air-conditioning plants. The main objectives of the present study were therefore:

i) To select one of the variants of the algebraic stress models in order to simulate the secondary motion found in duct-flows, and extend it to fully-elliptic form.

ii) To present some special features of the calculation procedure for solving the relevant equations in the duct-flow case.

iii) To compare the present computations with the avaialble experimental data and the results of previous numerical studies.

6.2 ALGEBRAIC STRESS TURBULENCE MODEL

6.2.1 The Choice of the Model

In the literature review of the previous section it was suggested that there are currently two simplified Reynolds stress models (usually termed algebraic stress models) that are capable of providing a reasonable simulation of the turbulence-induced, secondary motion in square ducts; the Launder and Ying (L-Y) and Naot and Rodi (N-R) closure approximations. The L-Y, and its variants, was found to produce roughly the correct behaviour of the secondary motion. However, Demuren and Rodi (119) noted that this was simply a fortuitous occurence, caused by the neglect of the secondary gradients. The latter gradients contribute significantly to the generation of the secondary shear stress component, $\overline{vu}$. Furthermore, Demuren and Rodi (119) argued that the sink term, A_3, in the vorticity equation (6.1) will be reduced significantly due to the neglect of the secondary gradients. As the secondary motion is controlled by a balance between A_3 and A_2 terms, the deriving term A_2 must be reduced to an unrealistically small value. They therefore concluded that the L-Y model produces the correct secondary motion, but for the wrong reasons!

The N-R model on the other hand does not suffer from the above shortcomings, since it retained the evaluation of these gradients. However, the D-R model which is an extension to the N-R model was treated the secondary velocity gradients in the same way as the primary gradients ones, which lead to more calculations and hence more complicity and computation. Furthermore, the predictions of the two models were found to be approximately identical. Therefore the choice was directed towards the N-R model in the present study.

6.2.2 Reynolds Stress Terms

The terms associated with Reynolds stresses in the momentum and enthalpy conservation equations may be written in the following manners (131 - 132):

$$S_u = \frac{\partial p}{\partial x} + \rho\frac{\partial}{\partial x}(-\overline{u^2}) + \rho\frac{\partial}{\partial y}(-\overline{vu}) + \rho\frac{\partial}{\partial z}(-\overline{wu}) \qquad 6.2$$

$$S_v = \frac{\partial p}{\partial y} + \rho\frac{\partial}{\partial x}(-\overline{vu}) + \rho\frac{\partial}{\partial y}(-\overline{v^2}) + \rho\frac{\partial}{\partial z}(-\overline{wv}) \qquad 6.3$$

$$S_w = \frac{\partial p}{\partial z} + \rho\frac{\partial}{\partial x}(-\overline{wu}) + \rho\frac{\partial}{\partial y}(-\overline{wv}) + \rho\frac{\partial}{\partial z}(-\overline{w^2}) \qquad 6.4$$

$$S_h = \rho\frac{\partial}{\partial x}(-\overline{uh}) + \rho\frac{\partial}{\partial y}(-\overline{vh}) + \rho\frac{\partial}{\partial z}(-\overline{wh}) \qquad 6.5$$

The streamwise (z-direction) derivatives have been retained for the stress components associated with the primary flow velocity fluctuations. The inclusion of these terms is possible only when a fully elliptic calculation procedure, such as the present one, is employed. The algebraic expressions for the stress components that appear in equations (6.2 - 6.4) were employed in reduced, parabolic form by Naot and Rodi (N-R model) and Demuren and Rodi (119). In the present study, these expressions were used in their fully elliptic form, given in Appendix B. It was convenient for the purpose of the present solution procedure to incorporate the terms that appear in equations (6.2 - 6.5) into the relevant transport equations through their respective source terms. The associated turbulence quantities were calculated via eddy viscosities determined using the 'standard' K-ε model of turbulence, as was discussed in chapters two and three. However, the model constants were given the following values, following the practice of Naot and Rodi (130) and Demuren and Rodi (119).

C_1	C_2	C_ϵ	C_K
1.44	1.93	1.225	1.225

6.3 THE CALCULATION PROCEDURE

The equations governing developing square duct-flow in their partial differential and finite-domain forms were detailed in chapters 2 and 3. These relevant to the Reynolds stress components are also given in section 2 of the present chapter. The resulting set of equations for momentum, turbulence quantities and enthalpy have been solved for a quadrant of the square duct (see figure 6.1) using the fully elliptic procedure (the ESCEAT code) discussed in chapter 5. An upwind differencing scheme was adopted for the primary velocity components (W) and the other scalar variables, while a power-law one has been employed for the cross-stream velocity components in order to obtain a better approximation for these small quantities. The main task of this section is to present the duct-flow boundary conditions, the solution procedure and an assessment of the grid independence of the solutions.

6.3.1 Boundary Conditions

The boundary conditions adopted for the duct geometry were as follows:

At inlet: A uniform distribution of all the variables was prescribed. Here the secondary velocity components (U and V) were set to zero, and the turbulence quantities (K and ε) were given such small values that the eddy viscosity (ν_t) was about 15 times that of the molecular viscosity (ν_l).

At solid wall: The velocity normal to the wall was set equal to zero at the wall; otherwise, the wall function approach (see section 2.5.2) was adopted at the node nearest to the wall. The boundary conditions for K,ε and H were also specified values at this node that are compatible with the logarithmic 'law of the wall'.

At symmetry plane: The velocity components normal to the symmetry plane was set equal to zero. In the case of all other quantities, their gradients normal to this plane were set equal to zero, while the appropriate coeffient (the six A's) were also set to zero in order to break the symmetry link.

At outlet (exist) plane: The variable gradients normal to this plane were set equal to zero.

These boundary conditions are similar to those adopted by Demuren and Rodi (119), who employed a three-dimensional parabolic solution procedure. Except that for the present, elliptic procedure, the additional boundary condition at the outlet plane was required.

Implementation of the wall functions was achieved via the transport equation source terms for each variable at the node nearest to the wall, in a manner similar to that described in section (3.3.4).

6.3.2 The Solution Procedure

The developing duct-flow computations were performed by replacing the three sweep procedure by one involving two sweeps applied together with an overall continuity correction (see section 3.4.4). This modification was found to be more suitable for the present flow configuration, since it automatically ensures that continuity is satisfied for the stream-wise velocity component at each plane. This is applied in addition to the line-by-line continuity correction provided by the use of the pressure correction-equation. The overall continuity correction was incorporated into the ESCEAT code as an option through the choice of the sweep number, and

therefore it does not alter the solution sequence itself. It was implemented in a similar manner to that adopted in the two-dimensional, CHAMPION code of Pun and Spalding (34). When employing the procedure, the lines to be solved should be in the cross-stream (X,Y) directions. The application of the overall continuity correction procedure, to these lines involves the following steps:

a) After the calculation of the star velocities (U_j^*, see equations 3.31), the overall continuity adjustment procedure is employed to correct the stream-wise velocity component (W) in the current plane, and to update the pressure (p) at all the downstream planes.

b) Following the solution of the pressure correction equation (p'), but prior to the adjustment of the velocity by (p'), an overall continuity adjustment is again used to update the W components at the plane upstream from the current one and p for all the planes downstream from this plane.

c) After the adjustment of the star velocity by (p'), the overall continuity correction is performed for a third time in the same manner as used in step (a).

6.3.3 Assessment of the Grid Independence of the Solutions

Computations have been performed with three different non-uniform (expanding) nodal networks consisting of 9x9x30, 11x11x30 and 11x11x35 nodes in order to find the optimum computational grid for the present flow geometry. The computed development of the axial velocity along the duct presented in figure 6.2 for each of the nodal networks. It can be seen from these distributions that the effect of grid refinement in the cross-stream (X-Y) plane (from 9x9 to 11x11 nodes) is quite significant. However, the axial velocity distribution can be seen to be less sensitive to grid refinement in the stream-wise direction (from 30 to 35 nodes). In view of this, an 11 x 11 x 30 nodal network was adopted for the remaining computations reported in

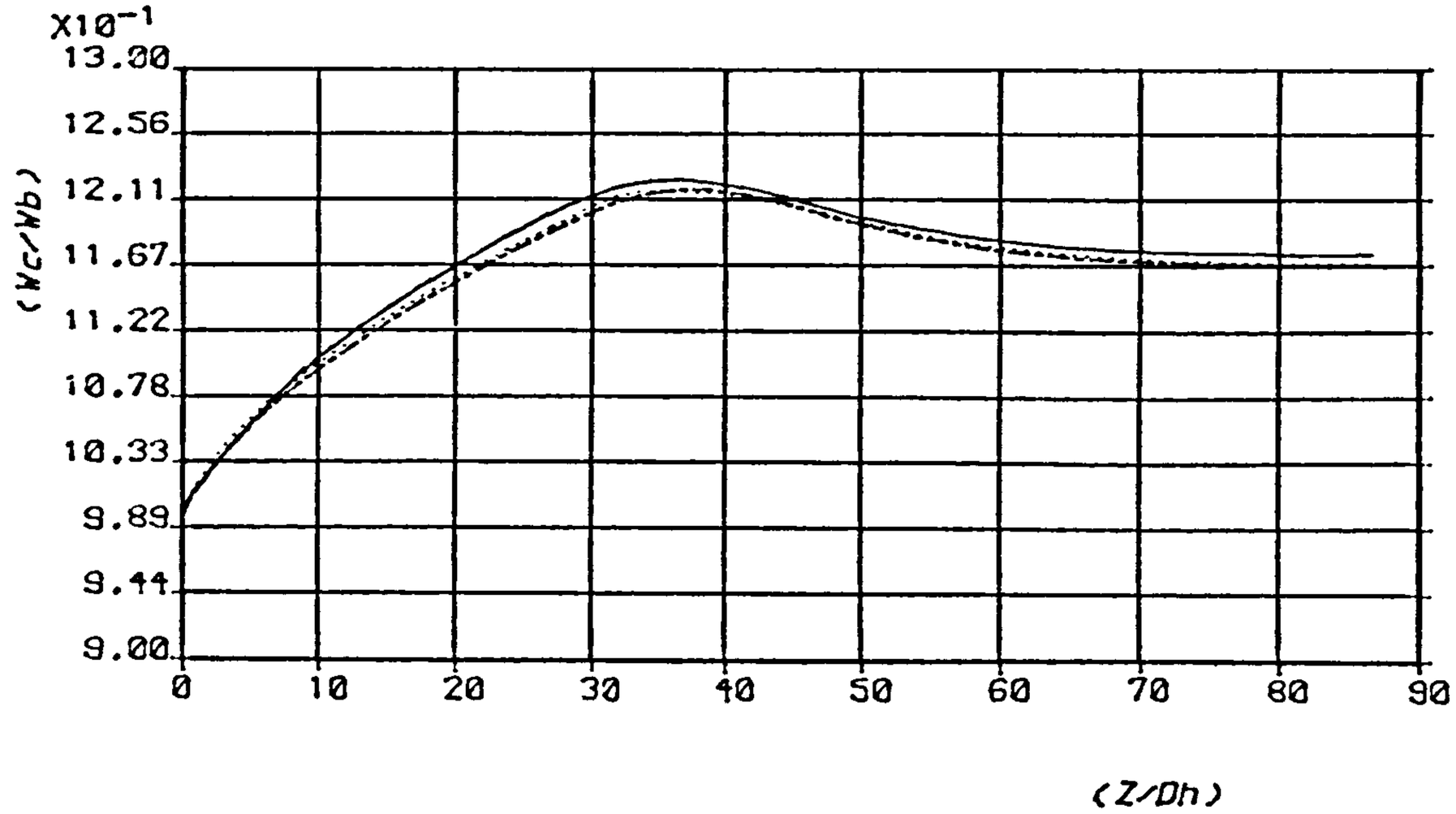

Fig. 6.2 :Development of center-line velocity along a square duct at Reynold's No=250000

this chapter. This coarse grid was chosen primarily for reasons of economy, but it will be shown below to produce most of the important features of developing duct-flow quite satisfactorily.

The rate of convergence of the solution procedure was found to slow with an increase in the number of cross-flow nodes. However, for the standard 11x11x30 grid, the time required to obtain a converged solution was about 53 minutes on a DEC VAX 11/782 computer, corresponding to 125 iterations.

6.4 COMPARISON OF PREDICTIONS AND EXPERIMENTS

In order to justify the present computations, comparisons have been made with several sets of experimental data and numerical predictions at varying Reynolds numbers. These comparisons include the axial (or primary) velocity variation along the duct, cross-stream profiles of the primary velocity and the turbulence kinetic energy distribution along the wall and corner bisectors at different axial stations. Computations of the cross flow velocity vectors at different axial stations have also been obtained.

6.4.1 Axial Flow Development

The computed development of the centre-line axial velocity component is shown in figure 6.3, where it is compared with the experimental data of Gessner and Emery (128) and the numerical predictions of Naot and Rodi (130) and Demuren and Rodi (119), all for a Reynolds number, Re = 250,000. This figure clearly shows a peak around $z = 40\ D_h$, which is obviously associated with the merging of the developing wall boundary layers at the duct core. The present calculations display good agreement with the previous studies, particularly the experimental one. A further comparison is shown in figure 6.4 with experimental data of Melling and Whitelaw (117) for Re = 42,000. Also shown in this figure are the numerical predictions of Demuren and Rodi (119) and Nakayama et al (131), both for Re = 50,000. Again the results agree well with the experiments, both

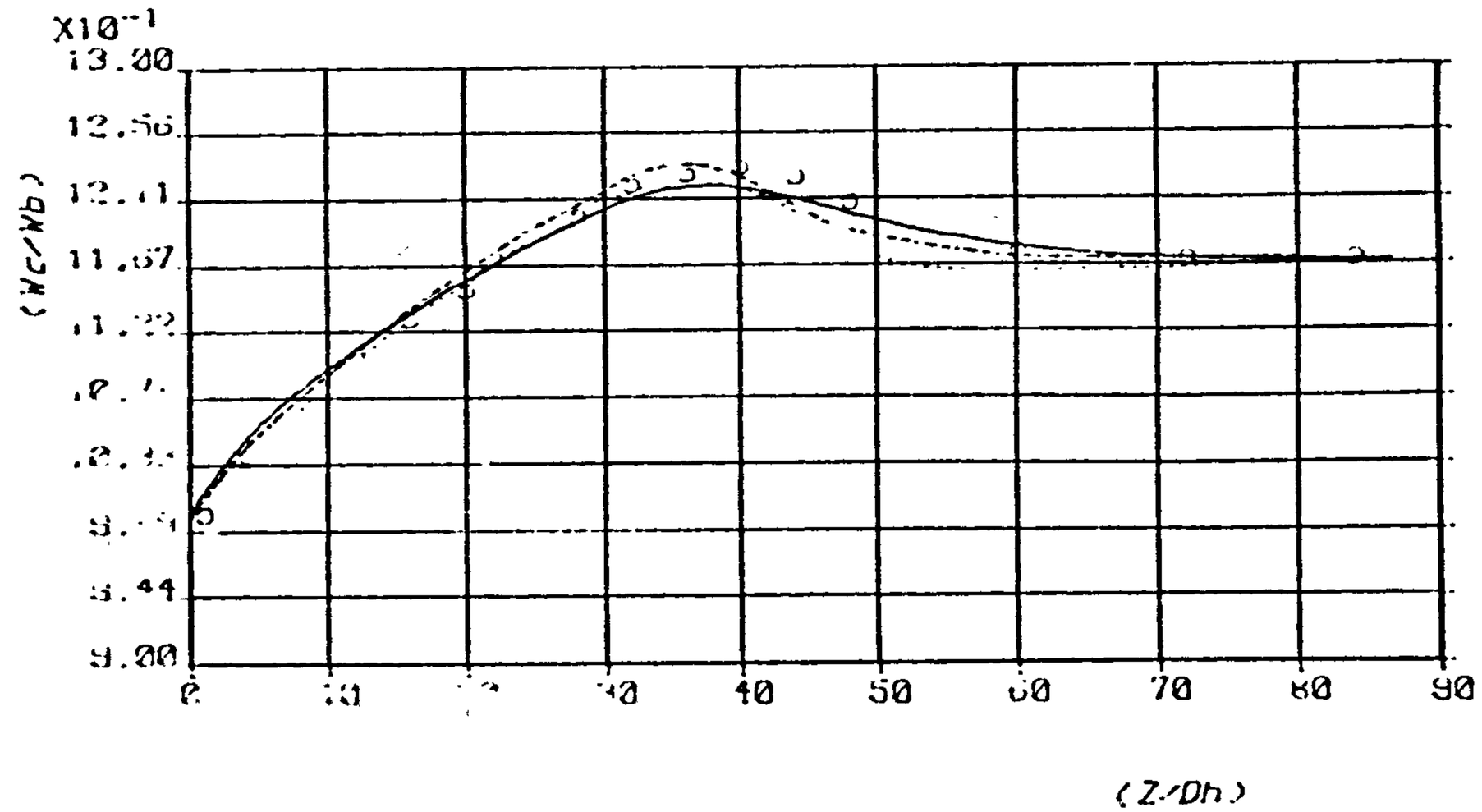

——— Present prediction

. . . . Pred. (128)

— — — Pred. (119)

o o Experimental data (128)

Fig.6.3 : Development of center-line velocity along a square duct at Reynold s No=250000

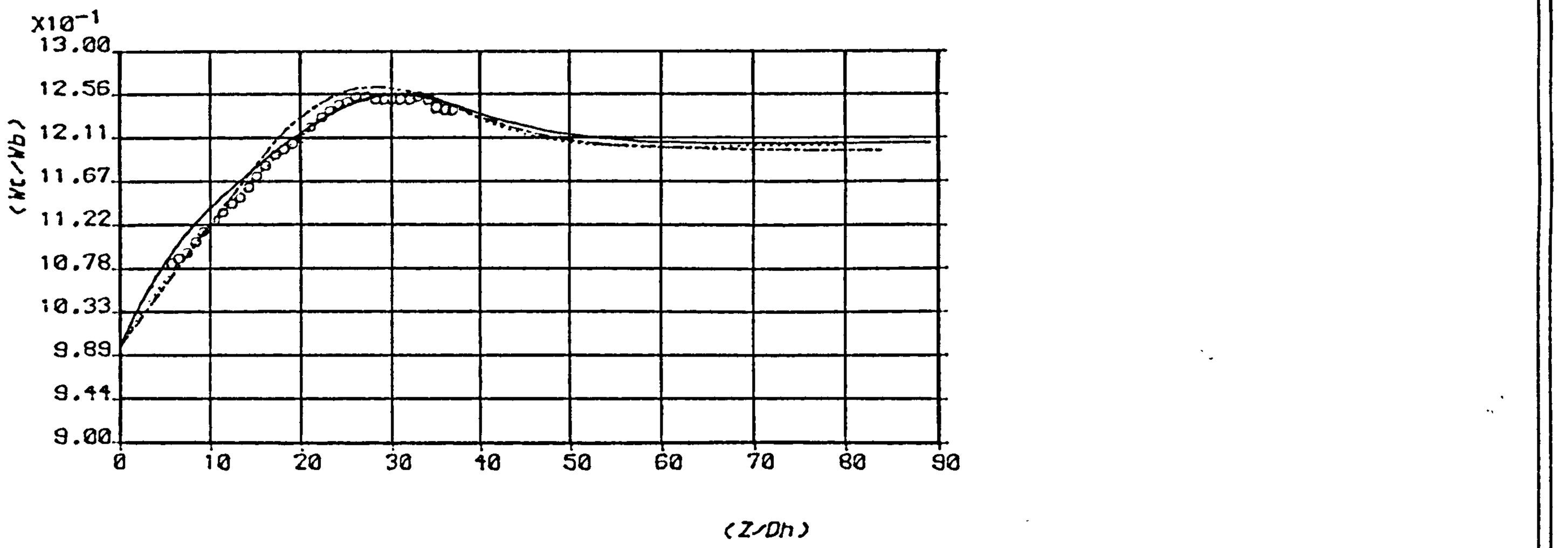

Fig. 6.4 : Development of center-line velocity along a square duct

in the developing flow region and in the shear layer interaction region where local peaking is observed at about $z \simeq 25\ D_h$.

Cross-stream axial velocity profiles computed using the present procedure are displayed in figures 6.5 and 6.6 for two axial stations ($z = 40\ D_h$ and $84\ D_h$). Here comparisons are shown with the measured data of Po (121) and the numerical prediction of Dumeren and Rodi (119) across both the wall and corner bisectors. The present computations of the wall bisector distribution (figure 6.5) are in good agreement with the previous studies, although those along the corner bisector (figure 6.6) lie slightly below the latter within the boundary layer region at both axial stations. A similar behaviour was observed by Gessner and Emery (128) when they compared a predicted profile obtained using the L-Y model and a 10 x 10 grid in the cross-flow plane.

6.4.2 The Turbulence Energy Distributions along Wall and Corner Bisectors

The present computations of the cross-stream turbulence kinetic energy (K) distributions along the wall and corner bisectors are shown in figures 6.7 and 6.8. comparisons are also displayed in these figures with the data of Po (121) and numerical predictions of Naot and Rodi (130). The wall bisector distributions are in fairly good agreement over the centre (or core) region of the duct, but there are noticeable discrepancies near the wall. Both the present computations and those of Naot and Rodi yield values of K near the wall that are rather low. Similar discrepancies were also noted by Demuren and Rodi (119). They suggested that the value of the eddy viscosity constant $C_D \simeq 0.09$ (and is adopted here), which is normally employed with the wall function approach might be the main cause of these discrepancies. This implies that no account is taken of the damping of the normal fluctuations and the associated reduction in momentum transfer in the immediate vicinity of the wall. They showed that the use of an algebraic expression to calculate the primary stresses ($\overline{wv}$ and $\overline{wu}$) instead of the isotropic eddy viscosity hypothesis gave the correct

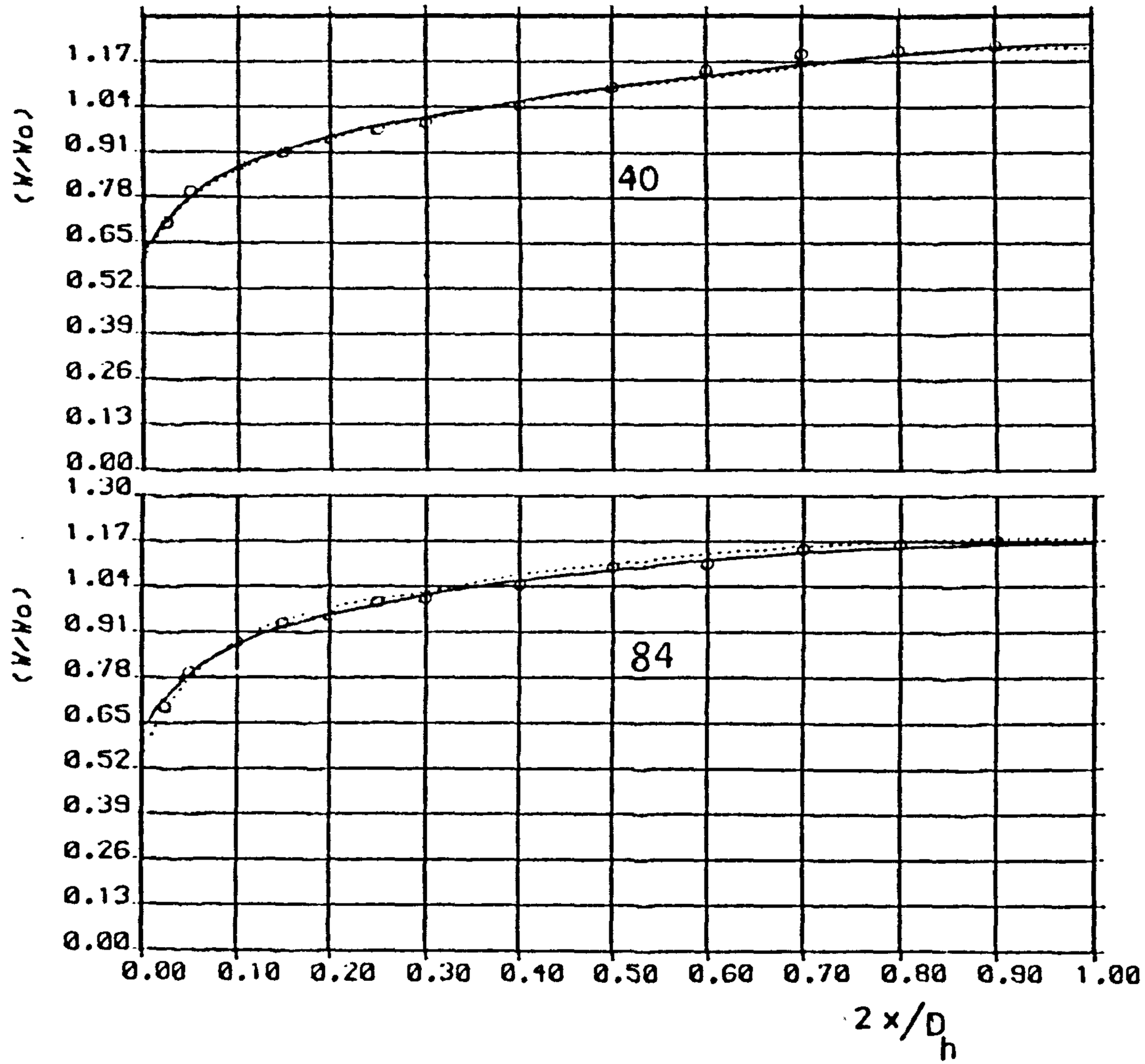

Fig. 6.5 : Stream-wise velocity profile along wall-bisector
Re=2.5x10^4 ,at Z/D_h =40.0 and 84.0 .

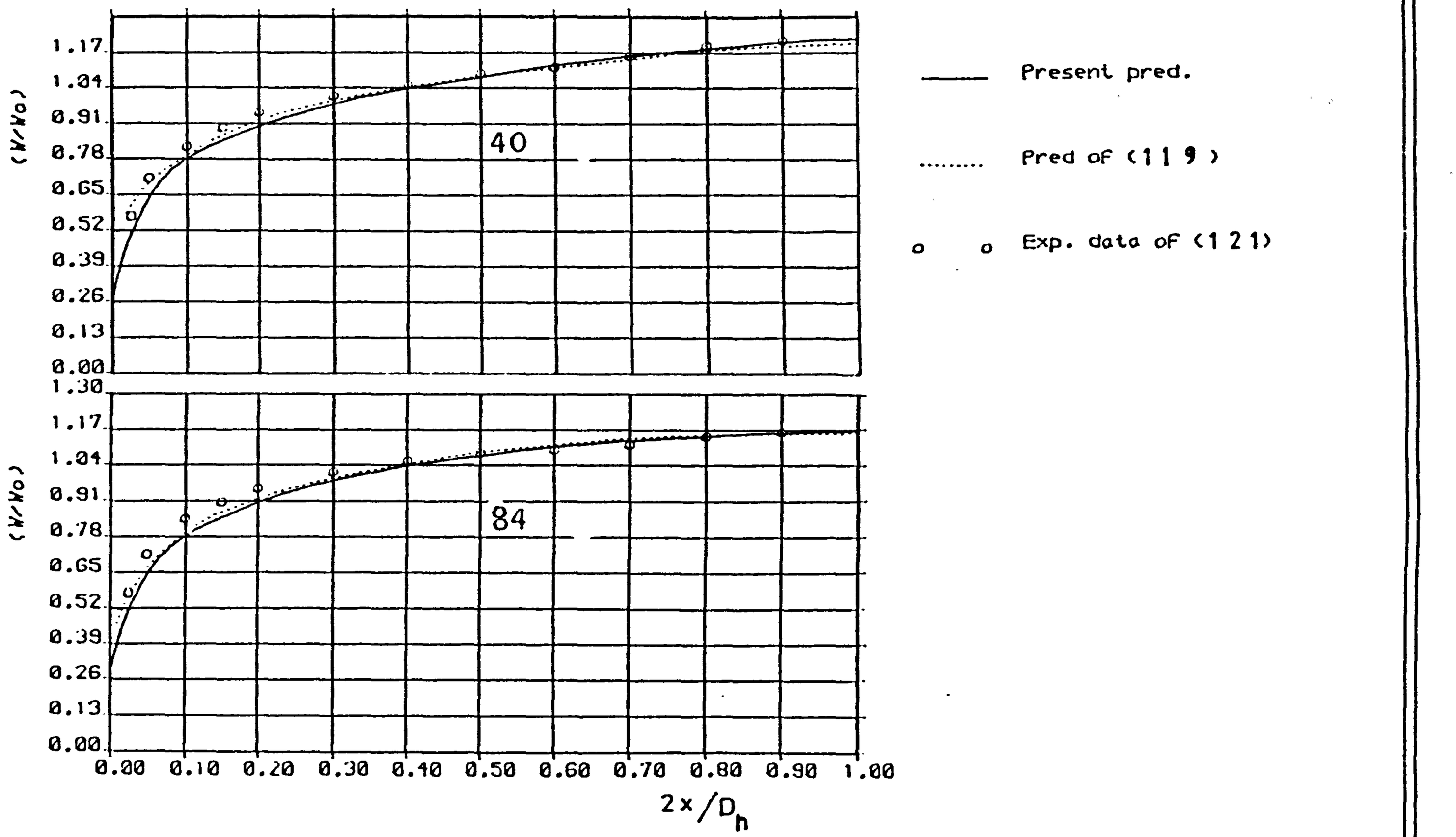

Fig. 6.6 : Stream-wise velocity profile along corner-bisector
Re=2.5x10^4 ,at Z/D_h =40.0 and 84.0 .

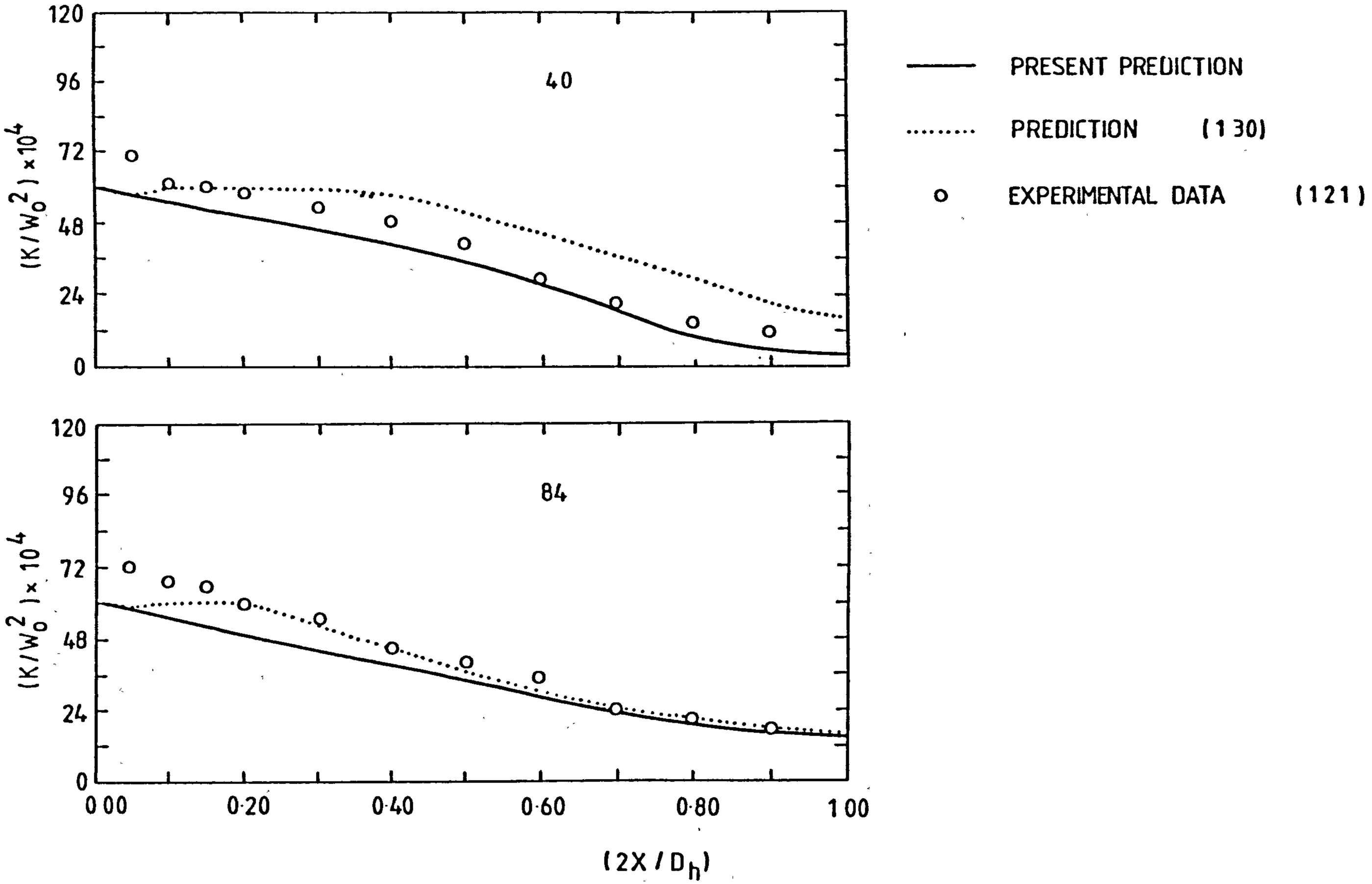

Figure 6.7 : Turbulent kinetic energy profile along wall-bisector ,Re=2.5x10 , at Z/Dh=40.0 and 84.0

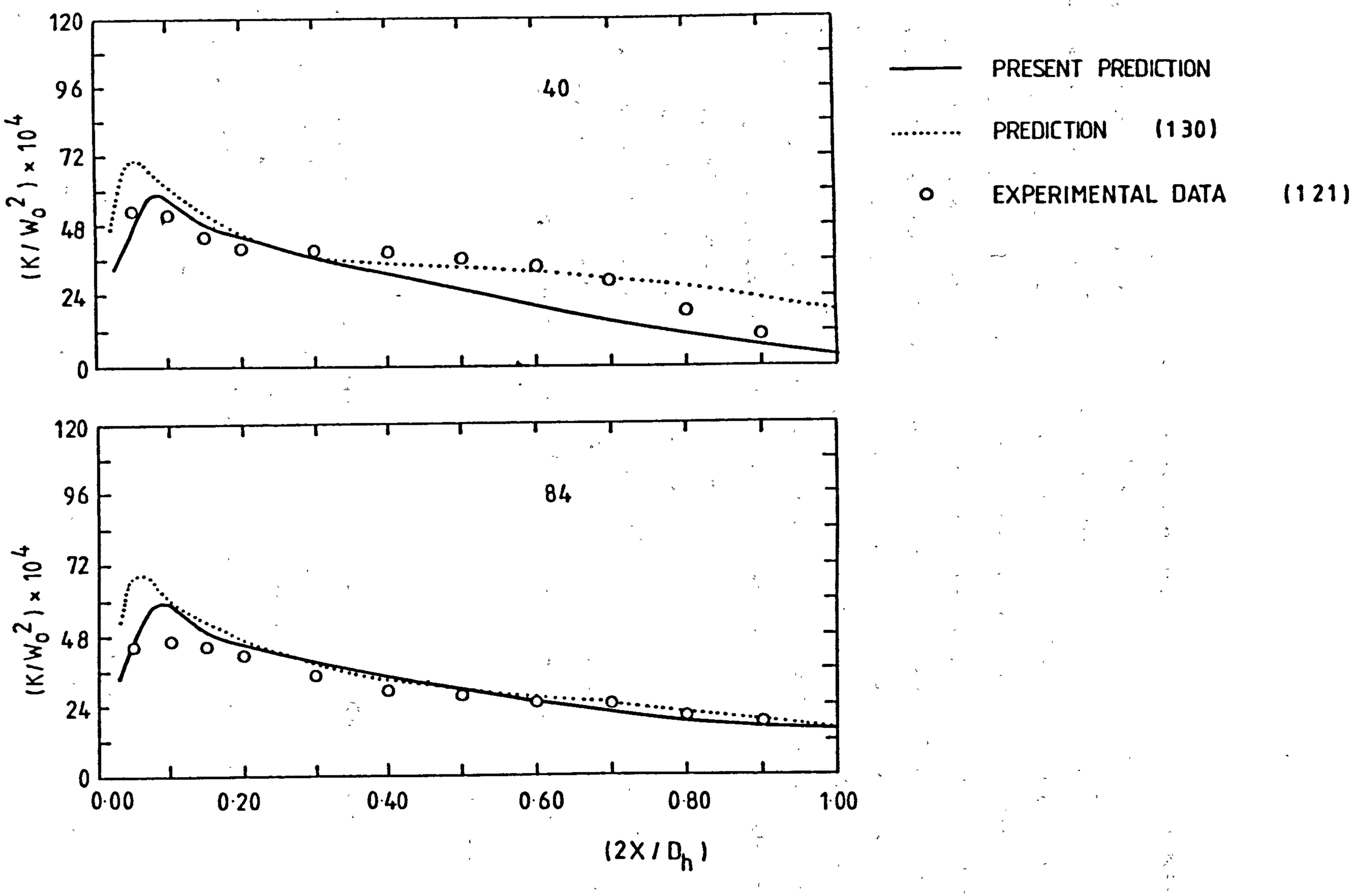

Figure 6.8 : Turbulent kinetic energy profile along corner-bisector ,Re=2.5x10 , at Z/Dh=40.0 and 84.0

value for K near the wall. Effectively C_D is reduced through the use of wall damping functions in these expressions (see the discussion in section 6.2.1 (ii) above). Nevertheless, in the corner bisector (see figure 6.8), the present computation with C_D = 0.09 displayed reasonable agreement with the experimental data at both stations, except in the corner region. In the latter region, the present computations and those of Naot and Rodi (130) display a qualitative discrepancy with the experimental data. Here K is forced to take a value at the node nearest to the wall that is produced by the wall function approach, and which is close to the experimental one. The subsequent rise in K away from the wall may be attributed to the over-estimation of the velocity gradients since these gradients are determined as part of the flow field solution. Forcing compatibility between the near wall and main flow values results in the peak value for K.

6.4.3 Secondary Velocities

The computed secondary velocity vectors are presented in figures 6.9 and 6.10 at four different axial stations along the duct (z = 18, 32, 41 and 82 D_h). It can be seen from these figures, the development of the secondary motion as the flow reaches the fully developed region at about z = 40 D_h. These figures also reflect the symmetry of the flow about the corner bisector. The quantitative comparison of the secondary motion was not however included in the present study, firstly because there are appreciable differences between the experimental work reviewed in section (6.2.1) regarding quantities such as the profiles of U and V, and secondly because the present coarse-flow grid (11x11) was found to underestimate these quantities. The minimum number of nodes required to successfully reproduce the secondary flow profiles appears to be 20 x 20 (according to previous workers 119, 128, 130). However,the differences in the recirculation pattern produced by such fine grids do not seem to produce any corresponding changes in the centre-line velocity (124).

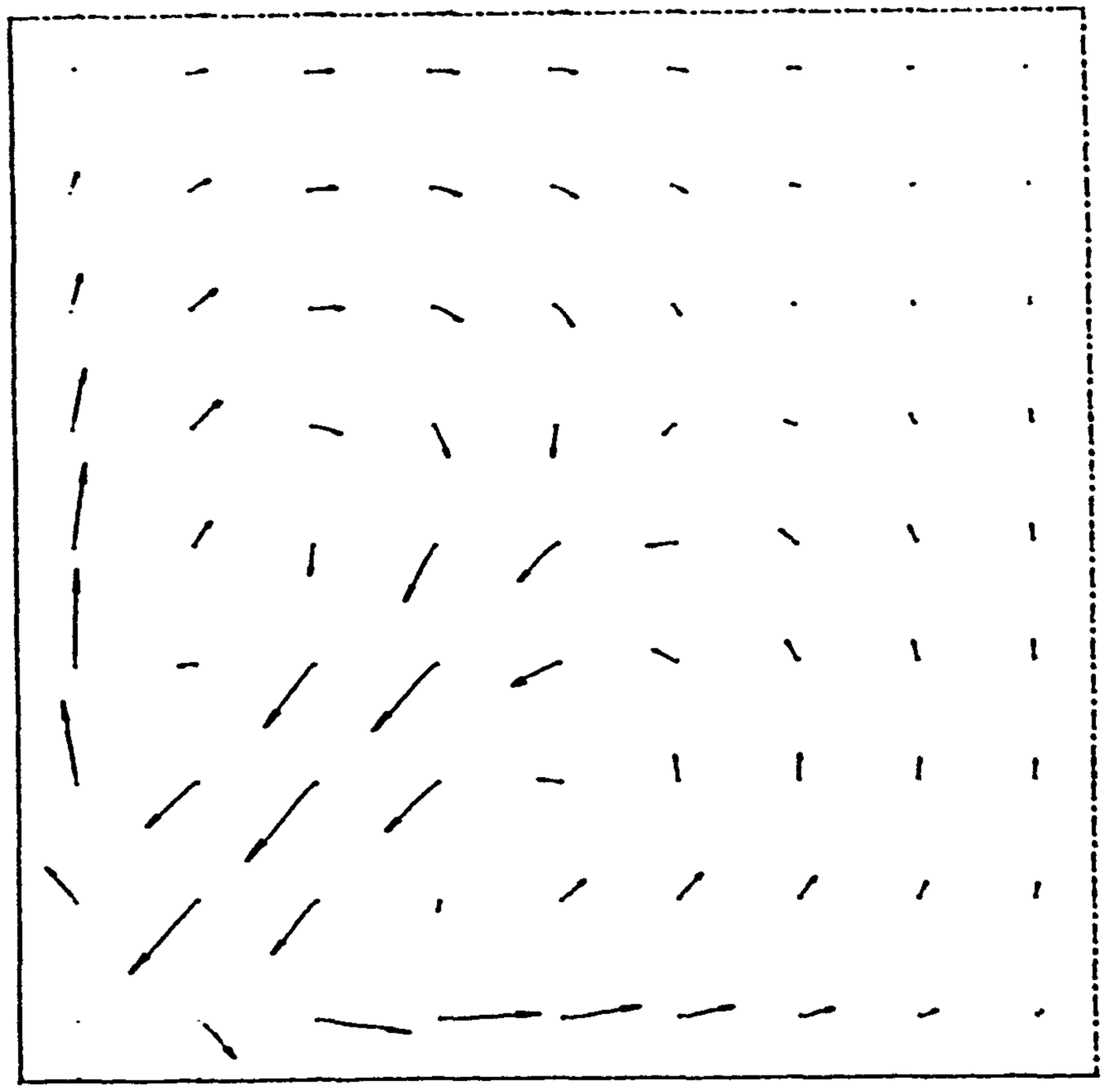

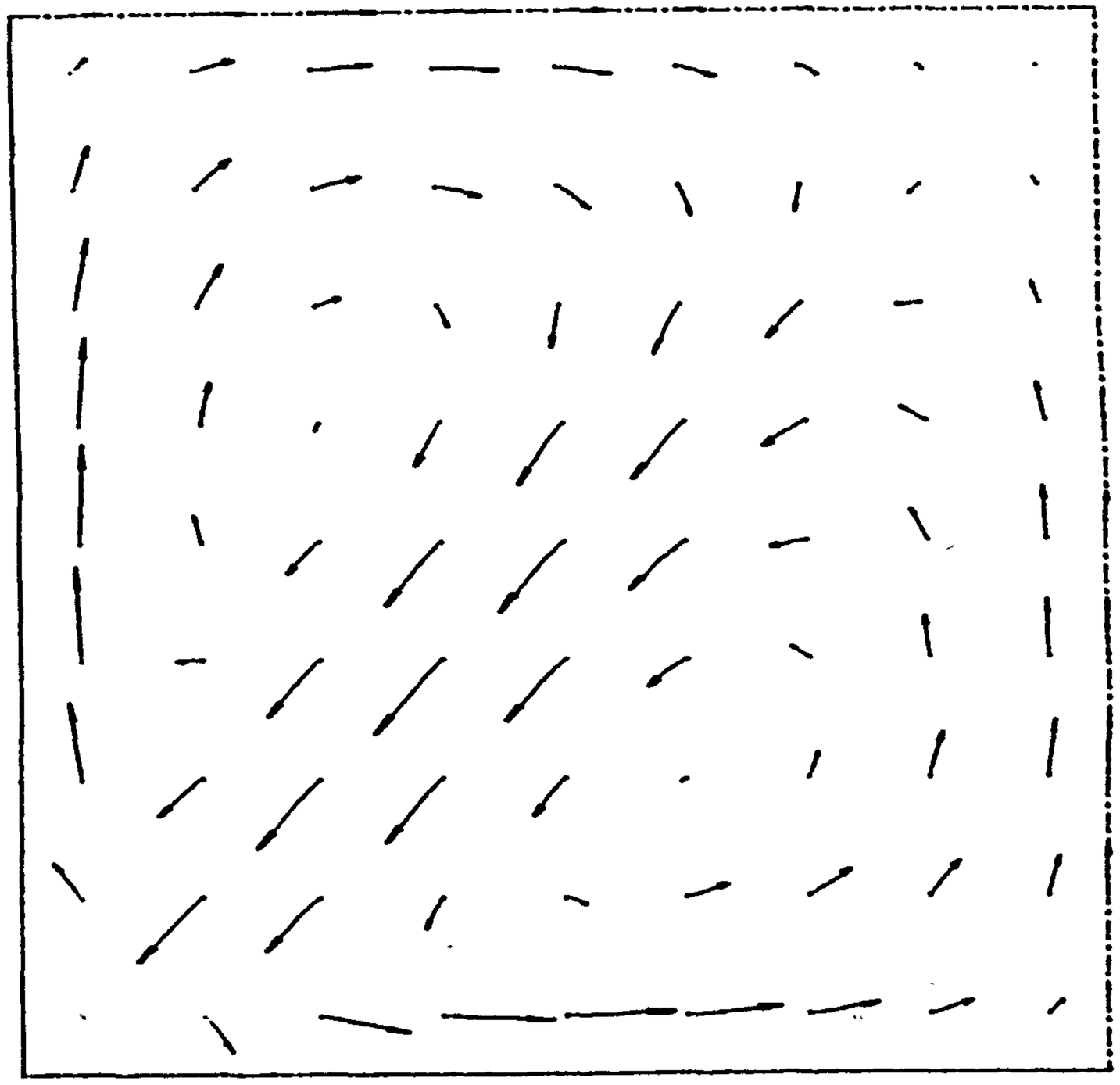

Fig. 6.9 : Secondary velocity vectors for 3-D turbulent
Flow in square duct at Z/Dh= 18.0 & 32.0

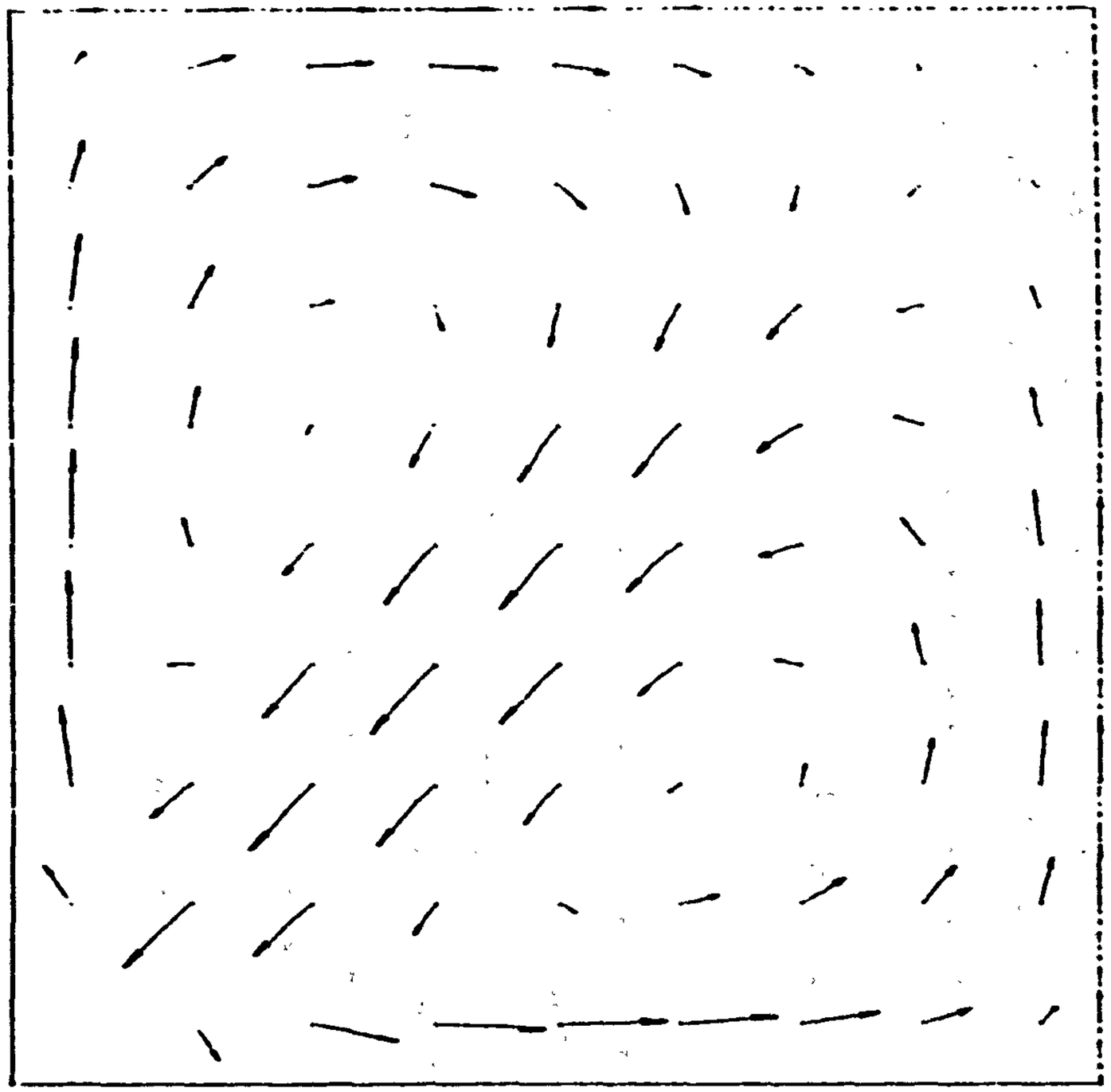

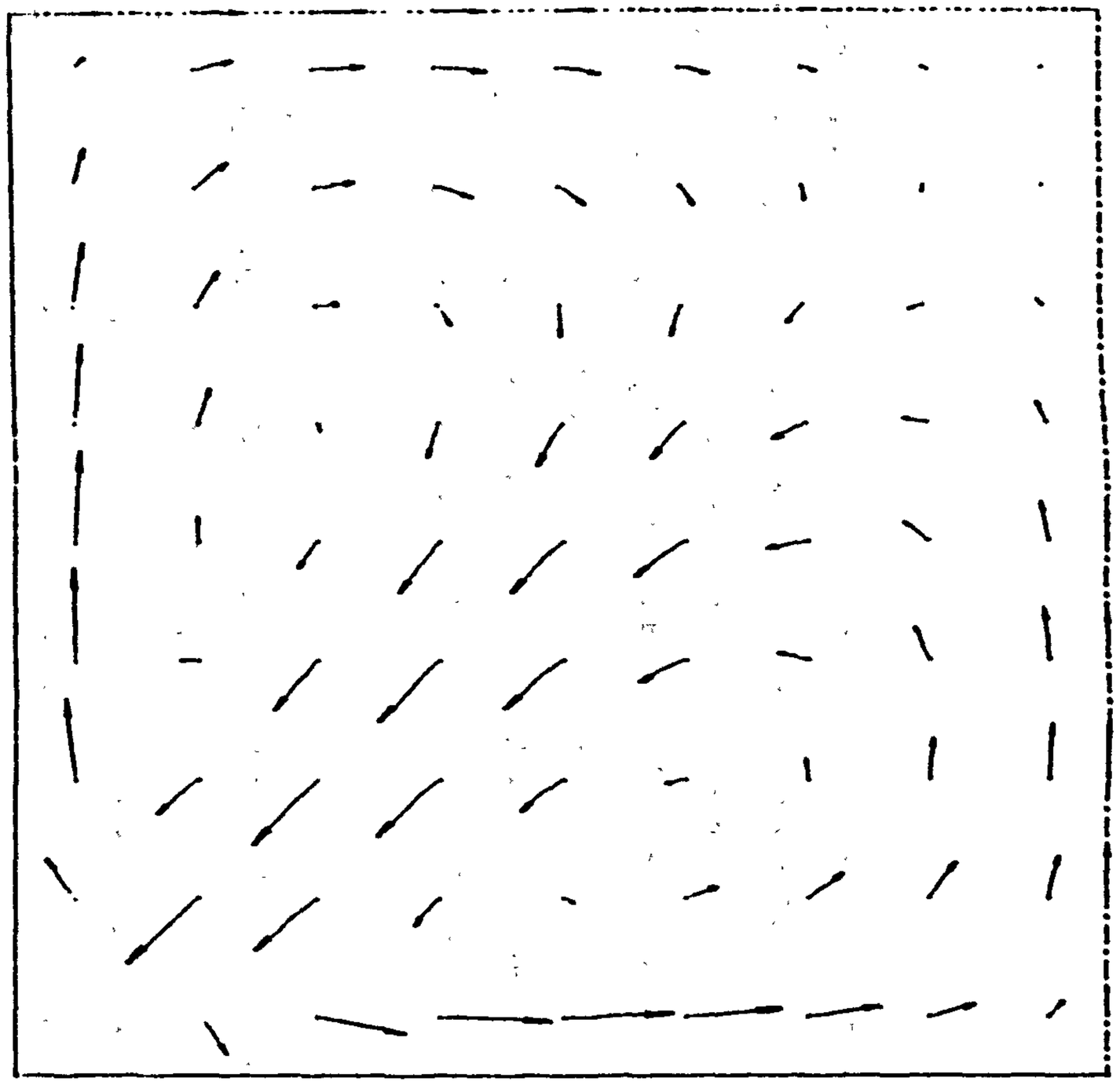

Fig. 6.10 : Secondary velocity vectors for 3-D turbulent flow in square duct at Z/Dh= 41.0 & 82.0

6.4.4 Duct Perimeter Heat Transfer

The present computations of the variation in the heat flux around the periphery of a square duct is shown in figure 6.11. Comparison is made in this figure with the experimental data of Brundrett and Baines (116) and the numerical predictions of Launder and Ying (52). Reasonable agreement is indicated with the maximum heat transfer rate being shown to occur at a value of $2x/D_h$ of approximately 0.5.

6.5 SUMMARY AND CONCLUSIONS

The aim of the material presented in this chapter was to assess the accuracy of coarse-grid computations using the ESCEAT computer code for developing turbulent flow in straight, square ducts. The simulation of the associated secondary motion has been achieved by incorporating an elliptic version of the N-R closure approximation. The choice of the N-R model was made for several reasons, among them its ability to provide a reasonable simulation of the flow over a wide range of Reynolds numbers. The relevant transport equations in finite-domain form were solved using the SIMPLEC algorithm along with an overall continuity correction procedure. The latter accelerated the convergence, as well as ensuring mass conservation. The verification of the present numerical procedure was undertaken by making comparisons with experimental data and previous predictions at various Reynolds numbers. These comparisons indicated that the present procedure is capable of computing the development of the streamwise velocity along the duct axis and its dependence on the Reynolds number fairly well. The distribution of the primary(or axial) velocity along the wall and corner bisectors at two axial stations were also well predicted. A reasonable simulation was also obtained for the distribution of the turbulent kinetic energy (K) along those sectors, except near the wall and corner regions. However, similar discrepancies were observed by previous numerical modellers in these two regions. Secondary velocity vector plots indicated the qualitative nature of this flow, and demonstrated that

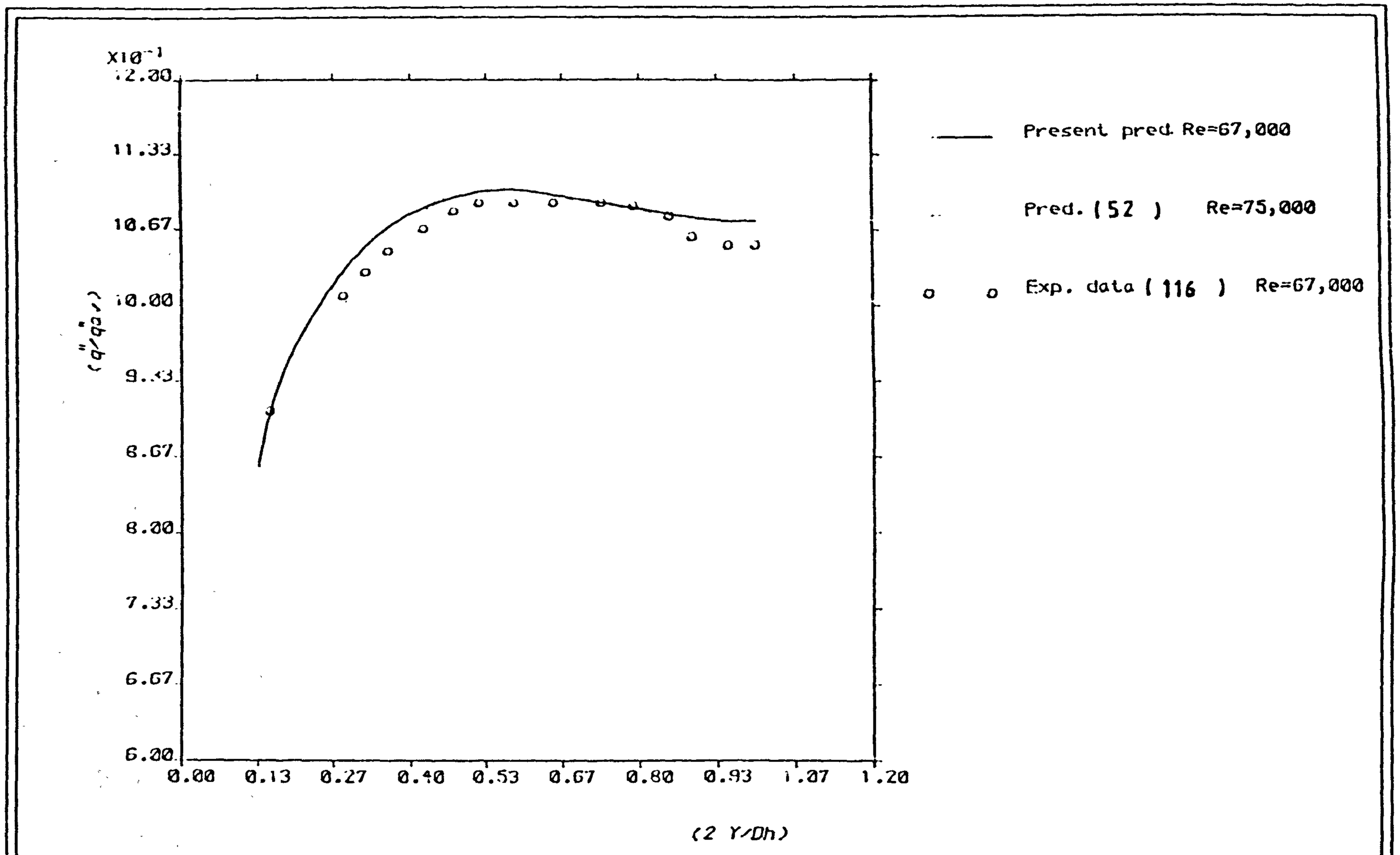

Fig. 6.11 : Variation of heat flux around perimeter in a square duct

the present calculation procedure is capable of reproducing the symmetry about the corner bisector. A comparison of the computed heat flux distribution around the duct perimeter again displayed a reasonable agreement with experimental data. On the whole, it appears that the present procedure has demonstrated its ability to successfully simulate the development of the complex turbulent flow in straight square ducts.

CHAPTER 7

CALCULATION OF FLOWS IN VENTILATED ROOMS

7.0 CALCULATION OF FLOWS IN VENTILATED ROOMS

7.1 INTRODUCTION

This chapter discusses the application of the ESCEAT computer code to the computation of three-dimensional turbulent flows within mechanically-ventilated rooms. Three different ventilation arrangements were simulated in the present study: isothermal, non-buoyant (constant property) and buoyancy-affected flows. The comparative assessment of different methods for calculating air flows and convective heat transfer within a warm-air heated room reported by Alamdari, Hammond and Mohammad (1986; bound paper) also forms an integral part of this study. A discussion of the relation between the present contribution and that of previous investigations may be found in the latter paper.

7.2 CALCULATION PROCEDURE

7.2.1 General Remarks

The dependent variables in the case of the problems considered were the three components of velocity (U,V,W), pressure, temperature, turbulent kinetic energy and its dissipation rate. All these variables, with the exception of pressure, may be assumed to obey the general form of the differential equation (2.34). The corresponding finite-domain equations, which were solved in the present study, were detailed in chapter 3. A power-law differencing scheme (69) was used in formulating the relevant finite-domain coefficients for all the variables, in an attempt to produce better approximation for the complex flow situations considered here than would be obtained with some of the earlier schemes. The SIMPLEC algorithm (70) was used to update the velocity components and pressure in the present study. This is a consistent varient of SIMPLE (68), and consequently induces a faster rate of convergence.

The following subsections present a description of the particular ventilation arrangements that were modelled, their

associated boundary conditions, problem-specific features of the solution procedure, and an assessment of the grid independence of the nodal network that was employed for the computations.

7.2.2 The Geometries Considered and their Associated Boundary-conditions

The geometrical arrangements that have been examined in the present study are illustrated in Figure 7.1 (a-c). The air distribution depicted in Figure 7.1 (a) is that used by Gosman etal (13) for predicting the isothermal flow properties of rooms with small ventilation openings. The second geometry (Figure 7.1(b)) was adopted by Hjertager and Magnussen (15) in order to model turbulent buoyant flow in a ventilated room. Unfortunately, these two geometries are rarely found in domestic and commercial office spaces in the U.K. Consequently, the warm-air heated room configuration illustrated in Figure 7.1(c) was also simulated as it represents a more practical configuration. This is a variant of that originally adopted by Alamdari and Hammond (25) to demonstrate the capabilities of their 'intermediate-level' convection model; the ROOM-CHT program [see also Alamdari (32) for a few additional results]. A full description of this geometry can be found in the bound paper (Alamdari, Hammond and Mohammad, 1986). In the present chapter, this geometry was used only to simulate a turbulent non-buoyant flow case. This case was studied in order to calculate the optimum grid system, and to enable the subsequent influence of buoyancy effects to be assessed. The latter was achieved by including additional buoyancy source terms in the momentum, K and ε transport equations. Comparison between buoyant and non-buoyant cases may then be made with all other factors, including the computational grid, remaining the same. The dimensions of all three geometries, which will hereafter be referred to as geometries, A,B and C respectively, are given in Table 7.1.

The boundary conditions needed for the solution were specified for the three geometries as follows:

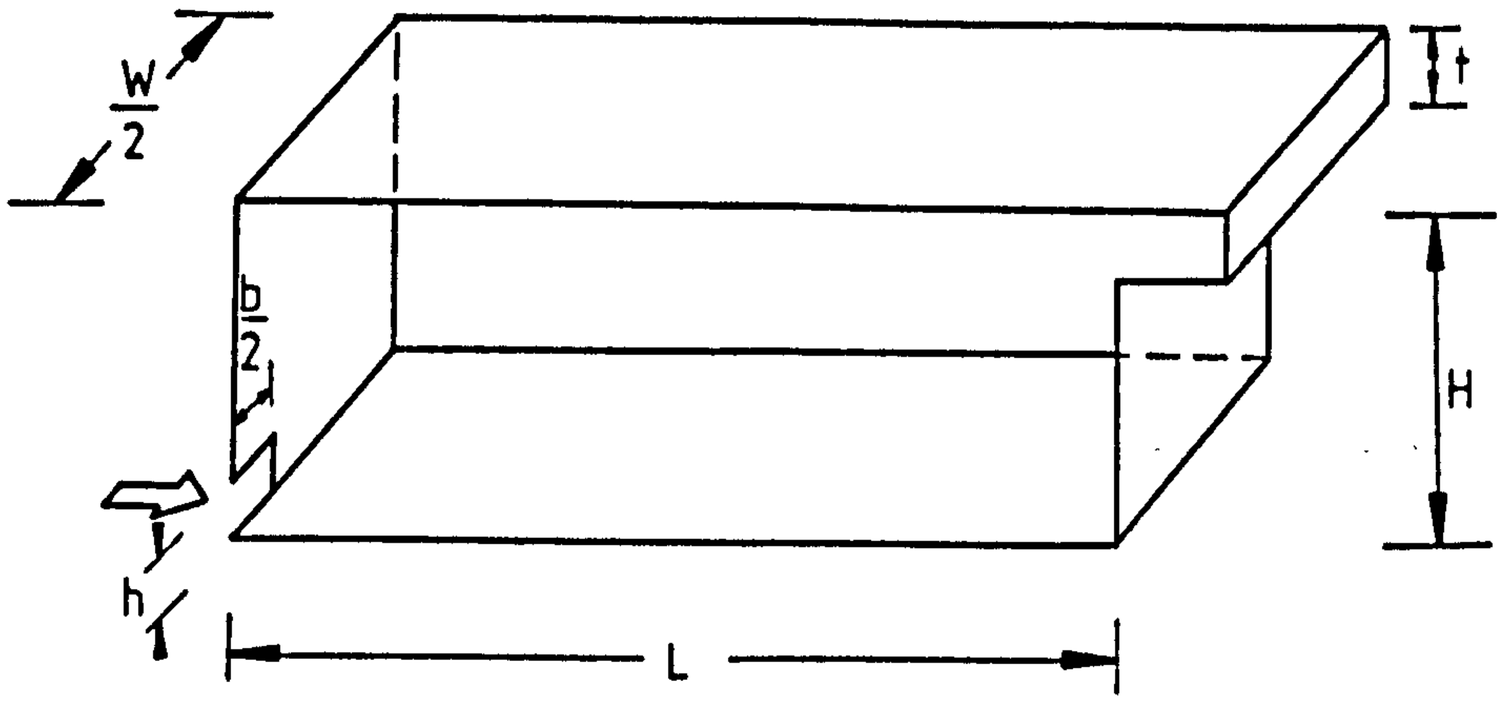

(a)

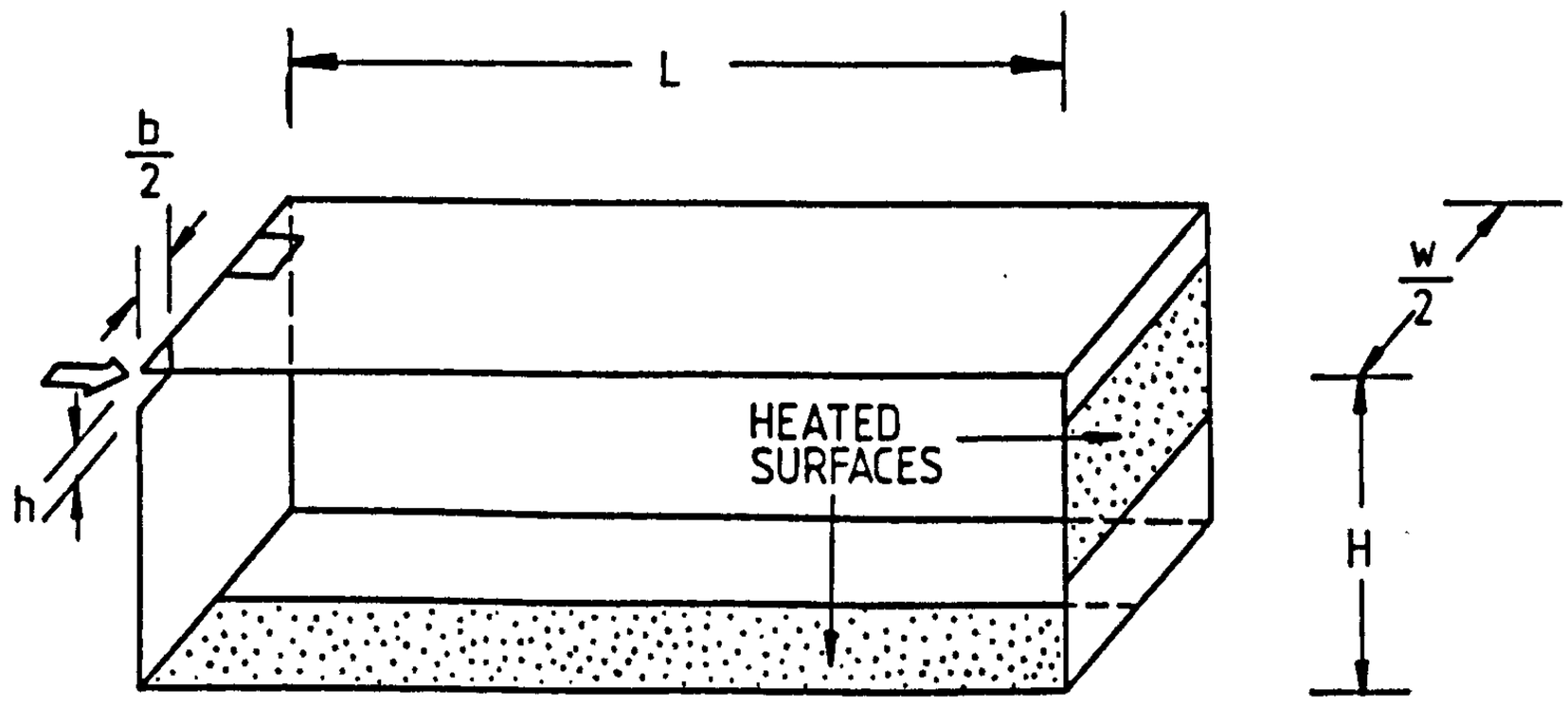

(b)

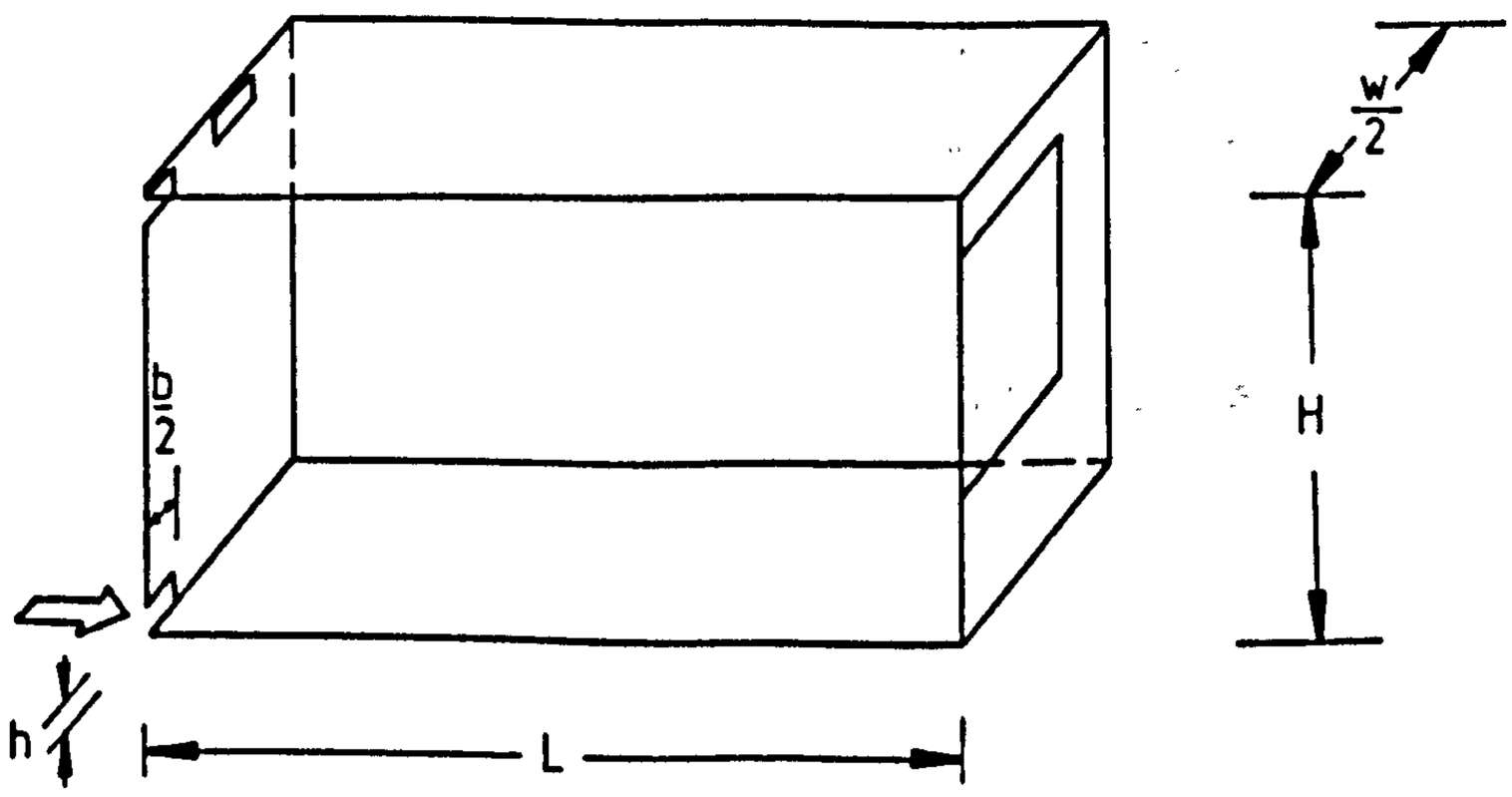

(c)

Fig. 7.1 : Schematic diagram of room flow configurations.

Inlet: a uniform profile was prescribed for all the variables at the inlet boundary. However, in the isothermal and non-buoyant cases, starting profiles were employed over a prescribed inlet cell as described in the next section.

Near-walls: the wall function approach was adopted in the same manner to that discussed in chapters 2,3 and 6.

Outlet: The gradients normal to the outlet plane for the related variables in geometry A,B and C were assigned equal to zero. However, in geometry A, the velocity components normal to this plane was given a value based on overall continuity requirements, while parallel ones were set equal to zero. Such approach has also been used by Gosman etal (13).

Geometry	Dimensions in metre (m)				
	L	W	H	h	b
A	0.2600	0.0893	0.0893	0.0268	0.0268
B	5.6000	2.9000	2.4000	0.0350	0.2430
C	4.3000	2.4500	2.4500	0.1200	0.2000

Table 7.1 Dimensions of geometry A,B and C.

The values for the velocity, temperature and turbulent quantities at the inlet and all the solid boundaries are given in Table 7.2 and the associated notes for each of the three geometries.

7.2.3 Starting Profile Over the Inlet Cell

A particular numerical difficulty encountered when simulating the flow in a large room supplied by a small slot/register (11-13,32) is that a large number of grid nodes are required to give a proper representation of the flow through and near to the supply opening. An early remedy for this difficulty was suggested by Nielsen etal (11), who prescribed the values of the dependent variables over an inlet cell adjacent to the supply opening. Thus, the area immediately surrounding the inlet was excluded from the normal calculations, and instead the inlet cell, over which the flow properties were specified via wall-jet experimental data, was imposed. The boundary of the inlet cell was then used as a starting profile (jet supply condition) for the room. This approach was also adopted in subsequent studies by Nielsen etal (12) and Gosman etal (13). In the latter work, three-dimensional wall-jet empirical data (107) was employed to prescribe the flow properties within the inlet cell for a three-dimensional, isothermal flow study. More recently, Alamdari etal (21) employed a similar approach in order to obviate the need for using a very finely-spaced grid in the inlet slot of a two-dimensional room. However, in their approach the wall-jet empirical data reviewed by Hammond (29-30) and the latter's profile analysis were used to prescribe the starting profile. Full details of this approach are given in Alamdari thesis (32).

In the present study, a starting profile similar to that adopted by Alamdari (32) was used for both the isothermal and non-buoyant flow cases. The additional information required to prescribe the flow properties within the inlet cell was based on the three-dimensional wall-jet empirical data reviewed by Rajaratnam (107). A schematic diagram of the present representation of the inlet cell is shown in Figure 7.2. The precise location of the starting profile in that cell (Z_{sp}) is unimportant (13,32) provided that it is kept small compared to the length of the room. In the present calculations, Z_{sp} was specified as being located at the nearest grid line to a quarter of

Variables	Geometry	Boundary-conditions					
		At Inlet	At walls				
			Floor	Far-wall	Ceiling	Near-wall	Left-wall
W	A	15.20	0	0	0	0	0
	B	2.42	"	"	"	"	"
	C	1.50	"	"	"	"	"
U & V	A,B & C	0	0	0	0	0	0
K	A,B & C	K_{in}	The gradients normal to the walls set equal to zero				
ε	A,B & C	ε_{in}	0	0	0	0	0
T °C	C	11	20 & 37	20 & 37	20	20	20
	B	65	16	16	21	21	21

Notes

1. The data for geometries A and B were taken from Gosman etal (13) and Hyertager and Magnussen (15) respectively.
2. $K_{in} = 0.00135\ W_{in}^2$ and $\varepsilon_{in} = C_D\ K_{in}^{3/2} \ / \ 0.03h$.
3. The coupled values that appear for the temperature represent the temperature of the partially heated surfaces (see Figure 7.1).
4. The temperature of the window in geometry C is 6 °C.
5. The boundary conditions of geometry C represents ther <u>high</u> demand condition reported by Alamdari, Hammond and Mohammad (the bound paper).

Table 7.2 Boundary Conditions for geometries A,B and C.

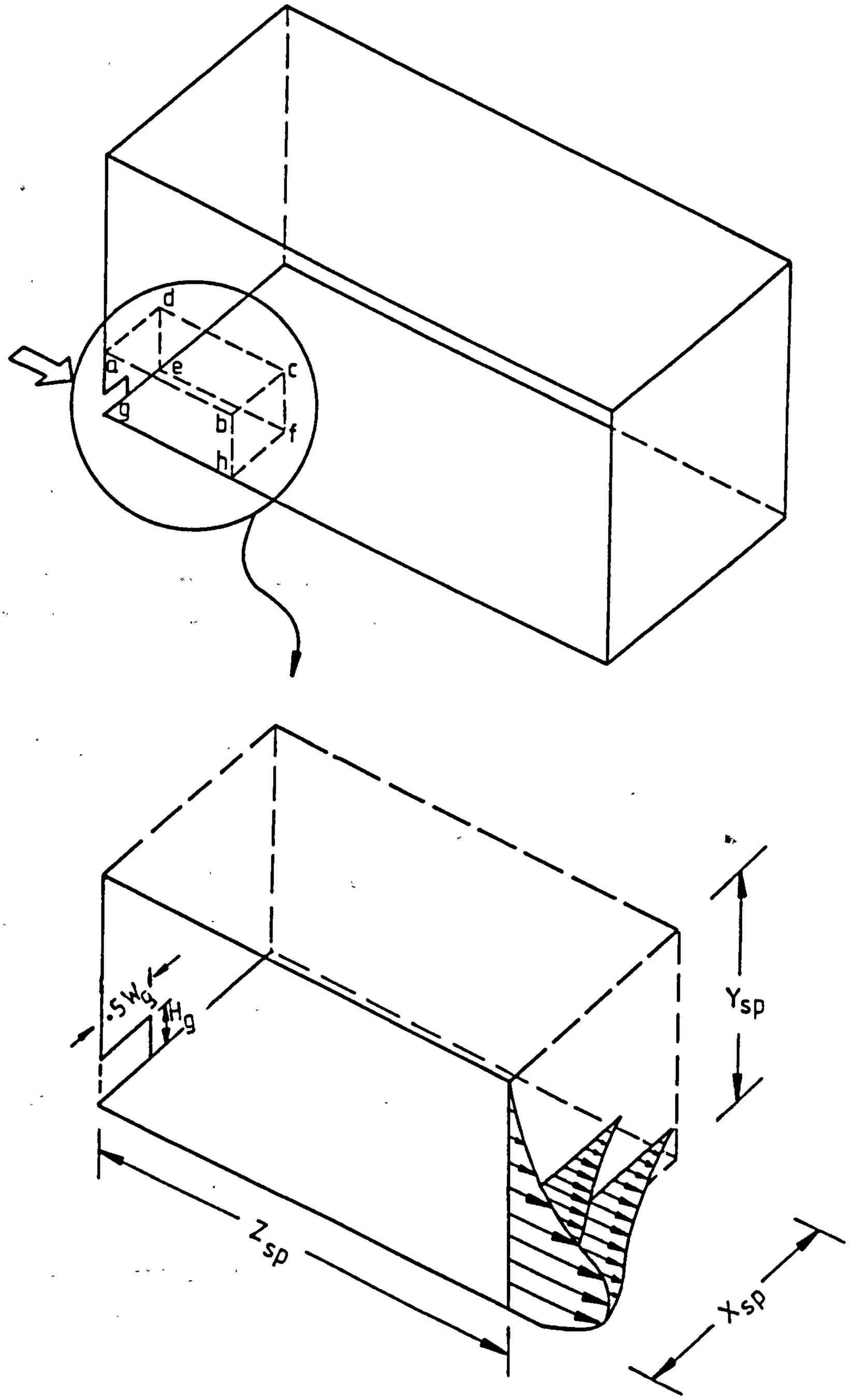

Fig. 7.2 : Schematic representation of three-dimensional, wall-jet inlet-cell .

the room length. The width and the height of the inlet cell (X_{sp} and Y_{sp} respectively) were estimated from the growth of the jet (Hammond, private communication). The relations that were used to describe the flow properties (W,K,ε and H) within the cell are given in Appendix C. The resulting profiles for these variables at the plane hbcf (see Figure 7.2) were used as the jet supply condition in the numerical procedure. The gradients of these variables normal to the planes abcd and edcf were assigned values equal to zero on the basis that these planes behave like outlet boundaries for the flow domain (13,32).

7.2.4 Solution Procedure

The procedure presented in chapter 5 was used in the present simulation. However, in the case of the computations reported by Alamdari, Hammond and Mohammad (bound paper), the third iteration sweep was replaced by a plane-by-plane block-correction adjustment applied by sweeping the flow domain in the Z-direction. This was adopted in order to stabilize the solution and enhance the convergence of this flow case, which was significantly influenced by buoyancy effects. The block adjustment was incorporated into the solution procedure using the following sequence:

a) An x-y plane was considered,

b) The block-adjustment coefficients (equation 3.62) for each ϕ were calculated and summed throughout the line-by-line sequence over that plane.

c) Step b was repeated for all x-y planes in the field, except the boundary ones.

d) At the end of each iteration, the block-adjustment equations (equation 3.65) were solved by the TDMA for each ϕ.

e) Increaments $\delta\phi$ were then added to the corresponding ϕ's on each x-y plane.

7.2.5 Grid Systems

Two basic criteria were considered in developing the finite-domain grid; firstly, that sufficient grid nodes should be located near the jet register and, secondly that the total number of grid nodes were minimized in order to reduce the computing requirements. A reasonable compromise between these needs was achieved by expanding/contracting the grid lines in such a way that the nodes were concentrated near to the walls and to the inlet opening. The grid systems used for the three flow geometries (A,B and C) are detailed below;

i) Geometry A.

This geometry was used to perform computations for the turbulent isothermal flow case. The influence of the nodal network on the computed results was tested via the use of two alternative grid systems; namely 11 x 15 x 11 and 13 x 17 x 15 nodes. The inlet cell approach was incorporated into the 11 x 15 x 11 system. The decay of the maximum velocity in the symmetry plane ($x/w = 0.0$), calculated using both systems, is presented in Figure 7.3. It is clear from this figure that the three profiles are very similar, with a maximum discrepancy less than three percent of the peak value. Nielsen etal (12) argued that this level of accuracy is likely to be adequate for most of practical purposes. Consequently, the 11 x 15 x 11 system with the inlet cell approach was adopted for the remaining calculations for this geometry.

ii) Geometry B.

This geometry was previously studied by Hjertager and Magnussen (15) who used it in their computations of turbulent buoyancy-affected flow. They adopted a nodal network of 9 x 9 x 9 nodes in their simulation. In the present study, the same flow problem was modelled using a grid (9 x 10 x 9) comparable to that of Hjertager and Magnussen (15). The main purpose of employing a similar grid formulation here was to facilitate a direct comparison between the performance of the latter calculation procedure and the present one.

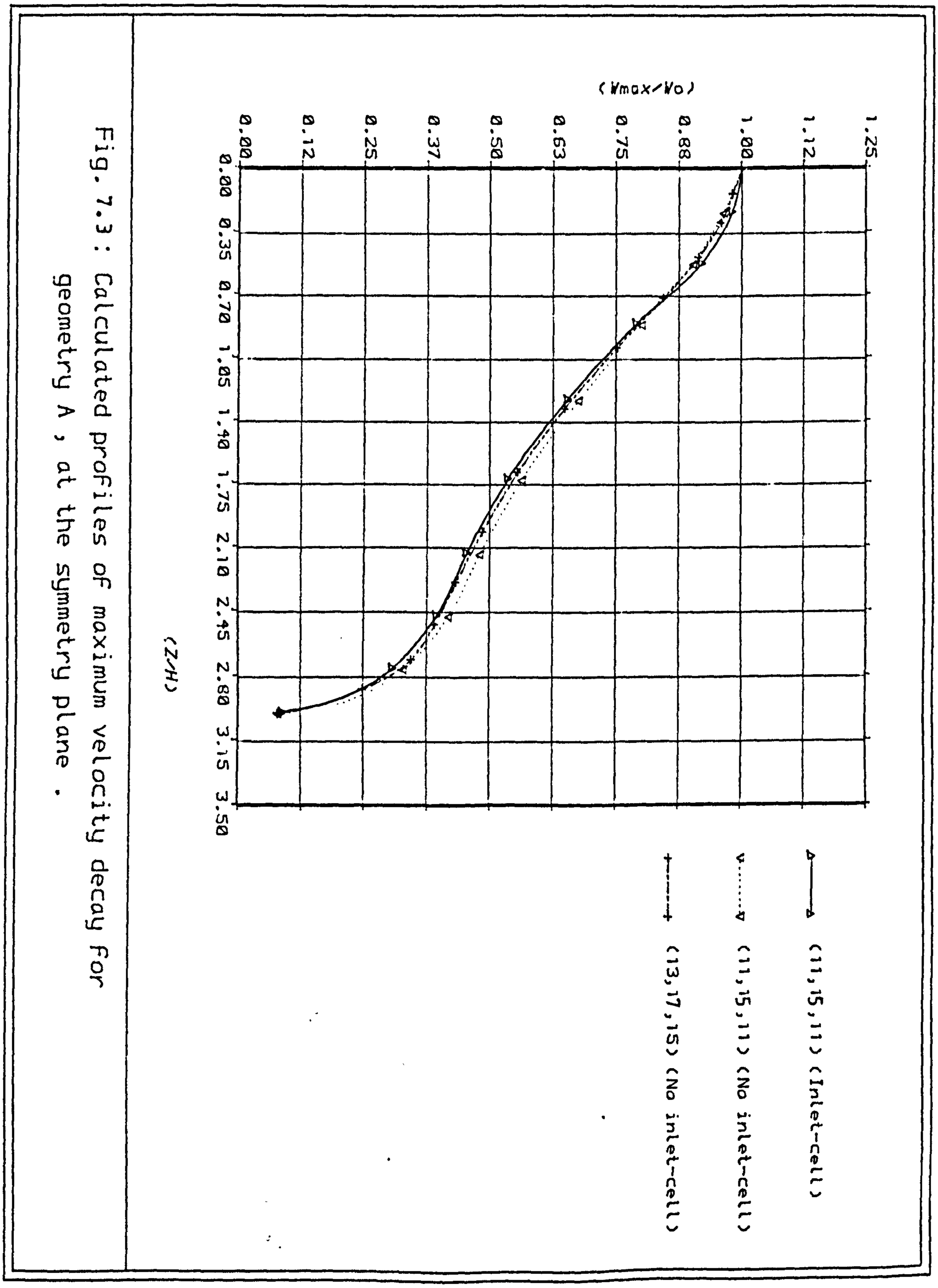

Fig. 7.3 : Calculated profiles of maximum velocity decay for geometry A , at the symmetry plane .

iii) Geometry C.

Geometry C was used to model a turbulent non-buoyant flow case. Two grid systems: 9 x 17 x 15 and 13 x 21 x 19 were employed to test the effect of the nodal mesh on the computed results. The simulated variation in the decay of the maximum velocity along the symmetry plane are presented in Figure 7.4 for both nodal networks. This displays a discrepancy between the two profiles of about 6% of the peak value at maximum. A similar level of precision was also found by Gosman etal (13). They argued that this is adequate for ventilation design purposes. The other factor which has to be taken into account when chosing the grid system is the associated computing requirements and cost. The coarse (9 x 17 x 15) mesh required a CPU time that was about 60% of that for the finer mesh system. On this basis, it was decided to use the coarse mesh for the remaining calculations.

The effect on the computations of the number of grid nodes in the inlet register was also tested using a comparison of results with and without an inlet cell. The distribution of the surface heat transfer coefficient over the internal surfaces was used as the test criteria. This coefficient has been calculated in a manner similar to that used by Alamdari and Hammond (25), and it can be written as;

$$h_c = \frac{q_w}{(\overline{T_R} - T_w)} \qquad 7.1$$

where q_w and T_w is the surface (or wall) heat flux and temperature respectively and T_R is the average temperature of the occupation or 'comfort' zone. The latter was defined; following Nevins and Miller (7), as the space that excludes all the structural surfaces; floor, ceiling and walls. The boundaries of this zone were located 0.6 metre away from the walls. The upper and lower 'surfaces' of the zone were positioned 1.8m and 0.07m respectively above the floor. The planar-average distributions of the convectin coefficient along the individual room surfaces (i.e. floor, far-wall and window, ceiling, near-wall and left-wall), calculated using equation 7.1, are presented in Figure 7.5. Both the distributions shown in this figure were

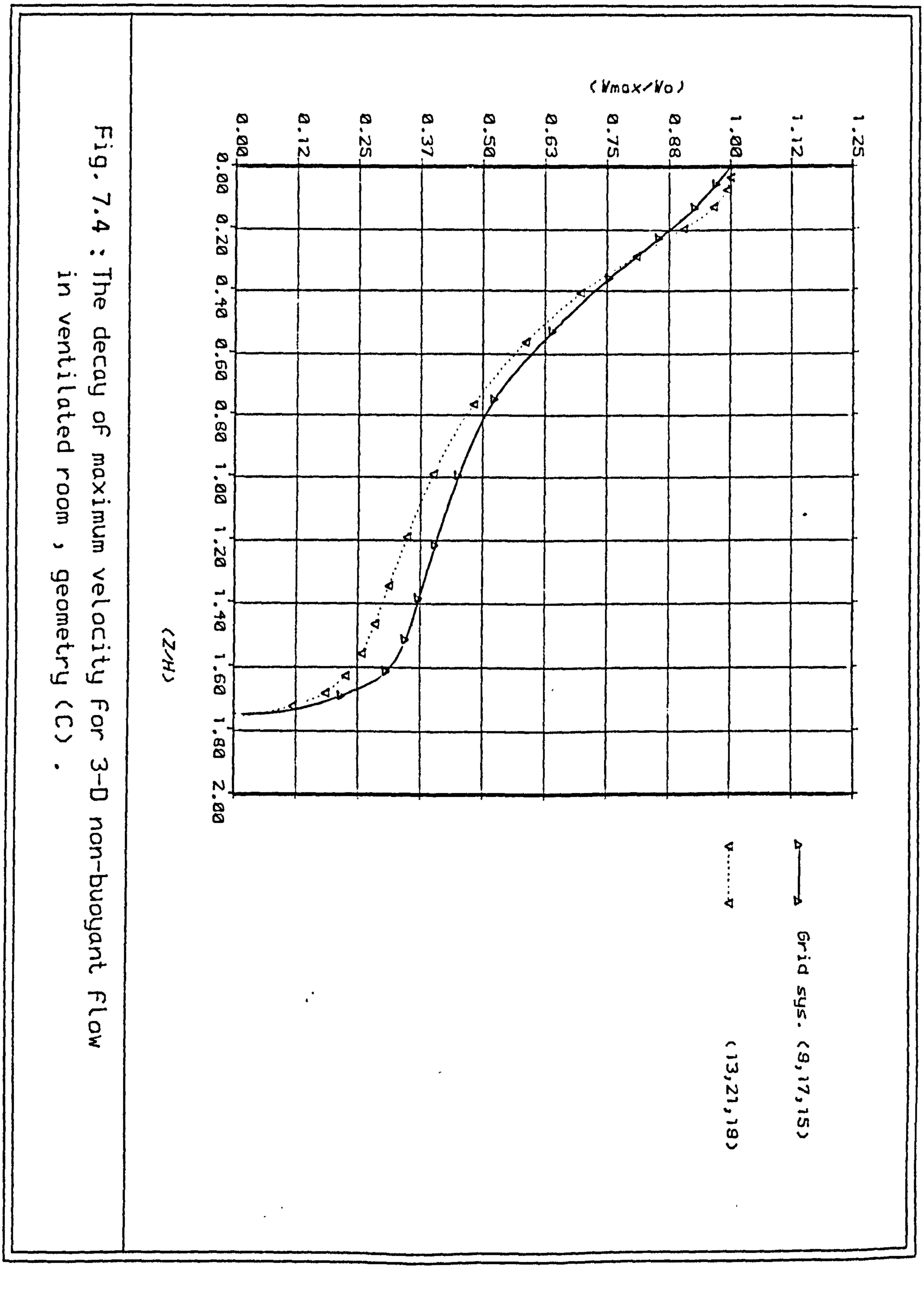

Fig. 7.4 : The decay of maximum velocity for 3-D non-buoyant flow in ventilated room , geometry (C) .

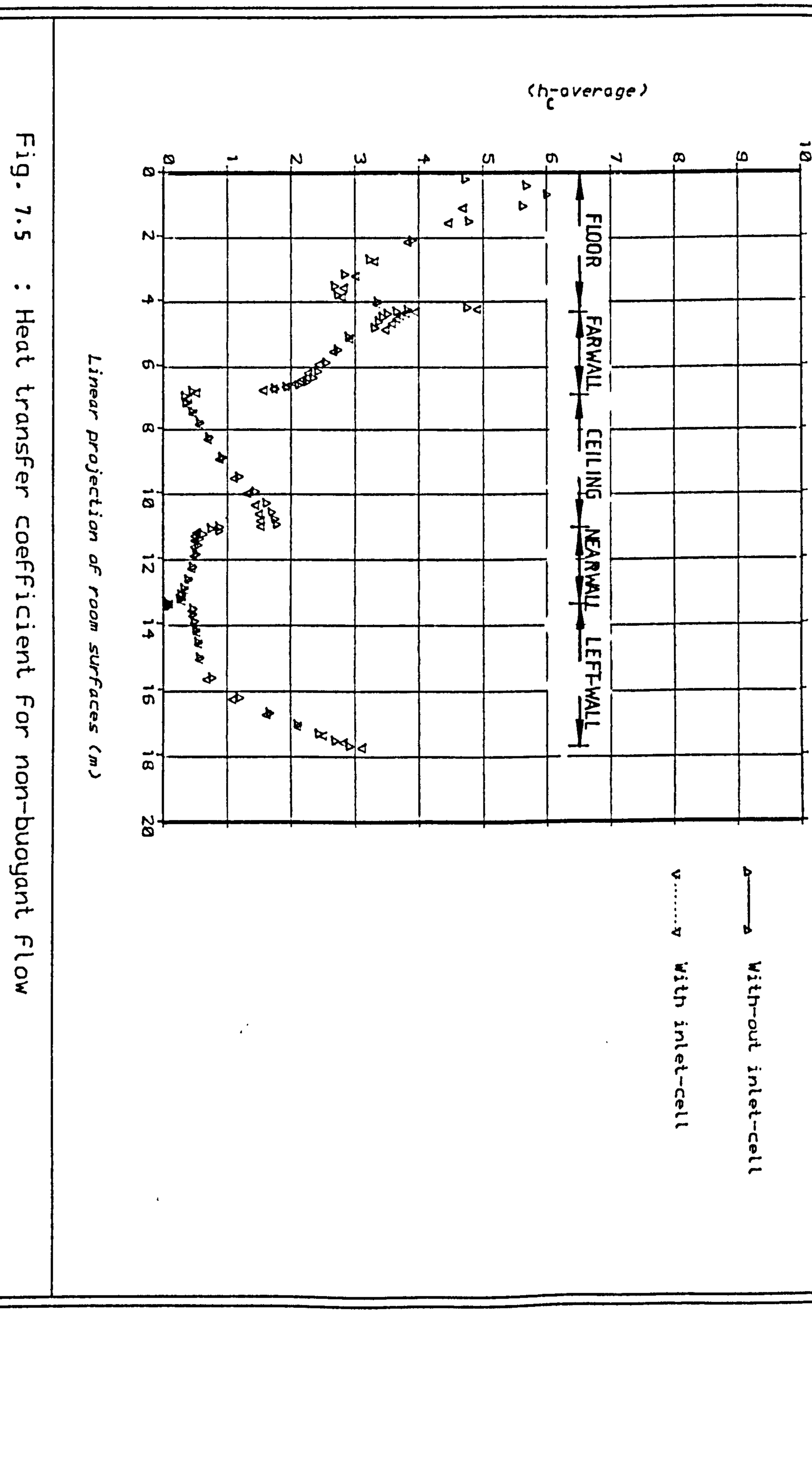

Fig. 7.5 : Heat transfer coefficient for non-buoyant flow in mechanically-ventilated room

obtained using the 9x17x15 grid system, and the differences results from the use or not of the inlet cell. It is clear that the two distributions are very similar; being close to each other over most of the domains. This suggests that it is not necessary to increase the number of grid nodes within the inlet opening (2 x 2 in the present formulation).

7.3 RESULTS AND DISCUSSION

The computed results obtained with the present elliptic code for each of the three flow geometries are presented in Figures 7.6-7.11, 7.12-7.13 and 7.14-7.21 respectively. Comparisons are also shown with the available experimental data and previous prediction from various sources.

Figure 7.6 shows a comparison between present calculations of the maximum decay along the symmetry plane of geometry A. These are compared with the predictions and experimental data of Gosman etal (13). The latter data shows a value of the velocity at the inlet opening that is greater than one. This was due to the fact that Gosman etal used a relatively long (0.27 metre) square duct in order to feed air to the aperature of their small-scale test rig, resulting in a parabolic inlet velocity profile. Nevertheless, it can be seen that the agreement between the present peak velocity variation and the experimental one is quite reasonable. The centreline velocity distribution is produced fairly well, with no discontinuity observable at the station where the starting profile was fitted. Moreover, the slight discrepancies between the present calculations and these of Gosman etal (13) may be attributed to differences in the specification of the starting profiles.

The primary (W) velocity profiles in two planes [$X/_W$ = 0.5 (symmetry axis) and $X/_W$ = 0.9 (near-wall) respectively] and at different longitudinal (or axial) stations are shown in Figures 7.7 - 7.8. The corresponding predictions and measurements obtained by Gosman etal (13) also appear in those Figures. It can be seen that the present computation produced reasonable agreement with both sets of data at the symmetry plane. However, some discrepancies can be observed in the near-wall plane ($X/_W$ = 0.9) especially in regard to

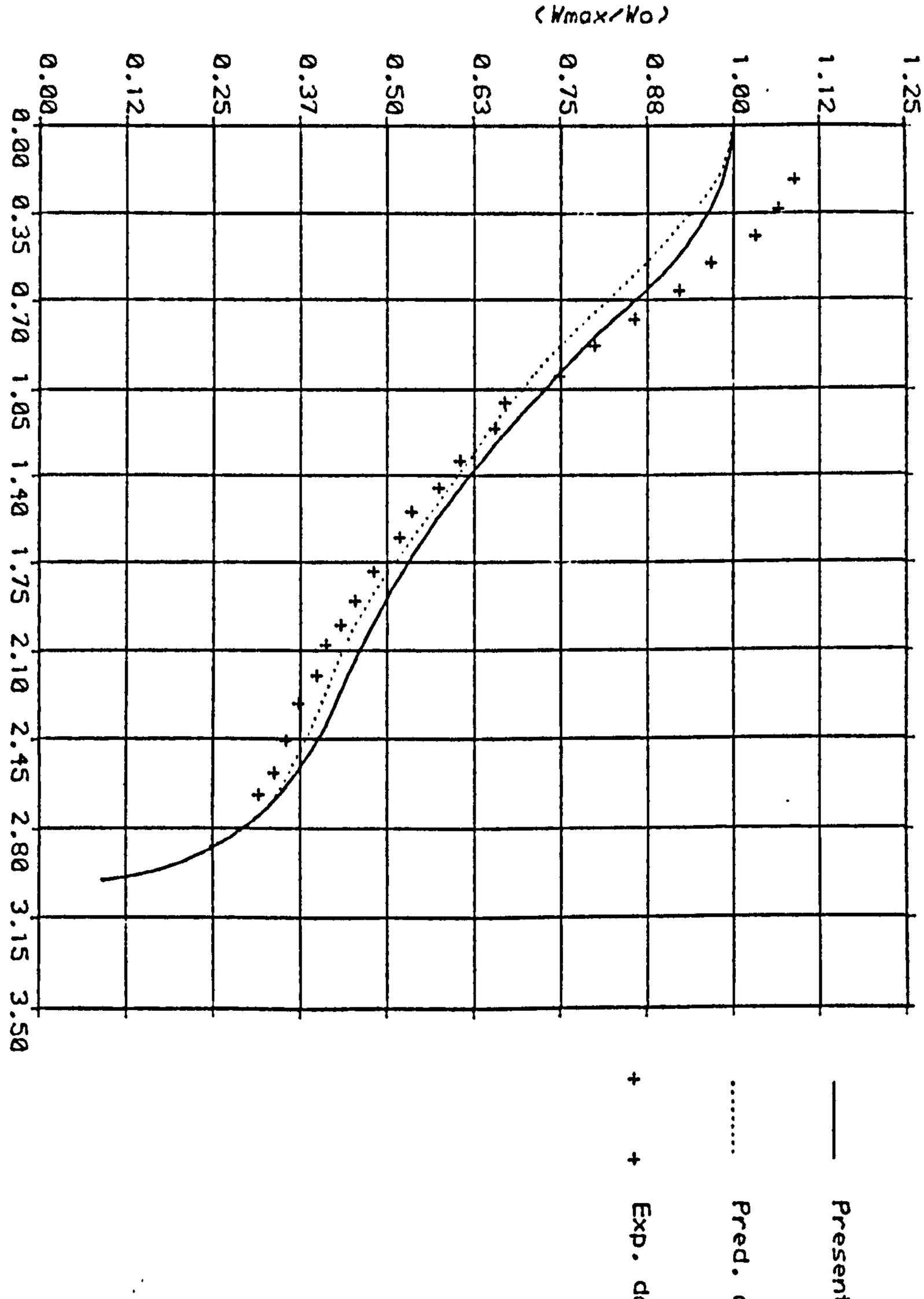

Fig.7.6 : Maximum velocity decay in the symmetry plane • a comparison of present prediction.

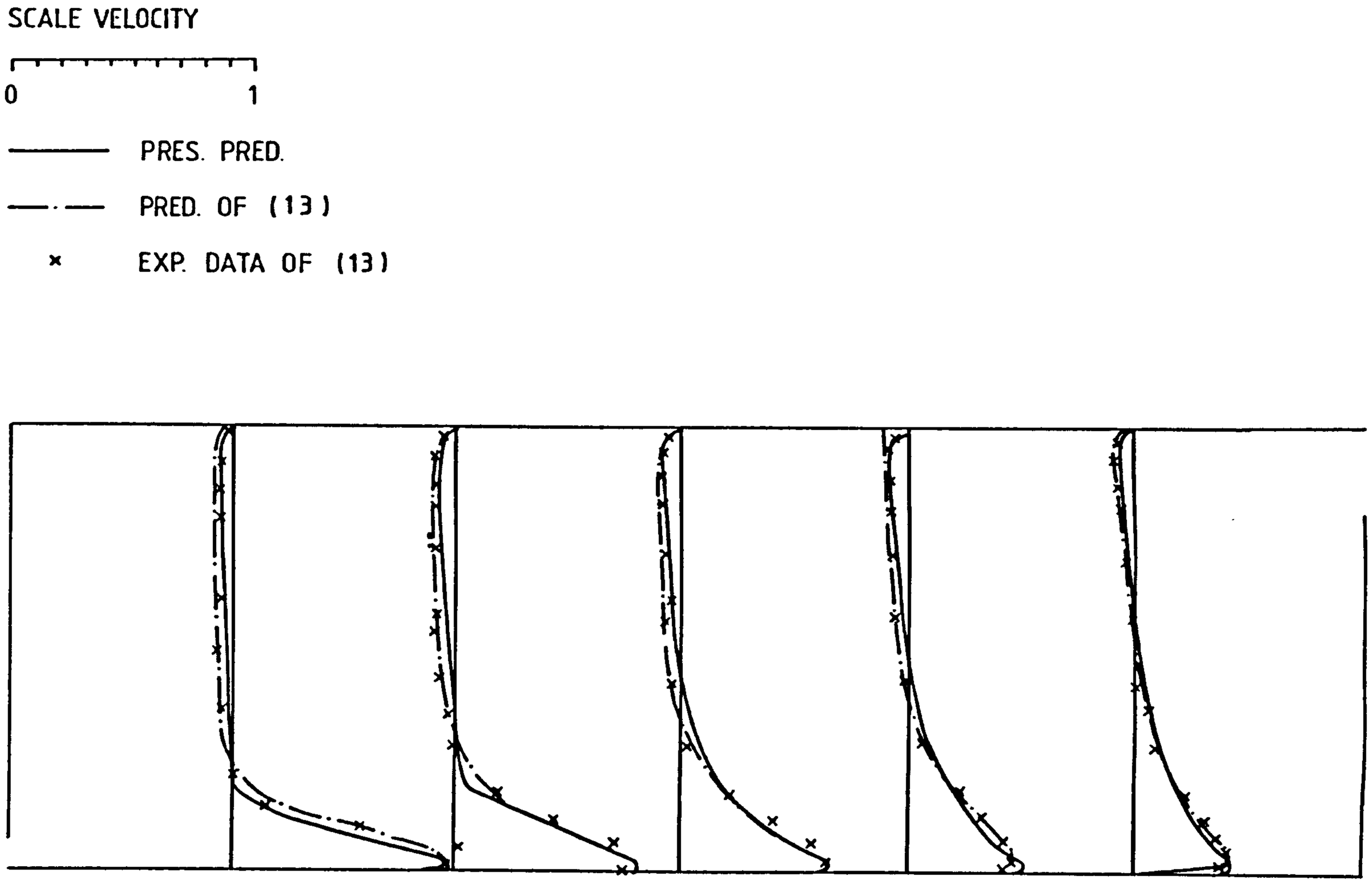

Figure 7.7 : Longitudinal velocity profiles at (Z/H)=0.5 ,1.0 1.5 ,2.0 ,2.5 and X/W=0.5.

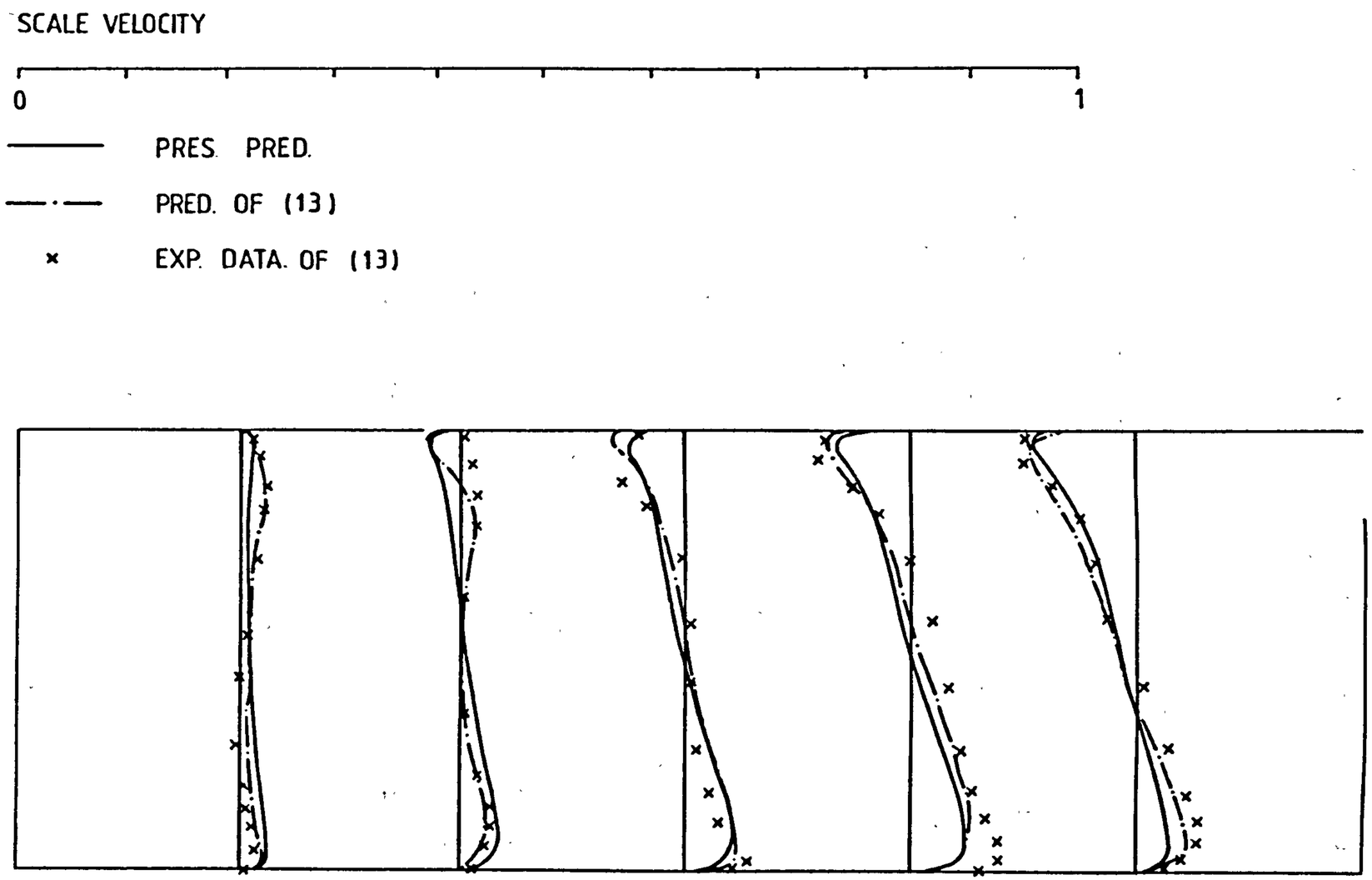

Figure 7.8 : Longitudinal velocity profiles at (Z/H)=0.5 ,1.0 1.5 ,2.0 ,2.5 and X/W=0.9.

the reverse flow close to the ceiling. Nevertheless, these discrepancies are less than 4.0% of the inlet velocity, even at the worst position (which is station $Z/_H$ = 1.0). A similar level of accuracy is also apparent in the predictions of Gosman etal (13).

The general features of the flow in this geometry are highlighted by ther velocity vector plots displayed in Figures 7.9 - 7.11 for three planes located at $X/_W$ = o.5, 0.83, and 0.98 respectively. The circulation patterns are clearly different in the three elevations, with the recirculating core of the flow being displaced upstream in near-wall position. This displacement is accompanied by a flow reversion near the bottom surface.

The computations of the flow field in geometry B will now be considered. In the published paper of Hjertager and Magnussen (15) the amount of the heat supplied [which was divided equally between panels in the far-wall and the floor, see Figure 7.1-b] was not given. In order to facilitate the simulation of this case for the present purposes, an arbitrary, uniform value for the temperature was employed for both the heater panels (see Table 7.2). In view of this, the comparisons between the present computations and those of Hjertager and Magnussen are of only qualitative rather than quantitative value.

Figure 7.12 shows the flow patterns in the symmetry plane computed using the ESCEAT code, along with its counterpart obtained by Hjertager and Magnussen (15). It can be seen that the location of the recirculation zones have been well reproduced by the present procedure, but the cold jet falls more rapidly toward the floor (a phenomenon known as 'dumping' in the heating and ventilating literature) than is suggested by Hjertager and Magnussen's predictions. This may indicate that the magnitude of the heat input assumed was rather higher than it should have been.

The computed distribution of the secondary velocity components are shown in Figure 7.13, where they are compared with the data of Hjertager and Magnussen (15). These are presented for six x-y planes, corresponding to Z = 0.5,1.5, 2.5, 3.5, 4.5 and 5.3 respectively. Both sets of computations are displayed as mirror images about the

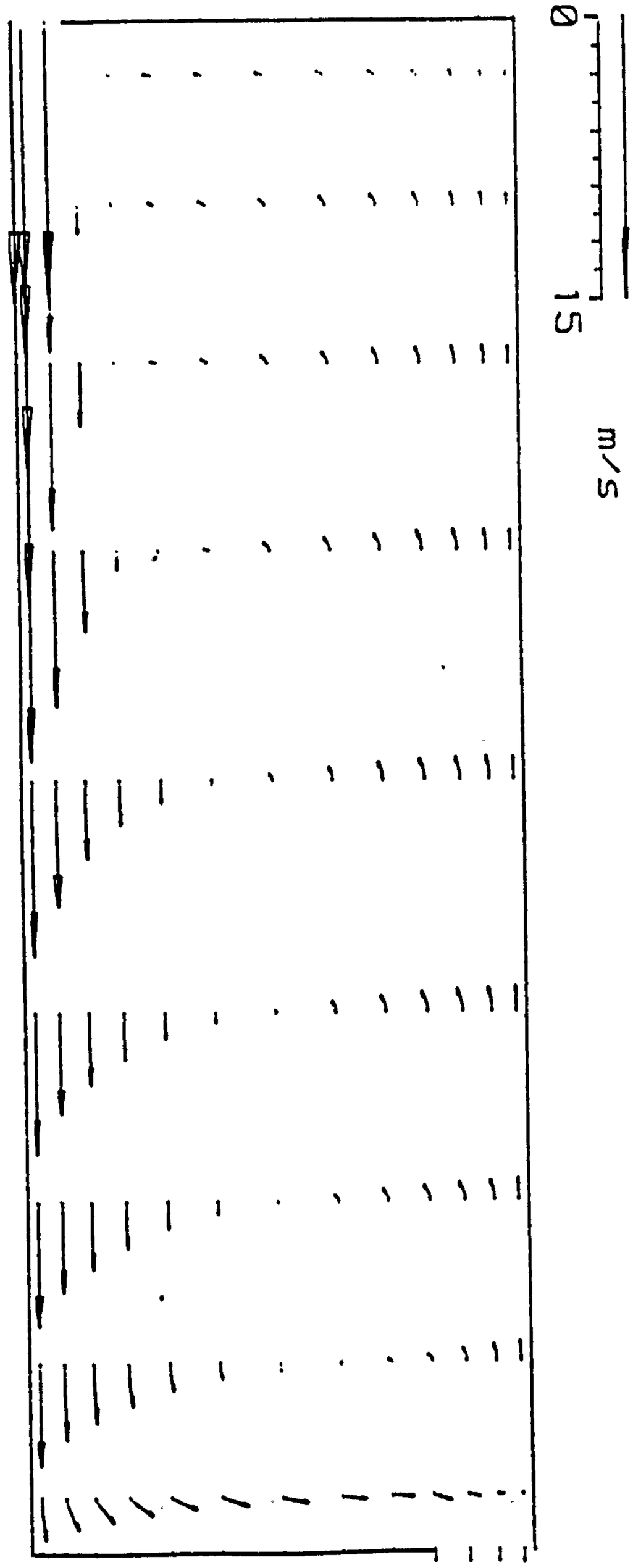

Fig. 7.9 : Velocity vectors at x/W=0.5 , geometry A .

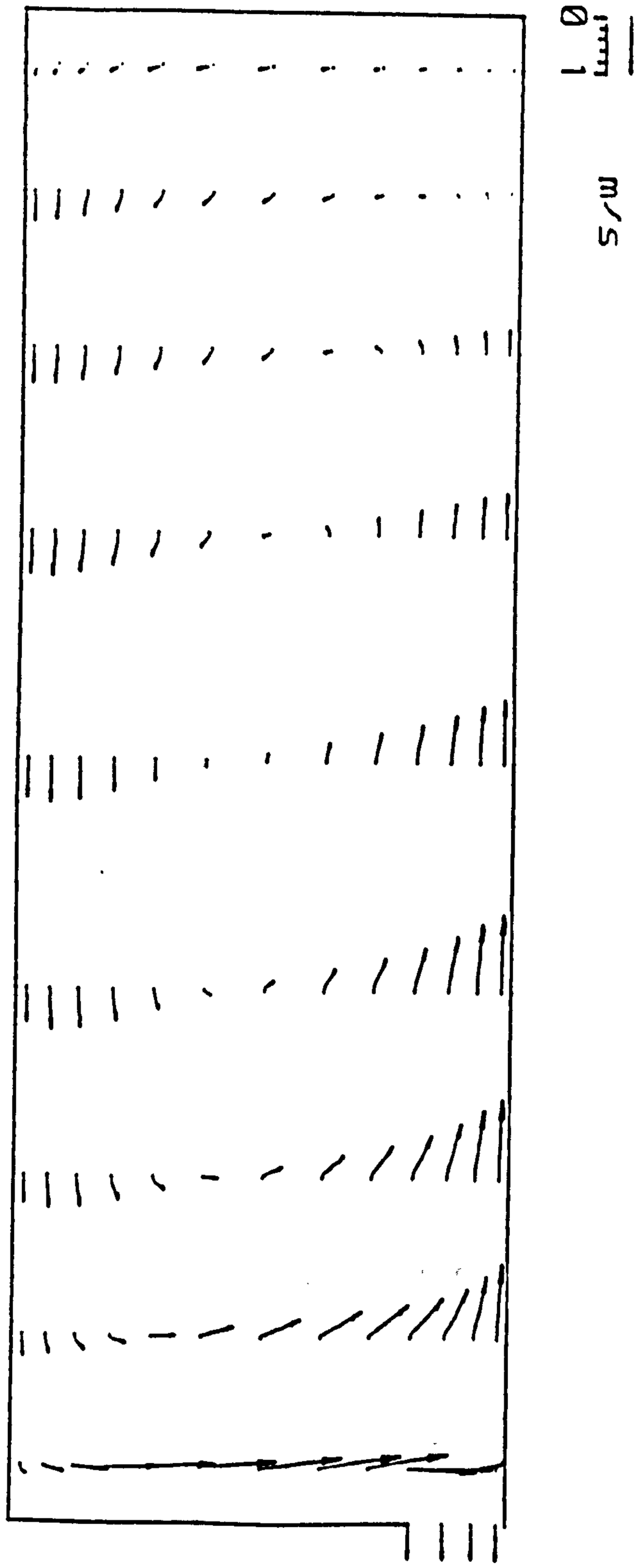

Fig. 7.10 : Velocity vectors at x/W=0.83 ,geometry A .

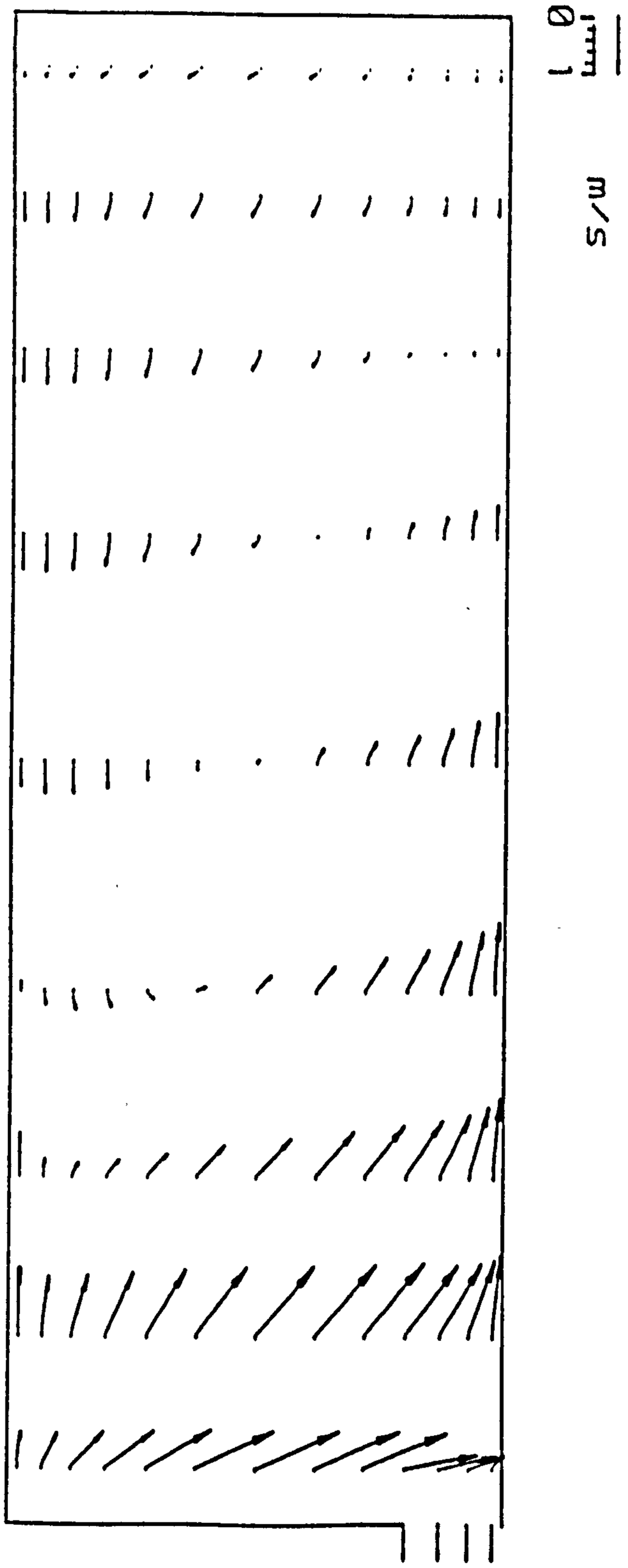

Fig. 7.11 : Velocity vectors at x/W=0.98 , geometry A .

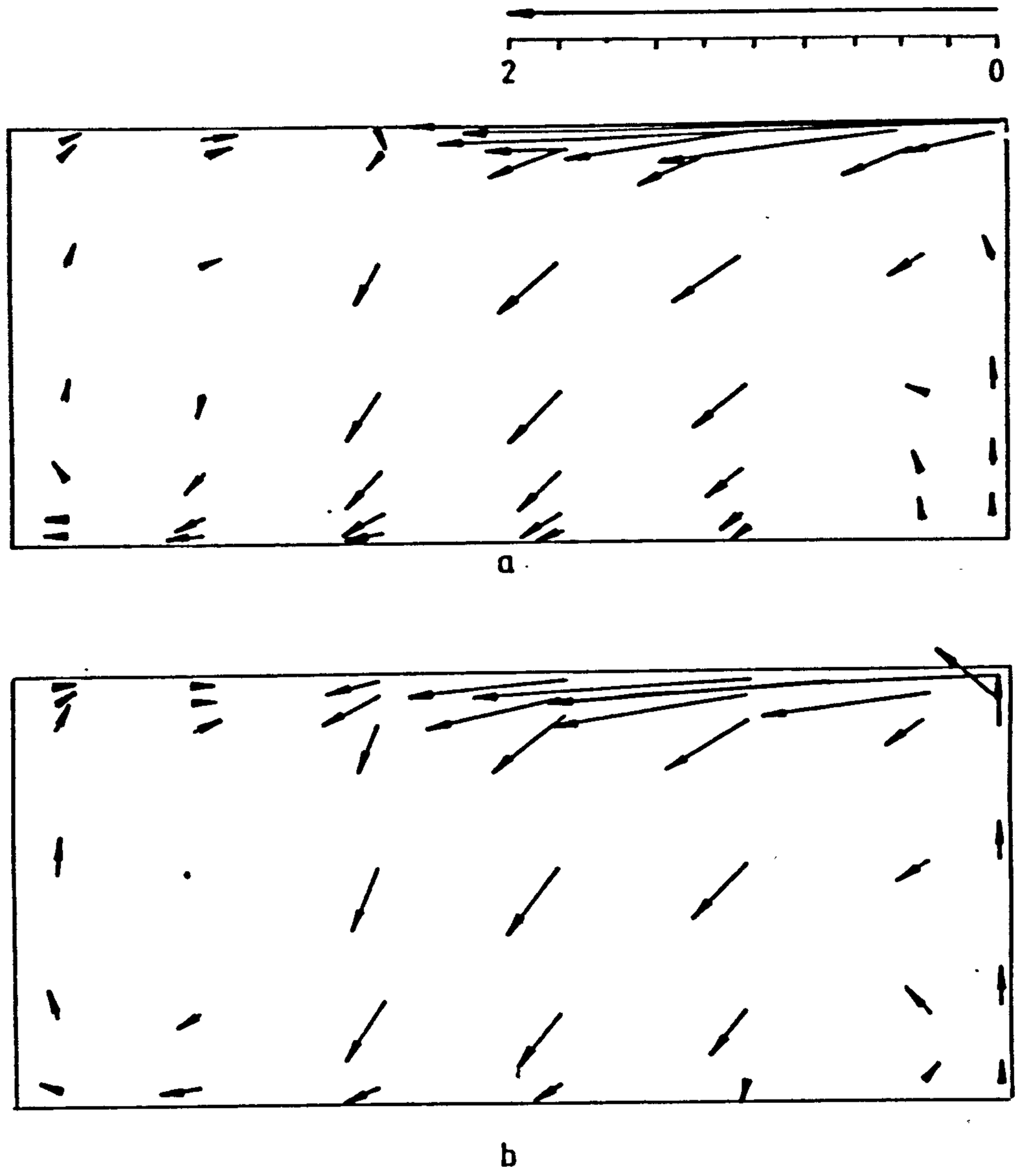

Fig. 7.12 : Comparison of velocity vectors in the symmetry plane of geometry B ,
(a) present computations ;and (b) pred. of (15).

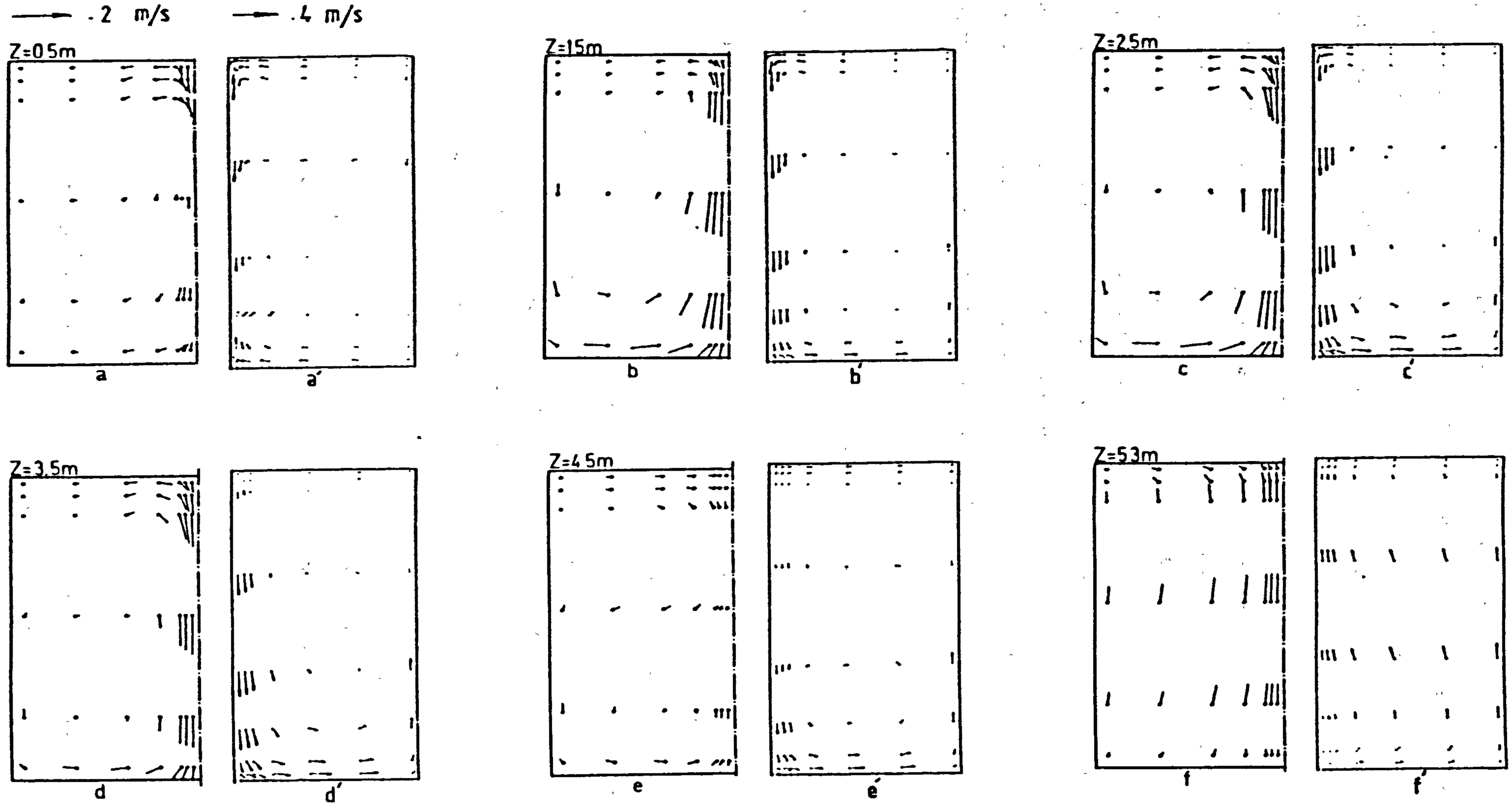

Fig. 7.13 : The distribution of the secondary veolcities in six X-Y planes of geometry C, (a'-f')present computation ;and (a-f) pred. of (15)

symmetry axis. It can be seen from these vector plots that the behaviour of the buoyancy-affected flow is reproduced reasonably well by the present code, despite the different grid distributions (especially in the Y-direction).

The results for the non-buoyant flow case (geometry C) are presented in Figure 7.14-20. In the following section these results are compared with the buoyant flow computations of Alamdari, Hammond and Mohammad (the bound paper) in order to highlight the influence of buoyancy effects on the flow and surface heat exchange.

The flow pattern induced by the non-buoyant jet is presented in Figures 7.14-15 as velocity vectors plots, at two cross planar locations; $X/_W$ = 0.5 and 0.75 respectively. The jet in these Figures appears to spread out from the inlet aperture and flow over the boundary surfaces, forming a single recirculating core close to the far-wall. Thus, there are significant differences between the present flow pattern and that generated by the buoyant jet [see Figure 3(b-c) of the bound paper]. The main difference is due to the damping (downdraught) effect caused by the cold window. The latter effect led to a counteracting downward movement of the air in the region adjacent to the window, and consequently to the generation of two recirculating flow zones within the room.

The surface distirbutions of the convective heat transfer coefficient are shown in Figures 7.16-20 for the five room surfaces; floor, far-wall and window, ceiling, near-wall and left-wall (when viewed from the supply register). The arrows that appears in these Figures show the direction of the flow over these surfaces. The variation of the convection coefficients in these Figures is caused only by the downstream decay of the jet velocities and temperatures, as no allowance is made for window downdraught. Nevertheless, it still gives a clear illustration of the overall distribution of these coefficients for the present non-buoyant flow case. The inclusion of buoyancy effects was found to greatly alter the surface heat transfer distributions (see Figures 4 (a-d and e) in the bound paper]. The damping effect of the cold window was again the main factor behind these changes, which are particularly evident in regard to the far-wall end window, ceiling and left-wall.

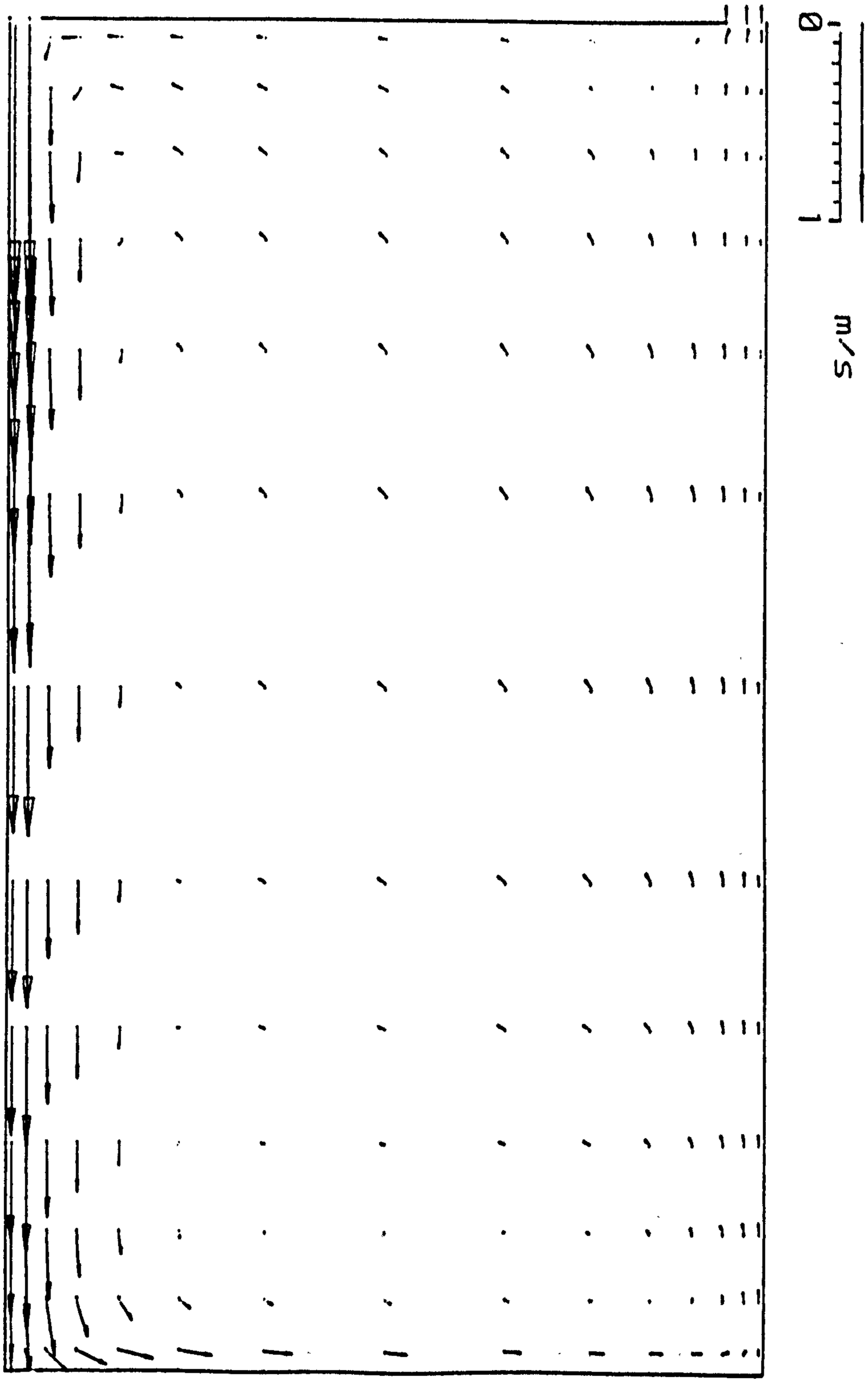

Figure 7.14 : Veolcity vectors at x/W=0.5, for the non-buoyant flow case .

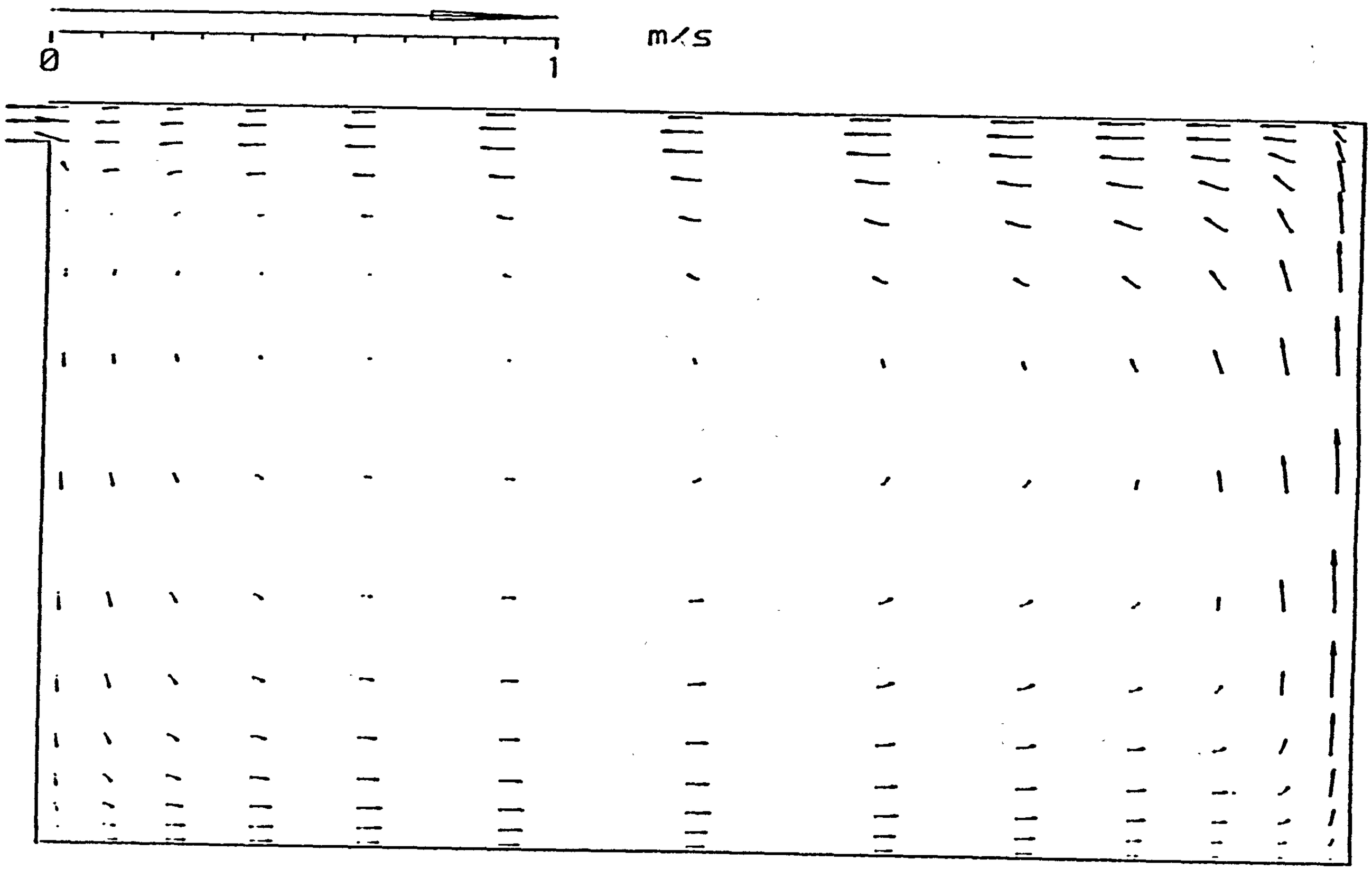

Figure 7.15 : Veolcity vectors at x/W=0.75 ,for the non-buoyant flow case .

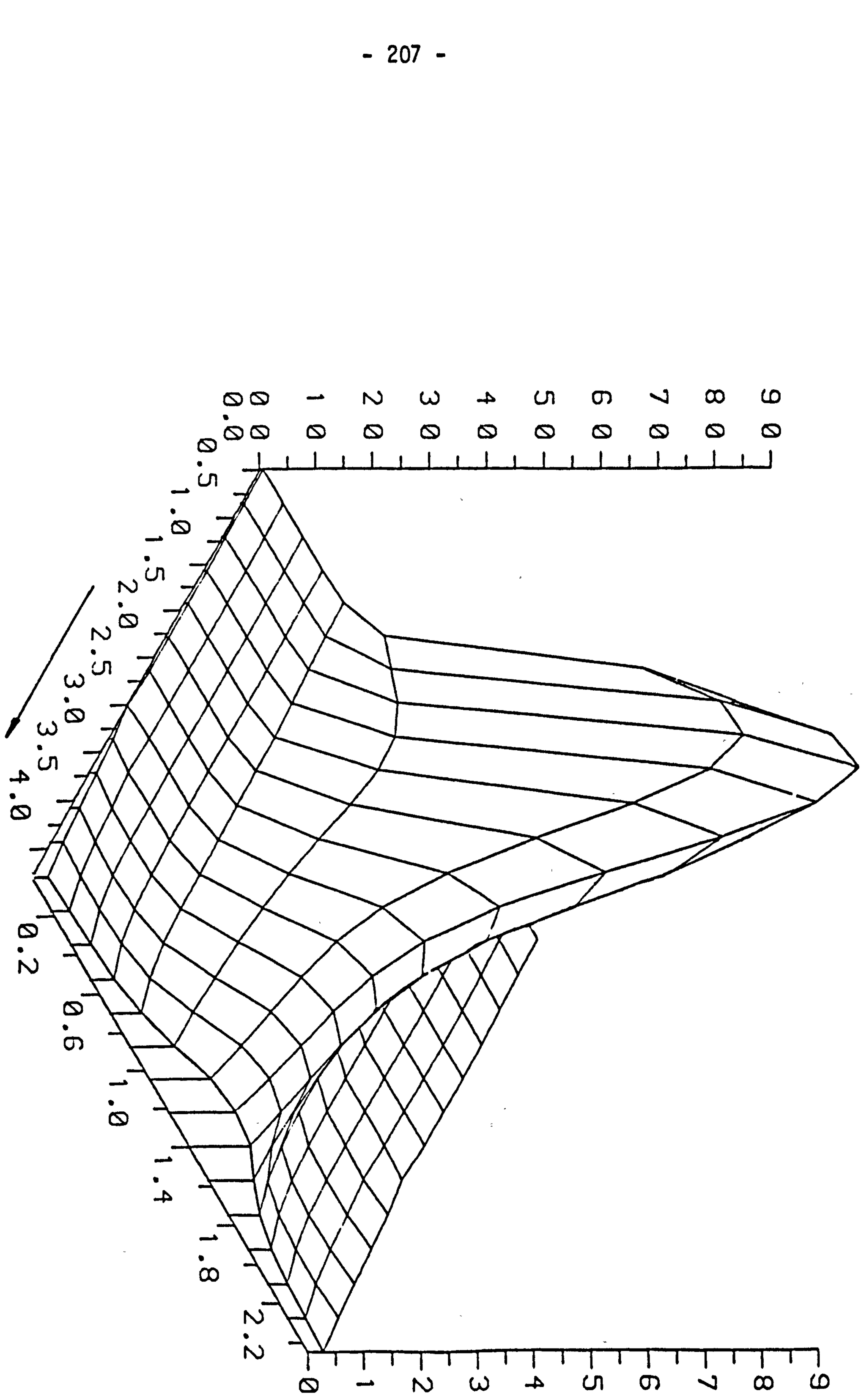

Fig. 7.16 : The distribution of heat-transfer coefficient over the floor.

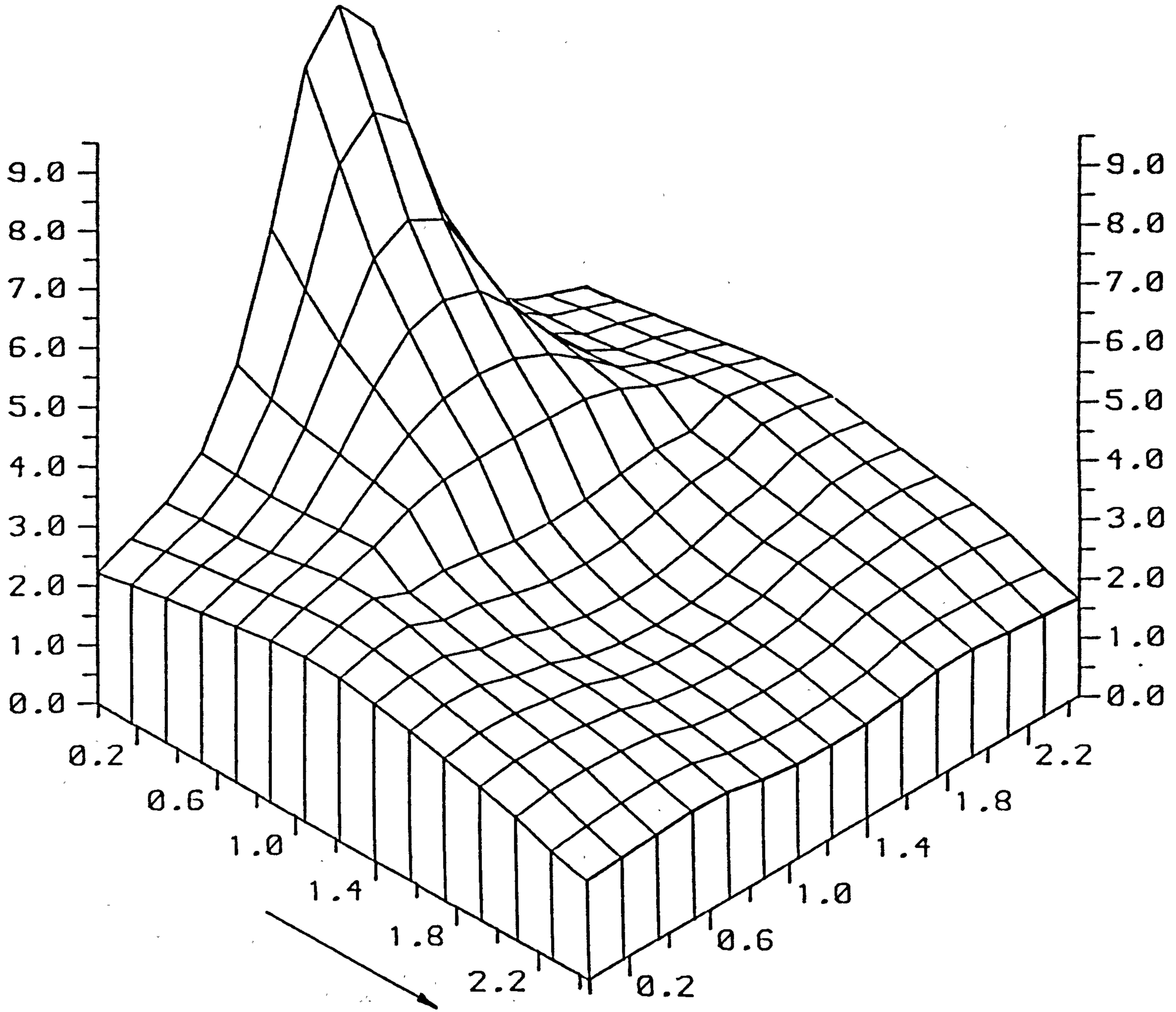

Fig. 7.17 : The distribution of heat-transfer coefficient over the far-wall and window

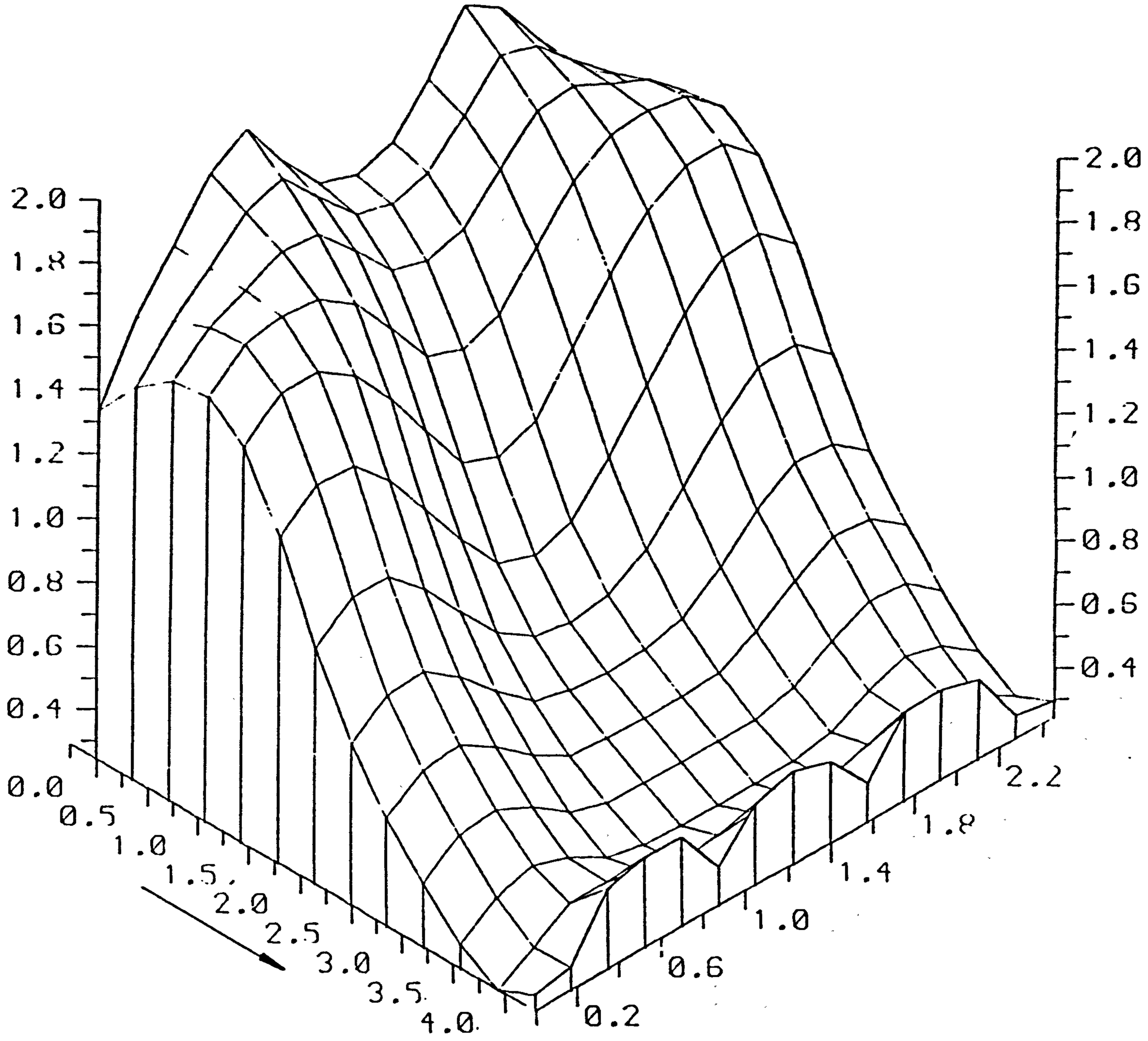

Fig. 7.18 : The distribution of heat-transfer coefficient over the ceiling.

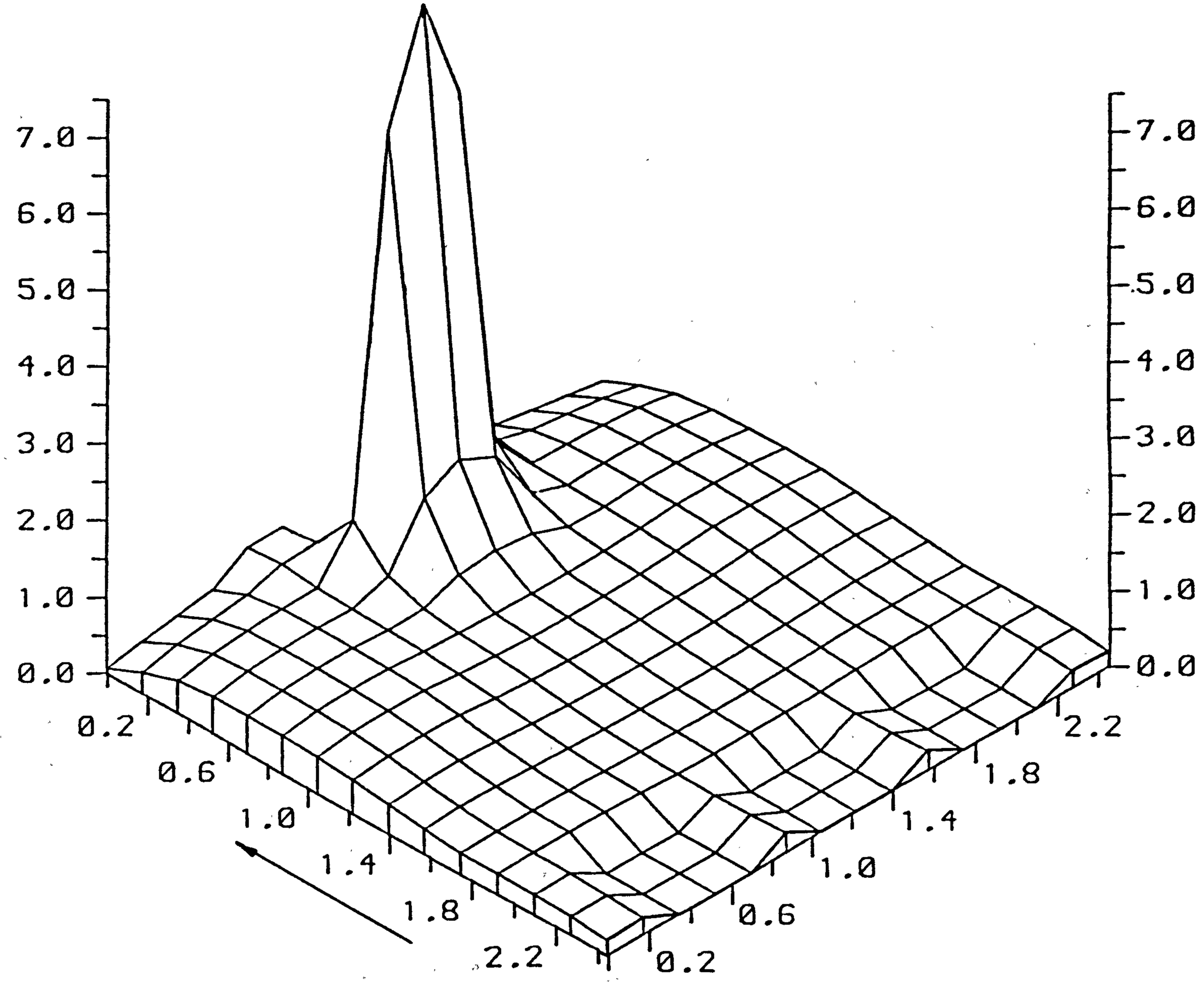

Fig. 7.19 : The distribution of heat-transfer coefficient over the near-wall.

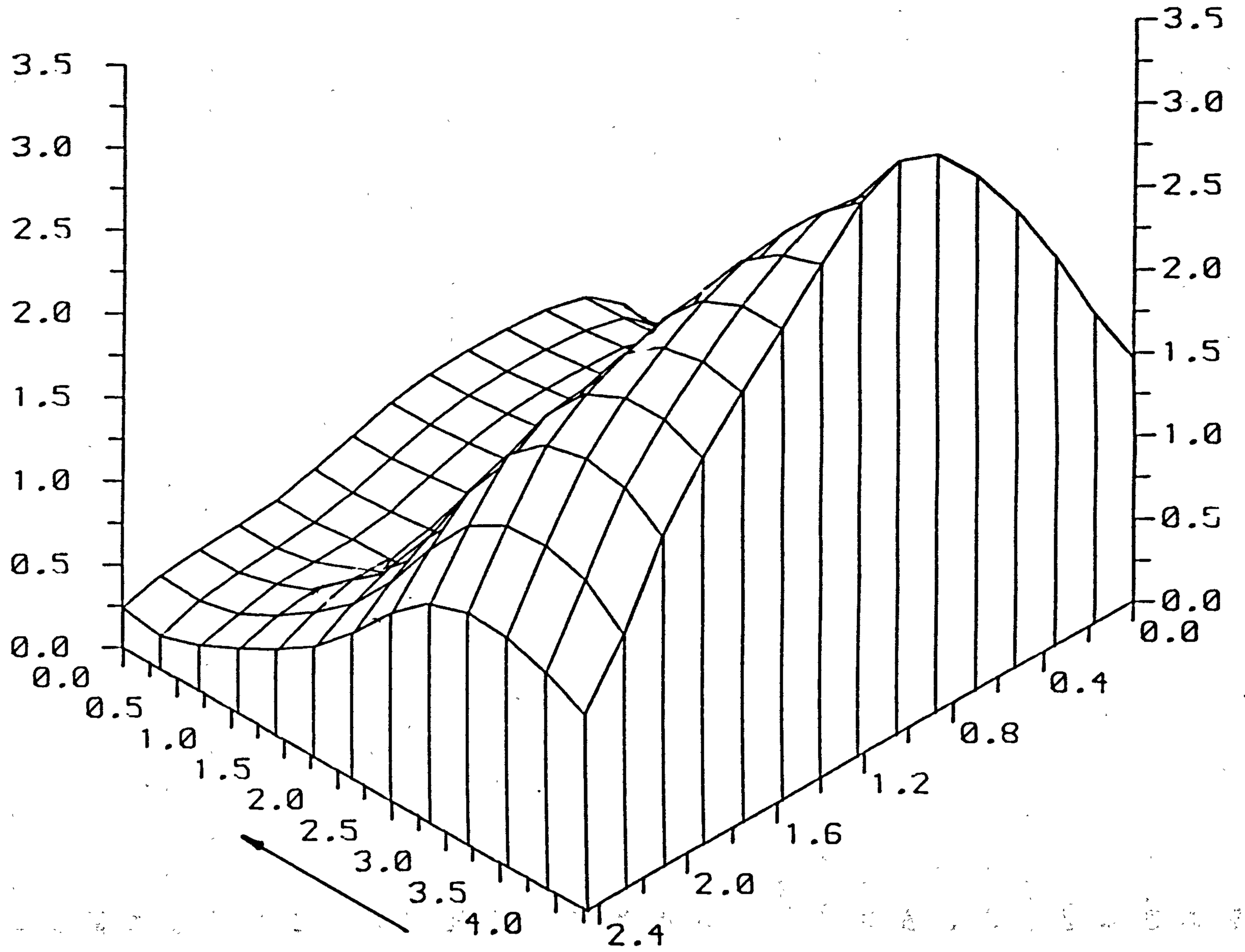

Fig. 7.20 : The distribution of heat-transfer coefficient over the left-wall.

The local distribution of the convection coefficient cannot be used directly in the dynamic building thermal models (see section 1.2.2 and the bound paper). Those models utilise surface-averaged values for each surface element; floor, ceiling, walls and windows (21,25). Such surface-averaged values are presented in Table 7.3, which also includes the corresponding buoyancy-affected flow values and those obtained from the intermediate-level computer code (the ROOM-CHT program) of Alamdari and Hammond (25). It is apparent from this table that the non-buoyant flow values are much closer to those of the ROOM-CHT Program than to the buoyancy-affected flow ones. This is simply because that the ROOM-CHT program also takes no account of the effect of buoyancy in its formulation. However, the ROOM-CHT program appears to give rather higher values for the convection coefficient, over all the room surfaces, than does the non-buoyant version of the ESCEAT code. This may be attributed to the neglect of flow interactions in the former code and the adoption of purely buoyancy-driven convective values if these are higher than the local wall-jet values. The ROOM-CHT program and the non-buoyant version of the ESCEAT code both predict the maximum surface-averaged value to occur over the floor element, while the buoyant version of the latter code suggests that it occurs on the ceiling. This is mainly due to the generation, in practice, of the counteracting air movement near the cold window that forces the hot, buoyant jet to rise upward as it emitted form the supply register [see Figure 3 (b-c) in the bound paper]. This consequently gives rise to a greater heat exchange with the ceiling. It is also clear from the Table (7.3) that the employment of a non-buoyant calculation procedure to simulate warm-air heating has led to relatively low values for the convection coefficient over most of the other room surfaces; particularly the ceiling, near-wall and left-wall. The national room-averaged coefficient given by this non-buoyant procedure was 1.9 Wm^{-2} K^{-1}, which is only about 45% of that obtained from the ROOM-CHT program and the buoyant version of the ESCEAT code. The overall conclusion that can be drawn from the above discussion is that the neglect of the influence of buoyancy in simulating practical air-conditioning situations leads to the computation of unrealistically low values for convection heat transfer.

Surface Elements	ESCEAT Code		ROOM-CHT program
	Buoyent Version	Non-buoyant Version	
Floor	2.4	4.1	6.4
Far-wall	2.4	2.9	3.5
Far-window	2.2	2.6	3.5
Ceiling	6.9	1.0	3.9
Near-wall	2.2	0.5	2.4
Left-wall	3.3	1.2	1.8

Table 7.3 Internal surface-averaged convection coefficients (h_c Wm^{-2} K^{-1})

While undertaking the computations for the above non-buoyant flow case, it was found that the heat balance on the ventilated room gave rise to very high temperature (34°C) in the occupation zone. However, this was reduced to 23.5 °C by modifying the wall functions in a way formerly employed [see Launder and Spalding (45)] for backward-facing surfaces in gas film-cooling simulations. Further details of this practice are given by Alamdari, Hammond and Mohammad (1986, bound paper), who employed it for the buoyant flow computations.

7.4 SOME COMPUTATIONAL ASPECTS

The above calculations were performed on a DEC VAX 8650 computer. The number of iterations required for a converged solution were found to be highly dependent on the number of grid nodes in the solution-domain, and the type of the flow (i.e. isothermal, non-buoyant or buoyant) to be simulated. The refinement of the grid, and consequent increase in the number of nodes, leads to a more than proportional increase in the computing time required to obtain a convergent solution. The simulation of buoyancy-affected flows was also found to require greater CPU time than the non-buoyant ones. The latter problem was reduced in the present study by the use of 'inertia relaxation' method devised by Ideriah (63) (for details see section 3.5.2). The time required to obtain a solution for the flow fields associated with each of the three test geometries are given in Table 7.4.

Geometry	Type of flow	Grid system	No. of iteration	CPU time (min)
A	Isothermal	11x15x11	110	≈ 20.0
B	Buoyant	9x10x9	208	≈ 23.0
C	Non-buoyant	9x17x15	112	≈ 35.0

Table 7.4. The CPU time required for solving the flow associated with geometry A,B and C.

7.5 CONCLUDING REMARKS

Several applications of the ESCEAT computer code, to three-dimensional turbulent flows within mechanically-ventilated rooms have been presented. These included the simulation of three different ventilation arrangements involving isothermal, non-buoyant and buoyancy-affected flows. The latter flows were simulated by including additional buoyancy source terms into the momentum, K and ε transport equations. A power-law differencing scheme was used in formulating the relevant finite-domain coefficients for all the variables. The velocity components and pressure were updated using the SIMPLEC algorithm (70), which is a consistent varient of SIMPLE (68) that induces rather faster rate of convergence.

Two of the ventilation arrangements that were examined had previously been simulated by earlier researchers. An additional geometry was examined in order to model a more practical geometry. This was a warm-air heated room previously adopted by Alamdari and Hammond(25). An inlet cell approach was employed to specify the flow properties near the supply register in these arrangements. This obviated the need for very finely-spaced grid in the inlet, and also helped to improve the agreement with the experimental measurements. However, it was not used for the buoyant flow case owing to the lack of the data appropriate for prescribing the properties in such a complex flow.

The computations of the field velocity distribution for both isothermal and buoyancy-affected flows, were shown to be in good agreement with available experimental data and previous numerical predictions. The flow pattern predicted by previous investigators were reproduced fairly well in the present study. In the case of the non-buoyant flow, the computed flow pattern and surface heat transfer distribution were compared with those of the buoyancy-affected flow reported by Alamdari, Hammond and Mohammad (1986, bound paper). The comparison reveals that the non-buoyant flow value of the convective coefficient was about 45% of its buoyant counterpart.

CHAPTER 8

CONCLUSIONS AND RECOMMENDATIONS

8.0 CONCLUSIONS AND RECOMMENDATIONS

8.1 CONCLUDING REMARKS

Several numerical studies have been undertaken to investigate the fluid flow and heat transfer that was induced by two- and three-dimensional wall-bounded jets. Such jets often determine the flow and thermal comfort conditions within mechanically-ventilated spaces that employ linear and rectangular 'diffusers'. The present studies involved the solution of finite-domain analogues to the governing 'elliptic' equations for the turbulent, recirculating flows. Closure of the time-averaged momentum equations was obtained through the use of an isotropic 'eddy' viscosity, or turbulent energy exchange coefficient for momentum, calculated via transport equations for both the turbulent kinetic energy and its dissipation rate. The transport of heat was modelled using the effective Prandtl number approach, while 'wall functions' were employed to bridge the steep dependent variable gradients in near-wall regions. Several alternative differencing schemes (including upwind, hybrid, power-law and QUICK formulations) have been employed in formulating the relevant finite-domain equations. Accuracy and economy were the main factors that determined the choice of a particular scheme. The SIMPLEC procedure devised by Doormaal and Raithby (70), and which is a rather more consistent version of the popular SIMPLE algorithm of Patankar and Spalding (68), has been used to solve these equations. It was adopted here because it has been shown to offer a rather faster rate of convergence. However, the latter was also enhanced by the use of either block-adjustment or overall continuity correction procedures.

The initial investigations involved the simulation of flows induced by two-dimensional turbulent off-set jets. A modified version of the CHAMPION code of Pun and Spalding (34) was used to solve the finite-domain equation in this case. The computations covered a wide range of offset ratios, and have been compared with several sets of experimental data for both the flow and thermal fields. Reasonable agreement was observed between the computed and measured properties especially within the so called wall-jet region of the flow domain. However, the computed reattachment point was under-predicted and this was attributed to the assumption regarding the approach (inlet)

profiles, the limitations of the turbulence model adopted (including the wall functions), and to the usual uncertainties associated with experimental data.

A fully elliptic computational procedure has been developed to carry out the three-dimensional part of the present investigations. This procedure has been incorporated into a computer program called ESCEAT, which is currently able to handle three-dimensional flows within rectangular geometries. The code was also extended to simulate buoyancy-affected flows by allowing for the effects of the buoyancy on the vertical velocity component and on the turbulence quantities.

The ESCEAT code was initially employed to simulate two relatively simple laminar flow test cases (the flow through a rectangular sudden expansion and flow in a cavity with moving lid), and then the more complex case of developing turbulent flow in a square duct. The latter flow is strictly 'partially-parabolic', as elliptic influences are limited to the secondary motion. Nevertheless, the simulation of all the test cases were basically undertaken in order to validate and assess the capabilities of the computer code. The computed results for these test cases displayed fairly good agreement with both measured data and the predictions of previous numerical modellers. The success of these computations led to the employment of the code to simulate the flow and thermal field found within mechanically-ventilated rooms. Three different ventilation arrangements were examined in this study. Two of these geometries were previously used by other researchers, and were partly adopted for validation purposes. The third geometry studies, warm-air heating of domestic rooms, was employed in order to represent a more practical flow geometry from the point of view of the built environment. Isothermal, non-buoyant and buoyancy-affected flows have been considered in these situations.

The jet supply conditions for both the isothermal and non-buoyant flows, were prescribed on the basis of jet development assumptions, using available data for three-dimensional wall-jets. This approach, which was primarily adopted [following Nielson et al (12)] to reduce the need for finely-spaced grid within and near small inlet registors of large ventilated rooms, did not cause any systematic deterioration

of prediction accuracy. However, it could not be employed for the simulation of buoyancy-affected flows, due to the lack of data required for prescribing the flow and thermal properties in such a complex situation.

The computations of the three flow geometries were again compared with various sets of experimental data and numerical prediction of previous researchers. The comparison of the isothermal flow revealed generally good agreement with earlier results. Qualitative agreement with previous numerical predictions was also obtained for the buoyancy-affected flow case. The non-buoyant simulation of the warm-air heated rooms, on the other hand, indicated that the neglect of the influence of buoyancy led to unrealistically low values for the convective heat transfer.

The ESCEAT code was finally used in a comparative study along with the intermediate-level convection model of Alamdari and Hammond (25) (see Alamdari, Hammond and Mohammad, bound paper). The latter model was designed to generate input convective heat transfer data for building thermal models. The warm-air heating case study, chosen for validation purposes, involved the simulation of turbulent flow with significant buoyancy effects. The computed heat transfer coefficients from both the higher and intermediate-level models was compared. This showed the intermediate-level model to be an attractive alternative method that can meet the needs of building thermal modellers by providing adequate accuracy for only a modest computing cost.

High-level flow models of the type used in the present study can be regarded as an effective alternative to the extensive measurements that are required to obtain comprehensive data on the flow and heat transfer within mechanically-ventilated rooms. This assertion is supported by the generally good agreement shown between the computations and experimental data.

8.2 SUGGESTIONS FOR FUTURE RESEARCH

The following lines of future research are suggested to improve both the accuracy and economy of the computations presented in this study.

Shortcomings were evident in the computed reattachment distance and the flow properties in the recirculation zone of the offset jet flows. These two-dimensional computations might be improved by accounting for the effects of wall-damping and streamline curvature in the K-ε model of turbulence. According to recent studies by Gooray et al (102), modifying the eddy viscosity coeffient (C_D) to simulate these effects leads to reattachment lengths which are consistent with measurements undertaken for flows through pipe expansions and over rear-ward facing steps. Attaching jet flows resemble some of the features associated with flows through pipe expansions and over rear-ward facing steps, and therefore the inclusion of these modifications might improve the present computations.

Improvement in the computation can also be anticipated by refinement in the wall functions to account for the low turbulence Reynolds number effects in the near-wall region, especially for the recirculating flows. The modelled form proposed by Chieng and Launder (57) is an example of such refinements. However, the emphasis in the research programme currently in progress at Cranfield is to generate improved wall functions for surface shear stress and heat transfer by employing a turbulent shear layer profile analysis, together with other assumptions about the turbulence structure within the diffusive sublayer. The first step in this direction is the recently published study by Hammond (133,134) of the behaviour of the turbulent Prandtl number within the constant stress/heat-flux region of a near-wall flow. The research now underway involves extensions to cases with variable stress/heat-flux distribution normal to the wall, and with surface roughness characteristics typical of the built environment.

The specification of the inlet (approach) profiles, especially for turbulence quantities such as the turbulent kinetic energy and its dissipation rate, are critical for computations that simulate recirculating flows. An effective way to minimise the sensitivity of

the computed results to these profiles is the use of information deduced from related experimental measurements.

An improvement to the rate of convergence when simulating flows with significant buoyance effect, might be achieved by retaining the use of the three sweep procedure, but with a better choice on the value of the constant α_I in Ideriah's inertia relaxation method (see equation (3.73).

The employment of a general coordinate system, in which the computational grid is matched to any complex-shaped flow field, could be obtained via three-dimensional co-ordinate transformation. It is desirable to develop such adjusting grids for the ESCEAT code.

REFERENCES

REFERENCES

1. LINKE W
"Aspects of jet ventilation", Kaltetechnick - Klinatislerong, Vol. 18, 1966, pp 122-126 (HVRA Translation 103).

2. YOUSOUFIAN H H
"Diffusion and distribution from ceiling and wall outlets", Heat. Pip. Air Condit., Vol. 38, 1966, pp 124-131.

3. STRAUB H E
"Principles of room air distribution", Heat. Pip. Air Cond., Vol. 41, 1969, pp 122-128.

4. JACKMAN P J
"Air movement in rooms with side-wall mounted grilles - a design procedure", HVRA Laboratory Report No.65, 1970.

5. JACKMAN P J
"Air movement in rooms with sill-mounted grilles - a design procedure", HVRA Laboratory Report No.71, 1971.

6. NEVINS P G
"Air distribution research", ASHRAE Journal, 1971, p 63.

7. NEVINS R G and MILLER P L
"Analysis of the performance of room air distribution systems", ASHRAE Trans., Vol. 78, 1972, pp 191-198.

8. NEVINS R G and MILLER P L
"Analysis, evaluation and comparison of room air distribution performance - summary", ASHRAE Trans., Vol. 2, 1972, pp 235-242.

9. CROOM D J and ROBERTS B M
"Air conditioning and ventilation of buildings", Pergamon Press, Oxford, 1975.

10. NIELSEN P V
"Prediction of air flow and comfort in air conditioning spaces", ASHRAE Trans., Vol. 81, 1975, p 247.

11. NIELSEN P V, RESTIVO A and WHITELAW J H
"The velocity characteristics of ventilated rooms", ASME, J. Fluid Eng., Vol. 100, 1978, pp 291-298.

12. NIELSEN P V, RESTIVO A and WHITELAW J H
"Buoyancy affected flows in ventilated rooms", Num. Heat Transfer, Vol. 2, 1979, pp 115-127.

13. GOSMAN A D, NIELSEN P V, RESTIVO A and WHITELAW J H
"The flow properties of rooms with small ventilation openings", Trans. SME, J. Fluid Mech., Vol. 102, 1980, pp 317-323.

14. SAKAMOTO Y and MASKSUO Y
"Numerical predictions of three-dimensional flow in a ventilated room using turbulence models", Appl. Math. Modelling, Vol. 4, 1980, pp 67-72.

15. HJERTAGER B H and MAGNUSSEN B F
"Numerical prediction of three dimensional buoyant flow in a ventilated room", Heat Transfer and Buoyant Convection, Hemisphere, Washington, Vol. 2, 1972, pp 429-441.

16. HJERTAGER B H and MAGNUSSEN B F
"Calculation of turbulent three-dimensional jet induced in rectangular enclosures", Comp. Fluid, Vol. 9, 1981, pp 395-407.

17. NIELSEN P V
"Mathematical models for room air distribution", Proc. International Conf. System Simulation in Buildings, Belgium, 1982.

18. HARRIS N C
"Modern air conditioning practice", McGraw-Hill International Book Company, 1983.

19. LIDDAMENT M and THOMPSON C
"A review of building air tightness and ventilation standards", IEA; Energy Conservation in Building and Community systems programme, Technical Note AIC 14, 1984.

20. CAROLL D
"Energy consumption and conservation in building; an international comparison", Proc. 3rd Int. Symp. "Energy conservation in the built environment", Dalsling, Ireland, 1A, 190, 1982.

21. ALAMDARI F, HAMMOND G P and MELO C
"Appropriate calculation methods for convective heat transfer from building surfaces", Proc. First UK National Heat Transfer Conf., Leeds, vol. 2, 1984, pp 1201-1211.

22. IRVING S J
"Energy program vilidation", Conclusion of IEA Annex 1, Computer-aided Design, Vol. 4, 1982, pp 33-38.

23. ASHRAE
"Handbook of Fundamentals", New York, 1981.

24. CIBSE GUIDE, C3.
"Heat Transfer", London, 1976.

25. ALAMDARI F and HAMMOND G P
"Time-dependent convective heat transfer in warm-air heated rooms", Proc. 3rd Int. Symp., Energy conservation in the built environment, Dublin, Vol. 4, 1982, pp 209-220.

26. YANESKE P P and FORREST I D
"The thermal response of rooms with intermitent force convective heating", Building Service Engineer, Vol. 46, 1978, pp 13-17.

27. ALAMDARI F, CHAN J K C and HAMMOND G P
"An intermediate-level model of heat transfer for mechanically ventilated enclosures with 'linear' supply aperatures", Cranfield Institute of Technology, UK, report, SME/J/84/04, 1984.

28. WATERS J R
"The experimental verification of a computerised thermal model for buildings", BSER & T, Vol. 1, 1980, pp 76-82.

29. HAMMOND G P
"Complete velocity profile and 'optimum' skin friction formulas for the plane wall-jet", ASME J., Fluid Eng., Vol. 104, 1982, pp 59-66.

30. HAMMOND G P "Profile analysis of heat/mass transfer across the plane wall-jet", Proc. 7th Int. Heat Transfer Conf., Munich, Vol. 3, 1982, pp 345-355.

31. ALAMDARI F and HAMMOND G P
"Improved data correlations for buoyancy-driven convection in rooms", BSER & T, Vol. 4, 1983, pp 106-112.

32. ALAMDARI F
"Convective heat transfer within mechanically ventilated spaces", PhD thesis, Cranfield Institute of Technology, UK, 1984.

33. ALAMDARI F, HAMMOND G P and MONTAZERIN N
"Heat/mass transfer beneath a two-dimensional wall-jet deflected by a normal, flate-plate obstruction", Proc. 8th Int. Heat Transfer Conf., San Francisco, 1986 (Hemisphere, Washington; in press).

34. PUN W M and SPALDING D B
"A general computer program for two-dimensional elliptic flows", Imperial College (London), Mech. Eng. Dept. Report HTS/76/2, Amended 1977.

35. CEBECI T and BRADSHAW P
"Momentum transfer in boundary layers", Hemisphere, Washington, 1977.

36. GOSMAN A D, PUN W M, RUNCHAL A K, SPALDING D B and WOLFSHTEIN M
"Heat and mass transfer in recirculating flows", Academic Press, London/New York, 1969.

37. BRADSHAW P
"An introduction to turbulence and its measurement", Pergamon, Oxford, 1971.

38. HINZE J O
"Turbulence", McGraw Hill, New York, 1959.

39. LAUNDER B E and SPALDING D B
"Mathematical models of turbulence", Academic Press, London/New York, 1972.

40. LAUNDER B E
"On the effects of a gravitational fields on the turbulent transport of heat and momentum", Journal of Fluid Mechanics, Vol. 67, 1975, pp 569-581.

41. LAUNDER B E, REECE G J and RODI W
"Progress in the development of Reynolds-stress turbulence closure", Journal of Fluid Mechanics, Vol. 68, 1975, pp 537-566.

42. RODI W
"Examples of turbulence model for incompressible flows", AIAA Journal, Vol. 20, 1982, pp 872-879.

43. REYNOLDS W C
"Computation of turbulent flows", Annual Review of fluid mechanics, vol. 8, 1976, pp 183-208.

44. BRADSHAW P, FERRISS D H and ATWELL N P
"Calculation of boundary-layer development using the turbulent energy equation", Journal of Fluid Mechanics, Vol. 28, 1967, pp 491-511.

45. LAUNDER B E and SPALDING D B
"The numerical computational of turbulent flows", Computer Methods in Appl. Mech. and Eng., Vol. 3, 1974, pp 269-289.

46. MATHEWS L and WHITELAW J H
"Plane-jet flow over a backward-facing step", Heat and Fluid Flow, Vol. 3, 1973, p 133.

47. JONES W P and McGUIRK J J
"Computation of a round turbulent jet discharging into a confined cross flow", Turbulent Shear Flow 2, Sprigner-Verlag, Heidelberg, 1980, pp 233-245.

48. AMANO R S
"A study of turbulent flow down-stream of an abrupt pipe expansion, AIAA Journal, Vol. 21, 1983, pp 1400-1405.

49. LEWELLEN W S, TESKE M and DONALDSON C dup
"Variable density flows computed by a second-order closure description of turbulence", AIAA Journal, Vol. 14, 1976, pp 382-379.

50. GIBSON M M and LAUNDER B E
"Ground effects on pressure fluctuations in the atmospheric boundary layer", Journal of Fluid Mechanics, Vol. 86, 1978, pp 491-511.

51. PATANKAR S V and SPALDING D B
"Heat and mass transfer in boundary layers", Intertext book, London, 1970.

52. LAUNDER B E and YING W M
"Prediction of flow and heat transfer in ducts of square cross-section", Heat and Fluid Flow, Vol.3, 1973, p 115.

53. POPE S B and WHITELAW J H
"The calculation of near-wake flows", Journal of Fluid Mechanics, Vol. 73, 1976, pp 9-32.

54. HARLAW F H and NAKAYAMA P
"Transport of turbulence energy decay rate", Los Alamos Scientific Lab, University of California, Report LA-3854, 1968.

55. McQUIRK J J, TAYLOR AM KP and WHITLAW J H
"Assessment of normal diffussion in upwind differencing calculation of turbulent recirculation flows", Turbulent Shear Flows, 1982, pp 206-224.

56. McGUIRK J J and RODI W
"A depth-averaged mathematical model for the near field of side discharges into open-channel flow", Journal of Fluid Mechanics, Vol. 86, 1978, pp 761-781.

57. CHIENG C C and LAUNDER B E
"On the calculation of turbulent heat transfer down-stream from an abrupt pipe expansion", Numerical Heat Transfer, Vol. 3, 1980, pp 189-207.

58. HASSAIN M S and RODI W
"Influence of buoyancy on the turbulence intensities in horizontal and vertical jets", Heat transfer and turbulent buoyant convection, Vol. 1, Hemisphere Publishing Corporation, Washington, 1977.

59. LAUNDER B E, PRIDDIN C H and SHARMA B I
'The calculation of turbulent boundary layer on spinning and curved surfaces", Journal of Fluid Engineering, March, 1977, pp 231-239.

60. RODI W
"Influence of buoyancy and rotation on equation for the turbulent length scales", Second Symp. on Turbulent Shear Flows, Imperial College, London, 1979, pp 10.37 - 10.42.

61. JAYATILLAKA C L
"The influence of Prandtl number and surface roughness on the resistance of laminar sub-layer to momentum and heat transfer", Progress in Heat and Mass Transfer, Vol. 1, 1969, pp 193-229.

62. KUMAR S and COX G
"The application of numerical field model of smoke movement to the physical scaling of compartment fires", Numerical Methods in Thermal Problems, Proceeding of the third International Conf., Seattly, USA, 1983, Pineridge Press, Swansea, UK, pp 837-848.

63. IDERIAH F J K
"Prediction of turbulent cavity flow driven by buoyancy and shear", Journal of Mechanical Engineering Science, Vol. 22, 1980, pp 287-295.

64. MARKATOS N C, MALIN M R and COX G
"Mathematical modelling of buoyancy-induced smoke flow in enclosures", Int. Journal of Heat and Mass Transfer, Vol. 25, 1982, pp 63-75.

65. PATANKAR S V
"Numerical heat transfer and fluid flow", Hemisphere, Washington, 1980.

66. HARLOW F H and WELCH J E
"Numerical calculation of time-dependent viscous incompressible flow of fluid with free surface", Physics of Fluids, Vol. 8, 1965, pp 2182 - 2189.

67. AMSDEN A A and HARLOW F H
"The SMAC Method", Los Alamos Scientific Laboratory Report LA-4370, 1970.

68. PATANKAR S V and SPALDING D B
"A calculation procedure for heat, mass and momentum transfer in three-dimensional parabolic flows", Int. Journal of Heat and Mass Transfer, Vol. 15, 1972, pp 1787-1806.

69. PATANKAR S V
"A calculation procedure for two-dimensional elliptic situation", Numerical Heat Transfer, Vol. 4, 1981, pp 409-425.

70. DOORMAAL J P and RAITHBY G D
"Enhancements of the SIMPLE method for predicting incompressible fluid flows", Numerical Heat Transfer, Vol. 7, 1984, pp 147-163.

71. RUNCHAL A K
"Convergence and accuracy of the three finite difference shemes for a two-dimensional convection and diffusion problem", Int. Journal of Numerical Methods in Engineering, Vol. 41, 1972, pp 541-550.

72. SPALDING D B
"A novel finite-difference formulation for differential expressions involving both first and second derivatives", Int. Journal of Numerical methods in Engineering, Vol. 4, 1972, pp 551-559.

73. RUNCHAL A K and WOLFSHTEIN M
"Numerical Integration procedure for steady state Navier-Stokes equations", Journal of Mechanical Engineering Science, Vol. 11, 1969, pp 445-453.

74. LEONARD B P
"A stable and accurate convective modelling procedure based on quadratic upstream interpolation", Comp. Meth. in Appl. Mech. Eng., Vol. 19, 1979, pp 59-98.

75. LESCHZINER M A
"Practical evaluation of three finite-difference schemes for the computation of stready-state recirculating flows", Comp. Meth. in Appl. Mech. Eng., Vol. 23, 1980, pp 293-312.

76. HAN T HUMPHARY J A C and LAUNDER B E
"A comparison of hybrid and quadratic-upstream differencing in high Reynolds number elliptic flows", Comp. Meth. in Appl. Mech. Eng., Vol. 29, 1981, pp 81-95.

77. IACOVIDER H and LAUNDER B E
"The computation of momentum and heat transfer in turbulent flow around pipe bends", First UK National Conf. on Heat Transfer, Leads University, 1984, The Institute of Chemical Eng., Symp. No.86, pp 1097-1114.

78. GOORAY A M, WATKINS C B and AUNG W
"A two-pass procedure for the calculation of heat transfer in recirculating turbulent flow", Num. Heat Transfer, Vol. 6, 1983, pp 423-440.

79. PARTAP S V and SPALDING D B
"Numerical computations of flow in curved ducts", Aero. Quart., Vol. 26, 1975, pp 219-228.

80. KREYSZIG E
"Advanced engineering mathematics", John Wiley and Sons, 1983.

81. PHILLIPS R E and SCHMIDT F W
"Multigrid techniques for the solution of the passive scalar advection-diffusion equation", Num. Heat Transfer, Vol.8, 1985, pp 25-43.

82. CARRIER CORPORATION
"Handbook of air-conditioning system design", New York, 1965, pp 2-65.

83. ALDRIDGE K G
"Linear air distribution, principles and practice", Building Service Engineer, vol. 40, 1972, pp 167-178.

84. BOURQUE G and NEWMAN B G
"Reattachment of a two-dimensional incompressible jet to an adjacent flat plate", Aero. Quart., Vol. 11, 1960, pp 201-232.

85. NEWMAN B G
"The Prediction of turbulent jets and wall-jets", Canadian Aero. and Space Journal, Vol. 15, 1969, pp 1246-1256.

86. KUMADA M, MABUCHI I and OYAKAYA K
"Studies on heat transfer to turbulent jet with adjacent boundaries (3rd report)", Bulletin of JSME, Vol. 16, 1973.

87. HOCH J and JIJI L M
"Two-dimensional turbulent offset jet boundary-interaction", Transactions of ASME, Vol. 103, 1981, pp 155-161.

88. HOCH J and JIJI L M
"Theoretical and experimental temperature distribution in two-dimensional turbulent jet-boundary interaction", Journal of Heat Transfer, Vol. 103, 1981, pp 331-336.

89. SAWYER R A
"The flow due to a two-dimensional jet issuing parallel to a flat plate", J. of Fluid Mech., Vol. 9, 1960, pp 543-560.

90. SAWYER R A
"Two-dimensional reattaching jet flows including the effect of curvature on entrainment", J. of Fluid Mech., Vol. 17, 1963, pp 481-498.

91. BRADSHAW P
"Effect of streamline curvture on turbulent flow", AGARD-AG-169, 1973.

92. METRAL A and ZENNER F
"The Coanda effect", Pub. Sci. et Tech. du Min. de I' Air, vol. 218, 1948, translated as US AEC-TR-3386.

93. HAMMOND G P, FUNG W S, O'CALLAGHAN P W and PROBERT S D
"Interferometric study of the temperature field created by a quasi-plane cold air jet and adjacent flat plate", J. Mech. Eng. Sci, Vol. 19, 1977, pp 47-57.

94. OMERE M M
"Behaviour of offset air jets adjacent to flat plate", M.Sc. thesis C.I.T., England, 1977.

95. AYAKAWA K and SHAKOUCHI
"Analysis of a jet attaching to offset parallel plate", Bulletin of JSME, Vol. 9, 1976, pp 395-401.

96. MARSTERS G F
"The attachment of a ventilated plane jet to an inclined plane wall" Aero. Quar, 1978, pp 60-72.

97. SCHWARTZBACH C
"An experimental investigation of curved two-dimensional turbulent jets," Turbulent Shear Flows, AGARD-CP-93, 1972, pp 1-12.

98. JOHNSON R W and LAUNDER B E
Discussion of "on the calculation of turbulent heat transport downstream from an abrupt pipe expansion", Num. Heat Transfer, Vol. 5, 1982, pp 493-469.

99. AMANO R S, JENSEN M K and GOEL P
"A numerical and experimental investigation of turbulent heat transport downstream from an abrupt pipe expansions", Transaction", of the ASME, Vol. 105, 1983, pp 862-869.

100. AMANO R S
"Development of a turbulent near-wall model and its application to separated and reattached flows", Num. Heat Transfer, Vol. 7, 1984, pp 59-75.

101. GOORAY A M, WATKINS C B and AUNG W
"Numerical calculation of turbulent heat transfer downstream of a rearward-facing step", Proceedings of 2nd International Conference on Numerical Methods in laminar and turbulent flow, Venice, Italy, 1981, pp 634-652.

102. GOORAY A M, WATKINS C B and AUNG W
"Improvements to K-ε model for calculations of turbulent recirculating flow", Proceeding 4th Symp. on turbulent shear flows, University of Karlsruche, F.R.G., 1983, pp 18.26 - 18.31.

103. HACKMAN L P, RAITHBY G D and STRONG A B
Numerical predictions of flows over backward-facing steps", International Journal for Num. Meth. in Fluids, Vol. 4, 1984, pp 711-724.

104. SPALDING D B
"Heat transfer from turbulent separated flows", J. Fluid Mech., Vol. 27, 1967, pp 97-106.

105. KHAN Z A, McGUIRK J J and WHITELAW J H
"A row of jets in a crossflow" AGARD-CPP-308, 1981, pp 10.1 - 10.11.

106. HAMMOND G P
"Private Communication", 1985.

107. RAJARATNAM N
"Turbulent jets", Elsevier Scientific Publishing Company, Amsterdam, Oxford, New York, 1976.

108. DE VAHL DAVIS D and MULLINSON G D
"False diffusion in numerical fluid mechanics", University of New South Wales, School of Mech. and Ind. Eng., Report 1972/FMT/1.0, 1972.

109. ROACHE P J
"Computational fluid mechanics", Hermosu publishers, 1976.

110. LESCHZINER M A and RODI W
"Calculation of anular and twin parallel jets using various discretization schemes and turbulent model variation", Transaction of the ASME, Vol. 103, 1981, pp 352-360.

111. RAITHBY G D
"Skew upstream differencing scheme for problems involving fluid flow", Comp. Meth. Appl. Mech. Eng., Vol. 9, 1976, pp 153-164.

112. RAITHBY G D
"A critical evaluation of upstream differencing applied to problems involved fluid flow", Comp. Meth. Appl. Mech. Eng., Vol. 9, 1976, pp 75-103.

113. CARETTO L S, GOSMAN A D, PATANKAR S V, and SPALDING D B
"Two calculation procedures for steady, three dimensional flows with recirculation", Proc. of Third Conf. on Numerical Method in Fluid Mechanics, Vol. 2, 1973, pp 60-68.

114. HJERTAGER B H and MAGNUSSEN B F
Computation of some three-dimensional laminar incompressible internal flows", Proc. Heat Transfer and Fluid Mechanics Institute, 1976, Stanford University Press, pp 436-451.

115. DURST F, MELLING A and WHITELAW J H
"Low Reynolds number flow over a plane symmetric sudden expansion", J. Fluid Mech., Vol. 64, 1974, pp 111-128.

116. BRUNDRETT E and BAINES W D
"The production and diffusion of vorticity in duct flow", J. Fluid Mech., Vol. 19, 1964, pp 375-394.

117. MELLING A and WHITELAW J H
"Turbulent flow in rectangular duct", J. Fluid Mech., Vol. 78, 1976, pp 289-315.

118. SEALE W J
"Turbulence generated secondary flows in ducts of non-circular cross-section", J. Mech. Eng. Sci. C, Vol. 24, 1982, pp 119-127.

119. DEMUREN A O and RODI W
"Calculation of turbulence-driven secondary motion in non-circular ducts," J. Fluid Mech, Vol. 140, 1984, pp 189-222.

120. LAUNDER B E and YING W M
"Secondary Flows in Ducts of Square Cross-section", J. Fluid Mech., Vol. 54, 1972, pp 289-295.

121. PO J K
"Developing turbulent flow in the entrance region of a square duct", M.Sc. thesis, University of Washington, 1975.

122. GESSNER F B and EMERY A F
"A length-scale model for developing turbulent flow in rectangular duct", J. Fluids Eng., June, 1977, pp 347-356.

123. GESSNER F B, PO J K and EMERY A F
"Turbulent flow in a square duct", Turbulent Shear Flow 1, 1977, pp 119-136.

124. EMERY A F, NEIGHBORS P K and GESSNER F B
"Computational procedure for developing turbulent flow and heat transfer in a square duct", Num. Heat Transfer, Vol. 2, 1979, pp 399-416.

125. LAUNDER B E and YING W M
"Prediction of flow and heat transfer in ducts of square cross-section", Proc. Instn. Mech. Engng., Vol. 187, 1973, pp 445-461.

126. HANJALIC K and LAUNDER B E
"A Reynolds stress model of turbulence and its application to thin shear flows", J. Fluid Mech., Vol. 52, 1972, pp 609-638.

127. BULEEV N I
"Theoretical model of the mechanism of turbulent exchange in fluid flow", AERE translation, 957, 1963.

128. GESSNER F B and EMERY A F
"The numerical prediction of developing turbulent flow in rectangular ducts", Trans. ASME., J. Fluid Eng., vol. 103, 1981, pp 445-455.

129. TATCHELL D G
"Convection prosses in confined three-dimensional boundary layers", Ph.D. thesis, Imperial College, London, 1975.

130. NAOT D and RODI W
"Numerical simulations of secondary currents in channel flow", J. Hydraulic. Div. ASCE. Vol. 108, 1982, pp 948-968.

131. NAKAYAMA A, CHOW W L and SHARMA D
Three-dimensional developing turbulent flow in square ducts", Bulletin JSME, Vol. 27, 1984, pp 1438-1445.

132. SCHLICHTING H
"Boundary layer theory", McGraw-Hill, New York, 1979.

133. HAMMOND G P
"Turbulent Prandtl number within a near-wall flow", AIAA Journal, Vol. 23, 1985, pp 1668-1669.

134. HAMMOND G P
"Turbulent Prandtl number distribution within the constant stress/heat-flux region of near-wall flow", Cranfield Institute of Technology, SME, Report 8401, 1984.

APPENDICES

A,B AND C

APPENDIX A

Formulation and Implementation of the Quick Scheme for a Staggered Grid

The formulation of the Quick scheme for non-uniform grid spacing are given by Leonard (74). The aim of this appendix is to illustrate this formulation for staggered grid situations. For simplicity, the steady one-dimensional flow considered in section (3.2.5) will also be used here.

a) Formulation of the scheme

Figure A-1 shows the definition of terms associated with the 'staggered' non-uniform grid. The velocity components are defined as positive to the right (as shown); their actual values either positive or negative. In quadratic interpolation the approximation of a curve of function ϕ at the control volume face e is achieved by using quadratic parabola which passes through the points (p, ϕ_p), (E, ϕ_E), (EE, ϕ_{EE}). It may be written in accurate form (80) as:

$$\phi_e = \phi_p + (X_e - X_p)\phi(X_p,X_E) + (X_e - X_p)(X_e - X_E)\phi(X_p,X_E,X_{EE}) + .. \quad \ldots . \text{(A.1)}$$

where the divided differences $\phi(X_p,X_E)$ and $\phi(X_p,X_E,X_{EE})$ are

$$\phi(X_p,X_E) = [\phi_E - \phi_p]/[X_E - X_p]$$

$$\phi(X_p,X_E,X_{EE}) = [\phi(X_E,X_{EE}) - \phi(X_p,X_E)]/(X_{EE} - X_p) \quad \ldots . \text{(A.2)}$$

The substitution of equations (A.2) into A.1 and rearranging gives

$$\phi_e = \phi_p + \frac{(X_e - X_p)}{(X_E - X_p)}(\phi_E - \phi_p) + \frac{(X_e - X_p)(X_e - X_E)}{(X_{EE} - X_p)} \left(\frac{(X_E - X_p)(\phi_{EE} - \phi_E) - (X_{EE} - X_E)(\phi_E - \phi_p)}{(X_{EE} - X_E)(X_E - X_p)} \right) \quad \ldots . \text{(A.3)}$$

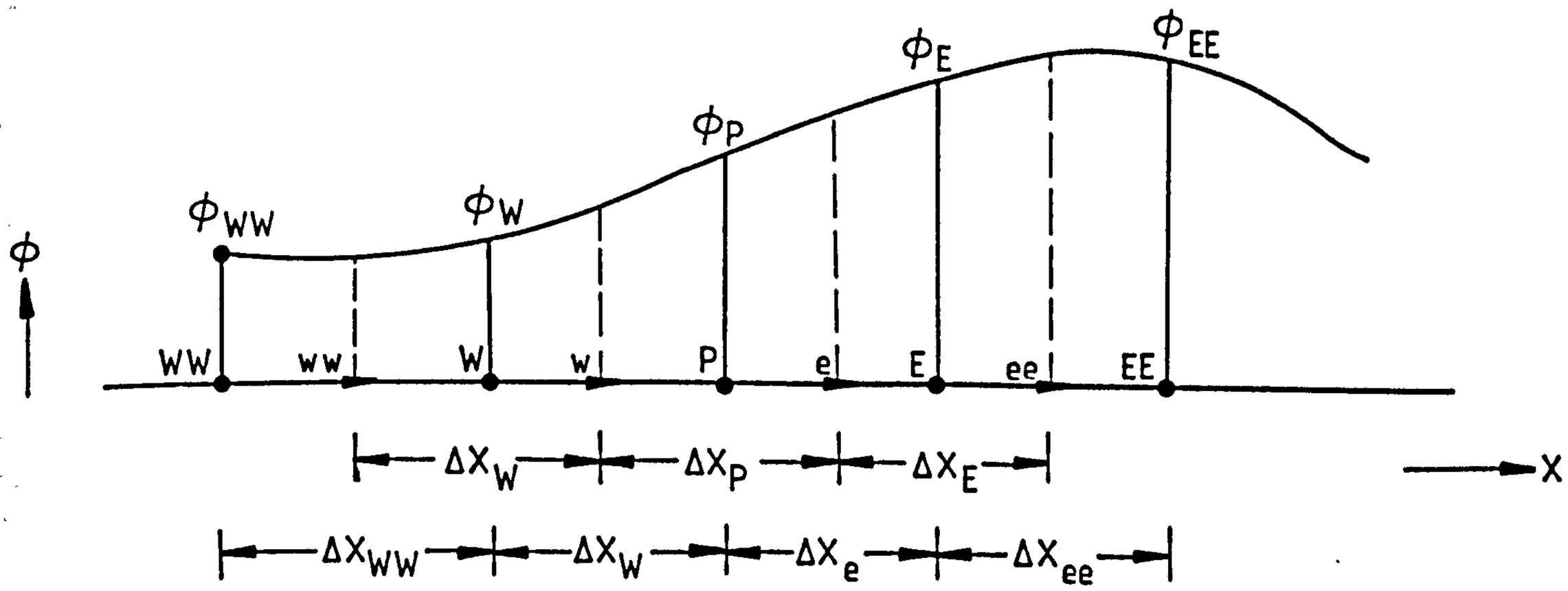

Figure A.1 : Notation employed with the QUICK scheme for a staggered grid [adapted from Leonard (74)] .

If the quadratic parabola passes through the points (W,ϕ_W), (p,ϕ_p), (E,ϕ_E), then the quadratic interpolation gives:

$$\phi_e = \phi_E + \frac{(X_e - X_E)(\phi_E - \phi_p)}{(X_E - X_p)} + \frac{(X_e - X_E)(X_e - X_p)}{(X_E - X_W)}$$

$$\left(\frac{(X_p - X_W)(\phi_E - \phi_p) - (X_E - X_p)(\phi_p - \phi_W)}{(X_E - X_p)(X_p - X_W)}\right) \quad \ldots\ldots (A.4)$$

The value of ϕ_e is determined according to the value of the corresponding velocity component at the control volume face U_e (74). If U_e negative ϕ_e is calculated from equation A.3, otherwise from equation A.4.

The value of ϕ at the west control volume face can similarly be written as:

$U_w > 0$

$$\phi_w = \phi_p + \frac{(X_w - X_p)}{X_p - X_W}\ (\phi_p - \phi_W) + \frac{(X_w - X_p)(X_w - X_W)}{(X_p - X_{WW})}$$

$$\left(\frac{(X_W - X_{WW})(\phi_p - \phi_W) - (X_p - X_W)(\phi_W - \phi_{WW})}{(X_p - X_W)(X_W - X_{WW})}\right) \quad \ldots\ldots (A.5)$$

$U_w < 0$

$$\phi_w = \phi_W + \frac{(X_w - X_W)}{(X_p - X_W)}\ (\phi_p - \phi_W) + \frac{(X_w - X_W)(X_w - X_p)}{(X_E - X_W)}$$

$$\left(\frac{(X_p - X_W)(\phi_E - \phi_p) - (X_E - X_p)(\phi_p - \phi_W)}{(X_E - X_p)(X_p - X_W)}\right) \quad \ldots\ldots (A.6)$$

Equation (A.3-6) may be written in the following forms:

$$\phi_e = \phi_p + XCEE(\phi_E - \phi_p) - (XPEEN(\phi_{EE} - \phi_E) - XEEE(\phi_E - \phi_p)) \quad U_e < 0$$

$$\phi e = \phi_E - XCE(\phi_E - \phi_p) - (XWPE(\phi_E - \phi_p) - XPEEP(\phi_p - \phi_w)) \quad U_e > 0$$

$$\phi_w = \phi_p - XCWW(\phi_p - \phi_W) - (XWWW(\phi_p - \phi_W) - XWPWP(\phi_W - \phi_{WW})) \quad U_w > 0$$

$$\phi_w = \phi_W + XCW(\phi_p - \phi_W) - (XWPWN(\phi_E - \phi_p) - XPEW(\phi_p - \phi_W)) \quad U_w < 0$$

. . . . (A.7)

where

$$XCEE = (X_e - X_p)/(X_E - X_p)$$

$$XPEEN = (X_e - X_p)\ (X_E - X_e)/((X_{EE} - X_p)(X_{EE} - X_E))$$

$$XEEE = (X_e - X_p)\ (X_E - X_e)/((X_{EE} - X_p)(X_E - X_p))$$

$$XCE = (X_E - X_e)/(X_E - X_p)$$

$$XWPE = (X_E - X_e)(X_e - X_p)/((X_E - X_W)(X_E - X_p))$$

$$XPEEP = (X_E - X_e)(X_e - X_p)/((X_E - X_W)(X_p - X_W))$$

$$XCWW = (X_p - X_w)/(X_p - X_W)$$

$$XWWW = (X_p - X_w)(X_w - X_W)/((X_p - X_{WW})(X_p - X_W))$$

$$XWPWP = (X_p - X_w)(X_w - X_W)/((X_p - X_{WW})(X_W - X_{WW}))$$

$$XCW = (X_w - X_W)/(X_p - X_W)$$

$$XWPWN = (X_w - X_W)(X_p - X_w)/((X_E - X_W)(X_E - X_p))$$

$$XPEW = (X_w - X_W)(X_p - X_w)/((X_E - X_W)(X_p - X_W))$$

. . . . (A.8)

Then the substitution of equation A.7 into the discretised form of equation (3.17), excluding the diffusion terms for simplicity gives:

$$[[F_e,0]](\phi_E - XCE(\phi_E - \phi_p) - (XWPE(\phi_E - \phi_p) - XPEEP(\phi_p - \phi_w)))$$

$$- [[-F_e,0]](\phi_p + XCEE(\phi_E - \phi_p) - (XPEEN(\phi_{EE} - \phi_E) - XEEE(\phi_E - \phi_p)))$$

$$- [[F_w,0]](\phi_p - XCWW(\phi_p - \phi_W) - (XWWW(\phi_p - \phi_W) - XWPWP(\phi_W - \phi_{WW})))$$

$$- [[-F_w,0]](\phi_W + XCW(\phi_p - \phi_W) - (XWPWN(\phi_E - \phi_p) - XPEW(\phi_p - \phi_W)))]$$

$$= \text{Diffusion} \quad \text{. . . . (A.9)}$$

Then using the discretised form of the continuity equation (3.18) and rearranging gives:

$$\{[[F_e,0]](XWPE + XCE + XPEEP - 1) + [[-F_e,0)]](XCEE + XEEE + XPEEN) +$$
$$[[F_w,0]](XWWW + XCWW + XWPWP) + [[-F_w,0]](XCW + XPEW + XWPWN - 1)\}\phi_p$$
$$= \{[[F_e,0]](XWPE + XCE - 1) + [[-F_e,0]](XCEE + XEEE + XPEEN)$$
$$+ [[-F_w,0]](XWPWN)\}\phi_E + \{[[F_w,0]](XWWW + XCWW + XWPWP) +$$
$$[[-F_w,0]](XCW + XPEW - 1) + [[F_e,0]](XPEEP)\}\phi_W - [[-F_e,0]](XPEEN)$$
$$(\phi_{EE} - \phi_p) - [[F_w,0]](XWPWP)(\phi_{WW} - \phi_p) + \text{Diffusion}$$

. . . (A.10)

The following coefficients could be obtained from equation A.10 with the recovering of the diffusion terms.

$$a_E = D_e + [[F_e,0]](XWPE + XCE - 1) + [[-F_e,0]](XCEE + XEEE + XPEEN)$$
$$+ [[-F_w,0]](XWPWN)$$
$$a_W = D_w + [[F_w,0]](XWWW + XCWW + XWPWP) + [[-F_w,0]](XCW + XPEW - 1)$$
$$+ [[F_e,0]](XPEEP)$$
$$a_{EE} = -[[-F_e,0]](XPEEN), \quad a_{WW} = -[[F_w,0]](XWPWP)$$
$$\text{and } a_p = a_E + a_W + a_{EE} + a_{WW}$$

. . . . (A.11)

b) <u>Implementation of the scheme</u>

The Quick Scheme is not unconditionally stable, unlike the upwind, hybrid and power-law schemes. This has led to a number of proposals for stabilizing the scheme and thereby overcoming the convergence problem (76, 78, 81). Most of these proposals involve the allocation of various terms in equation (A.10) to source and non-source groupings. However, in the present study several other practices have been tested in addition to these early ones. The following was found to give the most satisfactory overall convergence rate:

Equation (3.10) may be written for the one-dimensional flow case as follows:

$$a_{p,PL}\,\phi_p = a_{E,PL}\,\phi_E + a_{W,PL}\,\phi_W + b_{QPL} \qquad \ldots\ldots (A.12)$$

where

b_{QPL} is a source term that is given by:

$$b_{QPL} = (a_{E,Q} - a_{E,PL})\,\phi_E + (a_{W,Q} - a_{W,PL})\,\phi_W - (a_{p,Q} - a_{p,PL})\,\phi_p + a_{EE,Q}\,\phi_{EE} + a_{WW,Q}\,\phi_{WW}$$

The subscripts Q and PL indicate that the associated coefficients were calculated via the Quick or power-law scheme (i.e. equation A.11 or 3.28). The source term b_{QPL} (which contain the algebraic difference between the Quick and power law formulation) has been linearised in the following manner:

$$b_{QPL}\Big|_m = S\Big|_{m-1} + S'\Big|_m \qquad \ldots\ldots (A.14)$$

where m is the iteration count;

$$S\Big|_{m-1} = (a_{E,Q} - a_{E,PL})\phi_E + (a_{W,Q} - a_{W,PL})\phi_W + a_{P,PL}\,\phi_P + a_{EE,Q}\,\phi_{EE} + a_{WW,Q}\,\phi_{WW} + [[(-a_{P,Q}),0]]\,\phi_P \qquad \ldots\ldots (A.15)$$

and

$$S'\Big|_m = -[[-(-a_{P,Q}),0]] \qquad \ldots\ldots (A.16)$$

This practice ensures that the coefficient in equation (A.12) is always positive, and that the finite domain equation matrix is always diagonally dominant.

The Quick scheme required a five-point formulation, and therefore the above practice was used to perform the calculation for all the grid points in the field, except those adjacent to the boundaries. Both power-law and hybrid differencing schemes were used to calculate these boundary nodes for test purposes. However, the power law scheme was preferred for the subsequent calculations, due to its better accuracy.

APPENDIX B

Algebraic Stress Model Employed in the Duct-Flow Studies

Naot and Rodi (130) have simplified the transport equations for the Reynolds stress devised by Launder et al (41) by neglecting the diffusion and convection terms in the Reynolds stress transport equation using the local equilibrium assumption. Demuren and Rodi (119) subsequently presented the resulting equations in the general elliptic form:

$$(1-\alpha)\left(-\overline{u_i u_l}\frac{\partial U_j}{\partial x_l}-\overline{u_j u_l}\frac{\partial U_i}{\partial x_l}\right)+\beta\left(\overline{u_i u_l}\frac{\partial U_l}{\partial x_j}+\overline{u_j u_l}\frac{\partial U_l}{\partial x_i}\right)-\gamma K\left(\frac{\partial U_i}{\partial x_j}+\frac{\partial U_j}{\partial x_i}\right)-\frac{\varepsilon}{K}\left[C_1\overline{u_i u_j}+\frac{2}{3}(1-\alpha-\beta-C_1)\delta_{ij}K\right]=0.0 \qquad \text{B.1}$$

Where α, β and C_1 are fuctions of a dimensionless distance from the wall, and γ is an empirical constant. These values are given below.

The stress components were obtained in the present study using equation B.1, but without neglecting the velocity gradients in the stream-wise direction. The individual stress components in this fully-elliptic form may be written as:

$$\overline{w^2}=\frac{2K}{\varepsilon C_1}\left\{\frac{\varepsilon}{3}(\alpha+\beta+C_1-1)-\overline{wv}\left[(1-\alpha)\frac{\partial W}{\partial y}-\beta\frac{\partial V}{dz}\right]-\overline{wu}\left[(1-\alpha)\frac{\partial W}{\partial X}-\beta\frac{\partial U}{\partial z}\right]-\gamma K\frac{\partial W}{\partial z}\right\}\Bigg/\left[1+\frac{2K}{\varepsilon C_1}(1-\alpha-\beta)\frac{\partial W}{\partial z}\right] \qquad \text{B.2}$$

$$\overline{v^2} = \frac{2K}{\varepsilon C_1}\left\{\frac{\varepsilon}{3}(\alpha + \beta + C_1 - 1) - \overline{wv}\left[(1-\alpha)\frac{\partial V}{\partial z} - \beta\frac{\partial W}{\partial y}\right]\right.$$

$$\left. - \overline{vu}\left[(1-\alpha)\frac{\partial V}{\partial x} - \beta\frac{\partial U}{\partial y}\right] - \gamma K\frac{\partial V}{\partial y}\right\}\Big/$$

$$\left[1 + \frac{2K}{\varepsilon C_1}(1-\alpha-\beta)\frac{\partial V}{\partial y}\right] \qquad \text{B.3}$$

$$\overline{u^2} = \frac{2K}{\varepsilon C_1}\left\{\frac{\varepsilon}{3}(\alpha + \beta + C_1 - 1) - \overline{wu}\left[(1-\alpha)\frac{\partial U}{\partial z} - \beta\frac{\partial W}{\partial x}\right]\right.$$

$$\left. - \overline{vu}\left[(1-\alpha)\frac{\partial U}{\partial y} - \beta\frac{\partial V}{\partial x}\right] - \gamma K\frac{\partial U}{\partial x}\right\}\Big/$$

$$\left[1 + \frac{2K}{\varepsilon C_1}(1-\alpha-\beta)\frac{\partial U}{\partial x}\right] \qquad \text{B.4}$$

$$\overline{vu} = \frac{2K}{\varepsilon C_1}\left\{\beta\left(\overline{wu}\frac{\partial W}{\partial y} + \overline{wv}\frac{\partial W}{\partial x}\right) - \left[(1-\alpha)\overline{v^2} - \beta\overline{u^2} + \gamma K\right]\right.$$

$$\frac{\partial U}{\partial y} - \left[(1-\alpha)\overline{u^2} - \overline{\beta v^2} + \gamma K\right]\frac{\partial V}{\partial x} - (1-\alpha)\left[\overline{wu}\frac{\partial V}{\partial z} + \right.$$

$$\left.\left.\overline{wv}\frac{\partial U}{\partial z}\right]\right\}\Big/\left[1 + \frac{K}{\varepsilon C_1}(1-\alpha-\beta)\left(\frac{\partial U}{\partial x} + \frac{\partial V}{\partial y}\right)\right] \qquad \text{B.5}$$

The stress components, $\overline{wv}$ and $\overline{wu}$ were determined as in the N-R model via an isotropic eddy-viscosity hypothesis:

$$\overline{wv} = -\nu_t\left(\frac{\partial W}{\partial y} + \frac{\partial V}{\partial z}\right) \qquad \text{B.6}$$

$$\overline{wu} = -\nu_t\left(\frac{\partial W}{\partial x} + \frac{\partial U}{\partial z}\right) \qquad \text{B.7}$$

Naot and Rodi (130) further simplified the partially parabolic version of equations B.3 - B.5 by approximating the secondary-velocity gradient terms in the numerators for $\overline{v^2}$, $\overline{u^2}$ and $\overline{vu}$. They adopted the following eddy-viscosity expressions and neglected the secondary-velocity gradients in the denominators, making these unity. Thus,

$$\frac{K}{\varepsilon C_1}\left\{\overline{wu}\left[(1-\alpha)\frac{\partial V}{\partial x} - \beta\frac{\partial U}{\partial y}\right] + \gamma K\frac{\partial V}{\partial y}\right\} \propto \nu_t\frac{\partial V}{\partial y} \qquad \text{B.8}$$

$$\frac{K}{\varepsilon C_1}\left\{\overline{vu}\left[(1-\alpha)\frac{\partial U}{\partial y}-\beta\frac{\partial V}{\partial x}\right]+\gamma K\frac{\partial U}{\partial x}\right\}\simeq \nu_t\frac{\partial U}{\partial x} \qquad \text{B.9}$$

$$\frac{K}{\varepsilon C_1}\left\{\left[(1-\alpha)\overline{v^2}-\beta\overline{u^2}+\gamma K\right]\frac{\partial U}{\partial y}+\left[(1-\alpha)\overline{u^2}-\beta\overline{v^2}+\gamma K\right]\frac{\partial V}{\partial x}\right\}$$

$$\simeq \nu_t\left(\frac{\partial U}{\partial y}+\frac{\partial V}{\partial x}\right) \qquad \text{B.10}$$

The substitution of equations B.8 - B.10 into equations B.3 - B.5 gives,

$$\overline{v^2}=\frac{2K}{\varepsilon C_1}\left\{\frac{\varepsilon}{3}(\alpha+\beta+C_1-1)-\overline{wv}\left[(1-\alpha)\frac{\partial V}{\partial z}-\beta\frac{\partial W}{\partial y}\right]\right\}$$

$$-2\nu_t\frac{\partial V}{\partial y} \qquad \text{B.11}$$

$$\overline{u^2}=\frac{2K}{\varepsilon C_1}\left\{\frac{\varepsilon}{3}(\alpha+\beta+C_1-1)-\overline{wu}\left[(1-\alpha)\frac{\partial U}{\partial z}-\beta\frac{\partial W}{\partial x}\right]\right\}$$

$$-2\nu_t\frac{\partial U}{\partial x} \qquad \text{B.12}$$

$$\overline{vu}=\frac{2K}{\varepsilon C_1}\left\{\overline{wu}\left[\beta\frac{\partial W}{\partial y}-(1-\alpha)\frac{\partial V}{\partial z}\right]+\overline{wv}\left[\beta\frac{\partial W}{\partial x}-(1-\alpha)\frac{\partial U}{\partial z}\right]\right\}$$

$$-\nu_t\left(\frac{\partial U}{\partial y}+\frac{\partial V}{\partial x}\right) \qquad \text{B.13}$$

Demuren and Rodi (119) noted that the three normal stresses ($\overline{w^2}$, $\overline{v^2}$ and $\overline{u^2}$) sum-up to twice the turbulent kinetic energy ($K = 0.5\ \overline{u_i u_i}$). They therefore suggested that the value of $(\overline{w^2})$ can be most conveniently calculated from K, $\overline{v^2}$ and $\overline{u^2}$, rather than from equation B.2. This practice was also adopted in the present study.

The turbulence enthalpy fluxes were approximated following long established practice (124-125) using the turbulent Prandtl number (Pr_t) concept as follows:

$$\overline{U_j h}=-\frac{U_i U_j}{Pr_t}\cdot\frac{\partial H}{\partial x_i}\Big/C_j \qquad \text{B.14}$$

where

$$C_j=\frac{U_i U_j}{\nu_t} \qquad \text{B.15}$$

Equation B.14 can be written for the individual components as follows:

$$\overline{wh} = - \frac{\nu_t}{Pr_t} \frac{\partial H}{\partial z} \qquad B.16$$

$$\overline{vh} = - \frac{\nu_t}{Pr_t} \frac{\partial H}{\partial y} \qquad B.17$$

$$\overline{uh} = - \frac{\nu_t}{Pr_t} \frac{\partial H}{\partial x} \qquad B.18$$

The isotropic eddy viscosity appearing in equation B.6-7, B.11-13 and B.16-18 was calculated as in the conventional K-ε model by relating it to the turbulent kinetic energy (K) and its dissipation rate (ε). The latter quantities appear in the above mentioned equations, and were calculated via the standard K-ε model (see section 2.4.2).

The surface-proximity effect on the turbulent stresses were accounted for by Launder et al (41) through the following equations [which also found in the papers of Demuren and Rodi (119) and Naot and Rodi (13)]:

$$\alpha = 0.7636 - 0.06\ f \ ;$$

$$\beta = 0.1091 + 0.06\ f \ ;$$

$$C_1 = 1.5 - 0.5\ f \ ; \text{ and}$$

$$\gamma = 0.186$$

where f is a function of the dimensionless wall distance. Naot and Rodi (130) proposed a quadratic relation to calculate the function f:

$$f = \frac{l^2}{\langle Y^2 \rangle} \qquad B.20$$

where l is the length scale determined from;

$$l = \frac{C_D^{3/4}\ K^{3/2}}{K\ \varepsilon} \qquad B.21$$

and $\langle \frac{1}{y^2} \rangle$ is given in Naot and Rodi (130) for rectangular ducts of dimension L and B by

$$\langle \frac{1}{y^2} \rangle = \frac{1}{\pi}\frac{1}{y^2}\left[\arctg\left(\frac{L-x}{y}\right) + \arctg\left(\frac{x}{y}\right) + \frac{1}{\frac{L-x}{y} - \frac{y}{L-x}} + \frac{1}{\frac{x}{y} + \frac{y}{x}}\right.$$

$$+ \frac{1}{(B-y)^2}\left[\arctg\left(\frac{L-x}{B-y}\right) + \arctg\left(\frac{1}{B-y}\right) + \frac{1}{\frac{L-x}{B-y} + \frac{B-y}{L-x}} + \frac{1}{\frac{x}{B-y} + \frac{B-y}{x}}\right.$$

$$+ \frac{1}{x^2}\left[\arctg\left(\frac{B-y}{x}\right) + \arctg\left(\frac{y}{x}\right) + \frac{1}{\frac{B-y}{x} + \frac{x}{B-y}} + \frac{1}{\frac{y}{x} + \frac{x}{y}}\right.$$

$$+ \left(\frac{1}{L-x^2}\right)^2\left[\arctg\left(\frac{B-y}{L-x}\right) + \arctg\left(\frac{y}{L-x}\right) + \frac{1}{\frac{B-y}{L-x} + \frac{L-x}{B-y}} + \frac{1}{\frac{y}{L-x} + \frac{L-x}{y}}\right.$$

B.22

Note that the duct corners are at:

(x=0,y=0), (x=0,y=B), (x=L,y=0) and (x=L,y=B)

APPENDIX C

An Alternative Approach to Specifying the Jet Supply Conditions in Rooms with Small Inlet Openings

Computation of fluid flow and heat transfer in large rooms ventilated by small supply register/slot, is often accompanied by a particular numerical difficulty (12-13,32). It lies in the distribution of grid nodes and particularly the correct representation of the flow through and near the supply opening. The task of the present appendix is to present an inlet cell (starting profile) approach that could obviate the need of such finely-spaced grid. This approach is based on a wall-jet empirical data reviewed by Rajaratnam (107) and the results of Hammond's profile analysis (29-30). The profiles that are given below are for the axial component of the velocity, the turbulent kinetic energy, the turbulent dissipation rate and the temperature.

a) Velocity profile

The experimental data reviewed by Rajaratnam (107) suggests that the centreline velocity decay in a three dimensional wall-jet may be expressed in the form:

$$\frac{W_{mo}}{W_{in}} = 8.325 \left(\frac{z}{\sqrt{A_g}}\right)^{-1} \qquad C.1$$

where A_g is the register area, $A_g (= H_g \times W_g)$, see also figure 7.2, and W_{mo} is the maximum velocity in centreline. According to Rajaratnam (107), the span-wise jet spread is well described by the equation;

$$\frac{b_x}{W_g} = 0.2\left(\frac{z}{W_g}\right) - 1.25 \qquad C.2$$

where b_x is the span-wise half-width.

Inspection of the available data supports a value for the span-wise width ratio (32) ;

$$\frac{\delta_x}{b_x} = 2.5 \qquad \text{C.3}$$

Equation C.2 breaks down for $z \leqslant 15\ W_g$ and in this region the spread is better represented by (107):

$$\frac{b_x}{W_g} = 0.12\ (\frac{z}{W_g}) + 0.2 \qquad \text{C.4}$$

Thus, the span-wise jet spread δ_x, may be calculated as follows:

<u>For the far field</u>;

$$\delta_x = 2.5\ W_g \times 0.20\ (\frac{z}{W_g}) - 1.25 \qquad \text{C.5}$$

<u>For the near field</u>;

$$\delta_x = 2.5\ W_g \times [0.12(\frac{z}{W_g}) + 0.2] \qquad \text{C.6}$$

The interaction between these two relations actually occurs at

$$\frac{z}{W_g} = 18.125$$

The span-wise velocity distribution may be written in the form (107);

$$\frac{W_m}{W_{mo}} = \exp[-\ 0.693(\frac{x}{b_x})^2] \qquad \text{C.7}$$

and the potential core length as:

$$z_c \simeq 8.235\sqrt{A_g} \qquad C.8$$

Using complete velocity profile formula and associated data correlation given by Hammond (29-30), the velocity distribution may be written as follows:

$$W = W_m \left(\frac{C}{2}\right)^{\frac{1}{2}} \left\{\frac{1}{\kappa} \ln\left[Re_m\left(\frac{C_f}{2}\right)^{\frac{1}{2}} \left(\frac{b_y}{y_m}\right) \left(\frac{y}{b_y}\right)\right] + B + C\,\omega\left(\frac{y}{b_y}\right)\right\} \qquad C.9$$

A quartic wake function was adopted:

$$\omega\left(\frac{y}{b_y}\right) = \sum_{i}^{n=4} a_n \left(\frac{y}{b_y}\right)^n \qquad C.10$$

While the local skin friction coefficient is given by;

$$\left(\frac{2}{C_f}\right)^{\frac{1}{2}} = \frac{1}{\kappa} \ln\left[Re_m \left(\frac{C_f}{2}\right)^{\frac{1}{2}}\right] + B + C\omega\left(\frac{y_m}{b_y}\right) \qquad C.11$$

and the wake function coefficient

$$C = -\left[\frac{1}{\kappa} \ln(2.5\, b_y^+) + B\right] \qquad C.12$$

$$b_y^+ = 0.283\, Re_m \qquad C.13$$

where W is the velocity component in z-direction

B and κ are the log-law constant (B = 5.2 and κ = 0.41)

b_y and y_m are defined in Figure C.1.

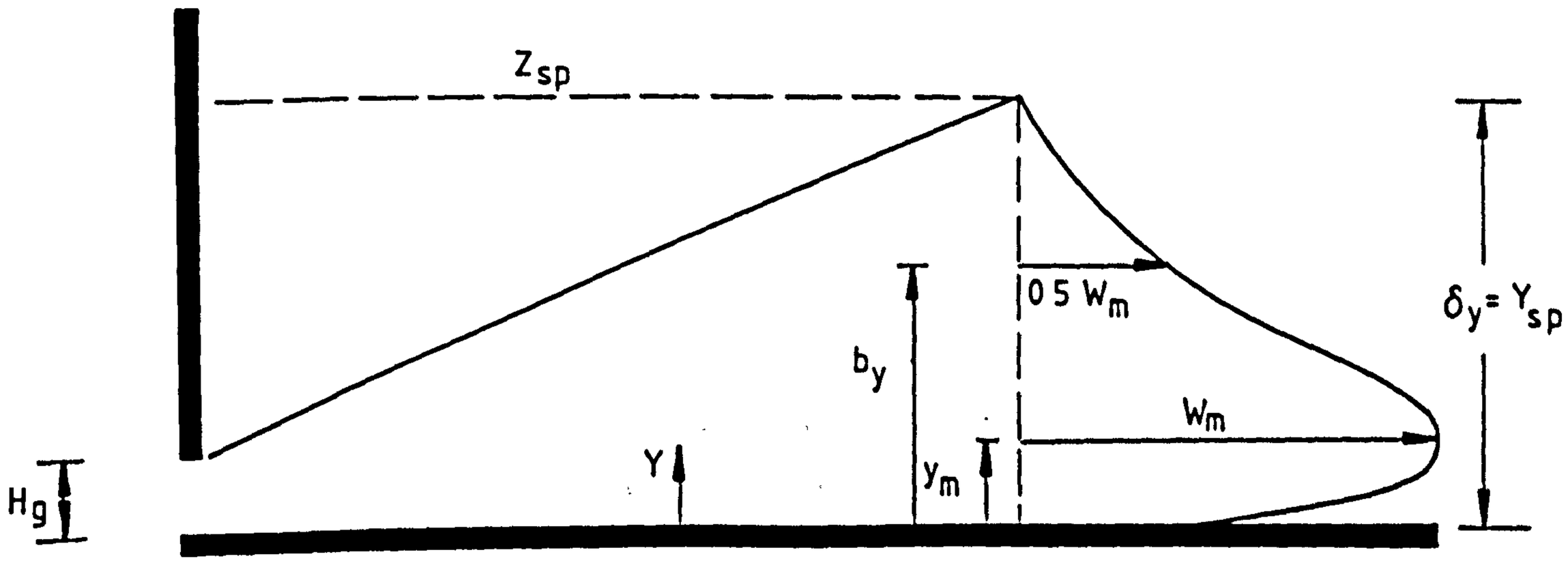

Figure C.1 : A two-dimensional view for the wall-jet starting profile .

Hammond (30) presented approximate values for the coefficient, a_n, as a power-law function of the local, wall-jet Reynolds number ($Re_m = \rho W_{mo} Y_m/\mu$):

$$\begin{aligned} a_1 &= 0.841 \quad Re_m^{(-0.1040)} \\ a_2 &= 0.233 \quad Re_m^{(+0.0917)} \\ a_3 &= -0.180 \quad Re_m^{(+0.0627)} \\ a_4 &= 0.030 \quad Re_m^{(+0.0555)} \end{aligned} \qquad \text{C.14}$$

These approximate relations were used to specify the W-component starting profile. It was assumed that the flow was fully developed and the velocity components in x and y directions were zero, (i.e. U = V = 0.0).

b) Enthalpy/Temperature profile

In the absence of appropriate experimental data for the temperature field, it is assumed the following relation may be applied (Hammond private communication, 1985).

$$\frac{\theta_{mo}}{\theta_o} = 9.125 \left(\frac{z}{A_g}\right)^{-1} \qquad \text{C.15}$$

where $\theta = T - T_a$ and T_a is the ambient temperature. The span-wise width ratio may be determined by analogy with Hammond's two-dimensional analysis (30), $b_x/b_{xo} = 0.85$, and then the temperature profile can be given by:

$$\frac{\theta_m}{\theta_{mo}} = \exp\left[-0.093\left(\frac{x}{b_{xo}}\right)^2\right] \qquad \text{C.16}$$

in a similar manner to the corresponding velocity profile. The lateral temperature distribution could then be written as follows, (Hammond, private communication, 1985):

$$\frac{\theta}{\theta_m} = 1 - \frac{y}{\delta_y} \qquad \text{C.17}$$

c) Turbulent kinetic energy profile

Hammond has derived an empirical expression for the turbulence kinetic energy profile across a wall-jet, which may be written in the form:

$$K = \left\{W\, k_1 \left[k_2 \left(\frac{y}{\delta_y}\right)^2 + 1.0\right]\right\}^2 \qquad \text{C.18}$$

where k_1 amd k_2 are 0.175 and 7.10 respectively.

d) Energy dissipation profile

Energy dissipation profile for wall-jet may be obtained via the mixing length hypothesis. Hammond has derived a dissipation length scale expression for plane wall jets in the form

$$\frac{L\varepsilon}{\delta_y} = 0.44 + 0.68\left(1 - \frac{y}{\delta_y}\right)^2 - 1.12\left(1 - \frac{y}{\delta_y}\right)^4 \qquad \text{C.19}$$

where L_ε is the dissipation length scale. The dissipation rate may then be obtained from the definition

$$\varepsilon = \frac{K}{L_\varepsilon}^{3/2} \qquad \text{C.20}$$

BOUND PAPER

F. ALAMDARI, G.P. HAMMOND and W.S.MOHAMMAD

COMPUTATION OF AIR FLOW AND CONVECTIVE HEAT TRANSFER WITHIN SPACE-CONDITIONED, RECTANGULAR ENCLOSURES

Paper Preprint

CIB 5TH INTERNATIONAL SYMPOSIUM

COMPUTATION OF AIR FLOW AND CONVECTIVE HEAT TRANSFER WITHIN SPACE-CONDITIONED, RECTANGULAR ENCLOSURES. †

F. ALAMDARI, G.P. HAMMOND and W.S. MOHAMMAD
Applied Energy Group, School of Mechanical Engineering, Cranfield Institute of Technology, Bedford MK43 OAL, U.K.

Computer simulations are reported of the airflow and convective heat exchange within a warm-air heated, rectangular (three-dimensional) enclosure for which buoyancy effects are significant. Emphasis is placed on meeting the needs of building thermal simulation programs for accurate input data on convective heat transfer. The computations are performed using the 'intermediate-level' convection model of Alamdari and Hammond (1982), and a recently developed high-level 'elliptic' finite-domain flow model. Comparisons are also made with the design recommendations given in some of the established guides. These alternative calculation methods are assessed in terms of the balance they provide between accuracy and economy.

INTRODUCTION

It has been estimated that building services account for about 40-50 per cent of primary energy consumption in industrialised countries (Carroll (1)). The need for efficient use of energy in buildings is therefore obviously important, particularly when viewed against a background of depleting oil and gas reserves. In order to develop realistic methods for the energy-conscious design of buildings, it is necessary to simulate the dynamic thermal response of the system (Clarke (2), Day (3) and Wiltshire (4)). This requires quite sophisticated computational techniques, and has led to an emphasis being placed on modelling the transient performance of the building fabric. In contrast, the air flow and convective heat exchange in and around the structure are simulated using only rough approximations. Indeed, a survey of the new generation of building thermal models for the International Energy Agency (Irving (5)) concluded that their accuracy is presently limited by uncertainties in the input data, particularly for air infiltration and convective heat transfer rates.

In order to obtain improved ways of determining convective heat transfer data appropriate to the needs of building thermal simulation programs, a hierarchy of interacting and interdependent calculation methods have been developed by the authors and their co-workers (see, for example, Alamdari et al (6)). These were originally developed for mechanically-ventilated enclosures, such as warm-air heated rooms or air-conditioned offices, in which the 'forced' convective motion induced by the air supply jet predominates. The calculation methods themselves ranged from 'lower-level' approaches, including analytical solutions and elaborate data correlations for limiting cases, to the development of a 'high-level' flow model that solves a discretized form of the governing partial differential equations for the complex, jet-induced room airflow. Both the higher and lower-level models have been used to develop and verify an 'intermediate-level' computer code (Alamdari and Hammond (7)), which formed the basis for generating input convective heat transfer data for dynamic building models. This code, known as the ROOM-CHT (Room Convective Heat Transfer) program, appears to offer the best prospect of meeting the needs for building thermal simulation in terms of accuracy, economy and user friendliness (6 and 7). The success of this approach led to the development of an analogous intermediate-level computer code for wind-induced, external convection from buildings (6).

The interrelationship between the various calculation methods developed by the authors for computing convection data is illustrated by the schematic diagram shown in Figure 1. The classification scheme adopted for different 'levels' was intended to reflect the potential generality of their range of application, rather than their scientific sophistication (see (6) for a fuller explanation of the choice of terms). The iterative process of developing and verifying intermediate-level methods is represented in Figure 1 by the blocks within the dashed line. Both experimental data, obtained from full and model-scale tests, and the computed results of a higher-level computer code have been used for verification purposes. This was conceived as a feedback process from which ad hoc corrections would be made to the intermediate-level computer

† The Fifth International Symposium on the Use of Computers for Environmental Engineering Related to Buildings, 6-9 July 1986, Bath, ENGLAND, In Press 1986.

codes where necessary.

In the present contribution a comparative assessment is reported of alternative methods for calculating convective heat exchange within a mechanically-ventilated, rectangular (three-dimensional) enclosure for which buoyancy effects are significant. The calculation methods employed for this 'mixed' convection problem include both the intermediate and higher-level computer codes developed by the authors, together with the design recommendations given in established guides (ASHRAE (8) and CIBSE (9 and 10)). Earlier reports by the authors on their use of a high-level flow model (Alamdari et al (6 and 11)) were limited to cases involving non-buoyant flows in 'two-dimensional' enclosures; restrictions which greatly simplify the computational task. The present evaluation of the various calculation methods is based on the requirements of building thermal simulation programs largely in terms of accuracy and economy.

SPACE-CONDITIONED ENCLOSURE

The warm-air heated room previously used to demonstrate the capabilities of the three-dimensional version of the ROOM-CHT program (7) was adopted for the present study. This represented a corner, ground-floor domestic living room (illustrated in Figure 2), having dimensions 4.30 m length, 2.45 m width and 2.45 m height. Modern practice in the UK would normally utilise warm-air injected through a 'low side-wall register' (12), with supply conditions regulated by a modulating control system (Pimbert (13)). Such a configuration has many potential advantages for 'low energy housing' (7), including good energy efficiency (70-75% over the heating season) and ease of control with rapid response to load changes.

A notional (reference) occupation zone air temperature of $23 \pm 0.5^{\circ}C$ was adopted for the simulated enclosure, while the surface temperature of the internal walls and ceiling were similarly assumed to remain constant at $21^{\circ}C$ over the heating season. The two external walls, incorporating single-glazed windows (1.45 m x 1.00 m in the far-wall and 1.80 m x 1.00 m in the side-wall), and the floor were given inside surface temperatures estimated on the basis of best current British practice U-values (14). These temperatures are given in Table 1 as a function of three representative heat loads. The full load condition corresponds to a supply warm-air ventilation rate of 3 air-changes per hour (ACH).

The size of the warm-air supply register was determined by the requirements for full load operation, with face velocities and temperatures within the limits recommended in the British design manual for gas fired systems (12). This suggested a rectangular grille (200 mm x 120 mm, 70% free area) located at the bottom centre of the interior wall, as shown in Figure 2. Such an arrangement gives rise to the formation of a three-dimensional 'wall-jet' (Rajaratnam (15)), which initially spreads out from the terminal device across the floor. Three room air extract grilles are positioned at high-level above the supply register, and these are also illustrated in Figure 2. The supply air conditions would be regulated by the modulating control system, which adjusts a variable-speed fan. This normally operates continuously to give a constant face velocity, whose value depends on the heat load. In contrast, the supply air temperature modulates very slightly about its load-dependent mean value, although this was neglected for the purposes of the present computations. The supply conditions that correspond to the three representative heat loads are

TABLE 1 - Demand-dependent Supply Air Conditions and Surface Temperatures

DEMAND	HEAT LOAD	OUTSIDE AIR TEMPERATURE ($^{\circ}C$)	INTERNAL SURFACE TEMPERATURES ($^{\circ}C$)		SUPPLY AIR CONDITIONS	
			Exterior Walls and Floor	Windows	Velocity (m/s)	Temperature ($^{\circ}C$)
High	Full	-1	16	6	1.50	65
Intermediate	65%	+7	18	11	1.21	55
Low	30%	+15	20	16	0.93	39

again given in Table 1, where the temperatures are those suggested by modern practice (7).

HIGHER-LEVEL MATHEMATICAL MODEL

Background

Air flow and convective heat transfer within an enclosure are governed by the principles of conservation of mass, momentum and thermal energy (or enthalpy). These 'conservation laws' may each be expressed in terms of 'elliptic' partial differential equations, the solution of which provides the basis for a high-level flow model. A discretized form of the governing equations may be obtained by dividing the flow domain into a finite set of small sub-domains, each surrounding a node of the computational grid. The discretized equations are then formulated in such a way that integral conservation requirements are satisfied for individual sub-domains or control volumes. This approach has been called the 'control-volume method' by Patankar (16), and the discretized equations might preferably be distinguished by the prefix 'finite-domain' or 'finite-volume', rather than the term 'finite-difference' commonly employed. The description 'finite-domain equations', suggested by Spalding (17), is adopted here. They are solved in the present higher-level mathematical model by methods similar to those used in the TEACH and CHAMPION family of finite-domain programs developed by Gosman and Pun (18) and Pun and Spalding (19) respectively. Both these codes employ the SIMPLE ('semi-implicit method for pressure linked equations') algorithm of Patankar and Spalding (20), but are restricted to two-dimensional geometries. The authors and their co-workers have therefore used their past experience in applying the CHAMPION code to mechanical ventilation problems (6 and 11) in order to develop a more general computer program capable of simulating three-dimensional flow fields (Alamdari et al (21)). This is called the ESCEAT (Elliptic Equation Solver for Convection and Heat Transfer) code, and was originally employed to compute convective heat transfer in developing, square duct-flow (21). In addition to its ability to handle complex geometries, the program incorporates a number of improvements (described below) in the numerical solution procedure for the finite-domain equations.

Several authors have reported high-level flow model computations for three-dimensional mechanically-ventilated enclosures with both buoyant and non-buoyant conditions. Hjertager and Magnussen (22) developed a finite-domain computer code based on the SIMPLE algorithm (20) which they used to predict the flow and thermal field in a room with a high side-wall register and adjacent ceiling extracts. Buoyancy effects were introduced by way of heated panels in the floor and far wall, together with a cooled air supply. Closure of the finite-domain equations for this turbulent flow was obtained using the popular 'two-equation', 'energy-dissipation' turbulence model (Launder and Spalding (23)), an extended form of which has been adopted for the present study. The authors' comparisons with experimental data (22) displayed good agreement for the isothermal case, although not for the buoyant one. They appear to have made an allowance for buoyancy effects in the mean-flow equations, but not in the turbulence model ones. It is therefore not surprising that their computations were less satisfactory for strongly buoyant flows. A subsequent study by Sakamoto and Matsuo (24) using an early finite-difference technique examined the isothermal flow in a rectangular room with a square, ceiling-mounted supply air 'diffuser' and a low side-wall extract. They employed two different turbulence closure approximations: the standard energy-dissipation model (23) and a more advanced 'large eddy simulation' approach. Comparison with their own experimental mesurements (24) displayed fairly good agreement for the mean-flow field, although not for some of the turbulence properties. Discrepancies were equally apparent with both turbulence closure assumptions, and the authors therefore recommended the use of the simpler energy-dissipation model on grounds of computational economy. Gosman et al (25) used this model, together with a three-dimensional version of the TEACH program, to compute the isothermal flow field in a rectangular enclosure having a square high side-wall register. They report comparisons with mean-flow data that they obtained using laser-Doppler anemometry in a small-scale test rig. This facility had an essentially 'through-flow' geometry with a large low-level slot extract in the far wall. The jet supply conditions were specified using wall-jet empirical data (15) to prescribe the flow properties within an inlet cell. This obviated the need for the very finely-spaced grid that would have been required if computations included the region near the inlet register. The practice also helps to ensure good agreement with the experimental mean-flow measurements. None of the authors of these previous studies (22, 24 and 25) utilised their computer codes to calculate surface heat exchange, as is done in the present one. Each study involved a rectangular cell with no provision for the realistic simulation of window effects. The influence of window downdraught on room air flow is usually very significant, even with forced convective heating or cooling systems.

Mathematical Framework

The governing time-averaged, elliptic equations for the turbulent flow and thermal field may be written in a common form, using tensor notation (25):

$$\underbrace{\frac{\partial}{\partial x_j}(\rho u_j \phi)}_{\text{CONVECTION}} = \underbrace{\frac{\partial}{\partial x_j}\left[\Gamma_\phi \frac{\partial \phi}{\partial x_j}\right]}_{\text{DIFFUSION}} + \underbrace{S_\phi}_{\text{SOURCES OR SINKS}} \quad \ldots\ldots\ldots\

Table 2 - Diffusion Coefficients and Source Terms in the Governing Elliptic Equations

CONSERVED PROPERTY	ϕ	Γ_ϕ	S_ϕ
Mass (continuity)	1	0	0
Direction - i momentum	u_i	μ_{eff}	$-\frac{\partial P}{\partial x_i} + \frac{\partial}{\partial x_j}\left(\mu_{eff}\frac{\partial u_j}{\partial x_i}\right) - \rho g_i \beta\theta$
Thermal energy (enthalpy)	H	$\frac{\mu_{eff}}{\sigma_{eff}}$	0
Turbulence Kinetic energy	k	$\frac{\mu_{eff}}{\sigma_k}$	$G_K + G_B - \rho\varepsilon$
Turbulence energy dissipation	ε	$\frac{\mu_{eff}}{\sigma_\varepsilon}$	$\frac{\varepsilon}{k}\left[C_1(G_K + G_B) - C_2\,\rho\varepsilon\right]$

Notes

1. $\mu_{eff} \equiv \mu + \mu_t = \mu + \frac{C_\mu \rho k^2}{\varepsilon}$; $\sigma_{eff} \equiv \mu_{eff} \Big/ \left(\frac{\mu}{\sigma} + \frac{\mu_t}{\sigma_t}\right)$

2. $G_K = \mu_t \frac{\partial u_i}{\partial x_j}\left(\frac{\partial u_i}{\partial x_j} + \frac{\partial u_j}{\partial x_i}\right)$; $G_B = g_i \beta \frac{\mu_t}{\sigma_t}\frac{\partial \theta}{\partial x_i}$

3. $\theta \equiv T - T_R$, where T_R is the reference temperature

4. Values for the turbulence model 'constants':

$C_\mu = 0.09$, $C_1 = 1.43$, $C_2 = 1.92$, $\sigma_t = 0.85$, $\sigma_k = 1.00$ and $\sigma_\varepsilon = 1.30$

where the velocities and coordinate directions are normal to the cell boundary (b) considered, and A_b is the area of this boundary. Here the first term summation is performed over all six boundaries of the cell, while the associated integrals represent the total transport (J_b) by convection and diffusion across each boundary. These integrals may be written in the following, finite-domain form (16):

$$J_b = C_b\phi_p + \left\{D_b\,\alpha(|Pe_b|) + [0, -C_b]\right\}(\phi_p - \phi_b) \quad \ldots\ldots(6)$$

where $C_b (\equiv \rho u_b A_b)$ is the convection term, $D_b (\equiv \Gamma_b A_b/\delta x_{np})$, is the diffusion term, $Pe_b (= C_b/D_b)$ is the 'cell Peclet number', and $\alpha(|Pe_b|)$ is a weighting function, while the symbol [a,b] denotes the greater of a and, b. In the ESCEAT code the weighting function is evaluated using a 'power-law' differencing scheme (16) $\alpha(|Pe_b|) = [0, (1-0.1|Pe_b|)^5]$. This scheme yields improved accuracy over some of the older approaches, such as the upwind (19) or hybrid (18 and 25) schemes. The source term integral in Equation (5) is evaluated using a linearised expression ($S_p + S_p'\phi_p$) in order to enhance numerical stability (16, 18 and 19). This is particularly important when S_ϕ is a function of the variable ϕ itself, such as in the case of the k and ε equations (see Table 2). Thus, integration of Equation (5) in the above manner leads to finite-domain equations for each of the dependent variables in the form:

$$(a_p - S_p')\,\phi_p = \sum_n a_n\phi_n + S_p \quad \ldots\ldots(7)$$

where the coefficients $a_n = D_n\,\alpha(|Pe_n|) + [0, \pm C_n]$, and $a_p = \sum_n a_n$. The velocity components are calculated in the ESCEAT code at staggered locations mid-way between adjacent grid nodes (20).

This practice has the advantage of ensuring that the velocities are directly available for calculating the convective fluxes of the scalar variables, as well as lying between the location of the static pressures that drive them. However, it necessitates minor changes to the coefficient expressions, as outlined in Mohammad's thesis (29).

The set of algebraic finite-domain equations represented by Equation (7) are solved in the ESCEAT code in an iterative, 'line-by-line' manner (16 and 19), using a tri-diagonal matrix algorithm (19 and 20). Here the velocities and pressures are calculated via the SIMPLEC algorithm, recently proposed by Van Doormaal and Raithby (30). This is a variant of the SIMPLE algorithm (20) which is more consistent, and consequently induces a faster rate of convergence. The latter is also enhanced by the adoption of a plane-by-plane 'block-correction' procedure applied by sweeping the flow domain in the x_3- direction (see Figure 2). These block adjustments were based on the requirements for overall mass and momentum conservation. The computational grid employed for the present simulation of the warm-air heated room utilised a 17x17x15, non-uniform nodal network, whose fineness can be judged by the velocity vector diagrams presented in Figure 3. In the previous two-dimensional high-level flow model computations by the authors (6 and 11) a jet inlet cell was utilised, over which the variation of the dependent variables was prescribed. This reduced the need for a finely-spaced grid near the supply register. However, it is difficult to prescribe the near-register flow and thermal field in a strongly buoyant situation. such as the present one. Consequently, a jet inlet cell has not been employed in the current study, for which about 700 iterations were required to obtain a converged solution. The latter was assumed to have been obtained when the finite-domain equations were satisfied to within 0.5% or less of the inlet mass flow, or the heat supplied in the case of the H-equation. Further details of the ESCEAT code, including the measures taken to ensure grid-independent solutions in the present case, will be reported elsewhere (29).

INTERMEDIATE-LEVEL MATHEMATICAL MODEL

The ROOM-CHT program (7) prescribes the flow and thermal field within mechanically-ventilated enclosures using the known characteristics of turbulent wall-jets (15). These jets are the normal means of air distribution in buildings with forced convective heating or cooling systems. They are assumed to spread out from their supply register and sequentially flow over the room surfaces. The code was developed in both two- and three-dimensional versions (7), to facilitate the simulation of enclosures with supply apertures in the form of either linear slots or rectangular grilles. The mean-flow properties for the three-dimensional version used here are calculated from wall-jet empirical data (15). These are then employed to determine the corresponding local heat transfer distribution over the room surfaces, using the 'optimum log-law' devised by Hammond (31) on the basis of wall-jet profile analysis. The convection coefficient h_c [$\equiv q_w/(T_R - T_W)$] may locally fall below that for buoyancy-driven motion at the corresponding temperature difference. Under such conditions the latest version of the code uses the improved correlating equations for buoyancy-driven convection recently developed by Alamdari and Hammond (32). These are rather elaborate, continuous functions that cover the full range of laminar, transitional and turbulent airflows.

The equations which constitute the ROOM-CHT program are generally explicit, algebraic ones, except for the heat transfer log-law which is implicit and is solved using the Newton-Raphson iterative method. Nevertheless, the estimation of initial values for the flow field parameters from experimental data (15) enables a convergent solution to be obtained very rapidly; typically in about three iterations. The computational grid normally employs around 10 uniformly-spaced calculation points per metre length of surface. The surface-averaged heat transfer coefficients are obtained by numerical integration of the local distributions. Fuller details of the mathematical content of the ROOM-CHT program are given in the previous papers of the authors (6,7,11,31 and 32).

A limitation of all intermediate-level models (6) is that they have a restricted range of application, and need to be used in conjunction with a broad flow classification scheme (see Figure 1). In the present case, the ROOM-CHT program is only valid for air distribution systems in which the supply air jet is emitted near, and runs parallel to, one of the room surfaces. Nevertheless, this is not a serious weakness as building thermal modellers are well used to working with problem-specific input data. A potentially more serious restriction for such models is that, because they are 'generalisations' of lower-level ones for simple shear flows, they cannot deal rigorously with the consequences of flow interactions. Wall-jets within space-conditioned enclosures, for example, are influenced by jet-impingement against backward-facing walls, and by 'secondary flows' or longitudinal vortices along streamwise corners (6 and 11). Rather ironically, it has recently been found (11) that in the former situation the ROOM-CHT program was better able to compute surface heat exchange than a high-level flow model. This was because the ability of models of the latter type to determine surface heat transfer is hampered by limitations in the present generation of turbulence model wall functions, despite the fact that they can more accurately simulate complex flow patterns. The flow interaction which is

of central concern to the present study is that induced by buoyancy effects. These are modelled explicitly in the ESCEAT code by incorporating buoyancy source terms in the x_2- direction momentum, k and ε transport equations (Equation (1) and Table 2). In contrast, the ROOM-CHT program is unable to take account of such effects in any rigorous manner. It is essentially a non-buoyant model, which only allows for buoyancy-driven convection when the corresponding heat transfer coefficient is greater than the prevailing forced convection value, and then only in an approximate way (6 and 7). Consequently, differences between the computed local heat transfer distributions reported in the following section are primarily due to this cause.

COMPUTATIONS

Flow Field

Velocity vector diagrams illustrating the flow pattern within the warm-air heated room under full heat load conditions are shown in Figure 3. These plots were obtained using the ESCEAT code, and display vectors in the $x_2 - x_3$ plane at three positions which coincide with those of the air extract grilles. Here the tail of each velocity vector indicates the location of a node in the finite-domain computational grid. It is therefore evident that these nodes were concentrated close to the room surfaces, as well as to the jet inlet. This arrangement was adopted in order to provide more nodes in those regions where there are steep dependent variable gradients. The computed flow pattern can be seen to be strongly influenced by buoyancy effects, due to the high temperature of the supply air and the counteracting cold downdraught induced by the windows. In particular, the downdraught from the window in the right wall (viewed from the supply register) clearly damps the rigorous buoyant flow in the rest of the enclosure. The pattern in the latter region is characterised by two recirculating flow regions: one dominated by the buoyant supply jet and the other by the cold downdraught from the window in the far-wall. The ability of high-level flow models to simulate complex flows, such as this, are their major achievement in comparison with intermediate-level ones. A velocity vector diagram produced by the ROOM-CHT program would simply show a wall-jet circulating around the enclosure, with no obvious influence of buoyancy. This would not be adequate for determining, for example, the thermal comfort conditions in the occupation zone, which would require a high-level simulation.

Convective Heat Transfer Coefficients

The local distribution for the convection coefficients corresponding to the above flow pattern are displayed as 'carpet' plots in Figure 4. Here the computed variation over each of the room surfaces according to both the ESCEAT and ROOM-CHT programs are presented. The almost flat distributions given by the intermediate-level code for the near- and side-walls arises because the surface coefficient there is computed from elaborate correlating equations for buoyancy-driven convection (32). These yield a constant, surface-averaged coefficient whenever the local forced convection coefficient would otherwise fall below this value. In contrast, the peculiar peak in the distribution predicted by the high-level flow model near the supply register (see Figure 4 (d)) is simply a consequence of air entrainment into the jet, which causes locally high velocities and heat transfer rates around this rectangular aperture. It is again clear from these carpet plots that the ESCEAT code is better able to simulate the influence of buoyancy, here on heat transfer. However, although there are obviously differences emanating from the neglect of buoyancy effects in the ROOM-CHT program, these are not significant from the point of view of building thermal simulation.

Dynamic building thermal models normally employ heat transfer coefficients that are surface-averaged over each building element (6 and 7): ceilings, floors, roofs, walls and windows. Such values are presented for the warm-air heated room and all three representative heat loads in Table 3, together with those recommended as 'typical' values in the section of the UK CIBSE Guide which deals with the thermal response of buildings (10). In contrast to the latter recommendations, the heat transfer section of the Guide (9) provides an approximate correction factor to buoyancy-driven convection data when the air velocity over a particular surface is non-zero. This practice is not, in reality, very helpful as the designer generally has no means of determining this velocity a priori (7). Nevertheless, the authors in a previous study estimated the surface-averaged air velocities for the present enclosure, using the ROOM-CHT program in order to determine the convection coefficient in this way. These turned out to be significantly lower than those given in Table 3 (see (7)), and only slightly above those that would apply for purely buoyancy-driven convection (32). The corresponding room-averaged coefficient at full heat load was found to be 2.3 $W\,m^{-2}K^{-1}$. This value may be compared with those computed by the ESCEAT code and the ROOM-CHT program, which were found to be some 60% higher and are given in Table 4. The ASHRAE Handbook in the USA (8) appears to ignore the possibility of forced convective heating or cooling, and employs only buoyancy-driven coefficients to obtain fabric 'U-values'. These would again fall well below the values given in Tables 3 and 4. It is apparent from these tables that the convection data obtained with the high-level and intermediate-level computer codes are in generally good agreement for this particular room/heating

TABLE 3 - Internal Surface-averaged Convection Coefficients (h_c, $Wm^{-2}K^{-1}$)

SURFACE ELEMENT	HEAT LOAD/ DEMAND	CALCULATION METHOD		
		ESCEAT	ROOM-CHT	CIBSE (10)
FLOOR	Full	2.4	6.4	1.5
	Intermediate	1.9	6.1	1.5
	Low	1.7	5.1	1.5
FAR-WALL	Full	2.4	3.5	3.0
	Intermediate	2.1	3.2	3.0
	Low	1.6	2.8	3.0
FAR-WINDOW	Full	2.2	3.5	3.0
	Intermediate	2.0	3.1	3.0
	Low	1.5	2.6	3.0
CEILING	Full	6.9	3.9	4.3
	Intermediate	6.9	3.4	4.3
	Low	4.1	2.2	4.3
NEAR-WALL	Full	2.2	2.4	3.0
	Intermediate	2.3	2.2	3.0
	Low	1.5	1.6	3.0
RIGHT-WALL	Full	3.6	2.5	3.0
	Intermediate	3.4	2.2	3.0
	Low	2.5	1.8	3.0
RIGHT-WINDOW	Full	2.2	3.5	3.0
	Intermediate	2.0	3.1	3.0
	Low	1.5	2.6	3.0
LEFT-WALL	Full	3.3	1.8	3.0
	Intermediate	3.2	1.7	3.0
	Low	2.2	1.5	3.0

system configuration, except for the ceiling and floor. The latter surfaces are the ones that are most directly affected by the upward trajectory of the buoyant jet on leaving the supply register (see Figures 3(b), 4(a) and 4(c)). It is rather surprising that the typical values suggested in the CIBSE Guide Part A5 (10) yields coefficients for this case that are of comparable accuracy to those of the ROOM-CHT program. This seems to be merely a fortuitous occurrence, which has arisen because these values are, in reality, significantly higher than those that would prevail with the buoyancy-driven convection that they purport to represent. They cannot be relied upon to yield accurate data for other mechanically-ventilated enclosures.

Economy

The present simulations using the ESCEAT code required about 5 hours of central processor unit (CPU) time per run (heat load) on a DEC VAX 11/785 computer. This compares with a CPU time of only one minute using the ROOM-CHT program. These dramatic savings in running time achieved by the intermediate-level model, are accompanied by a need for only one third of the computer storage

TABLE 4 - Notional Room-averaged Convection Coefficients (h_c, $Wm^{-2}K^{-1}$)

HEAT LOAD/ DEMAND	CALCULATION METHOD		
	ESCEAT	ROOM-CHT	CIBSE (10)
Full	3.7	3.5	3.0
Intermediate	3.5	3.2	3.0
Low	2.4	2.6	3.0

requirement. Thus, high-level flow models require computational resources that are of the same order as building thermal models themselves. It would not therefore be a realistic approach to directly couple such computer codes together (6). Any gain in terms of accuracy, over lower- and intermediate-level methods, would be far outweighed by the extra resources consumed.

CONCLUDING REMARKS

Several lessons may be drawn from the computations of air flow and convective heat transfer within a warm-air heated room presented here. It is evident that high-level flow models, such as the ESCEAT finite-domain program, are capable of simulating the complex flow patterns generated within the enclosure. Accurate prediction of the flow and thermal field would be needed in order to determine, for example, the occupation zone thermal comfort conditions. However, the far greater computer resources that they require, compared to simpler calculation methods, would prohibit their direct use in providing input heat transfer data for building thermal simulation programs. In contrast, the authors and their co-workers previously demonstrated (6) that their intermediate-level convection models can be fairly readily incorporated into these programs as subroutines. A better use of high-level flow models in the context of heat transfer would therefore be for the development and verification of intermediate-level calculation methods. The simple guidelines for specifying convection coefficients that are contained in Part A5 of the CIBSE Guide (10) were shown to give surprisingly good agreement with the ESCEAT code surface-averaged values. Nevertheless, it has been argued here that this was only a fortuitous occurrence, that does not justify the use of these guidelines for enclosures employing other mechanical-ventilation systems. This is particularly so in warm-air heated rooms where the supply air is discharged vertically over an adjacent window, giving rise to high convection rates from the latter element. Likewise, air-conditioned offices using linear diffusers would also lead to locally high heat transfer rates over the surface near the supply aperture that could not be accounted for using the CIBSE guidelines. Intermediate-level calculation methods could be readily adapted to handle these situations.

ACKNOWLEDGEMENTS

The work reported here was partially supported by a UK Science and Engineering Research Council research grant GR/C/2419.0, and forms part of the Council's specially promoted programme on 'Energy in Buildings'. One of the authors (WSM) is grateful to the Military Technical College, Baghdad, Iraq, for the sponsorship that enabled him to contribute to this study. All the authors appreciate the care with which Mrs. A. Stalley prepared the camera-ready typescript and Mrs. K. O'Connell traced the figures.

The authors' names appear alphabetically.

SYMBOLS USED

A_b = area of finite-domain cell boundary [Equation (5)]

a = coefficients in finite-domain equations [Equation (7)]

C_b, C_n = convection term in finite-domain equations [Equations (6) and (7)]

C_p = fluid specific heat at constant pressure (J $Kg^{-1}K^{-1}$)

C_μ, C_1, C_2 = 'constants' in the k-ε turbulence model [Table 2]

D_b, D_n = diffusion term in finite-domain equations [Equations (6) and (7)]

E = wall function log-law 'integration' constant [Equation (2)]

f_ε = near-wall k-equation dissipation term parameter [Equation (4)]

G_B = buoyancy generation term in the k-equation [Table 2]

G_K = shear generation term in the k-equation [Table 2]

g_i = gravitational vector ($g_1 = g_3 = 0$, $g_2 = -9.81$ m s^{-2})

h_c = convective heat transfer coefficient (W $m^{-2}K^{-1}$)

H = enthalpy (J Kg^{-1})

J_b = total transport by convection and diffusion across finite-domain cell boundaries [Equation (6)]

k = turbulence kinetic energy (m^2s^{-2})

n = normal distance from a surface or wall (m)

n^+ = $u_\tau n/\nu$

Pe_b, Pe_n = finite-domain cell Peclet number [Equation (6) and (7)]

P_J = Jayatillaka's P-parameter [Equation (3)]

$\dot{q}$ = convective heat flux (W m^{-2})

Sp, Sp' = coefficients in linearised finite-domain source expression [Equation (7)]

S_ϕ = sources or sinks for the variable ϕ [Equation (1)]

t = temperature (C)

T = absolute temperature (K)

T^+ = $\rho\ Cp\ u_\tau\ (T - T_W)/q_W$

u_i = velocity components in the x_i -direction (m s^{-1})

u_τ = 'wall shear' velocity ($\equiv \sqrt{\tau_W/\rho}$, m s^{-1})

v = resultant velocity in planes parallel and close to a surface or wall (m s^{-1})

v^+ = v/u_τ

W = x_1 — direction width of the enclosure (m)

x_i = coordinate directions (m)

Greek Symbols

β = coefficient of cubic expansion ($\simeq T_R^{-1}$ for air, K^{-1})

Γ_ϕ = effective diffusion coefficients for each variable ϕ [Equation (1)]

ε = turbulence energy dissipation rate ($m^2\ s^{-3}$)

θ = $T - T_R$ (K)

κ = von Karman's constant [Equation (2)]

μ = dynamic viscosity (kg $m^{-1}s^{-1}$)

ν = kinematic viscosity (m^2s^{-1})

ρ = fluid density (Kg m^{-3})

σ = Prandtl number

τ = shear stress (N m^{-2})

ϕ = any dependent variable [Equation (1)]

Subscripts

eff = effective (laminar plus turbulent)

n = neighbouring node in finite-domain grid

p = central node in finite-domain grid

R = reference (or occupation zone) conditions

t = turbulent

w = wall (or surface) conditions

REFERENCES

1. Carroll, D., 1982, "Energy Consumption and Conservation in Buildings : An International Comparison", Proc. 3rd Int. Symp. "Energy Conservation in the Built Environment", 1A, 190, Dublin, Ireland.

2. Clarke, J.A., 1985, "Energy Simulation in Building Design", Adam Hilger, Bristol, England.

3. Day, B., 1982, Computer-aided Design 14, 49.

4. Wiltshire, T.J., 1983, Sun at Work in Britain, No.16, 19.

5. Irving, S.J., 1982, Computer-aided Design 14, 33.

6. Alamdari, F., Hammond, G.P., and Melo, C., 1984, "'Appropriate' Calculation Methods for Convective Heat Transfer from Building Surfaces", Proc. First UK National Heat Transfer Conf., 2, 1201, Leeds, England.

7. Alamdari, F., and Hammond, G.P., 1982, "Time-dependent Convective Heat Transfer in Warm-air Heated Rooms", Proc. 3rd Int. Symp. "Energy Conservation in the Built Environment", 4, 209, Dublin, Ireland.

8. ASHRAE, 1981, "Handbook of Fundamentals", ASHRAE, New York, USA.

9. CIBSE Guide, C3 : "Heat Transfer", 1976, CIBSE, London, England.

10. CIBSE Guide, A5 : "Thermal Response of Buildings", 1979, CIBSE, London, England.

11. Alamdari, F., Hammond, G.P., and Montazerin, N., 1986, "Heat/Mass Transfer Beneath a Two-dimensional Wall-jet Deflected by a Normal, Flat-plate Obstruction", Proc. 8th Int. Heat Transfer Conf., San Francisco, USA, (In Press).

12. Warm Air Group - SBGI, 1976, "Gas Fired Warm Air Heating : British System Design Manual", Ernest Benn, London, England.

13. Pimbert, S.L., 1978, Gas Marketing 22(8), 6.

14. The Electricity Council, 1981, "The Medallion Award Specification", EC 4155.

15. Rajaratnam, N., 1976, "Turbulent Jets", Elsevier, Amsterdam, Netherlands.

16. Patankar, S.V., 1981, Numerical Heat Transfer 4, 409.

17. Spalding, D.B., 1981, Mathematics and Computers in Simulation 23, 267.

18. Gosman, A.D., and Pun, W.M., 1974, "Calculation of Recirculating Flows", Imperial College (London Univ.) Mech. Eng. Dept. Report HTS/74/2 (Second Edition).

19. Pun W.M., and Spalding, D.B., 1976, "A General Computer Program for Two-dimensional Elliptic Flows", Imperial College (London Univ.) Mech. Eng. Dept. Report HTS/76/2 (Amended 1977).

20. Patankar, S.V., and Spalding, D.B., 1972, Int. J. Heat Transfer 15, 1787.

21. Alamdari, F., Hammond, G.P., Macaskill, C., and Mohammad, W.S., 1986, "Thermal Boundary Condition Effects on Turbulent Heat Transfer in Developing, Square Duct-flow", Paper in preparation.

22. Hjertager, B.H., and Magnussen, B.F., 1977, "Numerical Prediction of Three-dimensional Turbulent Buoyant Flow in a Ventilated Room", Spalding, D.B., and Afgan, N. (Editors), "Heat Transfer and Turbulent Buoyant Convection", 2, 429, Hemisphere, Washington, USA.

23. Launder, B.E., and Spalding, D.B., 1974, Comput. Methods Appl. Mech. Eng. 3, 269.

24. Sakamoto, Y., and Matsuo, Y., 1980, Appl. Math. Modelling 4, 67.

25. Gosman, A.D., Nielsen, P.V., Restivo, A., and Whitelaw, J.H., 1980, ASME J. Fluids Eng. 102, 316.

26. Rodi, W., 1980, "Turbulence Models and Their Application in Hydraulics", International Association for Hydraulics Research, Delft.

27. Hammond, G.P., 1985, AIAA Journal 23, 1668.

28. Nevins, R.G. and Miller, P.L. 1972, ASHRAE Trans. 78, 235 (Paper No. 2258)

29 Mohammad, W.S., 1986, PhD. Thesis, Cranfield Institute of Technology, (In preparation).

30. Van Doormaal, J.P., and Raithby, G.D., 1984, Numerical Heat Transfer 7, 147.

31. Hammond, G.P., 1982, "Profile Analysis of Heat/Mass Transfer Across the Plane Wall-jet", Proc. 7th Inst. Heat Transfer Conf., 3, 349, Munich, Germany (FRG).

32. Alamdari, F., and Hammond, G.P., 1983, BSER & T 4, 106.

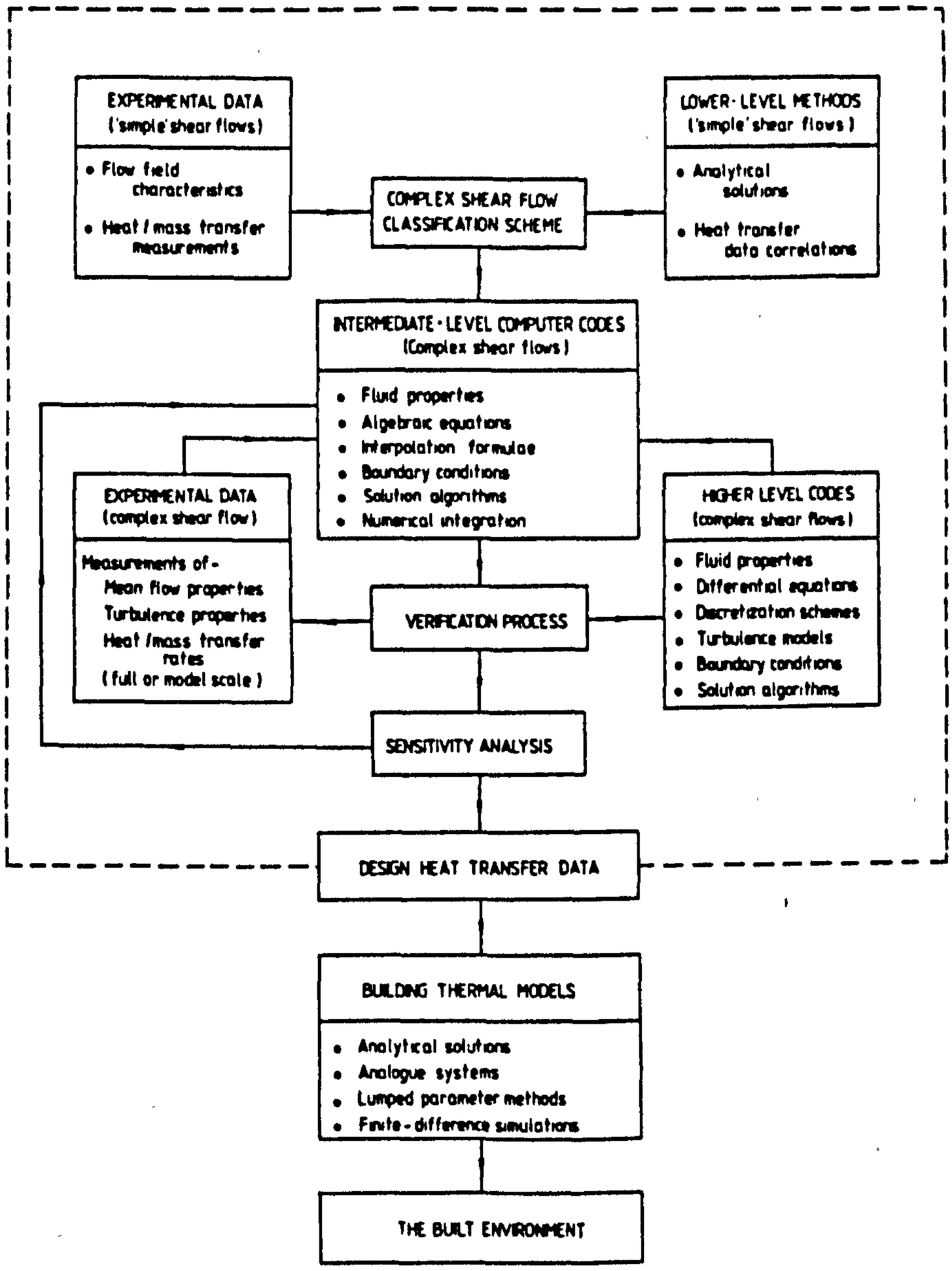

Figure 1. Interrelationship Between the Various Calculation Methods for Building Convective Heat Transfer (6)

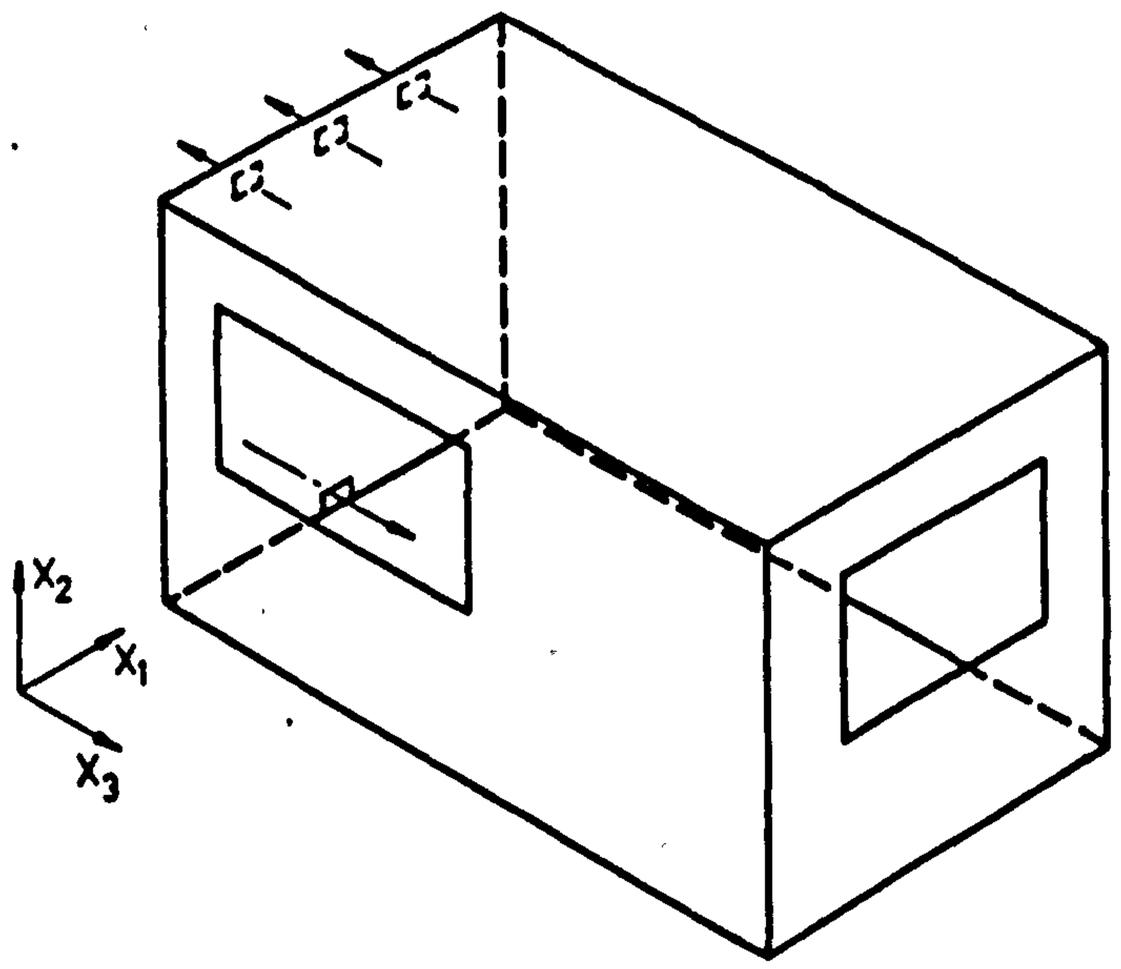

Figure 2. Schematic Diagram of Warm-air Heated Room with 'Low Side-wall Register' (7)

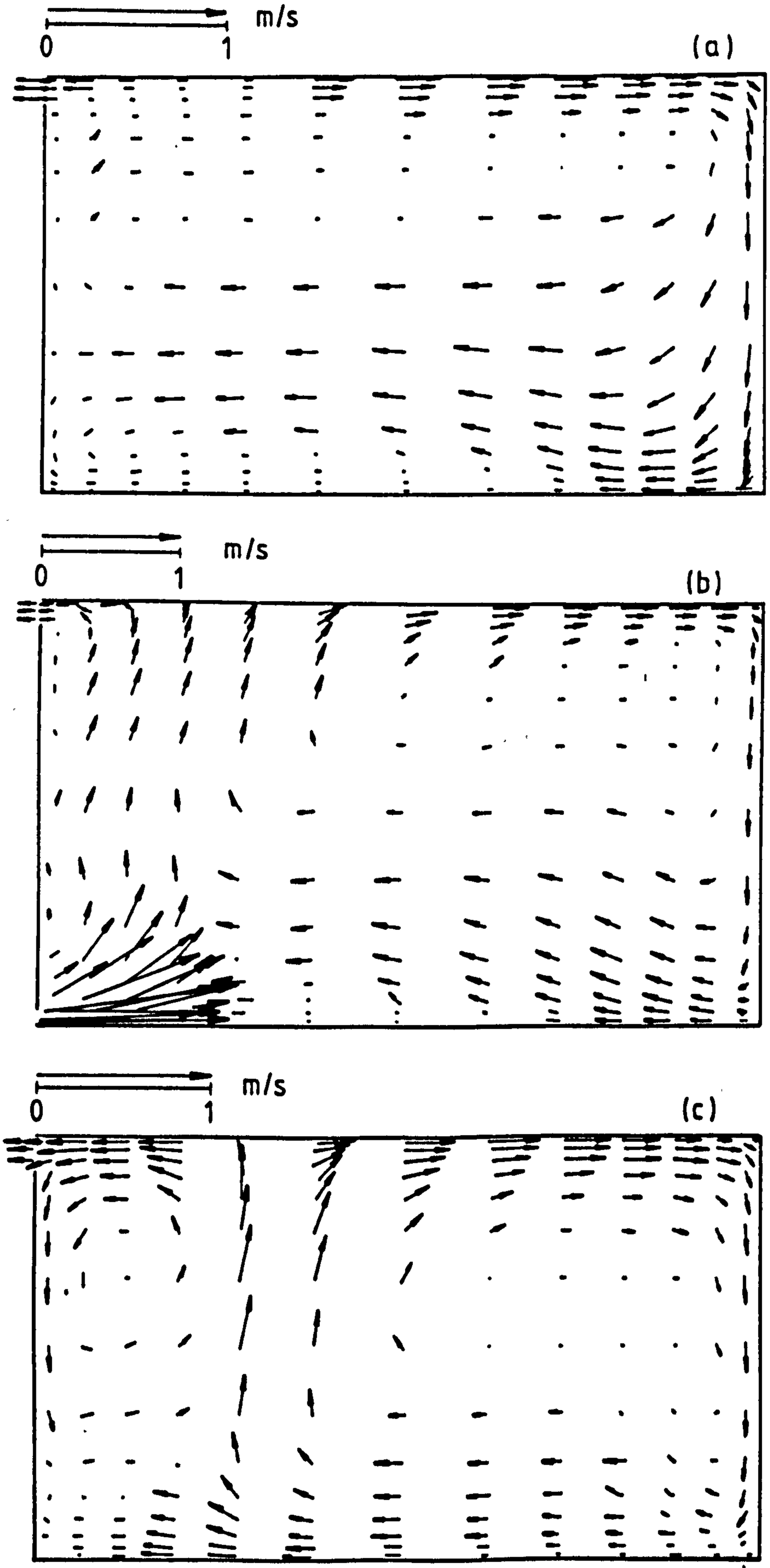

Figure 3. Flow Field Velocity Vectors (Computer Using the ESCEAT Code) : (a) $x_1/W = 0.25$, (b) $x_1/W = 0.50$, (c) $x_1/W = 0.75$ [Note scale change.]

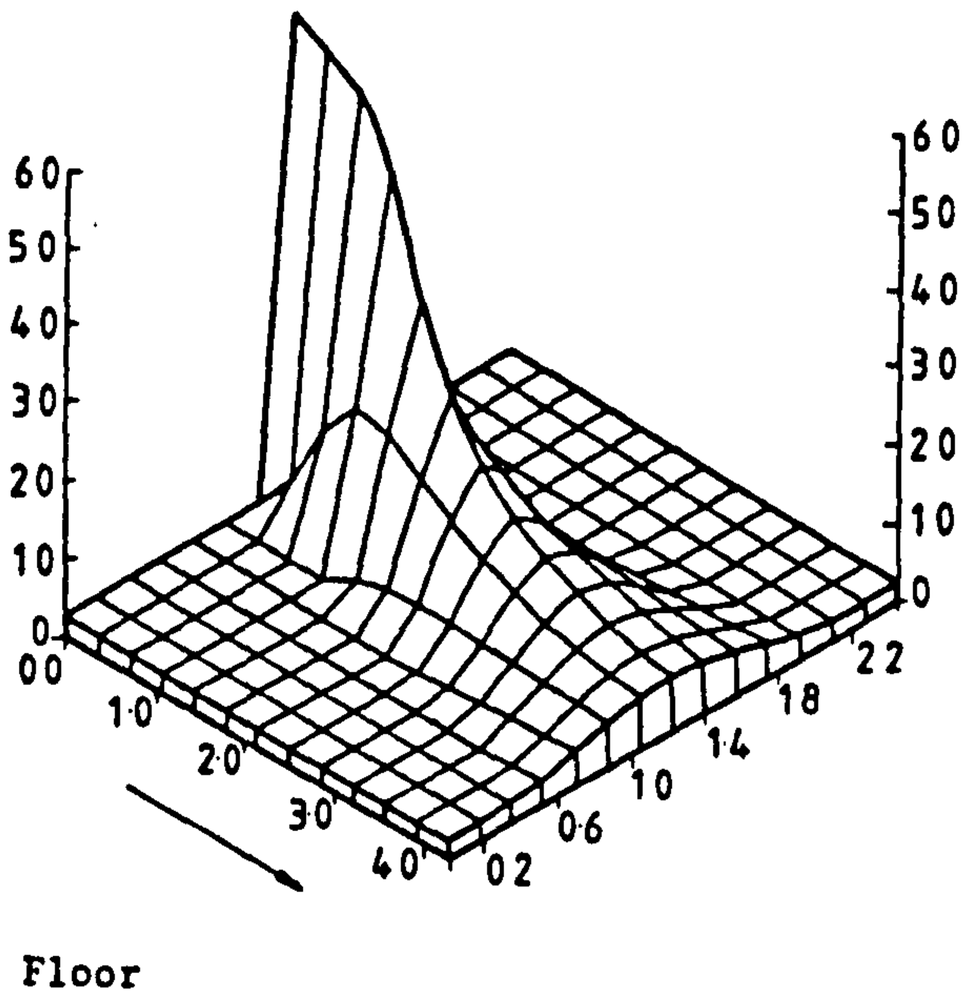

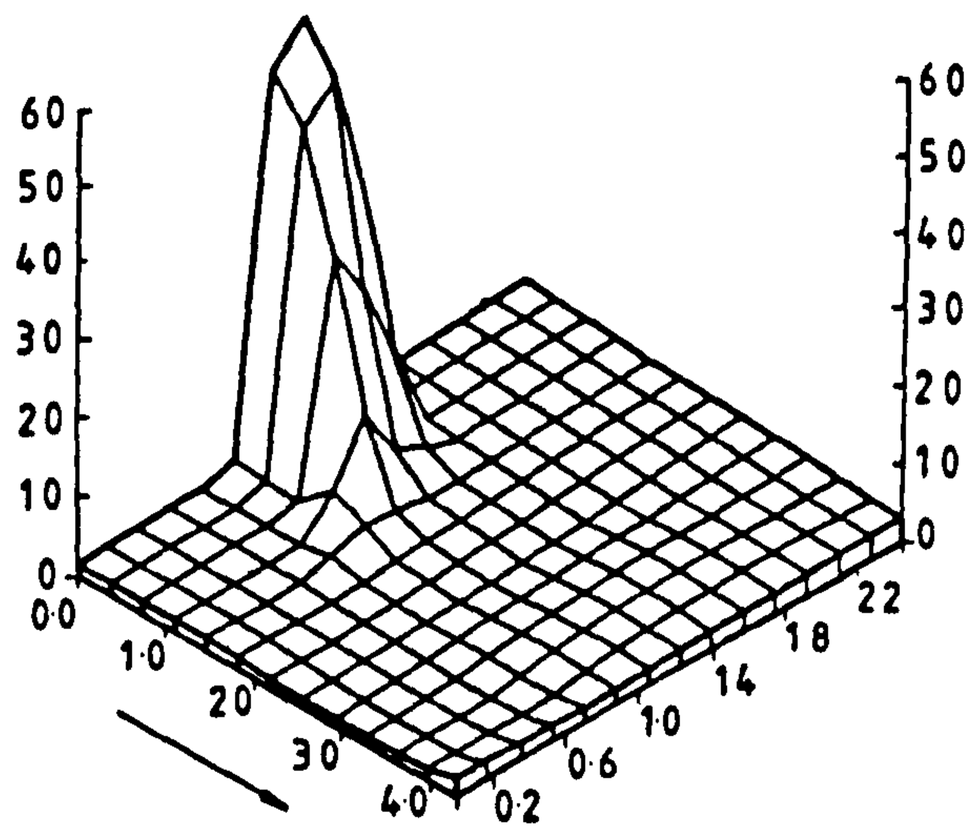

(a) Floor

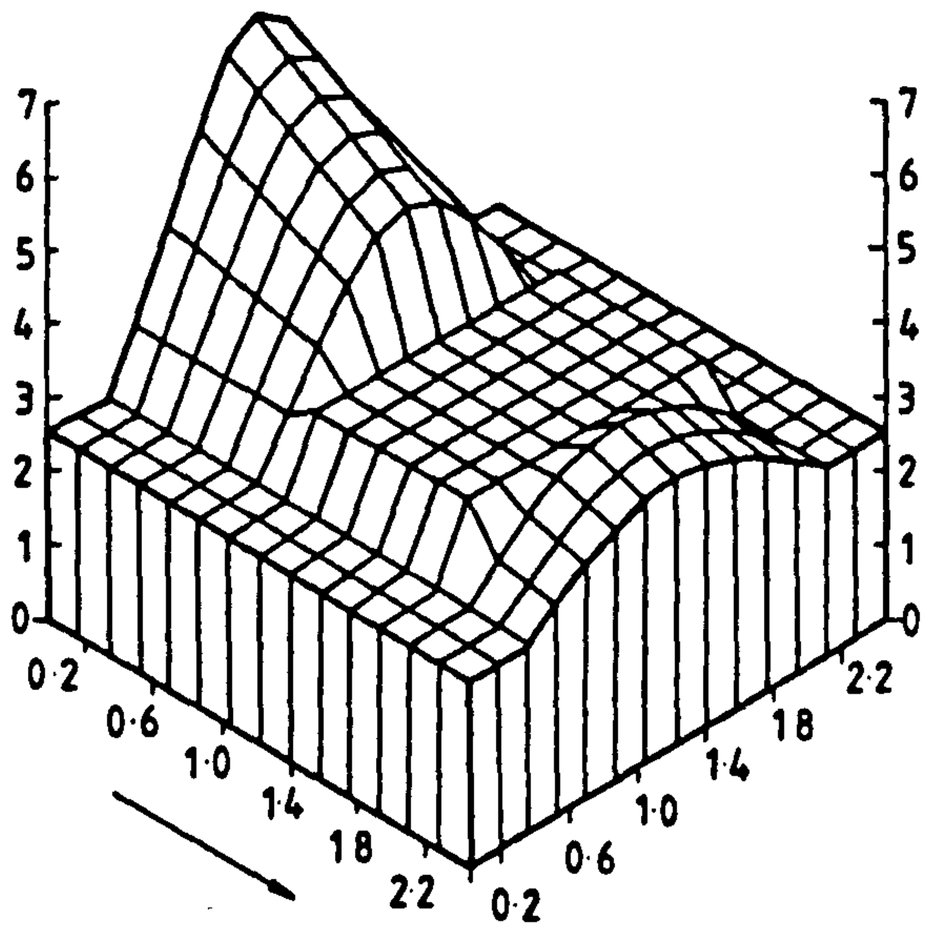

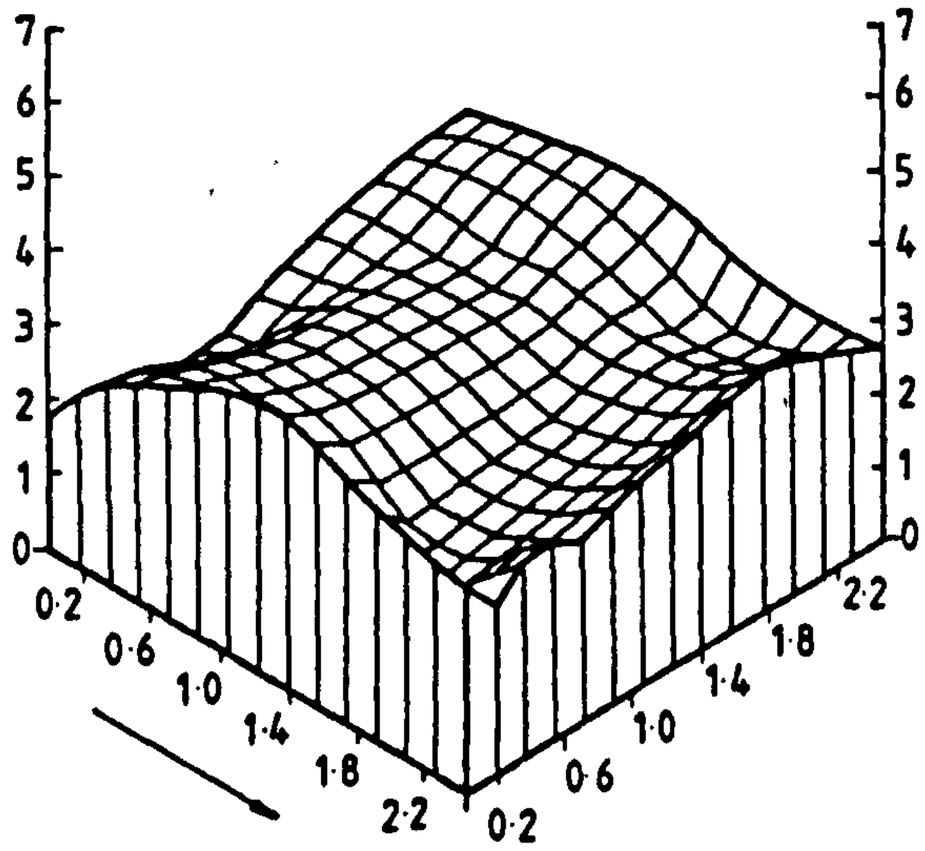

(b) Far-wall and window

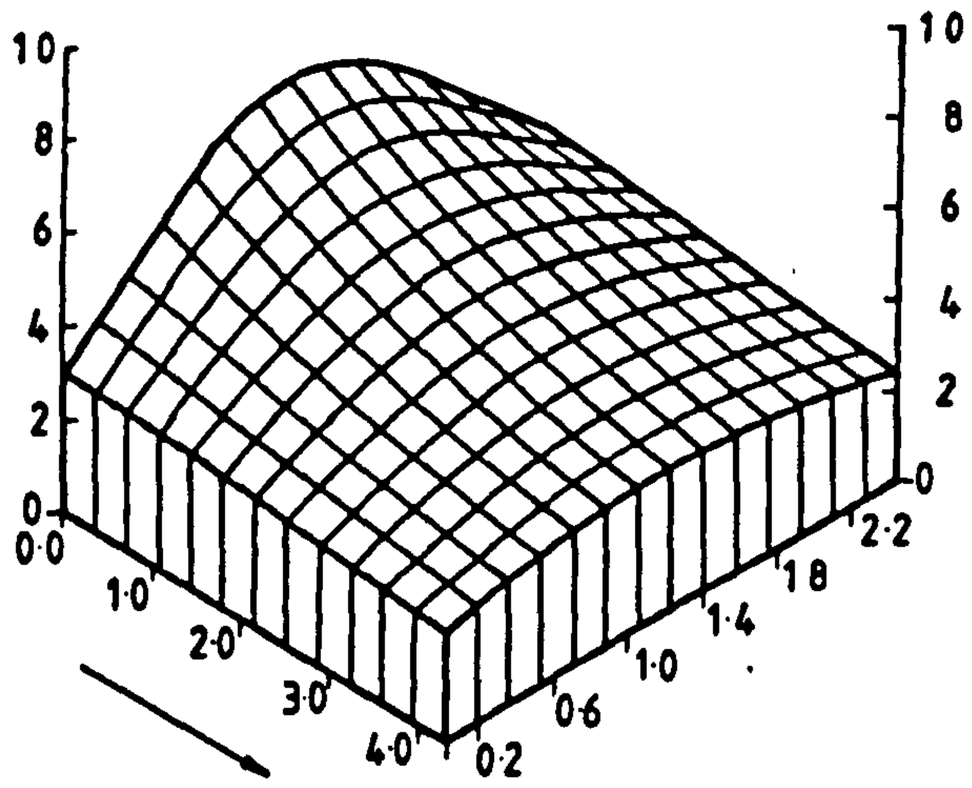

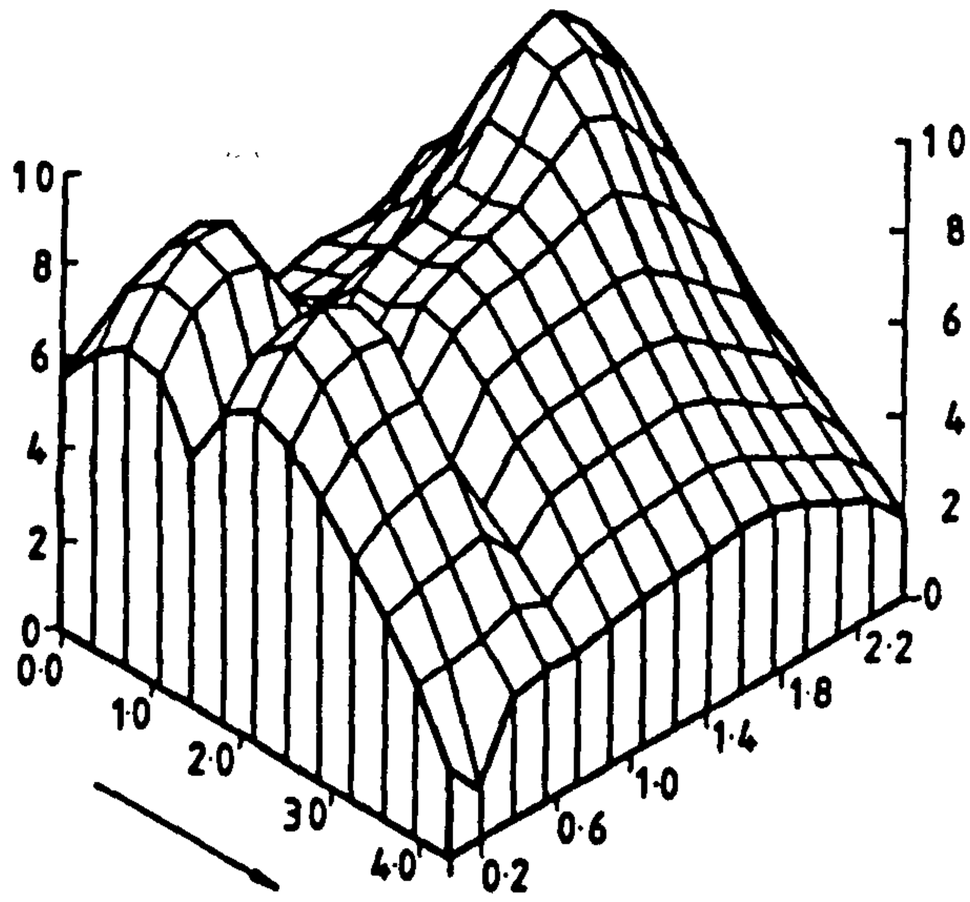

(c) Ceiling

Figure 4. Room Surface Convective Heat Transfer Distributions (h_c, $W \cdot m^{-2}K^{-1}$)
: LHS - ROOM-CHT Program, RHS-ESCEAT Computer Code.

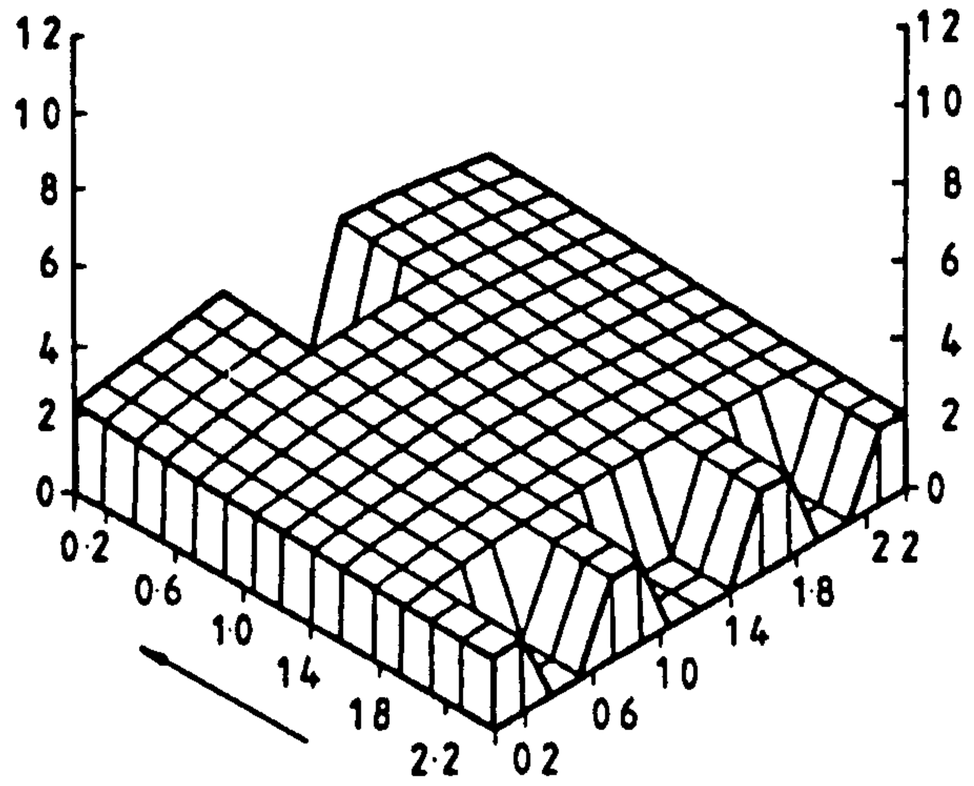

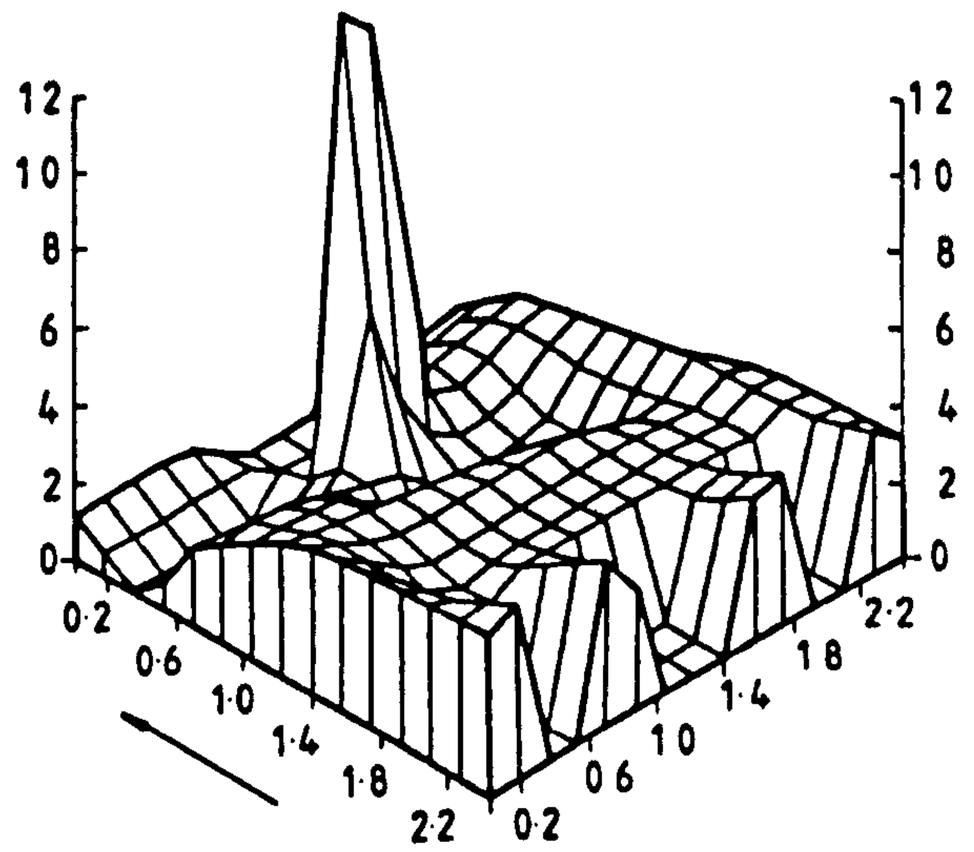

(d) Near-wall

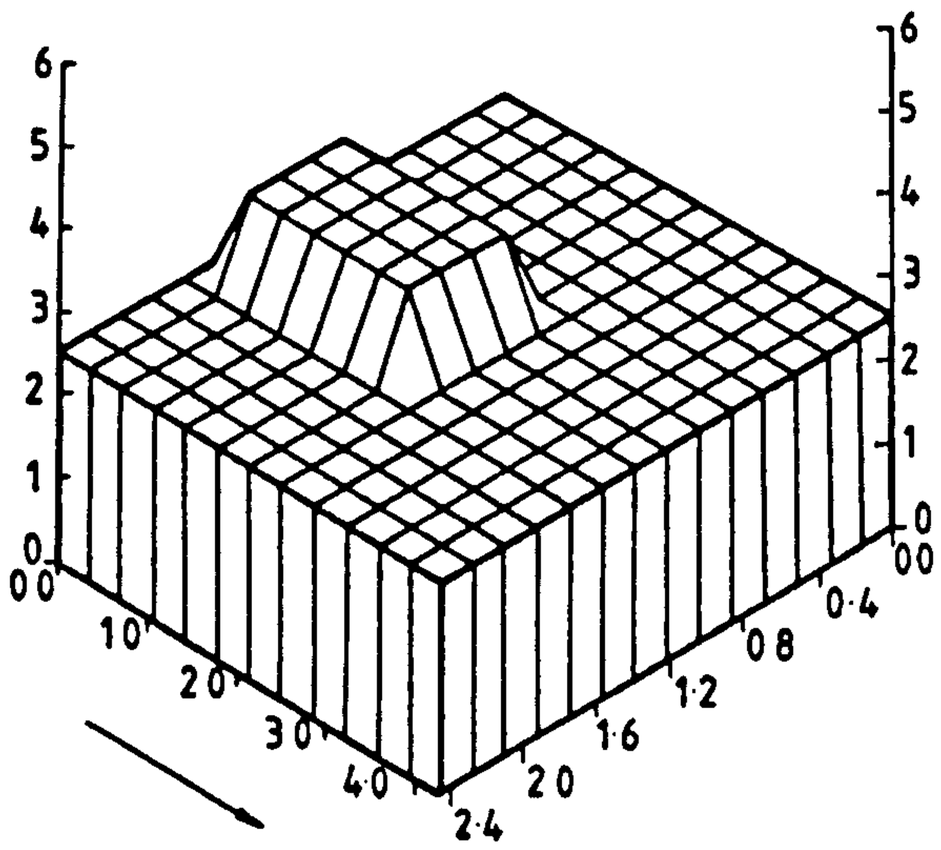

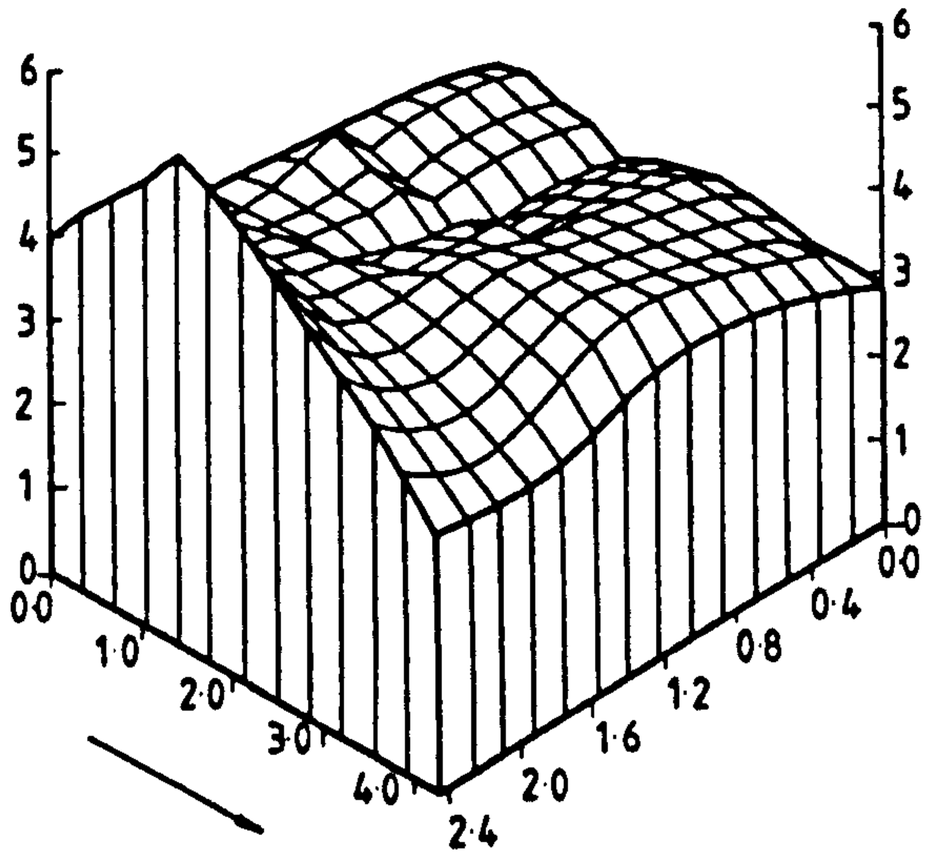

(e) Right-wall and window

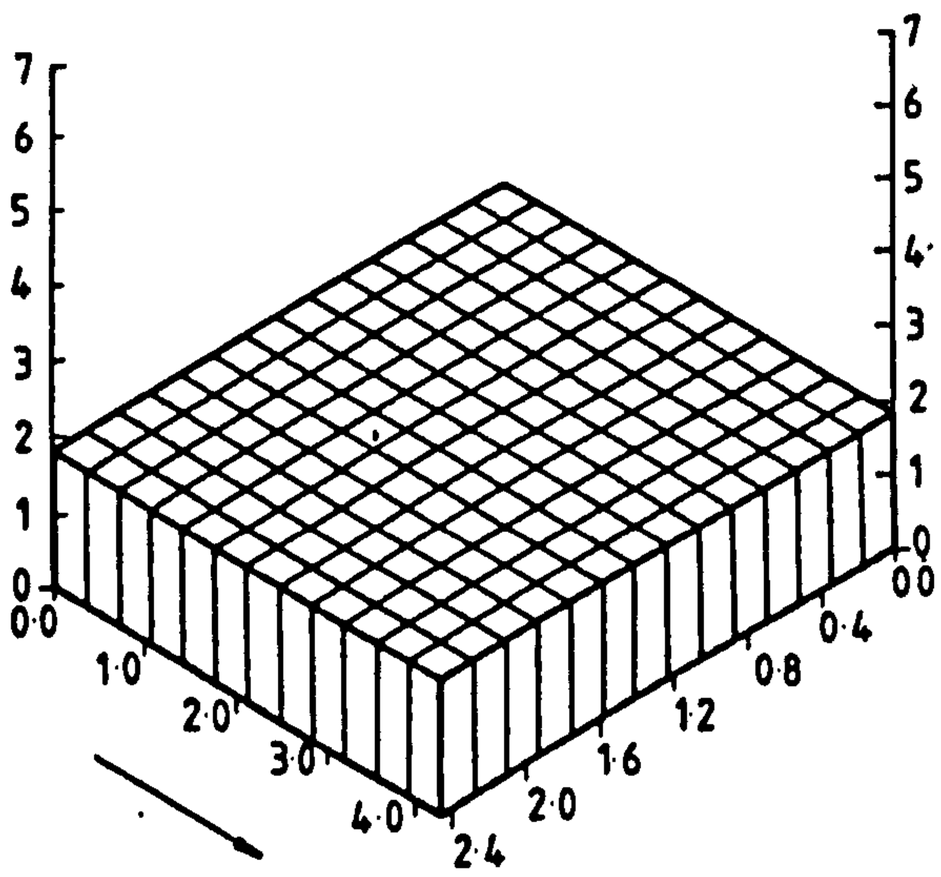

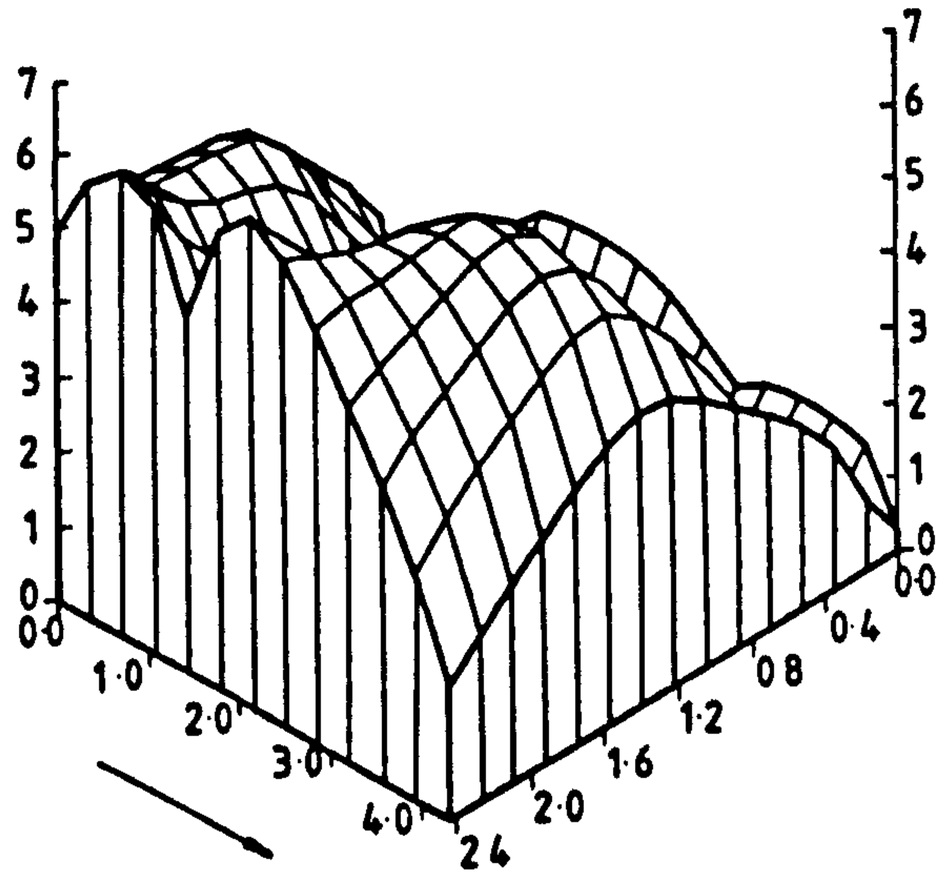

(f) Left-wall

Figure 4 continued...